DGK Ausschuss Geodäsie (DGK)
der Bayerischen Akademie der Wissenschaften

Reihe C | Dissertationen | Heft Nr. 964

Johannes Kröger

# Estimation and Validation of multi-GNSS multi-Frequency Phase Center Corrections

München 2025

Verlag der Bayerischen Akademie der Wissenschaften, München

ISSN 0065-5325 ISBN 978-3-7696-5376-2

DGK Ausschuss Geodäsie (DGK)
der Bayerischen Akademie der Wissenschaften

Reihe C Dissertationen Heft Nr. 964

# Estimation and Validation of multi-GNSS multi-Frequency Phase Center Corrections

Von der Fakultät für Bauingenieurwesen und Geodäsie
der Gottfried Wilhelm Leibniz Universität Hannover
zur Erlangung des akademischen Grades
Doktor-Ingenieur (Dr.-Ing.)
genehmigte Dissertation

von

Johannes Kröger, M. Sc.
Geboren am 20.02.1992 in Hannover

München 2025

Verlag der Bayerischen Akademie der Wissenschaften, München

ISSN 0065-5325 ISBN 978-3-7696-5376-2

Adresse des Ausschusses Geodäsie (DGK)
der Bayerischen Akademie der Wissenschaften:

Ausschuss Geodäsie (DGK) der Bayerischen Akademie der Wissenschaften
Alfons-Goppel-Straße 11 ● D – 80 539 München
Telefon +49 – 89 – 23 031 1113 ● Telefax +49 – 89 – 23 031 - 1283 / - 1100
e-mail post@dgk.badw.de ● http://www.dgk.badw.de

Prüfungskommission:
Vorsitzender: Prof. Dr.-Ing. Ingo Neumann
Referent: Prof. Dr.-Ing. Steffen Schön
Korreferenten: Prof. Dr.-Ing. Rolf Dach
Prof. Dr.-Ing. habil. Christian Heipke

Tag der mündlichen Prüfung: 21.03.2025

:

Diese Dissertation ist auf dem Server des Ausschusses Geodäsie (DGK)
der Bayerischen Akademie der Wissenschaften, München unter <http://dgk.badw.de/>
sowie unter Wissenschaftliche Arbeiten der Fachrichtung Geodäsie und Geoinformatik
der Leibniz Universität Hannover (ISSN 0174-1454), Nr. 414,
<https://repo.uni-hannover.de/handle/123456789/19598>, Hannover 2025, elektronisch publiziert

© 2025 Ausschuss Geodäsie (DGK) der Bayerischen Akademie der Wissenschaften, München

Alle Rechte vorbehalten. Ohne Genehmigung der Herausgeber ist es auch nicht gestattet,
die Veröffentlichung oder Teile daraus zu vervielfältigen.

ISSN 0065-5325 ISBN 978-3-7696-5376-2

# Abstract

For highly accurate and precise positioning, navigation, and timing based on Global Navigation Satellite System (GNSS) signals, it is essential to consider Phase Center Corrections (PCC). Typically, GNSS processing estimates coordinates that refer to an easily accessible point, usually the antenna's substructure, known as the Antenna Reference Point (ARP). However, GNSS carrier-phase measurements relate to the electronic reception point, which varies based on the azimuth and elevation angles of incoming satellite signals and differs between antenna models, types, and frequencies. Corrections, which consider the differences between the ARP and the electronic receiving point, are required in order to achieve precise positioning. These corrections, known as PCC, can be determined in an anechoic chamber using artificially generated signals or in the field using a robot and real signals. In the past, the accuracy and precision of multi-GNSS, multi-frequency positioning were degraded due to the lack of robot-based PCC for newer signals and systems.

This thesis presents the successful estimation of multi-GNSS, multi-frequency PCC using a robot and real GNSS signals. A key innovation of this work is the parameterization of PCC using an adapted version of hemispherical harmonic functions, as opposed to the commonly used spherical harmonic functions. This advancement ensures a stable normal equation system and enables the calculation of reasonable formal errors for the estimated PCC.

A clear and standardized strategy for comparing PCC sets is still lacking. In response, various strategies for comparing different PCC sets are presented using both simulated and real difference patterns. Based on these analyses, the benefits and challenges of each strategy are discussed. Characteristic values for assessing the similarity of PCC sets are introduced, and a standardized simulation approach is developed. This approach allows for the assessment of the impact of $\Delta$PCC on geodetic parameters, such as topocentric coordinate differences, receiver clock error, and tropospheric parameters. Comparisons with common strategies using real data demonstrate that the developed approach is thorough and efficient, representing a substantial step toward standardizing the comparison of different PCC sets.

To identify the specific causes limiting the higher repeatability of PCC estimation and to understand why discrepancies between different calibration facilities occur, a thorough evaluation of specific steps and processing parameters within the antenna calibration procedure is conducted. The analysis reveals that the quality of observations, rather than differences in observation distribution on the antenna hemisphere, has the greatest influence on the repeatability of PCC estimation.

The thesis also addresses the challenges of independently validating PCC within the observation domain, particularly due to predominant error sources such as multipath (MP) effects. It is demonstrated that different PCC sets can be validated by applying them to Single Differences (SD) in a short baseline, common clock setup. Applying PCC estimated with the developed algorithm to uncorrected SD time series shows mean improvements in standard deviations up to 1.33%. The overall magnitude of these improvements is relatively small because of the application of an accurate a priori Phase Center Offset (PCO) to the *uncorrected* SD to prevent large drifts. Also, other remaining error sources complicate the validation process. Thus, a new approach for validating PCC, based on time-differenced SD using a calibration process, has been proposed. Initial results are promising, showing mean improvements in the standard deviation of the dSD time series of up to 8%.

**Keywords:** Absolute GNSS Antenna Calibration, PCC, Multi-GNSS Processing, PCC Validation Strategies, Hemispherical Harmonics

# Zusammenfassung

Für eine hochgenaue und präzise Positionierung, Navigation und Frequenzübertragung basierend auf Global Navigation Satellite System (GNSS)-Signalen ist die Berücksichtigung von Phasenzentrumskorrekturen (PCC) unerlässlich. Normalerweise werden bei der GNSS-Prozessierung Koordinaten geschätzt, die sich auf einen leicht zugänglichen Punkt beziehen, meist auf die Unterkonstruktion der Antenne, den Antennenreferenzpunkt (ARP). Die GNSS-Trägerphasenmessungen beziehen sich jedoch auf den elektronischen Empfangspunkt (EEP), der mit Azimut- und Elevationswinkel der eingehenden Satellitensignale variiert und sich je nach Antennentyp und Frequenz unterscheidet. Um eine präzise Positionierung zu erreichen, müssen Korrekturen angebracht werden, die die Unterschiede zwischen dem ARP und dem EEP berücksichtigen. Diese als PCC bezeichneten Korrekturen können in einer echolosen Kammer oder im Feld mit einem Roboter und echten Signalen bestimmt werden. In der Vergangenheit wurden die Genauigkeit und Präzision der Multi-GNSS-Mehrfrequenz-Positionierung durch das Fehlen von mittels Feldverfahren bestimmter PCC für neuere Signale und Systeme vermindert.

In dieser Arbeit wird die erfolgreiche Schätzung von Multi-GNSS-Multifrequenz-PCC unter Verwendung eines Roboters und echter GNSS-Signale vorgestellt. Eine Schlüsselinnovation dieser Arbeit ist die Parametrisierung von PCC unter Verwendung einer angepassten Version von hemisphärischen harmonischen Funktionen, im Gegensatz zu den üblicherweise verwendeten sphärischen harmonischen Funktionen. Dieser Fortschritt sorgt für ein stabiles Normalgleichungssystem und ermöglicht die Berechnung formaler Fehler für die geschätzten PCC.

Eine klare und standardisierte Strategie für den Vergleich von PCC-Sätzen ($\Delta$PCC) fehlt noch immer. Daher werden verschiedene Strategien zum Vergleich von $\Delta$PCC vorgestellt, wobei sowohl simulierte als auch reale Differenzpattern verwendet werden. Darauf basierend werden die Vorteile und Herausforderungen der einzelnen Strategien diskutiert. Es werden charakteristische Werte für die Bewertung der Ähnlichkeit von PCC-Sätzen eingeführt und ein standardisierter Simulationsansatz entwickelt. Dieser Ansatz ermöglicht die Bewertung der Auswirkungen von $\Delta$PCC auf geodätische Parameter. Vergleiche mit gängigen Strategien unter Verwendung realer Daten zeigen, dass der entwickelte Ansatz effektiv ist und einen wesentlichen Schritt zur Standardisierung des Vergleichs verschiedener PCC-Sätze darstellt.

Um die spezifischen Ursachen zu ermitteln, die die höhere Wiederholbarkeit der PCC-Schätzung einschränken, und um zu verstehen, woher Diskrepanzen zwischen verschiedenen Kalibrierungseinrichtungen kommen, wird eine gründliche Analyse des Antennenkalibrierungsverfahrens durchgeführt. Diese zeigt, dass die Qualität der Beobachtungen und nicht die Unterschiede in der Beobachtungsverteilung auf der Antennenhemisphäre den größten Einfluss auf die Wiederholbarkeit der PCC-Schätzung haben.

Auch werden die Herausforderungen einer unabhängigen Validierung der PCC innerhalb der Beobachtungsebene aufgezeigt. Es wird gezeigt, dass verschiedene PCC-Sätze validiert werden können, indem sie auf Einzeldifferenzen (SD) in einem kurzen Basislinien-Setup angewendet werden. Die Anwendung der mit dem entwickelten Algorithmus geschätzten PCC auf unkorrigierte SD-Zeitreihen zeigt mittlere Verbesserungen der Standardabweichungen von bis zu 1,33%. Die Gesamtgröße dieser Verbesserungen ist relativ gering, da ein genauer a priori Phasenzentrumsoffset auf die unkorrigierten SD angewendet wird, um große Driften zu verhindern. Daher wird ein neuer Ansatz für die Validierung der PCC vorgeschlagen, der auf zeitlich differenzierten SD unter Verwendung eines Kalibrierungsprozesses basiert. Erste Ergebnisse zeigen eine mittlere Verbesserung der Standardabweichung der dSD-Zeitreihe von bis zu 8%.

**Schlüsselwörter:** Absolute GNSS-Antennenkalibrierung, PCC, Multi-GNSS-Prozessierung, PCC-Validierungsstrategien, Hemisphärische Harmonische

# Contents


**1 Introduction** **1**

**2 Fundamentals** **5**
2.1 Receiver Antennas and GNSS Observation Equations . . . 5
2.1.1 Antenna Specification Parameters . . . 5
2.1.2 Primary Observation Types . . . 12
2.1.3 Linear Combinations . . . 17
2.1.4 Observation Differencing and Position Determination . . . 19
2.2 Receiver Antenna Calibration . . . 23
2.2.1 Definition of Phase Center Corrections . . . 23
2.2.2 Format Standards and Application of Phase Center Correction Values . 25
2.2.3 State of the Art of Calibration Methods & Current Developments . . . 27

**3 Strategies for Comparing Phase Center Corrections** **37**
3.1 Computing Differences . . . 37
3.2 Analyses at Pattern Level . . . 38
3.2.1 Graphical Measures . . . 38
3.2.2 Numerical Measures . . . 41
3.3 Analysis in Observation and Parameter Domain . . . 44
3.3.1 Observation Domain . . . 44
3.3.2 Parameter Domain . . . 46
3.3.3 Precise Point Positioning . . . 51

**4 Developed Methodology for Determining Phase Center Corrections** **53**
4.1 Preparatory Work . . . 53
4.2 Data Acquisition and Preprocessing . . . 56
4.2.1 Data Acquisition . . . 56
4.2.2 Data Preprocessing . . . 58
4.3 Estimation of Phase Center Corrections . . . 62
4.3.1 Determination of HSH Coefficients . . . 62
4.3.2 ANTEX Conform Output . . . 65
4.3.3 Methods to Separate PCC into PCO, PCV and Constant Parts . . . 67
4.4 Quality Analysis of Calibration Procedure . . . 70
4.4.1 Residuals and A Posteriori Variance Factor . . . 70
4.4.2 Formal Errors . . . 71
4.4.3 Condition Number of Normal Equation System . . . 71
4.4.4 Closed-loop Simulation . . . 71
4.4.5 Comparison with External Data . . . 74

**5 Estimated Phase Center Corrections** **75**
5.1 Estimated PCC of Individual Calibrations . . . 76
5.2 Comparison of Estimated PCC of Different AUTs and their Quality . . . 88
5.3 Repeatability of Individual Calibrations . . . 92
5.4 Repeatability with Different Receivers . . . 98
5.5 Differences between Identical Frequencies from Different GNSS . . . 103
5.6 Comparison to Type-mean Calibration Values . . . 107

**6 Variation of Processing Parameters** **109**
6.1 Calibration Time and Length . . . 110

6.2 Degree and Order of Hemispherical Harmonics . . . 115
6.3 Methods to Stabilize the Normal Equation System . . . 121
6.4 Weighting Schemes . . . 132
6.5 Grid Resolution . . . 140
6.6 Summary . . . 146

**7 Analysis of Phase Center Correction Values for Geodetic Applications 147**
7.1 Observation Domain . . . 147
7.1.1 Single Differences . . . 147
7.1.2 Time-differenced Single Differences . . . 151
7.2 Parameter Domain . . . 152
7.2.1 GNSS Reference Stations . . . 152
7.2.2 GNSS Coordinate Time Series . . . 154
7.2.3 Location-dependency . . . 157
7.2.4 GNSS-based Frequency Transfer . . . 158

**8 Conclusions 163**

**Annex 167**

**A Estimated PCC 167**
A.1 Geodetic Pinwheel Antenna: NOV703.GGG R2 . . . 167
A.2 Geodetic 3D Choke Ring Antenna: LEIAR2.R3 NONE . . . 169
A.3 Mass Market Antenna: ANN-MB1 NONE . . . 171

**B Quality Assessment of Estimated PCC 173**
B.1 LEIAR25.R3 NONE . . . 173
B.2 ANN-MB1 NONE . . . 175

**Bibliography 177**

**List of Figures 185**

**List of Tables 189**

**Acronyms 191**

**Acknowledgement 193**

# 1 Introduction

For highly accurate and precise positioning, navigation, and timing based on Global Navigation Satellite System (GNSS) signals, it is crucial to consider Phase Center Corrections (PCC). Additionally, PCC are essential for GNSS global network solutions to contribute to the scale determination of the reference frame for a global terrestrial network, such as the International Terrestrial Reference Frame (ITRF) (Villiger et al., 2019). Typically, coordinates estimated through GNSS processing correspond to an easily accessible point, usually at the antenna's substructure, known as the Antenna Reference Point (ARP). However, GNSS carrier-phase measurements relate to the electronic reception point, which varies depending on azimuth and elevation angles of the incoming satellite signals, and differs between antenna models, types, and frequencies. Appropriate corrections are must be applied to account for discrepancies between the ARP and the electronic reception point to achieve precise positioning. These corrections, referred to as PCC, can be determined in an anechoic chamber using artificially generated signals, or in the field using a robot and real signals. If PCC are not considered in GNSS processing, it can result in coordinate differences of several centimeters, particularly in the Up-component. The impact of neglected PCC depends significantly not only on the antenna model used and its pattern but also on the positioning mode.

PCC have been widely used in Global Positioning Service (GPS) and Globalnaja Nawigazionnaja Sputnikowaja Sistema (GLONASS) dual-frequency positioning since the mid-1990s. To enhance positioning accuracy and because nations seek political independence, existing GNSS are being modernized, and new systems are available, expanding coverage for more reliable positioning. Consequently, signals are now transmitted on additional frequencies. Since PCC are frequency-dependent, applying corrections to observations from newer frequencies is crucial to fully exploit multi-GNSS and multi-frequency processing. Key benefits of newer or modernized signals include higher signal strength and faster ambiguity resolution using triple frequencies, essential for positioning in dense urban areas or for autonomous driving.

In the past, only dual-frequency PCC for GPS and GLONASS from robot calibrations were publicly available, e.g., provided by the International GNSS Service (IGS) (Johnston et al., 2017). At this work's inception, multi-GNSS, multi-frequency processing was already common, though a lack of robot-based PCC for newer frequencies limited full constellation benefits. A mix of chamber- and robot-based PCC can cause position deviations, creating high demand for robot-based multi-GNSS, multi-frequency PCC.

This demand motivated the development of a GNSS receiver antenna calibration system capable of estimating PCC for newer signals and systems. Based on Kersten (2014), successful implementation was shown in contributions in 2019 (Kröger et al., 2019a,b,c), showcasing the effective estimation of multi-GNSS, multi-frequency PCC. Since then, several calibra-

tion facilities have updated or developed their PCC estimations, widely reported in scientific publications detailing calibration algorithms and results.

With growing demand for higher precision in geodetic applications, comprehension and improvement of PCC is increasingly important. This work aims to explore key questions surrounding PCC optimization, and to harmonize the comparison of different PCC sets ($\Delta$PCC).

To achieve this, it is essential to understand how different calibration facilities determine PCC by analyzing hardware setups, measurement principles, and algorithms. It is also crucial to assess how PCC sets are compared. Thus, a comprehensive study of current comparison methods is conducted. Based on this, existing methods for comparing $\Delta$PCC, as well as innovative strategies, are evaluated using simulated and real $\Delta$PCC data to clearly demonstrate the benefits and challenges of various comparison strategies, including limitations of PCC validation in the observation domain.

Given the impact of $\Delta$PCC on geodetic parameters such as topocentric coordinate differences, estimated receiver clock error, and tropospheric estimates, a clear comparison strategy is crucial. Different processing parameters significantly affect outcomes, necessitating a standardized comparison method. A standardized simulation approach has been developed to facilitate PCC comparison under various conditions. Performance analyses of typical comparison strategies, like position differences using different PCC sets, show the efficacy of the tools developed in this thesis.

During the development of the multi-GNSS, multi-frequency PCC estimation algorithm, a major challenge emerged: observation distribution on the antenna hemisphere. Despite the antenna's tilt and rotation during calibration, observations are mainly available on the upper hemisphere, while common PCC parameterization, like Spherical Harmonics (SH), are defined for a full sphere, leading to an ill-conditioned Normal Equation System (NES) during estimation. Even small observation vector distortions can significantly impact the estimated parameters, and calculating reasonable formal errors to assess PCC quality is impossible without modifications. Testing different stabilization methods revealed that parameterizing PCC with an adapted version of Hemispherical Harmonics (HSH) instead of SH is effective.

Calibration results reveal differences not only among institutions estimating PCC, but also between calibration sets using identical setups. Research examines the impact of various processing parameters on estimated PCC. An in-depth analysis of antenna calibration processing steps is essential to understand differences across institutions and sets. This analysis involves assessing different calibration sets and the influence of calibration time, duration, and the distribution of observations on the antenna hemisphere. Furthermore, the impact of the GNSS receiver used during calibration has not been analyzed in detail yet. Therefore, assessing whether system calibration, including both the antenna and receiver, is necessary to optimize PCC estimation. Additionally, the research scope includes evaluating if different PCC sets are required for different GNSS, even if they share the same frequency, given that PCC are frequency-dependent.

Different calibration institutions use varying degrees and orders for SH to parameterize PCC. Thus, understanding the influence of changes in these parameters on the resulting PCC and their effect on geodetic parameters is of great interest. PCC are typically provided on a regular grid with a resolution of $5^\circ$ for elevation and azimuth angles. The research question here is whether this resolution is sufficient to capture the complete pattern information.

Validating PCC, and especially $\Delta$PCC, remains challenging due to their small magnitude compared to the expected observation noise in standard GNSS processing. To further explore this, the validation of estimated PCC is conducted in the observation domain using Single Differences (SD). Additionally, testing whether PCC can be validated using the calibration

**Table 1.1:** Main contributions of this thesis.

| **Challenges** | **Section** |
|---|---|
| Clear and standardized strategy for comparing different PCC sets is missing | 3 |
| GNSS-based positioning is degraded due to the lack of multi-GNSS, multi-frequency PCC | 4 |
| Observation distribution on antenna hemisphere leads to unstable NES | 4.3 |
| Explicit causes limiting the higher repeatability of PCC estimation remain unidentified | 5 & 6 |
| Limited comprehension of the impact of varying settings and processing parameters on PCC estimations | 6 |
| Validation of PCC in the observation domain is challenging | 7.1 |
| Lack of clear assessment strategies for evaluating how ΔPCC impacts geodetic applications | 7.2 |

process based on time-differenced Single Differences (dSD) shows promising first results. Further analysis is conducted to determine how different PCC sets impact geodetic applications. Real data and the developed simulation approach are used to assess these impacts.

In summary, the **main contributions** of this thesis are as follows: At the outset of this work, there was a lack of multi-GNSS, multi-frequency PCC necessary for positioning and navigation. By successfully implementing an estimation algorithm, this research gap has been addressed. Throughout the development process, various research questions and challenges related to robot-based receiver antenna calibration and PCC comparison emerged. These are thoroughly addressed and discussed in this thesis. Table 1.1 summarizes the primary challenges and the sections where they are tackled.

The structure of this thesis is as follows: Chapter 2 provides the necessary fundamentals for this thesis. It discusses various antenna specification parameters essential for designing a GNSS antenna. These parameters result in a non-isotropic pattern, necessitating consideration of PCC during GNSS processing. The chapter also covers an introduction into primary GNSS observation types, related linear combinations, and concepts of observation differencing and position determination. Additionally, it provides the definition of PCC and offers a comprehensive literature review regarding receiver antenna calibration.

Chapter 3 introduces various strategies for comparing PCC differences (ΔPCC). It includes basic formulas for computing differences, followed by tools for analyzing ΔPCC at the pattern level, using both graphical and numerical measures. It also discusses options for comparing PCC sets within the observation and parameter domains, with a particular emphasis on a developed simulation approach aimed at standardizing PCC comparisons.

The main contribution of this work, a developed methodology for determining multi-GNSS, multi-frequency PCC, is presented in Chapter 4. This chapter focuses on the motivation and implementation of an adapted version of HSH instead of SH for PCC parameterization. It includes a detailed analysis of separating PCC into its individual components, namely Phase Center Offset (PCO), Phase Center Variations (PCV), and a constant part, to generate an Antenna Exchange Format (ANTEX)-compliant output that meets the standards. In addition, several tools and methods to assess the quality of the calibration procedure are presented.

Chapter 5 presents estimated PCC values for three different GNSS antenna types, along with quality analyses: a geodetic pinwheel antenna, a geodetic 3D choke ring antenna, and a mass-market antenna. It investigates the repeatability of individual calibrations and those with different receivers. Furthermore, it offers an in-depth analysis of $\Delta$PCC between identical frequencies from different GNSS systems.

Chapter 6 analyzes the influence of changed processing parameters on estimated PCC. This includes the calibration time and length, as well as the selected degree and order for PCC parameterization using HSH. It also examines the influence of different weighting models and the resolution for transferring estimated HSH coefficients to a regular grid representing PCC. Special attention is given to analyzing various methods for stabilizing the NES, validated using manipulated observations and closed-loop simulations.

Chapter 7 analyzes PCC values for geodetic applications. This includes validating PCC sets in the observation domain and assessing their impact in the parameter domain. The assessment covers GNSS reference stations and GNSS coordinate time series. The chapter also briefly examines location dependency and evaluates the impact of different PCC sets on GNSS-based frequency transfer.

The thesis concludes in Chapter 8, summarizing the key findings and providing an outlook for future work.

# 2
# Fundamentals

This chapter provides the fundamentals of this work, which are summarized and illustrated in Figure 2.1. The non-colored part is based on Won and Pany (2017) and describes the digital signal processing of a Global Navigation Satellite System (GNSS) receiver. Since this is not treated further within this work, details are not provided in the fundamentals. Instead, interested readers are referred to the technical literature.

Since GNSS antennas are the first element in the processing chain of GNSS signals and are crucial for the quality of GNSS observations and the resulting position estimates, the most important antenna specification parameters are first pointed out in Section 2.1.1. Next, the four primary GNSS observation types as they are written by the receiver into the binary file, which can be converted into the Receiver Independent Exchange Format (RINEX) file, are described in Section 2.1.2. With these, different linear combinations can be formed and observation differencing can be carried out so that specific error sources cancel out. The methodologies for forming these combinations, as well as Precise Point Positioning (PPP) as one position determination algorithm are provided in Section 2.1.4. The chapter closes with the definition of Phase Center Corrections (PCC), format standards and an overview of different calibration methods as well as current developments in this research field.

## 2.1 Receiver Antennas and GNSS Observation Equations

### 2.1.1 Antenna Specification Parameters

The main purpose of GNSS receiver antennas is the reception of navigation signals transmitted by GNSS satellites (Maqsood et al., 2017). Since the antenna acts as a spatial and frequency filter, it directly impacts the quality of the received signal and thus the position quality (Rao et al., 2013). This section briefly describes the main key parameters of GNSS receiver antennas.

The receiver antenna converts the electromagnetic waves (radio waves) transmitted by the satellite into electric currents. GNSS antennas transmit the signals in the L-band of the Radio Frequency (RF) spectrum, which covers a total frequency of 1-2 GHz. In this range, the frequencies of 1164 MHz – 1300 MHz and 1559 MHz – 1610 MHz are assigned to Radio Navigation Satellite Services (RNSSs) by the International Telecommunications Union (ITU). This is the case for all GNSS satellites except for Indian Regional Navigation Satellite System (IRNSS) and the third-generation BeiDou system. They also use a frequency near 2.2 GHz (S-band) for selected frequencies (Maqsood et al., 2017). Figure 2.2 shows the allocated frequencies for individual GNSS. It is worth noticing that selection of the close or even overlapping frequency range is beneficial for receiving multiple signals from different GNSS with one single wideband antenna. However, the possibility of interference between different

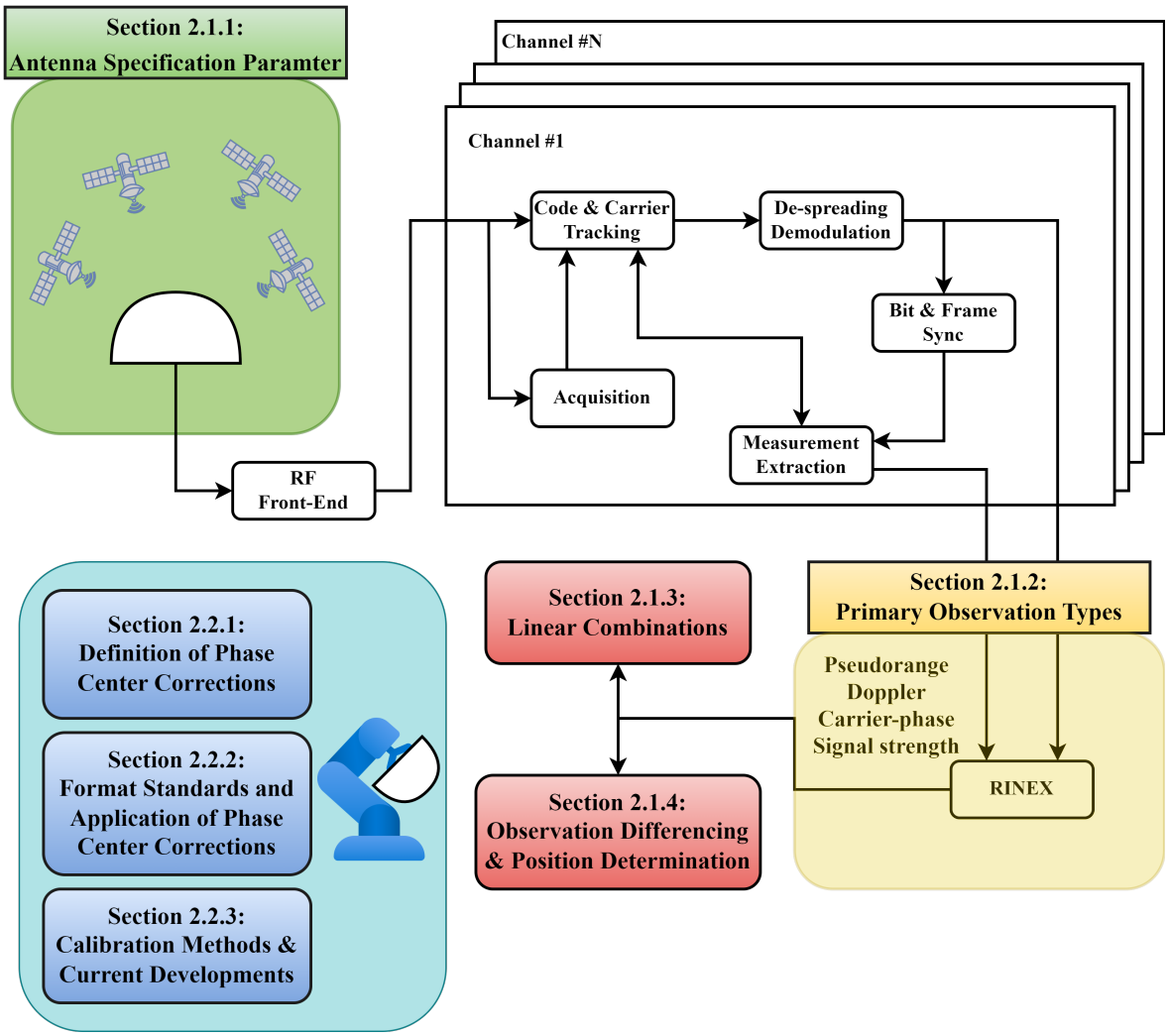


**Figure 2.1:** Flowchart illustrating the structure of the fundamentals.

systems does exist. Since all GNSS use different signal formats and modulation schemes, a natural immunity against the interference is provided (Maqsood et al., 2017).

In the following, the main antenna specification parameters, which need to be considered when a GNSS antenna is designed, are briefly introduced. These parameters indicate the operating specifications and can also be utilized by users to assess the expected performance of different GNSS antennas. However, based on specific applications, one or the other parameter might play a superior role. In addition, further requirements like size and weight might need to be considered (Rao et al., 2013).

### Center Frequency

The center frequency, or operating frequency, is the specific value for which the entire RF system (including the antenna) is designed. Civilian Global Positioning Service (GPS) uses three center frequencies: L1 (1575.42 MHz), L2 (1227.60 MHz), and L5 (1176.45 MHz). The L1 frequency serves as the primary GPS frequency and is designated for the Standard Positioning Service (SPS). In contrast, the Precision Positioning Service (PPS) employs both the L1 and L2 frequencies to enable ionospheric corrections. With the introduction of the new civil L2C signal on the L2 frequency, similar capabilities are now accessible to general users. Additionally, a

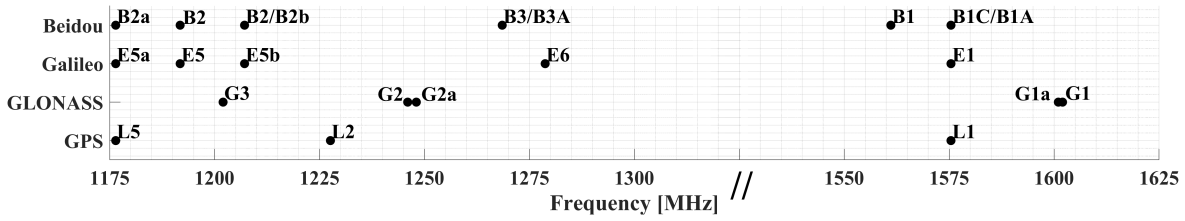


**Figure 2.2:** Overview of center frequencies and respective frequency band specificators for BeiDou, Galileo, GLONASS, and GPS signals.

L5 signal has been introduced, primarily targeting aviation users. To support all related applications, a modern GPS antenna must cover at least the L1, L2, and L5 frequencies. A multi-GNSS antenna needs to encompass an even broader range of center frequencies, as illustrated in Figure 2.2 (Maqsood et al., 2017). Here, the center frequencies for BeiDou, Galileo, Globalnaja Nawigazionnaja Sputnikowaja Sistema (GLONASS) and GPS are depicted along with their frequency band specificators. As it can be seen, each GNSS transmit at least on three different center frequencies. Also, it can be seen that BeiDou, Galileo and GPS are transmitting partly on the same frequencies, e.g. Galileo E1 and GPS L1 or BeiDou B2a and GPS L5.

### Bandwidth

The bandwidth of an antenna is generally defined as the frequency range in which the antenna operates successfully and meets all design requirements. The general term *bandwidth* can be further divided into impedance bandwidth and gain bandwidth. The gain bandwidth describes over which bandwidth the antenna provides a gain which is at minimum necessary to acquire GNSS measurements over a specific range, typically for the upper antenna hemisphere, i.e. $0° \leq el \leq 90°$. The impedance bandwidth describes the frequency range in which the antenna transmits power efficiently due to good impedance matching (Rao et al., 2013). Details on the different subdivisions of *bandwidth* are provided in the respective paragraph further below. For GNSS antennas, in general, it is important to ensure that the antenna maintains the required Right-Hand Circular Polarization (RHCP) within the specified bandwidth. A standard bandwidth of approximately 10.23 MHz is required to receive all signals transmitted by GPS satellites (L1, L2, L5) at their respective center frequencies, see Figure 2.2 (Maqsood et al., 2017).

### Radiation Pattern

The Radiation Pattern (RP) of an antenna describes the radiation properties such as the electric field or power as a function of spatial coordinates. It can be either two-dimensional (2D) or three-dimensional (3D) and is usually represented as functions of observation angles around the antenna, including both elevation and azimuth angles. A clear distinction is made between the amplitude field pattern, which represents the received electric field at a constant radius, and the amplitude power pattern, which shows the spatial variation of power density along a constant radius. GNSS receiving antennas are designed to have a hemispherical pattern directed towards the transmitting satellite, usually in the direction of the zenith. Conversely, the transmitting antennas onboard satellites are designed with a sharp directional pattern to compensate for free-space losses, which increase with the square of the distance (Maqsood et al., 2017).

### Polarization

When antennas emit electromagnetic waves, associated electric and magnetic field vectors are generated. The polarization of an antenna is typically defined by the orientation of its electric (E) field vector. If the E-field vector is aligned with the horizon, the antenna is considered to be horizontally polarized. Conversely, if the E-field vector is aligned perpendicular to the horizon, the antenna is considered to be vertically polarized. For GNSS, the standard polarization is neither horizontal nor vertical, but is RHCP. This means that the electric field of a GNSS signal comprises two orthogonal waves of equal amplitude with a 90° phase shift, causing the resulting E-field to circulate in a clockwise direction. Upon reflection, the polarization can change, resulting in Left-Hand Circular Polarization (LHCP) waves. In an ideal case, a GNSS receiving antenna would completely suppress these LHCP signal components (Maqsood et al., 2017).

### Axial Ratio

The Axial Ratio (AR) describes the ratio of the magnitudes of the major and minor axes of the polarization ellipse. It is equal to one for purely circular polarization and increases with greater ellipticity. For linear polarization, the AR becomes infinite because one of the orthogonal components of the field is zero. Ideally, a GNSS antenna would have an AR value of 0 dB, but a value of less than 3 dB is generally acceptable. Since the AR increases with the boresight angle, it is common to specify the range of boresight angles within which this condition is met. The 3 dB AR beamwidth is a crucial parameter for evaluating the performance of circularly polarized antennas. The wider the beamwidth, the better the antenna's ability to suppress Multipath (MP) signals (Maqsood et al., 2017).

### Antenna Gain

Antenna gain is a measure of how effectively an antenna can receive or transmit power from/in a specific direction. This measurement is taken in comparison to an idealized, lossless isotropic antenna. This is the main difference to the RP, which provides the spatial distribution of the emission/reception energy and describes the relative strength of the signal in different directions.

GNSS receiving antennas are typically designed as low-gain antennas to ensure that signals can be received over a wide range of angles, i.e. the full upper hemisphere of the antenna. The transmitting antennas, in contrast, are designed to be highly directional in order to illuminate the Earth from a high altitude of approximately 22,000 km (Maqsood et al., 2017).

GNSS satellites transmit electromagnetic waves. Since they undergo polarization changes when propagating through ionized gases or the Earth's magnetic field, all current GNSS use RHCP signals. This avoids the fact that linear-polarized waves transform into elliptical or circular waves (Meurer and Antreich, 2017). When the RHCP signals undergo specular reflection off a surface at normal incidence, they are reflected as LHCP signals. However, with different angles of incidence, the reflected signal becomes a mix of polarizations. As the incidence angle increases, the LHCP component of the reflected signal decreases, while the RHCP component increases. At Brewster's angle, the magnitudes of the two components become equal. Beyond Brewster's angle, the RHCP component prevails. The specific Brewster's angle varies based on the signal frequency and the properties of the reflecting surface. For L-Band GNSS signals, Brewster's angle is approximately 89° for metallic surfaces, about 85° for seawater, and near 70° for soil. Reflected signals are always delayed in comparison to direct signals and generally

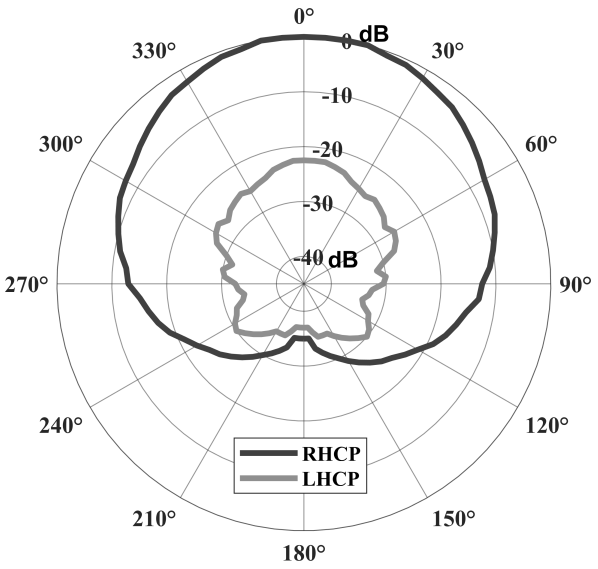


**Figure 2.3:** GPS L1 antenna gain of a *NOV703GGG.R2 NONE* antenna for RHCP and LHCP signals, digitalized from Novatel (2011).

have lower amplitude unless the direct signals are obstructed or weakened (McGraw et al., 2021). Consequently, these signals should be avoided in GNSS positioning. One method is the design of the GNSS antenna, i.e. by damping LHCP signals.

Figure 2.3 depicts the GPS L1 antenna gain of a *NOV703GGG.R2 NONE* antenna for RHCP and LHCP signals. It can be clearly seen that the RHCP signal component is less damped over the whole antenna sphere compared to the LHCP signal component. Also, the maximum gain is present in the zenith direction (top of the figure at 0°) so that GNSS signals received from satellites at high elevation angles are not damped. This antenna gain provides a filter against MP effects.

### 3 dB Beam Width

The antenna beam width is generally used to define the area of maximum power concentration. Graphically, it is represented by the angular distance between two identical points around the peak of the antenna's RP. The two most common methods of representing antenna beam width are the Half Power Beam Width (HPBW) and the First-Null Beam Width (FNBW). When expressed in decibels, the HPBW is also referred to as the 3 dB beam width. For GNSS receiving antennas, the required beam width should be as wide as possible to ensure maximum satellite visibility. Conversely, transmitting satellites require a narrow beam width to focus power in a specific direction, as discussed in the paragraph about RP (Maqsood et al., 2017).

### Impedance Matching and Return Loss

Impedance matching and return loss are crucial parameters that indicate how effectively an antenna will receive incoming power. Regardless of the antenna type or operating frequency, it is essential for the antenna to have good impedance matching with the feed line and exhibit a high return loss. The input impedance requirement for a GNSS antenna is usually 50 Ω, a common standard that ensures compatibility among antennas from different manufacturers with the RF system, i.e. the GNSS receiver connectors and cables. Return loss measures the ratio between the power supplied to a transmit antenna and the power reflected back into the

feed cable. Typically, a return loss of less than -10 dB is required, which indicates that at least 90% of the incoming power is transmitted to the antenna for radiation. Alternatively, the reflection coefficient $s_{11}$ and Voltage Standing Wave Ratio (VSWR) can be provided to describe the return loss (Maqsood et al., 2017)

$$\text{return loss} = -20\log|s_{11}| \; = -20\log\left|\frac{\text{VSWR}-1}{\text{VSWR}+1}\right|. \tag{2.1}$$

### Front-to-Back and Multipath Ratio

According to Maqsood et al. (2017), the Front-to-Back Ratio (FBR) quantifies the ratio of the antenna energy directed in the boresight direction (main lobe) to the energy directed towards the backlobes. Thus, it also reflects the antenna's resistance to MP. For GNSS antennas, a high FBR is required so that e.g. ground reflections can be attenuated. It is affected by the antenna's backside shielding and the sensitivity to LHCP signals. A related measure is the Multipath Ratio (MPR), which compares the gain $G$ of RHCP signals at a specific boresight angle $\theta$ with the gain of both RHCP and LHCP radiation received from the angle $180° - \theta$ (Maqsood et al., 2017)

$$\text{MPR} = \frac{G_{\text{RHCP}}(\theta)}{G_{\text{LHCP}}(180° - \theta) + G_{\text{RHCP}}(180° - \theta)}. \tag{2.2}$$

Thus, the MPR is a crucial indicator for assessing the MP mitigation performance of an antenna. A related measure is given by the Multipath Suppression Indicators (MPSI) described below.

### Phase-Center Stability and Group Delay Variations

The Phase Center (PC) of an antenna is the point within its RP from which all power radiates (for a transmitting antenna) or converges (for a receiving antenna). Typically, this point differs from the geometric center of the antenna and varies with the signal frequency and the direction of the incoming signal since the actual wavefronts deviate from the ideal concentric spherical shell (Maqsood et al., 2017). Thus, in order to achieve accurate and precise GNSS-based positioning and navigation, PCC need to be taken into account. Its definition is provided in Section 2.2.1 and methods to properly calibrate the GNSS transmitting and receiving antennas are described in Section 2.2.3. In general, maintaining high PC stability is in particular challenging for wide- or multiband antennas (Maqsood et al., 2017).

Similar effects are present not only for carrier-phase but also for pseudorange observations. The Group Delay (GD) is a measure of the time delay experienced by the receiving antenna. When its value is multiplied with the speed of light $c$, a metric correction term known as Codephase Center Corrections (CPC) is obtained.

Among with the Phase Wind-Up (PWU) error described in Section 4.2.2, the GD and PC errors are antenna-induced errors in GNSS measurements (Rao et al., 2013). In order to take these errors adequately into account, CPC, PCC and corrections due to the carrier PWU need – depending on the specific application – to be considered.

### Multipath Susceptibility Indicators

One of the crucial key parameters of GNSS receiving antennas is the capability to suppress multipath (Caizzone et al., 2021). In order to calculate the MPSI for different antennas and GNSS frequencies, the respective gain patterns are used. Referring to Caizzone et al. (2018), the MPSI are defined as follows

$$\begin{aligned} \mathrm{MSPI_{Up}} &= \begin{cases} \log_{20}(-\mathrm{XPD_{max,db}}) & \text{if } \mathrm{XPD_{max,db}} < 0 \\ 0 & \text{if } \mathrm{XPD_{max,db}} > 0 \end{cases} \\ \mathrm{MSPI_{Down}} &= \begin{cases} \log_{20}(-\mathrm{DUR_{max,db}}) & \text{if } \mathrm{DUR_{max,db}} < 0 \\ 0 & \text{if } \mathrm{DUR_{max,db}} > 0 \end{cases} \end{aligned} \tag{2.3}$$

with

$$\begin{aligned} \mathrm{XPD_{max}} &= \frac{\max(\mathrm{Gain_{LHCP}}(z > 0, \forall\alpha))}{\mathrm{Gain_{RHCP}}(z_s, \alpha_s)} \\ \mathrm{DUR_{max}} &= \frac{\max(\mathrm{Gain_{TOT}}(z < 0, \forall\alpha))}{\mathrm{Gain_{RHCP}}(z_s, \alpha_s)}, \end{aligned} \tag{2.4}$$

where $z$ indicates the zenith angle, $\alpha$ the azimuth angle and $s$ the index of a specific value.

Figure 2.4 shows the calculated $\mathrm{MPSI_{Up}}$ and $\mathrm{MPSI_{Down}}$ for the *NOV703GGG.R2 NONE* antenna. $\mathrm{MPSI_{Up}}$ refers to satellite signals received from above the antenna horizon and $\mathrm{MPSI_{Down}}$ describes the signals received from below the antenna horizon. It can be clearly seen that $\mathrm{MPSI_{Up}}$ values are larger than 0.75 for $z \geq 90°$ indicating an excellent to good multipath suppression. Since the antenna is a geodetic pinwheel antenna, the results match the expectations. The $\mathrm{MPSI_{Down}}$ values indicate still a medium to good multipath suppression capability for $0° \leq z \leq 75°$. These received signals are most likely reflected signals.

Table 2.1 gives an overview over typical MPSI values and their interpretation based on Caizzone et al. (2021). The MPSI can range from 0, indicating that the antenna has no MP suppression capability, to values greater than 1, indicating that the antenna has an excellent MP suppression capability.

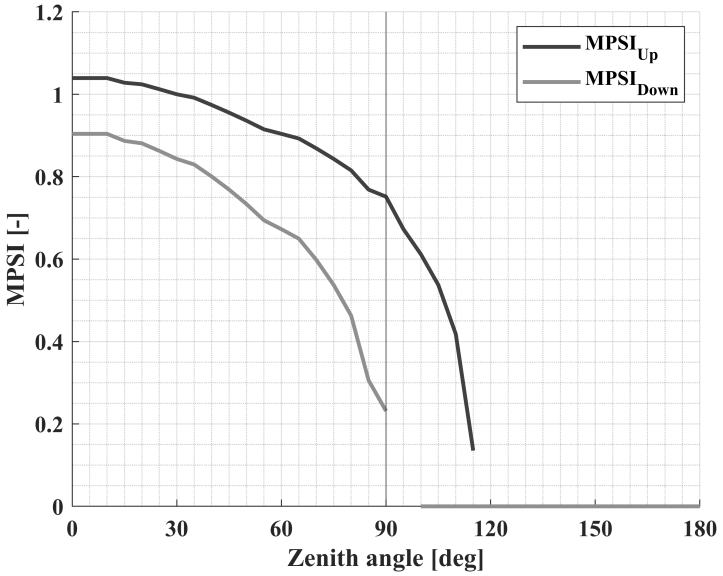


**Figure 2.4:** MPSI values for *NOV703GGG.R2 NONE* antenna.

**Table 2.1:** Typical MPSI values and their interpretation based on Caizzone et al. (2021).

| MPSI | Multipath Suppression Capability |
|---|---|
| 0 | none |
| 0.5 | medium |
| 0.75 | good |
| $>1$ | excellent |

#### Closing Remarks

Since all the above described antenna specification parameters need to be considered and also application-specific conditions (e.g. size and weight of the antenna) need to be taken into account when designing a GNSS antenna, they typically do not have an isotropic pattern. Consequently, there is the need to take the differences into account. These are defined as PCC, see Section 2.2.1 for their definition. Along with their calibration and validation, they form the main basis of this work.

### 2.1.2 Primary Observation Types

This section provides the fundamental observations captured by a GNSS receiver. Starting with the primary observation type, the four basic observations (pseudorange, carrier-phase, Doppler and signal strength measurements) are deduced. Based on these, typical linear combinations as well as different types of differencing are derived. For the sake of clarity, the particular receiving epoch $t$ as well as a frequency-specific index is not contained in the following equations.

#### Pseudorange Measurements

The basic measure of a GNSS receiver is the apparent signal travel time $\tau$ from the satellite $k$ to the user $A$. This is obtained of the receiver's Delay Lock Loop (DLL) which generates a replica of the signal's code and aligns it with the received signal. Thus, the corresponding time shift is a measure of the apparent transit time modulo the code chip length (Hauschild, 2017a). By combining it with the number of complete code chips, complete code repeats and additional information from the navigation data, the unambiguous apparent signal time is obtained. If this is multiplied with the speed of light $c$, the pseudorange is formed.

However, this range differs from the *true* range since both clocks, satellite and receiver, are not synchronized w.r.t to a common timescale. Thus, offsets occur with regard to the GNSS system time. In addition, other errors and signal delays are present (Hauschild, 2017a). This leads to the observation equation for pseudorange measurements, with any time arguments, such as signal reception time and propagation time, omitted for clarity

$$P_A^k = \rho_A^k + c \cdot \left(\delta t_A - \delta t^k\right) + \delta t_{A,rel}^k + I_A^k + T_A^k + \epsilon_A^k \ \text{[m]}, \tag{2.5}$$

with

$P_A^k$ Pseudorange observation [m]

$\rho_A^k$ Geometric range [m]

$c$ Speed of light $[\frac{\text{m}}{\text{s}}]$,

$\delta t_A$ Receiver clock correction [s],

$\delta t^k$ Satellite clock correction [s],

$\delta t^k_{A,rel}$ Relativistic correction [m],

$T^k_A$ Tropospheric correction [m],

$I^k_A$ Ionospheric correction [m],

$\epsilon^k_A$ Noise/unmodeled effects [m].

The geometric range $\rho^k_A$ can be written as

$$\rho^k_A = \sqrt{\left(X^k - X_A\right)^2 + \left(Y^k - Y_A\right)^2 + \left(Z^k - Z_A\right)^2} \tag{2.6}$$

and contains the satellite and receiver coordinates X, Y, Z in an Earth-Centered, Earth-Fixed (ECEF) coordinate frame.

The different parameters in Equation 2.5 may be estimated, corrected for, or neglected based on application and desired accuracy. A pseudorange-based positioning algorithm, e.g. Single Point Positioning (SPP), typically estimates the receiver/user position, which is contained in $\rho$, and the receiver clock error. External data is used for atmospheric corrections, satellite clock errors and positions (Hauschild, 2017a).

### Carrier-Phase Measurements

A receiver measures both pseudorange and carrier-phase using the Phase Lock Loop (PLL). The PLL functions by aligning a replica of the carrier signal with the incoming signal from the satellite and measuring the fractional phase shift. When the range between the user and the satellite changes by more than one cycle, the receiver counts the full cycles, allowing for a continuous measurement (Hauschild, 2017a). Carrier-phase measurements are more precise than pseudorange measurements due to the short wavelength of the carrier signal $\lambda$, which is approximately 19-25 cm, depending on the signal frequency, see Figure 2.2. However, unlike pseudorange measurements, carrier-phase measurements cannot provide an unambiguous satellite-to-receiver range. This ambiguity arises because the integer number of cycles between the satellite and the receiver at the start of tracking remains unknown.

The carrier-phase measurement equation $\varphi^k_A$ between satellite $k$ and receiver $A$ contains several components, which are in principle equal to those for pseudorange measurements in Equation 2.5

$$\varphi^k_A = \rho^k_A + \xi^k_A + c \cdot \left(\delta t_A - \delta t^k\right) + \delta t^k_{A,rel} - I^k_A + T^k_A + \lambda(\omega^k_A + N^k_A) + \epsilon^k_A \ \text{[m]}. \tag{2.7}$$

It is important to note that the sign of the ionospheric refraction differs from that in the pseudorange observation equation. Additionally, the term $\xi$ is introduced in this equation. This term accounts for Phase Center Offset (PCO) and Phase Center Variations (PCV) for both transmitting and receiving antennas, and it is dependent on the specific phase pattern of the antennas and the frequency used. While a similar effect exists for pseudorange measurements - referred to as Group Delay Variations (GDV) or CPC — it is combined into $\epsilon$ in Equation 2.5. However, since PCC are the main focus of this thesis, they are explicitly addressed here.

Moreover, the PWU correction $\omega$ is essential to account for changes in the measured phase due to antenna rotations. As it will be later seen, this is a crucial part in the case of receiver

antenna calibration. The unknown integer number of cycles $N$ is inherently present in the carrier-phase measurement and is converted into a metric unit using the carrier wavelength $\lambda$. The combined effect of receiver carrier-phase tracking noise and MP is encapsulated in the residual error term $\epsilon$ (Hauschild, 2017a).

### Doppler Measurements

Due to the relative motion of the receiver and satellite, the observed frequency of a satellite signal deviates from the nominal frequency, which is referred to as Doppler shift (Hauschild, 2017a). In addition, the receiver's or satellite's clocks may experience a frequency offset or drift. In the receiver's PLL, the phase discriminator drives the Numerically Controlled Oscillator (NCO) to synchronize the frequency and phase of a local carrier-phase replica with the received signal. To compensate for the Doppler effect caused by the relative motion between the receiver and the satellite, or for frequency deviations in the receiver or satellite clocks, the NCO's frequency must be adjusted to maintain synchronized phases. This frequency adjustment in the PLL is reported by the receiver as the Doppler measurement (Hauschild, 2017a). Since Doppler measurements are not handled within this work, the interested reader is instead referred to the technical literature, e.g. Wieser (2007).

### Signal Strength Measurements

The observation equations for pseudorange measurements (Equation 2.5) and carrier-phase measurements (Equation 2.7) contain in each case MP error and receiver noise, denoted as $\epsilon$. Measurement noise arises due to imperfections in various electrical components in the signal processing chain. This includes the antenna, cables, connectors, and the receiver itself. Furthermore, the antenna receives noise from both natural and artificial sources in its surroundings (Hauschild, 2017a). This noise introduces unpredictable errors in both pseudorange and carrier-phase observations, which can degrade the position estimates. The relative strength between this ambient environmental noise and the GNSS hardware, compared to the received signal from a navigation satellite, serves as an indicator of signal quality.

One widely used measure is the Carrier-to-Noise-Power-Density Ratio ($\mathrm{C/N_0}$) which signifies the ratio between the carrier signal's power level $C$ and the noise power $N_0$ within a 1 Hz bandwidth. For high $\mathrm{C/N_0}$ values ($> 35$ dB-Hz), the standard deviation of the measurement noise of a code tracking loop for Binary Phase Shift Keying (BPSK)-modulated signals using an early-minus-late correlator can be approximated according to Hauschild (2017a) as

$$\sigma_{DLL} \approx \sqrt{\frac{d_{\mathrm{corr}} \cdot B_L}{2 \cdot C/N_0}} \cdot \lambda_c \ \ [\mathrm{m}]. \tag{2.8}$$

Here, $d_{\mathrm{corr}}$ denotes the correlator in units of code chips, $B_L$ the equivalent code loop noise bandwidth in [Hz] and $\lambda_c$ is the wavelength of the code. It can directly be seen that $\sigma_{\mathrm{DLL}}$ decreases by increasing $\mathrm{C/N_0}$ values. In addition, the resulting noise depends on the correlator, the tracking loop design and the code chip length of the signal (Hauschild, 2017a).

It should also be noted that this formula for the approximation is only valid for BPSK-modulated signals and need to be adapted for modernized signals like Binary Offset Carrier (BOC) or Alternative BOC (AltBOC) signals used for Galileo signals. Detailed information on GNSS receiver architecture and signal tracking can be found e.g. in Ward (2017), Won and Pany (2017) and Morton et al. (2020).

A similar approximation for carrier-phase observations can be calculated using Equation 2.9.

By use of the carrier loop noise bandwidth $B_P$ in [Hz], the carrier-phase wavelength $\lambda$ in [m] and high $C/N_0$ values, the standard deviation of the PLL $\sigma_{\mathrm{PLL}}$ can be approximated by (Hauschild, 2017a)

$$\sigma_{\mathrm{PLL}} \approx \sqrt{\frac{B_P}{C/N_0}} \cdot \frac{\lambda}{2\pi} \ \text{[m]}. \tag{2.9}$$

Figure 2.5(a) shows GPS L1 $C/N_0$ values (GS1C) with respect to the corresponding elevation angles of the satellites. A clearly elevation-dependent behavior can be observed due to the antenna gain of the used geodetic pinwheel antenna (*NOV703GGG.R2 NONE*). This means that GPS signals (especially RHCP, see Figure 2.3) received at high elevation angles are more amplified than those at low elevation angles. In addition, noisier $C/N_0$ values at low elevation angles are visible. All in all, the $C/N_0$ values range between 18 dB-Hz at low elevation angles ($el < 10°$) and 52 dB-Hz at high elevation angles. The minimum value can be explained by the settings of the used Septentrio POLARX5TR receiver. With the typical values for the carrier loop noise bandwidth ($B_P = 15$ Hz), $\sigma_{\mathrm{PLL}}$ is depicted as a function of high $C/N_0$ values ($> 25$ dB-Hz) in Figure 2.5(b). It can be seen, that the standard deviation of carrier-phase noise is less than 1 mm for $C/N_0$ values equal to or greater 40 dB-Hz.

This example shows not only the high dependence of $C/N_0$ values on the antenna gain, but also the dependence of the used antenna-receiver combination and the applied receiver settings, e.g. for $B_P$. In practice, the signal strength is not only used as a quality indicator for the received signal, but also for weighting schemes (Brunner et al., 1999; Hartinger and Brunner, 1999), MP analyses (Rost and Wanninger, 2009; Smyrnaios et al., 2013) and GNSS reflectometry (Larson et al., 2008).

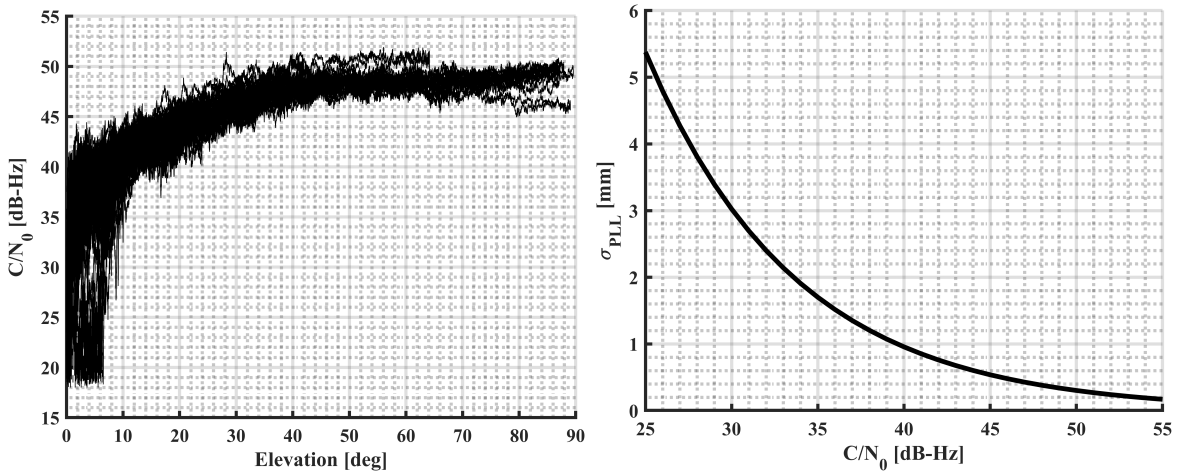


(a) $C/N_0$ values (GS1C) versus elevation angles for a static *NOV703GGG.R2 NONE* antenna.

(b) Standard deviation of the phase lock loop $\sigma_{\mathrm{PLL}}$ as a function of high $C/N_0$ values ($> 25$ dB-Hz) using 15 Hz for the carrier loop noise bandwidth.

**Figure 2.5:** $C/N_0$ values versus elevation angle and their influence on the standard deviation of carrier-phase noise.

**Closing Remarks** In this work, the different frequencies and signals are named in conformity with the newest RINEX 4.01 specifications (IGS, 2023, pp. 26 – 33) or the respective frequency band, when no specific GNSS receiver is involved. Figure 2.2 gives an overview over the frequencies from different GNSS. Since in different IGS products partly different specifications are used, Table 2.2 provides an overview of the used specifications in RINEX or Antenna

**Table 2.2:** Frequency specifications for GNSS frequencies in ANTEX and RINEX files. For GLONASS Frequency Division Multiple Access (FDMA) frequencies, $k_R$ specifies the individual frequency multiplier, which ranges nowadays from -7 to +7. Note that ANTEX frequencies marked with ***** are not officially listed in the format description (Rothacher and Schmid (2010)) but are included in the most recent International GNSS Service (IGS)-ANTEX file *igs20_2317.atx*. ANTEX frequencies marked with ****** are not listed in the format description and are provided for a slightly different center frequency: R04 serves as R01 and R06 as R02. For ANTEX frequencies marked with *******, there is misleading information in the format description regarding BeiDou signals. Superscripts **2** and **3** indicate the respective BeiDou Navigation Satellite System (BDS) generation.

| GNSS | Band | Freq. [MHz] | ANTEX | RINEX carrier-phase code |
|---|---|---|---|---|
| GPS | L1 | 1575.42 | G01 | GL1C, GL1S, GL1L, GL1X, GL1P GL1W, GL1Y, GL1M, GL1N, GL1R |
| | L2 | 1227.60 | G02 | GL2C, GL2D, GL2S, GL2L, GL2X GL2P, GL2W, GL2Y, GL2M, GL2N |
| | L5 | 1176.45 | G05 | GL5I, GL5Q, GL5X |
| GLONASS | G1 | $1602+k_R \cdot \frac{9}{16}$ | R01 | RL1C, RL1P |
| | G1a | 1600.995 | R04** | RL4A, RL4B, RL4X |
| | G2 | $1246+k_R \cdot \frac{7}{16}$ | R02 | RL2C, RL2P |
| | G2a | 1248.06 | R06** | RL6A, RL6B, RL6X |
| | G3 | 1202.025 | R03* | RL3I, RL3Q, RL3X |
| Galileo | E1 | 1575.42 | E01 | EL1A, EL1B, EL1C, EL1X, EL1Z |
| | E5a | 1176.45 | E05 | EL5I, EL5Q, EL5X |
| | E5b | 1207.140 | E07 | EL7I, EL7Q, EL7X |
| | E5 (E5a+E5b) | 1191.795 | E08 | EL8I, EL8Q, EL8X |
| | E6 | 1278.75 | E06 | EL6A, EL6B, EL6C, EL6X, EL6Z |
| BeiDou | B1**2,3** | 1561.098 | C02*** | CL2I, CL2Q, CL2X |
| | B1C**3** | 1575.42 | C01*** | CL1D, CL1P, CL1X |
| | B1A**3** | 1575.42 | | CL1S, CL1L, CL1Z |
| | B2a**3** | 1176.45 | C05* | CL5D, CL5P, CL5X |
| | B2**2** | 1207.140 | C07*** | CL7I, CL7Q, CL7X |
| | B2b**3** | 1207.140 | | CL7D, CL7P, CL7Z |
| | B2**3** (B2a+B2b) | 1191.795 | C08* | CL8D, CL8P, CL8X |
| | B3**2,3** | 1268.52 | C06*** | CL6I, CL6Q, CL6X |
| | B3A**3** | 1268.52 | | CL6D, CL6P, CL6Z |

Exchange Format (ANTEX) files along with their frequency band and center frequency. A detailed format description of the ANTEX file format is provided in Section 2.2.2.

Referring to Table 2.2, it is worth noting that for GLONASS frequency bands G1 and G2 a specific factor $k_R$ is included for the listed frequencies. Since GLONASS uses the FDMA modulation to uniquely assign satellites, satellites transmit signals on slightly different frequencies around the center frequency of 1602 MHz for G1 and 1246 MHz for G2. This is defined by the multiplication factor $k_R$, which ranges nowadays from -7 to +7. However, as part of the GLONASS modernization, Code Division Multiple Access (CDMA) signals will also be transmitted on these frequencies band so that the interoperability with other GNSS is improved (Revnivykh et al., 2017). These frequency bands are denoted as G1a, G2a and G3.

Additionally, it is notable that BeiDou lists a total of nine frequency bands. However,

B1C and B1A, B2 and B2b, as well as B3 and B3A, each share the same center frequency. The wide range of specified frequency bands is linked to the three developmental phases of the BDS: BDS-1, a regional Radio Determination Satellite Service (RDSS); BDS-2, a regional RNSS; and BDS-3, which provides a global service (Yang et al., 2017). The assignment of each frequency band to its respective BDS generation is indicated with superscripts in Table 2.2.

### 2.1.3 Linear Combinations

This section briefly introduces different linear combinations. They are formed from observations from one satellite and one receiver, whereby different frequencies might be combined. In addition to the combinations presented here, further linear combinations exist. As these are not used in this work, only the most important ones are shortly mentioned below. More details can be found e.g. in Misra and Enge (2011) and Hauschild (2017b).

#### Ionosphere-Free Linear Combination

Since the ionosphere is a dispersive medium, the ionospheric delay varies inversely with the carrier frequency squared (Misra and Enge, 2011). Thus, the first-order ionospheric delay can be eliminated with dual-frequency pseudorange or carrier-phase measurements, while preserving the geometry. For two different frequencies $f_a$ and $f_b$, the Ionosphere-Free Linear Combination (IF-LC) for carrier-phase measurements reads according to Hauschild (2017b)

$$\varphi_{\mathrm{IF}} = \frac{f_a^2}{f_a^2 - f_b^2}\varphi_a - \frac{f_b^2}{f_a^2 - f_b^2}\varphi_b. \tag{2.10}$$

In more general terms, and again skipping the receiver and satellite identifier for clarity, the formula can be rewritten to

$$\varphi_{\mathrm{IF}} = \beta_a\varphi_a + \beta_b\varphi_b. \tag{2.11}$$

Assuming identical noise $\sigma$ for both frequencies and uncorrelated observations, the noise of the IF-LC $\sigma_{\mathrm{IF}}$ can be calculated following the law of error propagation

$$\begin{aligned} \sigma_{\mathrm{IF}} &= \sqrt{\beta_a^2 + \beta_b^2} \cdot \sigma \\ \sigma_{\mathrm{IF}} &= f_\sigma \cdot \sigma. \end{aligned} \tag{2.12}$$

Table 2.3 exemplarily provides the $\beta_a$ and $\beta_b$ coefficients along with the amplification factor $f_\sigma$ for all GPS and selected Galileo, GLONASS and BeiDou frequencies. Since the coefficients, and thus the amplification factor depends on the used frequencies, they are identical for identical frequencies, e.g. GPS L1/L5, Galileo E1/E5a and BeiDou B1C/B2a.

Also, it can be clearly seen that the noise is more amplified, when frequencies close to each other are used for calculating the IF-LC, see Figure 2.2. Accordingly, it is beneficial to combine L1/L5 or E1/E5a, respectively, to assure a moderate increase ($\approx 2.6$) of the noise. Moreover, it should be noted that the amplification is even higher for the non-listed Galileo, GLONASS and BeiDou frequencies, as the frequencies are very close together, for example E5/E5b or G3/G2a. Here, the noise would be amplified by a factor of $\approx 18.8$. Since these linear combinations are not used in practice, they are not listed in Table 2.3.

IF-LC are widely used in GNSS processing, especially for position determination algorithms, in which the ionospheric effect is not canceled out. This holds true for absolute positioning schemes, like PPP, and for relative positioning with baselines longer than 10 km. For carrier-

**Table 2.3:** Conspectus of different GPS and Galileo coefficients $\beta_1$ and $\beta_2$ for calculating the IF-LC and their resulting noise amplification factors $f_\sigma$.

| **GNSS** | $\mathbf{f_a}$ | $\mathbf{f_b}$ | $\beta_\mathbf{a}$ | $\beta_\mathbf{b}$ | $\mathbf{f}_\sigma$ |
|---|---|---|---|---|---|
| GPS | L1 | L2 | 2.546 | -1.546 | 2.979 |
| | L1 | L5 | 2.261 | -1.261 | 2.589 |
| | L2 | L5 | 12.255 | -11.255 | 16.639 |
| Galileo | E1 | E5a | 2.261 | -1.261 | 2.589 |
| | E1 | E6 | 2.931 | -1.931 | 3.510 |
| | E1 | E5b | 2.422 | -1.422 | 2.809 |
| | E1 | E5 | 2.338 | -1.338 | 2.694 |
| | E5a | E6 | -5.51 | 6.51 | 8.529 |
| GLONASS | G1 | G2 | 2.531 | -1.531 | 2.958 |
| | G1 | G3 | 2.288 | -1.288 | 2.626 |
| | G1 | G6 | 2.544 | -1.544 | 2.976 |
| | G2 | G1a | -1.536 | 2.536 | 2.965 |
| | G3 | G1a | -1.292 | 2.292 | 2.631 |
| | G1a | G2a | 2.549 | -1.549 | 2.983 |
| BeiDou | B1C/B1A | B2a | 2.261 | -1.261 | 2.589 |
| | B1C/B1A | B3/B3A | 2.844 | -1.844 | 3.389 |
| | B1C/B1A | B2/B2b | 2.422 | -1.422 | 2.809 |
| | B1 | B2a | 2.314 | -1.314 | 2.661 |
| | B1 | B3/B3A | 2.944 | -1.944 | 3.528 |
| | B1 | B2/B2b | 2.487 | -1.487 | 2.898 |

phase measurements, the resulting wavelength $\lambda_{\mathrm{IF}}$ is especially important for ambiguity resolution and reads according to Hauschild (2017b)

$$\lambda_{\mathrm{IF}} = \frac{\lambda_a \lambda_b}{i_a \lambda_a + i_b \lambda_b}. \tag{2.13}$$

If the factors $i_a$ and $i_b$ are selected so that the integer nature of $\lambda_{\mathrm{IF}}$ is preserved, the corresponding wavelength is very short, e.g. 6 mm for GPS L1/L2, which poses a challenge for ambiguity resolution. Non-integer choices for $i_a$ and $i_b$, however, result into non-integer combined ambiguities, which degrade for example PPP position estimates. Therefore, combinations with signals from more than two frequencies can be used to eliminate the ionosphere while preserving the integer nature of the combined ambiguities (Hauschild, 2017b).

### Multipath Linear Combination

The Multipath Linear Combination (MP-LC) can be used to get an understanding of the magnitude of the code MP error. To assess the pseudorange MP error, usually the MP-LC using one pseudorange observation $P_a$ and two carrier-phase observations on two frequencies $(\varphi_a, \varphi_b)$ is calculated. According to Hauschild (2017b), skipping station and satellite identifier, the MP-LC reads

$$P_{a,\mathrm{MP}} = P_a - \varphi_a - 2\beta_b(\varphi_a - \varphi_b), \tag{2.14}$$

where $\beta_b$ can be computed analogously as

$$\beta_b = \frac{f_b^2}{f_a^2 - f_b^2}. \tag{2.15}$$

The MP-LC is geometry-free and ionosphere-free. However, it still contains PC and Codephase Center (CC) errors, signal biases, PWU effects, ambiguities, MP from both pseudorange and carrier-phase observations as well as receiver noise. The magnitude of MP effect as well as the noise from carrier-phase observations is much smaller than those from pseudorange measurements, and can therefore be neglected. All other parts are constant over time and can be removed by estimating and subtracting the mean value of $P_{a,\mathrm{MP}}$ so that the peak-to-peak MP behavior for $P_a$ can be assessed (Braasch, 2017). With three frequencies, it is possible to separate the MP errors from pseudorange and carrier-phase observations to some extent.

### 2.1.4 Observation Differencing and Position Determination

In general, two position methods exist. The first uses undifferenced observations, like SPP with pseudorange measurements and PPP with carrier-phase measurements. The second method relies on differenced observations, also known as relative positioning. This section provides details on relative positioning, specifically focusing on the two-station case. As the name suggests, the position is determined *relative* to the known coordinates of a second station. This means that a reference station with known coordinates is required. Then, the differential measurement processing can be carried out using the advantage of spatiotemporal correlation of measurement errors in order to (largely) reduce or eliminate error sources (Bisnath, 2021). In principle, three different types of combinations of multi-satellite and multi-receiver observations exist (Hauschild, 2017b)

1. Between-receiver Single Differences (SD), also known as receiver-to-receiver SD
2. Between-satellite SD, also known as satellite-to-satellite SD
3. Double Differences (DD), combining both types of SDs.

All of these combinations can additionally be time-differenced, e.g. time-differenced Single Differences (dSD) or time-differenced Double Differences (dDD), also known as Triple differences.

#### Receiver-to-Receiver Single Differences

When time-synchronized measurements of the identical satellite $k$ are observed by two GNSS receivers ($A$, $B$), receiver-to-receiver SD can be formed

$$\Delta\varphi_{A,B}^k = \varphi_B^k - \varphi_A^k. \tag{2.16}$$

This measurement setup is depicted in Figure 2.6(a). Two aspects should be noted for Equation 2.16. Firstly, since this work focuses on carrier-phase measurements ($\varphi$), the equation is provided for those measurements. Details on pseudorange measurements can for example be found in Hauschild (2017b). Secondly, the signal index is skipped for clarity. Usually, the observation combination is computed between identical signals, while these do not need to be necessarily one of the primary observation type but could also be for example the IF-LC computed for both stations (Hauschild, 2017b). In order to clearly show which GNSS measurement errors are strongly reduced or eliminated by the different differencing strategies, the error budget based on Bisnath (2021) is summarized in Table 2.4. The errors are distinguished by

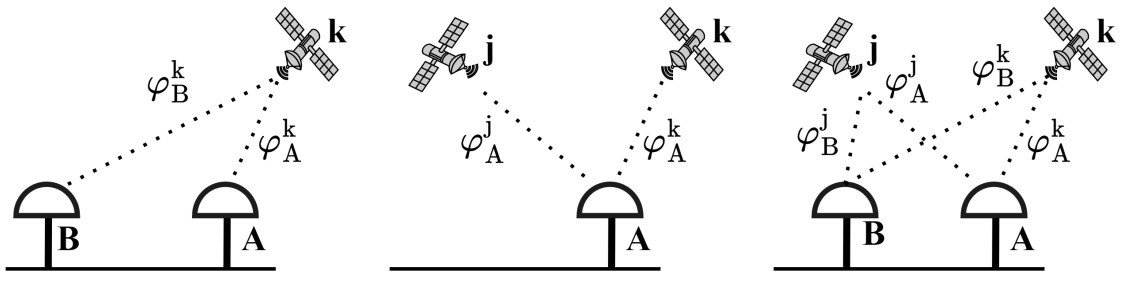


(a) Receiver-to-receiver SD (b) Satellite-to-satellite SD (c) Double Differences

**Figure 2.6:** Sketches of observation differencing strategies.

their origin: occurring at the satellite (*Transmission*), during transmission (*Propagation*) and at the receiving station (*Reception*). Additionally, their notation in the observation equations for pseudorange measurements (Equation 2.5) and carrier-phase measurements (Equation 2.7) are provided.

For time-synchronized carrier-phase measurements, the satellite clock offset, relativistic effects for the satellite clock and orbit errors are identical for both measurements at the respective stations and therefore cancel out. For stations located close to each other of only up to a few 100 m, the signal transmitting path are virtually the same so that the ionospheric and tropospheric error as well as the differential relativistic space–time curvature correction cancel out. Also, the errors due to the variations of the PC for the transmitting antenna $\xi^k$ are eliminated, as long as the azimuth and elevation angles of the satellite $k$ are practically identical at both stations. For larger baselines, the effects decorrelate and thus need to be modeled accordingly (Hauschild, 2017b). If receivers with identical correlators are used, the combined satellite and receiver biases can be split into the individual terms. In this case, the satellite biases are dropped out. However, a differential receiver-dependent part is still present within the SD.

In conclusion, assuming a short baseline and identical receiver types at both stations, the differential receiver clock offset and hardware delays, differential PCC between the two receiv-

**Table 2.4:** Major GNSS error sources based on Bisnath (2021).

| **Source of Error** | **Error** | **Notation in Eq. 2.5/2.7** |
|---|---|---|
| Transmission | Orbit error | contained in $\rho$ |
| | Clock error | $\delta t^k$ |
| | Antenna biases | contained in $\xi^k$ |
| | Equipment delays | contained in $\epsilon$ |
| Propagation | Relativistic effects | $\delta t_{rel}$ |
| | Ionospheric refraction | $I$ |
| | Tropospheric refraction | $T$ |
| | Phase Wind-Up | $\omega$ |
| Reception | Multipath | contained in $\epsilon$ |
| | Antenna biases | contained in $\xi_A$ |
| | Equipment delays | contained in $\epsilon$ |
| | Clock error | $\delta t_A$ |
| | Receiver noise | contained in $\epsilon$ |
| | Site displacements | contained in $\epsilon$ |

ing antennas $\Delta\xi_{A,B}$, PWU effects, and ambiguities as well as noise and MP errors (summarized in $\epsilon$) remain in the observation equation. Thus, the equation for SD reads

$$\Delta\varphi^k_{A,B} = \Delta\rho^k_{A,B} + \Delta\xi_{A,B} + c(\Delta\delta t_{A,B} + \Delta d_{A,B}) + \lambda(\Delta\omega^k_{A,B} + \Delta N^k_{A,B}) + \Delta\epsilon^k_{A,B}. \tag{2.17}$$

The differential PWU correction term $\Delta\omega^k$ depends on the relative orientation of satellite and antenna. During antenna calibration, the Antenna Under Test (AUT) is tilted and rotated by a robot while the antenna at the reference station does not change its orientation. Thus, the PWU effect does not cancel out and needs to be modeled accordingly. The basic algorithm for the case *antenna calibration* is provided in Section 4.2.2. The differential ambiguities $\Delta N$ introduce an offset into the carrier-phase SD. It should be noted that the noise of the SD is increased by a factor of $\sqrt{2}$ assuming no correlation and identical standard deviations $\sigma$ for the uncombined observables

$$\sigma_{\mathrm{SD}} = \sqrt{2} \cdot \sigma. \tag{2.18}$$

#### Satellite-to-Satellite Single Differences

Observation differencing can also be applied using one single station $A$ and observations from two satellites ($k$, $j$), as it is depicted in Figure 2.6(b)

$$\Delta\varphi^{k,j}_{A} = \varphi^j_A - \varphi^k_A. \tag{2.19}$$

In this case, the receiver clock error drops out from the observation equation. All other error sources are still contained, whereas the handling of the PWU effect and ambiguities are more complicated because Inter System Biases (ISB) might be introduced when forming differences between satellites from different constellations. Details can be found in Hauschild (2017b).

#### Double Differences

If time-synchronized carrier-phase measurements from two stations and two satellites are available, DD can be formed, as illustrated in Figure 2.6(c)

$$\Delta\varphi^{k,j}_{A,B} = \varphi^j_{A,B} - \varphi^k_{A,B}. \tag{2.20}$$

With this measurement setup, receiver and satellite clock offsets, along with relativistic corrections, are eliminated. For short baselines, similar to SD, tropospheric and ionospheric delays are also canceled. If receivers with compatible front-ends and correlator designs are used – for example, identical receivers at both stations – carrier-phase biases are further eliminated. Additionally, for baselines shorter than a few hundred kilometers, the PWU term cancels out in static conditions or when the relative rotations of receiving antennas are equal.

The DD still contain the differences in geometric range $\Delta\rho^{k,j}_{A,B}$, the differential PCC between the two receiving antennas $\Delta\xi_{A,B}$, the differential ambiguities $\Delta N^{k,j}_{A,B}$ as well as differential receiver noise and differential MP effects, summarized in $\Delta\epsilon^{k,j}_{A,B}$. Thus, the equation for DD assuming a short baseline reads

$$\Delta\varphi^{k,j}_{A,B} = \Delta\rho^{k,j}_{A,B} + \Delta\xi_{A,B} + \lambda \cdot \Delta N^{k,j}_{A,B} + \Delta\epsilon^{k,j}_{A,B} \tag{2.21}$$

The noise of the DD $\sigma_{\mathrm{DD}}$ are increased by a factor of $\sqrt{2}$ compared to the SD, resulting in

$$\sigma_{\mathrm{DD}} = 2\sigma, \tag{2.22}$$

with $\sigma$ denoting the standard deviation of the undifferenced observations and assuming uncorrelated stochastic errors (Hauschild, 2017b).

### Time Differenced Observations

When SD or DD are additionally time-differenced, all constant parts are removed, especially when the time interval $t_i - t_{i-1}$ is small. Time-differenced receiver-to-receiver SD (dSD) are computed following Equation 2.16

$$\mathrm{dSD}^k_{A,B} = \varphi^k_{A,B}(t_i) - \varphi^k_{A,B}(t_{i-1}). \tag{2.23}$$

In this case, for short baselines, only the receiver noise including MP effects and the differential receiver clock drift remain in the dSD. This, however, can be avoided if one external frequency is connected to both receivers. In the case of two static antennas, the PWU effect also cancels. Unfortunately, this is not the case during the antenna calibration process and is therefore described in Section 4.2.2.

Following the law of error propagation, assuming uncorrelated observations, the noise of $\sigma_{\mathrm{SD}}$ is amplified by factor $\sqrt{2}$, resulting in the overall noise of $\sigma_{\mathrm{dSD}}$

$$\sigma_{\mathrm{dSD}} = \sqrt{2} \cdot \sigma_{\mathrm{SD}} = 2 \cdot \sigma. \tag{2.24}$$

Analogously to the formula for calculating dSD, Equation 2.20 is taken to form time-differenced DD, i.e. dDD

$$\mathrm{dDD}^{k,j}_{A,B} = \varphi^{k,j,}_{A,B}(t_i) - \varphi^{k,j}_{A,B}(t_{i-1}) \tag{2.25}$$

Here, for short baselines, the receiver noise $\epsilon$ (including MP effects) remains in the observation equation. However, when equal noise for both DD observation is assumed, the standard deviation is again amplified by factor $\sqrt{2}$ w.r.t. $\sigma_{\mathrm{DD}}$ and reads for the dDD

$$\sigma_{\mathrm{dDD}} = \sqrt{2} \cdot \sigma_{\mathrm{DD}} = 2 \cdot \sqrt{2}\sigma. \tag{2.26}$$

### Precise Point Positioning

PPP enables the user to calculate a position with high accuracy using a single GNSS receiver (Teunissen, 2021). To achieve this, several adaptions with respect to the SPP algorithm need to be done. The main differences are that carrier-phase observations in addition to codephase observations are used, that precise satellite orbits and clock corrections are needed, e.g. provided by the IGS (Johnston et al., 2017), and that usually more than one frequency is used in order to eliminate the ionospheric effect by building the IF-LC (Teunissen, 2021). In general, using PPP, not only positions ($X^{\mathrm{ECEF}}$, $Y^{\mathrm{ECEF}}$, $Z^{\mathrm{ECEF}}$) and the receiver clock error $\delta t$ are estimated, but also tropospheric estimates are determined.

Since no baseline processing is carried out and therefore no error sources cancel out by differencing, several a priori corrections need to be applied, which are summarized in Table 2.5. However, since no reference station (network) is (directly) needed, it is a cost-efficient method to determine a position anywhere on the globe relying on orbit and clock products. In addition, PPP can not only be used to determine the user's position, but it also enables the possibility for e.g. water vapor estimation, ionospheric estimation and time transfer (Teunissen, 2021).

In this work, the PPP algorithm is used to assess the impact of different PCC sets ($\Delta$PCC) on geodetic parameters. Since the analysis in this work focuses solely on the differences

between two PPP runs, which differ only on their input receiver PCC, only a brief introduction is provided here. More details can be found e.g. in Teunissen (2021) and Kouba et al. (2017).

**Table 2.5:** PPP a priori corrections and their magnitudes based on Teunissen (2021) and Kouba et al. (2017).

| | Correction | Approx. Magnitude |
|---|---|---|
| **Satellite** | Phase Center Offset | 0.5 - 3 m |
| | Phase Center Variations | 5 - 15 mm |
| | Clock offset | $< 1$ ms |
| | Relativistic clock effect | 10 - 20 m |
| | Differential Code Bias | Up to 5 m |
| **Atmosphere** | Troposphere (dry, vertical) | 2.3 m |
| | Ionosphere (vertical) | Up to 30 m |
| **Receiver** | Phase Center Offset | 5 - 15 cm |
| | Phase Center Variations | Up to 3 cm |
| | Phase Wind-Up | Up to 10 cm |
| **Site Movement** | Plate motion | Up to 0.1 m/y |
| | Solid Earth tide | Up to 0.4 m |
| | Ocean loading | 1 - 10 cm |
| | Pole tide | 25 mm |
| | Atmospheric loading | Up to 20 mm |

## 2.2 Receiver Antenna Calibration

This section provides the fundamentals of receiver antenna calibration, i.e. determining PCC or CPC (also known as GDV). The definition of PCC, calibration methods as well as format standards and the application of PCC on GNSS observations are discussed. In addition, the most recent developments in the field of receiver antenna calibration are presented.

### 2.2.1 Definition of Phase Center Corrections

Since GNSS antenna reception characteristics deviate from an ideal omnidirectional pattern, the electric phase center – representing the reception point of GNSS measurements – depends on the azimuth and zenith angles of the incoming GNSS signals. The deviations from the ideal isotropic radiator (and therefore also for the receptor) occur since GNSS antennas are dependent on various individual design parameters, which are described in detail in Section 2.1.1 (Rao et al., 2013).

Due to the directional pattern, corresponding corrections – known as PCC – need to be taken into account in order to achieve highly accurate GNSS positioning. Following the convention of the IGS, PCC are expressed in a left-handed antenna-fixed coordinate system, with the origin being located in the Antenna Reference Point (ARP) (Rothacher and Schmid, 2010). The location of the ARP for various GNSS antennas (and for all antennas used at IGS stations) are provided in the *antenna.gra* file (IGS, 2024). Following the metadata in the header of the *antenna.gra* file, the ARP should preferably be located at an easily accessible point on the lowest non-removable horizontal surface of the antenna. In addition, the dimension of the antenna is provided in the *antenna.gra* file.

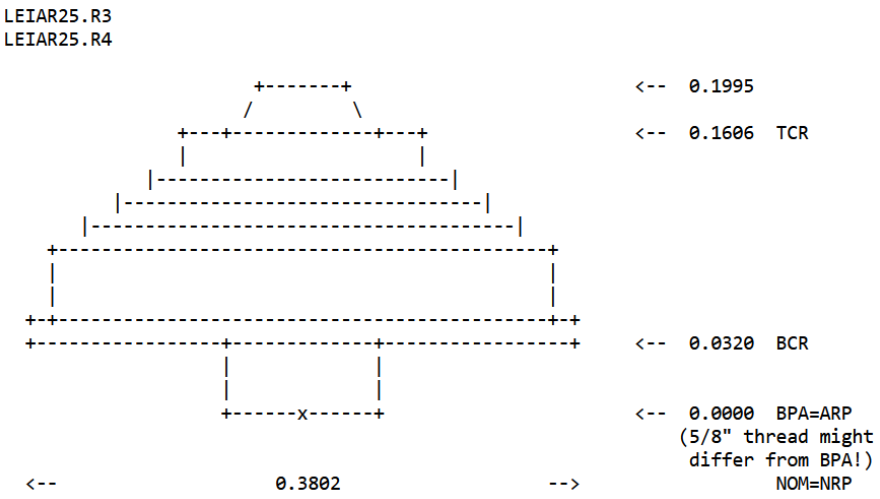


**Figure 2.7:** Extract from the *antenna.gra* file for a *LEIAR25.R3*/*LEIAR25.R4* antenna.

As an example, Figure 2.7 depicts the relevant information for *LEIAR25.R3* as well as *LEIAR25.R4* antennas. In their cases, the ARP is defined as the Bottom of Preamplifier (BPA). Thus, the PCC of the respective antennas need to be taken into account as range corrections (as a function of the direction of the incoming satellite signal) w.r.t. the BPA (= ARP). The North direction is usually the antenna cable connector. This holds also true for the provided example in Figure 2.7. However, in this case the North Reference Point (NRP) is also marked by a North Orientation Mark (NOM), which is an arrow placed on the antenna by the manufacturer (and which coincides in this case with the cable connector).

PCC can be (arbitrarily) divided into a PCO vector given in the topocentric antenna frame, i.e. North, East, Up, projected on the line-of-sight vector $\vec{e}$ and azimuth $\alpha$ and zenith $z$ dependent PCV. The azimuth angle counts clockwise from the North to East. In addition, a constant part $r$ is also present. A detailed discussion on the separation of the components and the role of $r$ is provided in Section 4.3.3. Equation 2.27 specifies the formula for calculating PCC from the individual parts

$$\mathrm{PCC}(\alpha^k, z^k) = -\mathrm{PCO} \cdot \vec{e}(\alpha^k, z^k) + \mathrm{PCV}(\alpha^k, z^k) + r. \tag{2.27}$$

Figure 2.8 depicts the geometrical interpretation of PCC. The dashed line indicates the theoretical omnidirectional radiation pattern. The deviations from this, shown as a solid line, indicate the real pattern. The differences in between are defined as PCC.

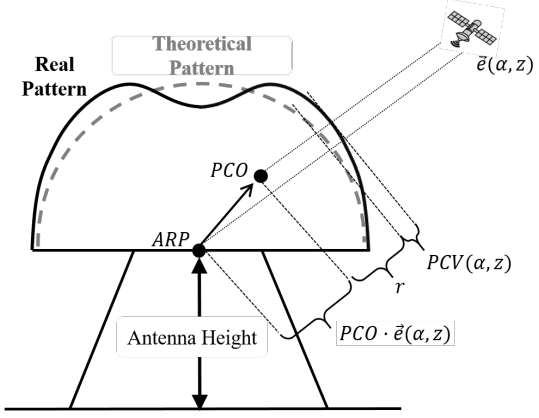


**Figure 2.8:** Geometric interpretation of PCC.

### 2.2.2 Format Standards and Application of Phase Center Correction Values

#### ANTEX File

Receiver antenna PCC are provided by the IGS, along with PCC values for the transmitting satellite antennas, in the ANTEX file. The general format description is given in (Rothacher and Schmid, 2010). Figure 2.9 additionally depicts a minimal example for representing estimated receiver antenna PCC in the ANTEX format. Essentially, it uses an equally spaced grid to present the correction values.

In general, the ANTEX file consists of a header section and a data block. Key points include that, for each antenna, the antenna name and serial number are specified before the correction values are provided. The antenna name follows the naming convention from the *rcvr_ant.tab* file (IGS, 2024). For receiving antennas, it is important to include information about the radome used, as it influences the actual PCC; `NONE` is used if the antenna has no radome. Additionally, it is crucial to distinguish between the two types of PCC: individual or type-mean calibrations. If a serial number is included, the PCC values are valid for the individual antenna (individual calibration). Otherwise, a type-mean calibration is provided, offering PCC values for all individual antennas of the specified antenna type, including the exact radome. In addition, the number of calibrations used to calculate the type-mean values is provided.

For each antenna, the resolution of the azimuth angles $\alpha$ and the interval (typically $0° \leq z \leq 360°$ with a step size of 5°) as well as the resolution of the zenith angles $z$ (typically $0° \leq z \leq 90°$ with a step size of 5°) are specified. The PCC values themselves are provided per GNSS and frequency, including the PCO components (North, East, Up) and averaged PCV values per zenith angle, and are listed in millimeters. Additionally, the PCV values for the specified azimuth and zenith angles can be tabulated, which is usually the case for receiver antennas. It should be noted that the tabulated PCV values might still contain PCO components or constant parts, i.e. $r$ in Equation 2.27. Furthermore, Root Mean Square (RMS) values can also be provided for the antennas, with a structure identical to that for PCC values (Rothacher and Schmid, 2010).

The codes used for the different systems and frequencies are provided in Table 2.2. Although the current ANTEX format 1.4 supports multi-GNSS antenna PCC values, the official format description does not list all currently used frequencies, such as R03. Furthermore, it should be

```
     1.4            M                                   ANTEX VERSION / SYST
A                                                       PCV TYPE / REFANT COMMENT
                                                        END OF HEADER
                                                        START OF ANTENNA
LEIAR20         LEIM2210004                             TYPE / SERIAL NO
robot              ife                    3    05-Dec-22 METH / BY / # / DATE
     5.0                                                DAZI
     0.0  90.0   5.0                                    ZEN1 / ZEN2 / DZEN
     5                                                  # OF FREQUENCIES
     5                                                  # OF FREQUENCIES
   G01                                                  START OF FREQUENCY
      0.95      0.12    123.91                          NORTH / EAST / UP
   NOAZI    0.00   -0.07   -0.30   -0.67   -1.14   -1.64   -2.14   -2.66   -3.19   -3.64   -3.89   -3.86   -3.58   -3.09   -2.28   -0.91    1.21    3.98    6.98
     0.0    0.00    0.08   -0.13   -0.60   -1.14   -1.62   -2.04   -2.47   -2.93   -3.31   -3.49   -3.46   -3.23   -2.74   -1.82   -0.35    1.68    4.14    6.85
     5.0    0.00    0.07   -0.15   -0.62   -1.16   -1.64   -2.05   -2.49   -2.94   -3.30   -3.46   -3.42   -3.20   -2.71   -1.81   -0.34    1.68    4.14    6.86
                                                                    ●   ●   ●
   360.0    0.00    0.08   -0.13   -0.60   -1.14   -1.62   -2.04   -2.47   -2.93   -3.31   -3.49   -3.46   -3.23   -2.74   -1.82   -0.35    1.68    4.14    6.85
   G01                                                  END OF FREQUENCY
   G02                                                  START OF FREQUENCY
      0.75      0.17    131.58                          NORTH / EAST / UP
   NOAZI    0.00   -0.08   -0.31   -0.68   -1.13   -1.59   -2.08   -2.61   -3.16   -3.58   -3.69   -3.43   -2.93   -2.39   -1.84   -0.95    0.71    3.36    6.67
     0.0    0.00   -0.00   -0.29   -0.77   -1.28   -1.72   -2.11   -2.57   -3.11   -3.58   -3.75   -3.50   -2.94   -2.31   -1.64   -0.64    1.16    3.99    7.48
     5.0    0.00   -0.00   -0.28   -0.75   -1.24   -1.68   -2.10   -2.56   -3.07   -3.48   -3.62   -3.38   -2.85   -2.16   -1.38   -0.30    1.47    4.19    7.55
                                                                    ●   ●   ●
   G02                                                  END OF FREQUENCY

                                                                    ●   ●   ●
                                                        END OF ANTENNA
```

Header section

Data block

**Figure 2.9:** Minimal example for representing PCC in the ANTEX format.

noted that PCC values are partially provided for different center frequencies (compare with Figure 2.2 and Table 2.2). As stated in Wübbena et al. (2019), Geo++ combines frequencies with minor frequency differences to one set of PCC, which applies to R01/R04 and R02/R06, respectively.

The ANTEX file is updated irregularly by the IGS. Generally, new ANTEX files are published with a new realization of the IGS reference frame, such as `IGS05`, `IGS08`, `IGS14`, and `IGS20`. In the meantime, additional ANTEX files with updated transmitting or receiving antenna patterns are made available. These files follow the naming convention `mmmmm_wwww` with the file extension `.atx`, where `m` represents the 5-character model name (e.g. `IGS20`). The model name changes only when existing PCC values are modified, not when new PCC values are added. The `wwww` part represents the GPS week of the last file update (Rothacher and Schmid, 2010). All previously published files can be accessed on the IGS server: https://files.igs.org/pub/station/general/pcv_archive/.

In the antenna committee meeting during the IGS workshop 2024 in Bern, a proposal was made for an ANTEX 2.0 version (Montenbruck et al., 2024). In principle, the ANTEX 2.0 format follows the basic format of the ANTEX 1.4 version. The main changes concerning the receiver antenna pattern are that three types of antenna patterns should be supported: PCC, GDV/CPC, and gain pattern. Additionally, a list of frequency bands (e.g., G01, S01, E01, J01) can now be provided in the updated record names `START OF PHV`, `START OF GDV`, and `START OF GAIN`. This update helps avoid redundancy by eliminating duplicated values for identical frequencies from different GNSS systems. The full format proposal along with test data can be found on the IGS server: https://files.igs.org/pub/station/general/atx_alternative/atx2/.

#### Application of Phase Center Corrections Values

During GNSS processing, the PCC for the receiver antenna are taken into account on the GNSS observations $\mathbf{l}_A^k$ for receiver $A$ and satellite $k$ as follows

$$\mathrm{OMC}_A^k = l_A^k - (\rho_A^k + \Sigma_{Corr} - \mathrm{PCO} \cdot \vec{e} + \mathrm{PCV} + r). \tag{2.28}$$

The Observed-Minus-Computed (OMC) values are determined by subtracting all corrections from the observations, i.e. carrier-phases $\varphi$. Thus, $\mathrm{OMC}_A^k$ are the corrected observations, $\rho_A^k$ is the geometrical distance between satellite $k$ and station $A$, $\Sigma_{Corr}$ denotes all further applied corrections, see Equation. 2.7. For example, these corrections include the PCC for the ransmitting antennas mounted on the satellites. Similar to PCC for the receiving antenna they are accounted for as -$\mathrm{PCO_{SAT}}$ + $\mathrm{PCV_{SAT}}$. The respective PCO and PCV corrections for both transmitting and receiving antennas are obtained from the ANTEX file and are determined for the actual satellite's azimuth and elevation angel by a bilinear interpolation of the gridded values. The influence of the grid size or more specifically the interpolation error is discussed in Section 6.5.

#### Antenna Gain Pattern

As described in Section 2.1.1, antenna gain is a measure of how effectively an antenna can receive or transmit power from/into a specific direction. This measurement is taken in comparison to an idealized, lossless isotropic antenna (Maqsood et al., 2017). Since this is also the case why PCC need to be taken adequately into account during GNSS processing, it can be stated that PCC and antenna gain are related to some extent. Thus, a short comment on antenna gain pattern is added in this section.

Antenna gain pattern of various antennas become more and more important in the geodetic community. They are not only of great interest for assessing the MP suppression capabilities of GNSS antennas (Caizzone et al., 2021), but also for $C/N_0$ prediction as a key parameter for network Real-Time Kinematic (RTK) integrity prediction (Karimidoona and Schön, 2023) or for GNSS spoofing detection (Liao et al., 2024). However, currently no official database of published gain patterns is available. Thus, the computation of, for example, the MPSI introduced before can be challenging in parts. Therefore, it would be beneficial for the geodetic community to create and provide an official file with antenna gain pattern or to include the gain information into the ANTEX file. This is currently also discussed in the IGS-Antenna Working Group (AWG) and underlines the scientific relevance of antenna gain patterns for the geodetic community. The proposed ANTEX 2.0 version would then contain the additional record name `START OF GAIN`. However, the lack of including LHCP antenna gain information would be present so that records `START OF RHCP` and `START OF LHCP` would be a more sophisticated solution.

### 2.2.3 State of the Art of Calibration Methods & Current Developments

Nowadays, in principle two calibration methods exist: absolute robot calibration (method `ROBOT`) and chamber calibration (method `CHAMBER`). The main difference between these calibration methods is that method `ROBOT` uses real GNSS signals, while method `CHAMBER` uses artificially generated GNSS signals at the center frequency to estimate PCC corrections. Figure 2.10 shows exemplarily the measurement setups for both calibration methods. In Figure 2.10(a), the anechoic chamber at University of Bonn is depicted (Zeimetz, 2010), whereas in this case neither the transmitter nor the AUT are placed in the chamber. The red lines indicate the position of the cables. Figure 2.10(b) shows an example of method `ROBOT`. Here, the AUT is placed on the robot in the foreground.

In the following sections, the different calibration methods and most recent developments are presented. The topicality and scientific relevance of the topic *antenna calibration* is especially reflected in the numerous developments at various research institutes and companies. This is also demonstrated in the framework of the IGS AWG, where an international collaboration to compare calibration results is currently ongoing (as of January 2025). The project is called *RingCalVal* and the overall goal, participating institutions and first results have been presented in Kersten et al. (2024a,b).

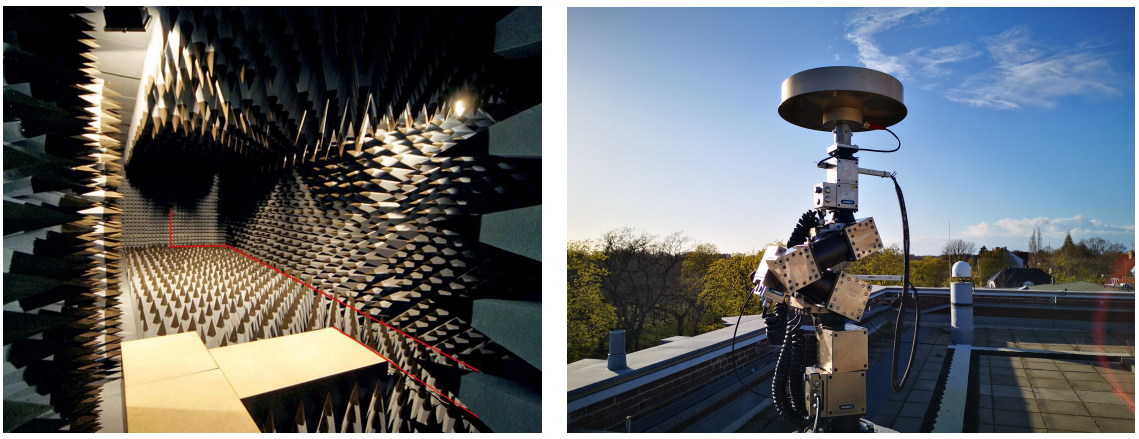

(a) `CHAMBER` (Zeimetz, 2010) (b) `ROBOT`

**Figure 2.10:** General calibration setups for method `CHAMBER` and `ROBOT`.

First, a brief overview over the historical development is provided. Next, the calibration methods CHAMBER and ROBOT among their developments are described. The section closes with information about research concerning the validation of PCC and its impact on geodetic parameters.

### Historical Development

First laboratory measurements of GPS antennas were conducted in the 1980s, as reported by Sims (1985) and Tranquilla and Colpitts (1989). The significance of PCC for satellite-based positioning was recognized by at least the late 1980s, following the publication of Geiger (1988), who analytically assessed the impact of PCC on GPS-based positioning. Since then, calibration methods, particularly for geodetic applications, were developed by Schupler and Clark (1991) in a controlled chamber environment.

The first field-based calibration systems were introduced by Rothacher et al. (1995) and Mader and MacKay (1996). In these approaches, PCC were determined relative to a reference antenna. This approach differs significantly from current field-based calibrations, now referred to as *absolute* antenna calibration, which are independent of any reference antenna. Procedures for *absolute* antenna calibration, i.e., determining PCC without a reference antenna, were initially described by Menge et al. (1998), Wübbena et al. (2000), and Böder et al. (2001). Since then, this method has been fundamentally retained and further developed, as described in the section on the calibration method ROBOT.

### Method CHAMBER

The principle measurement setup for chamber calibrations based on Zeimetz (2010) is illustrated in Figure 2.11. The AUT is mounted on a rotation platform, which has in this case a distance of 6.5 m to the transmitter. The distance varies with the calibration facility and depends on the dimensions of the chamber and further boundary conditions. Details can be found in Zeimetz (2010). The Network Analyzer (NWA) generates a signal with a specified frequency and transmission power. It is sent to the transmitter, which emits the signal. The AUT receives the signal and forwards it back to the NWA, which measures the phase shift and the ratio between transmitted and received signal power. The phase shift is a result of the total signal path, including cable lengths, free space propagation, internal signal paths, as well as the influence of transmitting and receiving antenna (Zeimetz, 2010). In order to avoid reflections, which makes the estimation of PCC more sophisticated, the entire chamber should be covered with absorbent material.

Since the absolute phase position is not known for both antenna positions, no absolute PCC can be estimated, i.e. the constant part $r$ remains in Equation 2.27. As a result, a complete sensing of the antenna hemisphere provides a relative description of the direction-dependent reception characteristics of the antenna (Zeimetz, 2010). This also holds true for the method ROBOT. Consequently, a datum has to be defined in order to compare different PCC sets, see Section 3.1.

In addition to chamber calibrations carried out at the University of Bonn, the Institut für Kommunikation und Navigation (IKN) at Deutsches Zentrum für Luft- und Raumfahrt (DLR) Oberpfaffenhofen uses the method CHAMBER in order to estimate PCC. In the past, the chamber was mainly used to estimate GDV/CPC (Caizzone et al., 2018, 2019, 2021). Currently, the IKN also participates in the *RingCalVal* project to verify its workflow for estimating PCC (Kersten et al., 2024b).

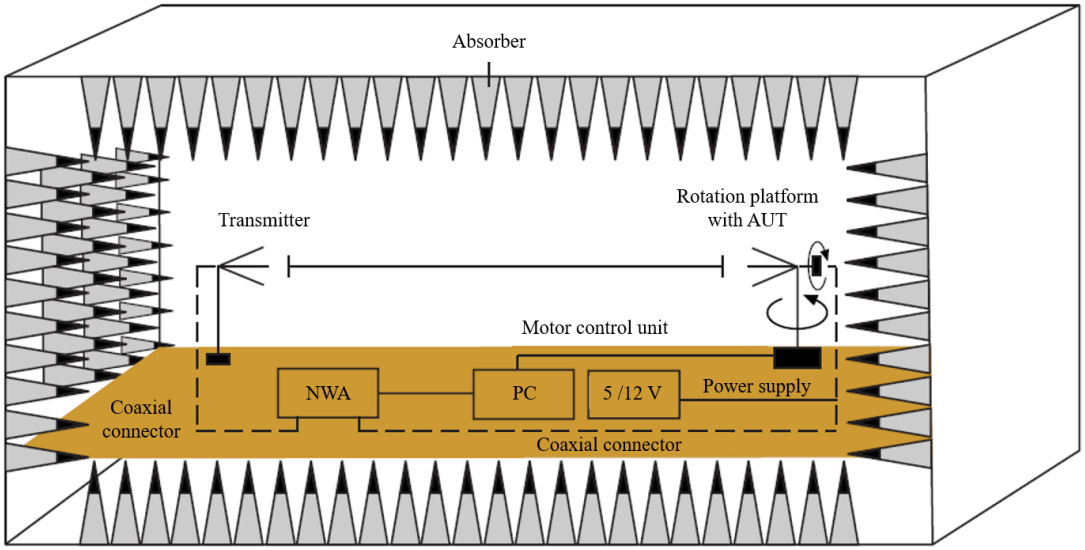


**Figure 2.11:** General measurement setup for method CHAMBER, adapted from Zeimetz (2010).

As stated in Zeimetz (2010), the benefits of the method CHAMBER are constant measurement conditions, low noise of the observations and low MP effects from the far-field. Moreover, due to the free choice of the frequencies, PCC can also be estimated for future GNSS missions and signals, or in regions where a specific system has limited satellite coverage. However, the exact signal modulation and tracking of GNSS receivers are not considered within this method. Furthermore, near-field MP effects might still be present.

### Method ROBOT

Most of the receiver antenna PCC contained in the IGS ANTEX file are determined by the calibration method ROBOT. It is an absolute robot-based GNSS antenna field calibration method. All calibration facilities, which develop and use method ROBOT, utilize an industrial robot to tilt and rotate the AUT. In addition, observations from a nearby located reference station are processed in order to eliminate most of the GNSS errors by forming observation differences (see Section 2.1.4). Nevertheless, the technical term *absolute* still applies, since the PCC are estimated without the impact of the antenna mounted on the reference station. This is a large difference w.r.t. the earlier conducted *relative* antenna calibrations.

In total, four different calibration facilities use identical soft- and hardware to estimate PCC: Geo++, Geoscience Australia (GSA), Senatsverwaltung für Stadtentwicklung Berlin (SenB) and Institut für Erdmessung (IfE) (Wübbena et al., 2019). The used approach was developed in Hannover in close cooperation between IfE and Geo++. This concept of absolute field calibration is described in Menge et al. (1998); Wübbena et al. (2000); Böder et al. (2001). However, since it is a commercial product, only a limited amount of information is publicly available. In addition to this concept, GSA has a second industrial robot with six axes of rotation and a payload of 60 kg. Thus, it is especially suited to calibrate antennas among with their site specific mountings (Hill et al., 2013). At IfE, in addition to the operational method, an independent approach has been developed (Kröger et al., 2021), which is one of the main focuses of this work and is described in detail in Section 4.

Furthermore, the company TOPOCON has built a robotic calibration system in Concordia, Italy, in an open field environment, where the sky is unobstructed down to 10° elevation angle

(Sutyagin and Tatarnikov, 2020). An industrial robot with six degrees of freedom is used to position the AUT with a repeatability of 0.03 mm. For computing the input observations for PCC estimation, a baseline of 20 m with a choke-ring antenna is used. As stated in Sutyagin and Tatarnikov (2020), one single receiver with two antenna inputs is employed. In addition, a common clock is used for both inputs so that receiver clock errors can be avoided in the carrier-phase SD, which serve as the input for the PCC estimation. Receiver-to-receiver SD are used in this approach, because the authors consider them to be more flexible in case of parallel displacements of the AUT by the robot. According to Sutyagin and Tatarnikov (2020), the SD seem to be more appropriate in the sense of treatment of the reference antenna effects. Following Wübbena et al. (1997), Spherical Harmonics (SH) expansions are used to represent PCC but with two special modifications. Firstly, the frequency-dependence of SH coefficients for simultaneous calibrations in different GNSS systems is considered. The PCC in each frequency range are expressed as an SH expansion, with coefficients that depend polynomially on the frequency. Secondly, the definition area of SH is adapted. An interval from 0° up to 150° zenith angle (and not the full sphere) is chosen. Since SD are used for the estimation of PCC, remaining error sources need to be considered. The SD phase ambiguities are solved by the LAMBDA method. The PCC of the reference antenna, MP effects at the reference station as well as hardware delays are estimated for each satellite individual by polynomial functions. Additionally, the PWU effect is eliminated following Beyerle (2009). Consequently, the observation equation contains the PCC of the AUT, possible MP effects at the robot station and observation noise.

In Sutyagin and Tatarnikov (2020), detailed analyses of possible errors have also been carried out. This includes far-field MP, near-field MP and errors of antenna positioning by the used robot. It is shown that the dominating remaining error of calibrations is the near-field MP caused by the body of the robot. The error related to far-field MP and geometry inaccuracies due to the installation are 0.1 mm. All in all, the total errors are 1.0 mm for rover-type antenna and 0.5 mm for choke-ring type antenna. This is also reflected in the accuracy of the estimated PCC, which is 0.7 mm and 0.3 mm, respectively.

Another absolute field calibration system has been developed most recently at the faculty of Geodesy at the University of Zagreb (Tupek et al., 2023). Here, a six-axis industrial robot is used to tilt and rotate the AUT. At a baseline length of approximately 5 m, the reference station with a *TRM57971.00 NONE* antenna is located. At both stations, identical receivers are connected to the respective antennas. For time synchronization of the receivers, the 1 Pulse-Per-Second (PPS) signal of the receiver located at the reference station along with the associated *TimeTag* message is used, so that also the clock of the computer used for control, is aligned to the GPS time. This allows a temporally filtering of the carrier-phase observations in post-processing (Tupek et al., 2023). During the calibration process, which has a duration of approximately 2 h, the AUT at each robot orientation is kept fixed for 2.5 s, and 10 Hz GPS raw data is captured. In post-processing, time-differenced DD, i.e. Tripple Differences (TD), are computed in order to estimate PCC. This approach is similar to those presented in Hu and Zhao (2018) and Willi and Guillaume (2019). The PCC of the AUT are parametrized by SH with degree and order equal to 8 and estimated by use of a Least-Squares Adjustment (LSA). Since observations are only present on the upper hemisphere, restrictions on the level of Normal Equation System (NES) are used to overcome the poorly conditioned system. Based on Willi et al. (2018) and Kröger et al. (2021), coefficients with an odd index sum are restricted to zero.

In Tupek et al. (2023), four individual calibration sets for GPS L1 of a *TRM57971.00 NONE* antenna are analyzed in terms of internal repeatability, and differences to an individual calibration carried out at Geo++ (of the identical antenna). The analysis of the repeatability shows a maximal range between the sets of 3.41 mm for the full antenna hemisphere, while

the value is decreased to 2.03 mm if a 10° elevation cut-off angle is applied. The average range reads 0.55 mm for the full antenna hemisphere and 0.42 mm for the reduced one. In addition, the standard deviation, i.e. the precision of the individual calibrations, is presented. This has a maximum of 1.5 mm and an average of 0.24 mm for the full antenna hemisphere when previously transformed to a common mean PCO (Tupek et al., 2023). To validate the estimated PCC, the results are compared with individual calibrations carried out by Geo++. An estimated agreement within 0.58 mm RMS for the entire antenna hemisphere and within 0.39 mm RMS for the elevation-reduced antenna hemisphere was achieved. The absolute maximum deviation without applying an elevation cut-off angle is up to 3.75 mm. The authors state that the large differences observed at low elevation angles are due to the fewer observations available in that region (Tupek et al., 2023).

Most recently, results for GPS L2 have also been published in Tupek et al. (2024). It is shown, that the GPS L2 differences w.r.t. the IGS type-mean calibration depict noticeably higher values than those for L1. This is for example reflected in the characteristic values of the ΔPCC for a *LEIAX1202GG NONE* antenna. The absolute maximum value reads 2.31 mm for L1 and 3.60 mm for L2 ($RMS_{L1}$ = 0.7 mm and $RMS_{L2}$ = 1.05 mm). In order to validate the results, 6 h GPS-only dual-frequency 15 s data is used to calculate a relative position w.r.t. in total three reference stations as part of the European Permanent Network (EPN) network. Details on the processing strategy can be found in Tupek et al. (2024). For analyzing the results, the differences between the two runs, where only the input PCC changed, are computed and transformed into topocentric coordinate differences. The results show differences of -3.5 mm for ΔNorth, 0.3 mm for ΔEast and 3.8 mm for ΔUp. They are explained in particular by the limitation of a type-mean calibration, so that its PCC cannot represent all individual antennas (Tupek et al., 2024).

First GPS L1 PCC estimations from the Astri/UWM calibration facility (University of Warmia and Mazury, Poland in cooperation with Astri Polska) are presented in Dawidowicz et al. (2021). Here, a short baseline (≈ 5 m), common-clock setup with same receiver types, same types and lengths of cables (to minimize hardware delays) is used in order to form dSD, which serves as input for the estimation of PCC. They are parametrized by SH with degree = 8 and order = 5. For the estimation, a two-step approach is used. First, PCO components are estimated and the corresponding residuals serve then as observation input to estimate the PCV in a second step. Dawidowicz et al. (2021) recommends to use 3 individual calibration sets for a stable PCC estimation, so that the total duration is ≈ 5 h. The assessed internal accuracy for two different geodetic antennas shows that ΔPCC remain within 2 mm across the entire antenna hemisphere, although notable differences appear at low zenith angles (0° to 30°), mainly due to variations in the PCO vertical components. At high zenith angles (80° to 90°), differences larger than 2 mm occur, likely due to increased noise affecting signals from low elevation angles. In addition, an external accuracy assessment of the estimated PCC by computing differences to the respective GPS L1 type-mean calibrations provided in the IGS ANTEX-file *igs14.atx* is presented. In these analyses, slightly larger differences up to 4 mm are reported (Dawidowicz et al., 2021).

Willi et al. (2018) report the development and results of the antenna calibration facility at Eidgenössische Technische Hochschule (ETH) Zurich. A six-axis robot (KUKA AGILUS KR 6 R900 sixx) is used to tilt and rotate the AUT. At a baseline length of 5 m, the reference station with same receiver types is set up. During the calibration, the AUT is kept in a fixed point in space with an accuracy of 0.1 mm (Willi and Guillaume, 2019). In total, 1440 different orientations are approached, whereas they are partly randomized to ensure a good coverage over the antenna hemisphere. At each orientation, the robot stands still for one second and the start and end of the robot motions is logged. At both stations, 20 Hz GNSS measurements

are recorded and the times are synchronized by a Network Time Protocol (NTP) time-server (Willi et al., 2018).

In post-processing, the PCC are parameterized by SH expansions with degree = order = 12. Since no observations are present on the upper hemisphere, odd terms of the SH expansion are restricted to zero. For the estimation approach, TD are used. As long as no cycle slips occur, the carrier-phase ambiguities are cancelled out. Potential cycle slips occur as outliers in the triple-difference residuals. Since the AUT is changing its orientation at short intervals, the PWU effect needs to be modeled. At ETH, every observation is only used once, a unity weighting is applied to the zero-difference observations and the variance-covariance matrix of the triple-differences is derived through error propagation. In Willi et al. (2018), GPS L1 PCC results are presented and the repeatability is assessed by computing PCC differences between three sessions, showing that the repeatability for this study is $< 1$ mm (RMS $\approx 0.6$ mm) (Willi et al., 2018).

In Willi et al. (2020), multi-GNSS, multi-frequency PCC for all available GPS and Galileo signals are presented and tested against anechoic chamber calibrations. It is shown that minor differences ($\approx 0.5$ mm RMS) are present, with one antenna showing unexplained discrepancies of $\approx 1.5$ mm RMS. Comparisons with Geo++ calibrations also confirmed sub-millimeter accuracy and compatibility. A field validation campaign, involving four sessions with short baselines and varying antenna positions, showed promising results for the single-frequency case, especially for Galileo, outperforming type-mean calibrations. Both, ETH Zurich and Geo++ calibrations showed similar outcomes for GPS. In addition, a comparison between Galileo-only and GPS-only coordinates obtained with the IF-LC is presented. The type-mean calibrations within the IGS repro3 file including Galileo PCC from Geo++ are the only PCC that significantly reduce the height difference between Galileo and GPS coordinates. Furthermore, lessons-learned and recommendations for the validation of PCC are provided in Willi et al. (2020). As shown in Kersten et al. (2024a,b), the ETH Zurich also participates in the IGS *RingCalVal* project.

At Wuhan University, China, a six-axis robot is operating at the calibration facility in order to estimate absolute receiver PCC (Hu et al., 2022). They use a TD approach where the remaining PWU effects are modeled, and possible cycle slips are detected and removed. For time synchronization, an atomic clock is used. At the robot and reference station, which form a baseline of 2–3 m, 2 Hz GNSS data is recorded. The stochastic model for the respective TD observations is derived from a full variance propagation, where the undifferenced observations are weighted elevation-dependent. For the estimation process, a two-step approach is used. First, the PCO components are estimated by a LSA. Second, the estimated PCO is introduced into the TD equation and PCV values are estimated by SH expansions up to degree and order 8. A tight constraint ensuring that PCV are zero at 0° zenith angle is used to overcome the rank deficit of the NES and an elevation cut-off angle of -5° is used to improve the PCV estimation at low elevation angles (Hu et al., 2022). In addition, Hu et al. (2022) analyze PCC results from GPS and BDS-3 signals for two different antennas. A comparison on the pattern level with PCC from the `igsR3.atx` file shows that the results for one antenna can exceed the 3 mm level at low elevation angles ($< 15°$) for L1 frequencies (GPS and BeiDou signals). Since the estimation precisions over multiple calibration sessions is at the 1 mm level for most of the antenna hemisphere, a good repeatability is reported by Hu et al. (2022). Also, the impact of different receivers on the calibration results is assessed: Differences can reach 0.15 mm, whereby calibrations with receivers of the same type are more consistent. Furthermore, a baseline positioning to validate the estimated PCC is carried out. Findings show that 5–6 mm offsets can occur when missing PCC are replaced by those from close or identical frequencies. All in all, the overall positioning accuracy is within 2 mm for all GPS

and BDS-3 signals (Hu et al., 2022). The calibration facility at the Wuhan University also participates in the IGS *RingCalVal* project (Kersten et al., 2024a,b).

In Bilich et al. (2018), the antenna calibrations carried out at the US National Geodetic Survey (NGS) are presented. Again, a six-axis robot with a maximum payload of 60 kg is used to tilt and rotate the AUT. TD serve as observation input for the PCC estimation, which are parametrized by a SH expansion with degree 8 and order 5, serves TD (Bilich et al., 2018; Bilich, 2021). Preliminary results for GPS L1 PCC for in total three different antennas are presented and compared to the `igs14` type-mean values. These first results showed a systematic vertical offset of $\approx 30$ mm for the vertical PCO component (Bilich et al., 2018). Further results for GPS, GLONASS and Galileo signals are shown and GPS L1/L2 results are compared with Geo++ results in Bilich (2021). Here, only small differences of maximum 3 mm for the North-component of the PCO vector are reported.

#### Impact on Geodetic Parameters

For station providers and users it is of most interest to assess the impact of different PCC models on geodetic parameters, e.g. position, receiver clock and tropospheric estimates. This topic is further addressed in Section 3.3.2.

First investigations are carried out in Geiger (1988). Here, the impact of PCC of different GPS antennas on GPS-based positioning are analytically assessed. In particular, the author analyze the extent to which specific PCC introduce position errors and the effects of the actual satellite constellation on these results.

Schupler and Clark (1991) investigate the effect of different antennas and antenna setups on the antenna response by carrying out measurements in an anechoic chamber. They conclude that similar antenna designs perform in general similarly, that almost any object near an antenna affects its response, and that changing parts of the antenna (e.g. the radome or amplifiers) can significantly change the response. In particular, the performance of several antenna designs critically depends on the coupling between the antenna and its radome.

Schmid et al. (2005) analyze the impact of the transition from relative to absolute PCVs in the IGS network. They show that this transition would cause jumps of 2-10 mm in all three topocentric coordinate components. However, the dependence of the coordinate results on the elevation cut-off angle could be significantly reduced and existing biased tropospheric parameters derived from GPS, w.r.t. Very Long Baseline Interferometry (VLBI) could be reduced. Dawidowicz (2013) studies the height differences caused by using different calibration models in GNSS observation processing within the regional Ground Based Augmentation System (GBAS) network, exemplarily studied based on the Polish GBAS network (ASG-EUPOS). The analysis is carried out using three days of GNSS data, which is collected with four different receivers and antennas. The whole data set is divided in 1 h observation sessions. The results of the calculations show that switching from relative to absolute PCV models may have a significant effect on the height determination in the ASG-EUPOS network. It is shown that jumps in the vertical component for L1 processing of up to 0.7 cm and for the IF-LC combination of up to 2.6 cm are present. In addition, the analyses show that the local satellite constellation has a significant impact, with changes of up to 2.6 cm for IF-LC, depending on the observation period.

Baire et al. (2014) investigate how different GPS receiver antenna calibration models contribute to GPS positioning errors. They compare station positions estimated with different calibration models by carrying out two PPP runs, where only the calibration model differs, and averaging the daily position differences. First, the impact is assessed, when switching

the PCC model provided in *igs05.atx* to *igs08.atx*. Here, the estimated position offsets are compared with the latitude-dependent model presented in Rebischung et al. (2012), which can be used for the position offsets induced by the igs05 to igs08 switch. Baire et al. (2014) show that the RMS of their position differences have an agreement of $\leq$0.3 mm for the horizontal components and 0.7 mm in the Up-components compared to the latitude-dependent model. In a second analysis, the switch from type-mean calibration to individual calibration is analyzed, similar to the studies carried out in Schmid et al. (2005) and Dawidowicz (2013). The resulting position offsets reach up to 1 cm in the Up-component, while the horizontal position offsets are generally smaller than 4 mm. Finally, the comparison of the position offsets obtained with individual calibrations provided by two different calibration facilities (Geo++: robot calibration, University of Bonn: chamber calibration) for six antennas shows an agreement of 2 mm in the horizontal components. However, in the Up-component a bias of 5 mm is detectable. In conclusion, Baire et al. (2014) state that all results demonstrate that the assumption that a type-mean calibration correctly represents the antenna PCC cannot be made for all antenna/radome types, especially if only a few samples have been used to generate the corresponding type-mean values.

Araszkiewicz and Völksen (2016) investigate the impact of PCC models on coordinate time series in the EPN. They estimate station positions with type-mean and then with individual calibration sets and analyze which model is most suitable to reduce seasonal signals. It is shown that neither individual nor type-mean calibrations remove or reduce seasonal signals in the time series. Furthermore, results show that differences between the two calibration models in the position can cause discrepancies of 10 mm for horizontal and vertical components. However, for most antennas, the deviations are below 2 mm for horizontal and 4 mm for vertical components. The authors also note that there is still a lack of comprehensive understanding regarding the interaction between the antenna environment and the used PCC models. Factors such as antenna mounting or ground conditions at the site, which can influence the computed position, are not fully understood.

Dawidowicz and Krzan (2016) also analyze the impact of switching from type-mean to individual calibration models by comparing station positions estimated using GLONASS-only observations when type-mean and individual calibration models are applied. The impact of switching between these models is investigated using one year of observations collected at eight selected ASG-EUPOS station. Post-processing is carried out using the PPP technique in daily observation mode and in pseudo-kinematic mode (15 minutes session). The authors demonstrate that using individual calibrations instead of type mean *igs08.atx* calibrations can result in position offsets of up to 0.5 cm in the Up-component for daily observations, while horizontal offsets generally remain below 0.1 cm. In pseudo-kinematic mode, the authors observe offsets of up to 1.0 cm in the Up-component and 0.5 cm in the horizontal components. It is also demonstrated that the differences in the calibration models propagate directly into the position domain, affecting both daily and sub-daily results and causing visible variations and systematic jumps. To detect the periodicity in the results, spectral analysis is used. The calculation of the Lomb-Scargle spectrum for the data revealed the presence of strong periodic signals in the pseudo-kinematic results, as well as some periodicity in the daily results.

Dawidowicz (2018) investigates the differences between position estimates obtained using individual and type-mean PCC sets. To this end, continuous GPS observations from selected Polish EPN stations were used to determine PPP position time series. The results show that the differences in the calibration models propagate directly into the position domain, affecting both daily and sub-daily results. In daily solutions, the position offsets, resulting from the use of individual calibrations instead of type-mean calibrations, can reach up to 5 mm in the topocentric Up-component. The offsets in the horizontal components stay generally stay below 1 mm. In addition, it is shown that increasing the frequency of sub-daily coordinate solutions

amplifies the effects of differences between type-mean and individual PCC sets. Here, periodic variations in time series of GPS position differences is visible, which is for example linked to the orbital periods.

Bergstrand et al. (2020) assess the performance of absolute antenna calibrations and their impact on precise positioning through a novel assessment method that integrates inter-antenna differentials with laser tracker measurements. This approach allows for the separation of calibration method contributions from those achievable via various geometric constraints, resulting in the development of calibration corrections. The study evaluates antennas calibrated by two IGS-approved institutions and, in the worst-case scenario, finds that the calibration's contribution to the vertical component exceeds 1 cm on the IF-LC. With respect to nearby objects, the method demonstrates $1\sigma$ accuracies in determining antenna phase centers within $\pm 0.38$ mm on L1 and $\pm 0.62$ mm on the IF-LC, the latter being applicable to global frame determinations where atmospheric influences are significant. In addition to offering calibration corrections, this approach can be used with an equivalent tracker combination to determine the phase centers of installed individual receiver antennas at critical system sites to an equivalent precision, without compromising the integrity of permanent installations.

Kersten et al. (2022) present a comparison strategy for antenna calibration values using a set of Leica AR25 antennas from the EPN, which have been individually and absolutely calibrated using both the robot method (by Geo++ company) and the chamber approach (by the University of Bonn). The authors discuss newly developed scalar metrics and highlight their benefits. By use of these metrics, the study successfully categorizes properties of 25 pattern pairs (robot/chamber) into seven individual groups. In order to assess the impact of PCC on geodetic parameters, a regional sub-network of the EPN is analyzed using DD and PPP methods. For DD, differences in estimated parameters between 1 mm and 12 mm are identified based on antenna categories, also affecting Zenith Wet Delay (ZWD). For PPP, the consistency of potential differences in the reference point of carrier-phase and codephase observations further influences the distribution among various parameters and residuals.

Stępniak et al. (2023) investigate the impact of antenna calibration models on the quality of tropospheric estimates. To this end, three different types of PCC sets (IGS14 type mean models, individual `ROBOT` calibrations, `CHAMBER` calibrations) are applied to the GNSS data processing, out of which three years Zenith Total Delay (ZTD) time series are obtained. In addition, the effect of different GNSS constellations are analyzed. The results indicate that the GNSS constellation has a more significant effect on the accuracy of the ZTD time series than the antenna calibration models. However, their influence is still important and should not be neglected. Moreover, validation against climate reanalysis data confirms that all approaches yield high-quality tropospheric delays. However, it is shown that the ZTD estimates derived using robotic and IGS14 calibrations align more closely with ERA5[1] reanalysis data compared to estimates obtained from anechoic chamber calibrations.

Dawidowicz and Bakuła (2024) investigate PPP position estimates using either individual or type-mean PCC models for selected EPN stations. They analyze eight different GNSS combinations, including GPS, Galileo, GLONASS, and BeiDou. Their study compares the *igs14_2035.atx* type-mean model to the individual PCC models provided in the EPN file `epn_14.atx`. The analyses reveal differences of up to 10 mm for L2 frequencies and 20 mm for IF-LC, with the largest deviations occurring between type-mean and individual calibrations derived using the `CHAMBER` method. Additionally, the study shows that adapting GPS PCC to other GNSS signals does not significantly increase position differences. To detect periodicity

[1]ERA5: fifth generation of climate reanalysis data produced by the European Centre for Medium-Range Weather Forecasts (Copernicus Climate Change Service, 2023).

in the time series, the authors calculate the Lomb-Scargle spectrum, demonstrating that variations can be linked to orbital periods or related to the number of orbital planes.

In Kersten et al. (2024b), first results from the IGS *RingCalVal* project are presented. Here, also the impact of individual GPS L1 PCC, estimated by the participating calibration facilities, versus IGS type-mean calibrations in the parameter domain is presented. The findings indicate that the influence on topocentric coordinate differences are up to -5 mm for the Up-component, with variations of nearly 7 mm between different solutions for this component. However, differences in the horizontal components between calibration facilities are mostly below 1 mm.

### Closing Remarks

In general, several approaches exist for estimating PCC using method ROBOT. Table 2.6 summarizes these approaches with the observations used, the additional models required, the parameterization used to estimate the PCC, and the noise amplification factor $f_\sigma$ w.r.t. undifferenced observations. It should be noted that the noise factor assumes that the undifferenced observations are uncorrelated and have the same standard deviation, see also Section 2.1.4.

In addition, the estimation and provision of GDV/CPC has a high scientific relevance. CPC are needed for instance for ambiguity resolution with PPP, especially when the magnitude of the respective antenna CPC is in the range of the Melbourne-Wübbena Linear Combination (LC) wavelength (Kersten and Schön, 2017). The estimation and investigation of various scientific questions is for example reported and described in Wübbena et al. (2008); Kersten (2014); Kersten and Schön (2017); Wanninger et al. (2017); Caizzone et al. (2018); Breva et al. (2019); Wübbena et al. (2019); Breva et al. (2024c); Kröger et al. (2024); Breva (2025). This underlines the importance of including GDV/CPC into the ANTEX file, as proposed in Montenbruck et al. (2024).

Moreover, this section highlights the existence of numerous contributions that address and investigate the impact of various PCC sets, underscoring their significant scientific relevance. However, a standardized or homogeneous comparison strategy has yet to be established. Therefore, Chapter 3 offers a detailed overview of the different existing strategies for comparing PCC differences. Additionally, it introduces newly developed comparison strategies.

**Table 2.6:** Summary of different calibration facilities using method ROBOT. The used observations and required models to estimate PCC, the applied PCC parametrization along with the maximum degree and order as well as the noise factor $f_\sigma$ are listed. Note that due to the commercial nature of the calibration facilities used by Wübbena et al. (2019), only limited information is available.

| **Calibration Facility** | **Obs.** | **Required models** | **Param.** | $\mathbf{f_\sigma}$ |
|---|---|---|---|---|
| Wübbena et al. (2019) | SD | not officially reported | SH(8,5) | $\sqrt{2}$ |
| Sutyagin and Tatarnikov (2020) | SD | PWU, hardware delays ambiguities Ref. station: MP, PCC | SH(8,5) | $\sqrt{2}$ |
| Dawidowicz et al. (2021) | dSD | PWU | SH(8,5) | 2 |
| Kröger et al. (2021) | dSD | PWU | SH(8,8) | 2 |
| **Kröger et al. (2024)** | dSD | PWU | HSH(8,8) | 2 |
| Hu and Zhao (2018) | TD | PWU | SH(8,8) | $2 \cdot \sqrt{2}$ |
| Willi and Guillaume (2019) | TD | PWU | SH(12,12) | $2 \cdot \sqrt{2}$ |
| Bilich (2021) | TD | PWU | SH(8,5) | $2 \cdot \sqrt{2}$ |
| Tupek et al. (2023) | TD | PWU | SH(8,8) | $2 \cdot \sqrt{2}$ |

# 3

# Strategies for Comparing Phase Center Corrections

This chapter gives an overview over various methods developed in this thesis for comparing different sets of PCC. The presented methods can be used for comparing different PCC sets between individual and type-mean calibrations, between identical antennas calibrated at different institutions or to investigate the role of the receiver used during the estimation of PCC.

First, the general approach for computing PCC differences, i.e. ΔPCC, is provided and two examples of ΔPCC pattern are introduced. With these examples, the differences at the pattern level, using graphical measures as well as numerical measures, are assessed. The section closes with the introduction of different methods to analyze ΔPCC in the observation and parameter domain.

## 3.1 Computing Differences

When different sets of PCC ($\mathrm{PCC}_i, \mathrm{PCC}_j$) should be compared, the differences ΔPCC at the pattern level can be computed between PCC sets

$$\Delta\mathrm{PCC} \coloneqq \mathrm{PCC}_i - \mathrm{PCC}_j. \tag{3.1}$$

It is important to consider the full sets of PCC, since analyzing PCO and PCV separately is not valid (Schön and Kersten, 2014). The ΔPCC might contain differences in the PCO, PCV variations and differences due to different datum definitions, i.e. a constant part $\Delta r$, see Equation 2.27 (Kersten et al., 2022).

If only small PCC differences should be studied, the different patterns can be transformed to a common PCO, as proposed by Menge et al. (1998)

$$\begin{aligned} \mathrm{PCV}_{1,2}(\alpha, z) &= (\mathrm{PCO}_2 - \mathrm{PCO}_1) \cdot \vec{\boldsymbol{e}}(\alpha, z) + \mathrm{PCV}_1(\alpha, z) + \Delta r \\ \overline{\mathrm{PCV}}(\alpha, z) &= \mathrm{PCV}_{1,2} - \mathit{PCV}_2. \end{aligned} \tag{3.2}$$

This procedure is for example beneficial when PCC contain a large $\mathrm{PCO}_{\mathrm{Up}}$ component. In such cases, detecting small differences can be challenging, so it is useful to transform different patterns to a common PCO. An alternative method to handle large $\mathrm{PCO}_{\mathrm{Up}}$ components is to subtract a common $\mathrm{PCO}_{\mathrm{Up}}$ component $\overline{d}$ from either both PCC sets or from ΔPCC resulting in PCC*

$$\mathrm{PCC}_i{}^* = \mathrm{PCC}_i - (\cos z \cdot \overline{d}). \tag{3.3}$$

This approach provides deeper insights into the variations of PCC or ΔPCC.

If linear combinations are calculated, it should be noted that ΔPCC are in general amplified. This is especially the case for the IF-LC (see Equation 2.10) (Dilssner et al., 2008; Schmid, 2013). In the case of GPS L1, L2 IF-LC, the $\Delta\text{PCC}_{IF}$ and Geometry-Free Linear Combination (GF-LC) read

$$\begin{aligned} \Delta\text{PCC}_{IF} &\approx 2.546 \cdot \Delta\text{PCC}_{L1} - 1.546 \cdot \Delta\text{PCC}_{L2} \\ \Delta\text{PCC}_{GF} &= \Delta\text{PCC}_{L1} - \Delta\text{PCC}_{L2} \end{aligned} \tag{3.4}$$

Certainly, the IF-LC can be calculated using other frequencies by applying Equation 2.10 or using the coefficients listed in Table 2.3.

Since the constant part $r$ can usually not be estimated, any addition and subtraction of a constant value to a pattern is a valid transformation (Kersten et al., 2022). Widely used is the zero zenith constraint by applying Equation 3.5

$$\text{PCV}(z = 0^\circ) \stackrel{!}{=} 0. \tag{3.5}$$

This is equivalent to subtracting the PCV value at $z$= 0° from all other PCV values. This change does not affect the position solution, but it does affect other geodetic parameters such as the receiver clock error or the ambiguities (Kersten et al., 2022).

In order to highlight the properties of the different proposed strategies for comparing different PCC sets, ΔPCC of two different scenarios are used in the following:

1. $\Delta\text{PCC}_{\texttt{sim}}$: Simulated ΔPCC with a $\Delta\text{PCO} = [-0.02,\ -0.5,\ -3.5]^{\text{T}}$ [mm], a differential constant part $\Delta r$ of 4 mm and uniformly distributed ΔPCV variations in the interval $[-0.01,\ 0.03]$ [mm].
2. $\Delta\text{PCC}_{\texttt{real}}$: Real differences between the calibration methods `ROBOT` and `CHAMBER` of a *LEIAR25.R4 LEIT* (#726209) antenna as part of the EPN (EPN, 2019).

## 3.2 Analyses at Pattern Level

### 3.2.1 Graphical Measures

In a first step, ΔPCC can be analyzed with different graphical measures. They can be displayed as a grid, similar to the format provided in the ANTEX file. Alternatively, ΔPCC can be represented using a stereographic projection, which allows for a more intuitive understanding of the differences on the antenna hemisphere by using azimuth and elevation angles. If the focus is only on mean ΔPCC values per elevation angle, these can be illustrated accordingly, making it easier to compare different PCC sets in a single plot. The same approach is applicable if absolute ΔPCC values are depicted in a cumulative histogram.

Figure 3.1(a) shows the $\Delta\text{PCC}_{\texttt{sim}}$ in a gridded plot over the whole azimuth (0° – 360°) and elevation (0° – 90°) range. In this representation, the differences are visualized as they are tabulated within the ANTEX file, taking PCO and PCV values into account (see Equation 2.27). Since no further transformations are applied, the highest differences are present at 90° elevation angle ($-\text{PCO}_{\text{Up}}$ + r = 7.5 mm, along with minor PCV values). Also, a clear elevation-dependent behavior of the differences ranging from ≈3 mm at low elevation angles to ≈7.5 mm at high elevation angles is visible. The same information is in general given in Figure 3.1(b). Here, $\Delta\text{PCC}_{\texttt{sim}}$ are visualized in a stereographic projection, where the eleva-

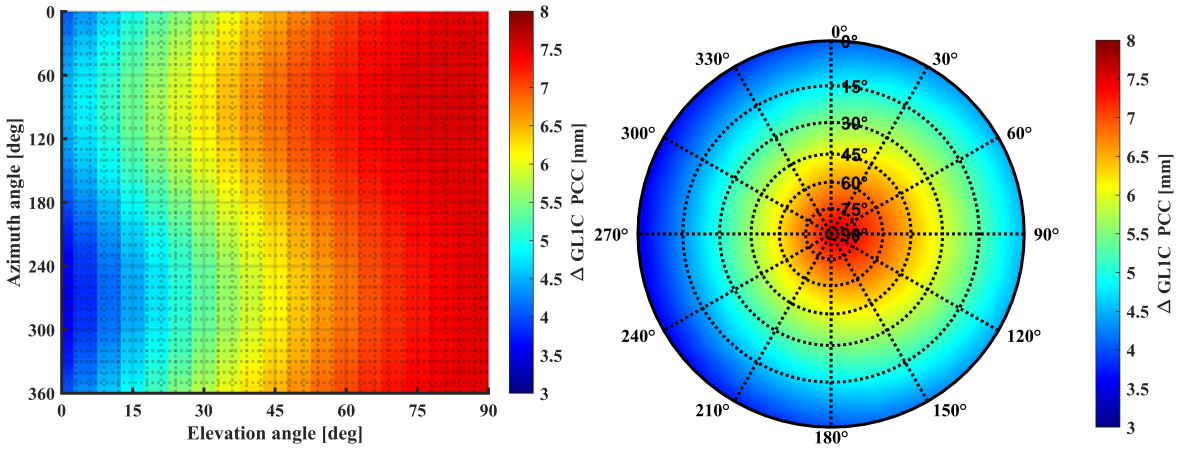


(a) Representation as grid (b) Stereographic representation

**Figure 3.1:** Different representations of $\Delta\mathrm{PCC}_{\mathrm{sim}}$.

tion angles count from 0° at the boarder of the figure to 90° elevation angle at the center. Azimuth angles count from the top of the figure (0°) clockwise to 360°. It can be seen that the difference pattern has a slight east-west slant (90° resp. 270° azimuth angle), which can be explained by the horizontal PCO differences of 0.02 mm for the North- and 0.5 mm for the East-component.

Figure 3.2 illustrates the effects of a distorted pattern by presenting $\Delta\mathrm{PCC}_{\mathrm{sim}}$ stepwise using stereographic projections. Each figure utilizes a different color scale, making the characteristic pattern behavior apparent when an error occurs in one of the PCO components. Specifically, a $\Delta\mathrm{PCO}_{\mathrm{North}}$ results in a north-south slope, while a difference in the east component causes an east-west slope. An offset in $\mathrm{PCO}_{\mathrm{Up}}$ produces an elevation-dependent pattern, reaching its full magnitude at 90° elevation angle. Since $\mathrm{PCO}_{\mathrm{Up}}$ is added with a negative sign to the PCV values, as seen in Equation 2.27, the maximum value reads 3.5 mm. The resulting $\Delta\mathrm{PCC}_{\mathrm{sim}}$, as depicted in Figure 3.1(b), is a summation of the three illustrated components along with the constant component $r = 4$ mm and the ΔPCV variations.

Figure 3.3 visualizes the $\Delta\mathrm{PCC}_{\mathrm{real}}$ for GPS L1 and L2. For L1, the differences range from ≈ -3 mm at low elevation angles to ≈ 3.5 mm at high elevation angles. However, the highest differences occur at ≈ 15° elevation angle and 90° – 270° azimuth angles. For GPS L2, the differences are in a range of -1 mm to -5 mm. Most of ΔPCC fall within -1 mm to -2 mm. Larger deviations occur at elevation angles between 15° and 20° in the northern part of the

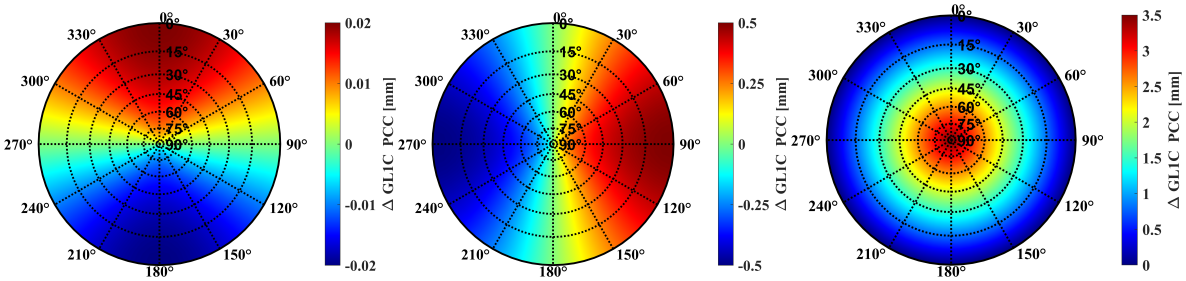


(a) Effect of $\Delta\mathrm{PCO}_{\mathrm{North}}$ (b) Effect of $\Delta\mathrm{PCO}_{\mathrm{East}}$ (c) Effect of $\Delta\mathrm{PCO}_{\mathrm{Up}}$

**Figure 3.2:** Representation of $\Delta\mathrm{PCC}_{\mathrm{sim}}$ broken down into its individual components. Note the different colorbar scales.

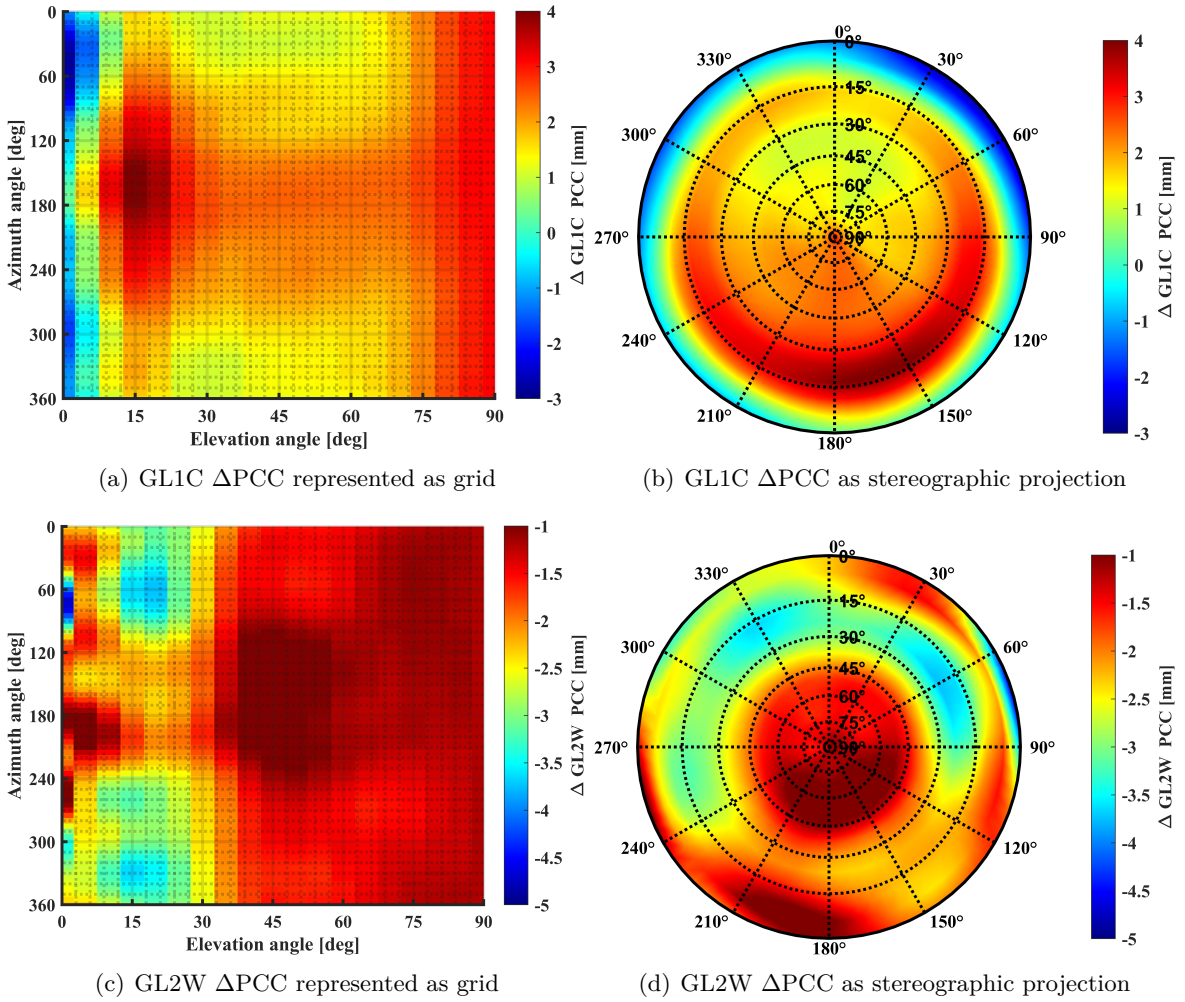


(a) GL1C ΔPCC represented as grid

(b) GL1C ΔPCC as stereographic projection

(c) GL2W ΔPCC represented as grid

(d) GL2W ΔPCC as stereographic projection

**Figure 3.3:** Different representations of $\Delta\mathrm{PCC}_{\mathrm{real}}$ for GPS L1 and L2. Note the different scales for the different frequencies.

antenna hemisphere. The maximum deviation of -5 mm is localized at a 0° elevation and an azimuth angle between 70° and 80°.

If only elevation-dependent differences are of interest, the mean value over all azimuth angles per elevation bin can be calculated and visualized. Figure 3.4(a) shows the mean $\Delta\mathrm{PCC}_{\mathrm{sim}}$ and mean $\Delta\mathrm{PCC}_{\mathrm{real}}$ per elevation angle (solid lines) among with the respective minimum and maximum deviations (dashed lines) and the standard deviations $\sigma$ per elevation bin (shaded areas). Again, the clear elevation-dependent behavior of $\Delta\mathrm{PCC}_{\mathrm{sim}}$ can be seen. At 90° elevation angle, the value reads 7.5 mm, which corresponds to -PCO+$r$ (-(-3.5 mm)+4 mm). At 0° elevation angle, the mean value over all azimuth angles is 4 mm, which reflects $r$. In between, the values follow the $(\sin(el)\cdot \mathrm{PCO}_{\mathrm{Up}}) + r$ function.

In the case of $\Delta\mathrm{PCC}_{\mathrm{real}}$, the mean differences per elevation angle have their maximum at $\approx$ 15° elevation angle and a mostly constant behavior between 30° – 70° elevation angles. It is worth noting that this tool for a graphical measure for comparing ΔPCC might be misleading, e.g. in the case of tilted $\Delta\mathrm{PCC}_{\mathrm{real}}$. In this case, the mean value over the azimuthal range for each elevation bin indicates small differences for the elevation-dependent range, although the PCC differ over the azimuth range.

Figure 3.4(b) depicts the absolute $\Delta\mathrm{PCC}_{\mathrm{real}}$ values in a cumulative histogram for GPS L1 and L2 frequencies, as well as for the IF-LC and GF-LC. The 95% percentile of the absolute

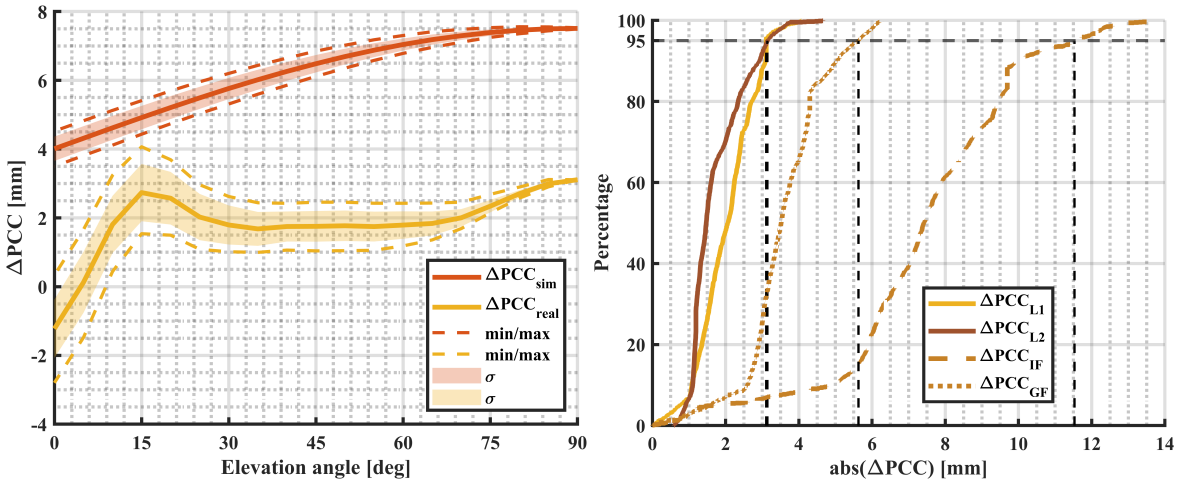


(a) Averaged ΔPCC per elevation angle bin. For $\Delta\mathrm{PCC}_{\mathrm{real}}$, GL1C ΔPCC are illustrated.

(b) Cumulative histogram of $\Delta\mathrm{PCC}_{\mathrm{real}}$ for GPS L1, L2 frequencies and their corresponding IF-LC and GF-LC.

**Figure 3.4:** Different graphical representations of $\Delta\mathrm{PCC}_{\mathrm{sim}}$ and $\Delta\mathrm{PCC}_{\mathrm{real}}$ for comparing different sets of PCC.

differences is 3.11 mm for L1 (solid orange line) and 3.14 mm for L2 (solid brown line). For the IF-LC (dashed brownish-orange line), the 95% percentile reads 11.53 mm, and for the GF-LC (dotted brownish-orange line), it is 5.63 mm. This underlines the fact that the differences increase when linear combinations are computed and used. This type of graphical measure is especially useful for comparing different sets of ΔPCC while taking also azimuthal variations into account. However, the drawback is that a spatial link to the azimuth or elevation angle is no longer possible.

### 3.2.2 Numerical Measures

If one measure should describe the similarity of two PCC sets, various characteristic values can be computed for ΔPCC. In this case, however, the spatial structure is lost. Since image similarity measures can consider spatial structures, their potential for describing ΔPCC is shortly discussed in this section, too. This part is based on Kröger et al. (2022c) and further elaborated in Kersten et al. (2022), where characteristic values are applied to a larger dataset, with detailed analysis of the results.

#### Characteristic Values

In order to assess the similarity of different PCC sets, various scalar measures, i.e. characteristic values, can be computed from ΔPCC or the individual sets $\mathrm{PCC}_1$ and $\mathrm{PCC}_2$. Table 3.1 lists the different measures, the inputs for computing them and their dependency on a constant part $r$. Additionally, the characteristic values for $\Delta\mathrm{PCC}_{\mathrm{real}}$ for GPS L1 are given for two cases:

1. Untransformed differences following Equation 3.1: $\Delta\mathrm{PCC}(z = 0) \neq 0$.
2. Transformed ΔPCC following Equation 3.5 so that the differences are zero at zenith: $\Delta\mathrm{PCC}(z = 0) = 0$.

It can be clearly seen that the measures *Maximum*, *RMS* and *95% percentile* are dependent on the applied transformation and thus on the constant part $r$. On the other hand, the measures

**Table 3.1:** Characteristic values for comparing different sets of PCC and their dependency on the constant part $r$. Values are given for $\Delta\mathtt{PCC}_{\mathtt{real}}$.

| **Characteristic Value** | **Input** | $\Delta$**PCC**$(z=0)\neq 0$ | $\Delta$**PCC**$(z=0)=0$ |
|---|---|---|---|
| Maximum [mm] | $\Delta$PCC | 4.07 | 5.91 |
| RMS [mm] | $\Delta$PCC | 2.16 | 1.67 |
| 95% percentile [mm] | abs($\Delta$PCC) | 3.11 | 3.81 |
| Standard deviation [mm] | $\Delta$PCC | 1.11 | |
| Range [mm] | $\Delta$PCC | 6.86 | |
| Spread [mm] | $\mathrm{PCC}_1, \mathrm{PCC}_2$ | -2.88 | |
| Correlation Coefficient | $\mathrm{PCC}_1, \mathrm{PCC}_2$ | 1.00 | |

*Standard Deviation*, *Range*, *Spread* and *Correlation Coefficient* $c_{corr}$ are independent of $r$. Equation 3.6 gives the formulas for the lesser-known characteristic values, with $\overline{\mathrm{PCC}_i}$ denoting the mean value, $\sigma_i$ the standard deviation and $n$ the total number of PCC values

$$\begin{aligned} \mathit{Range} &= \max(\Delta\mathrm{PCC}) - \min(\Delta\mathrm{PCC}) \\ \mathit{Spread} &= (\max(\mathrm{PCC}_1) - \min(\mathrm{PCC}_1)) - (\max(\mathrm{PCC}_2) - \min(\mathrm{PCC}_2)) \\ c_{corr} &= \frac{1}{n}\sum_{i=1}^{n}\left(\frac{(\mathrm{PCC}_A - \overline{\mathrm{PCC}}_A)}{\sigma_{\mathrm{PCC}_A}}\right)\cdot\left(\frac{(\mathrm{PCC}_B - \overline{\mathrm{PCC}}_B)}{\sigma_{\mathrm{PCC}_B}}\right). \end{aligned} \tag{3.6}$$

Since the mean value or the span of the PCC or $\Delta$PCC is taken into account, all characteristic values given in Equation 3.6 are independent of a constant part $r$.

Comparing the characteristic values which are dependent on a constant part $r$, it can be seen that the untransformed $\Delta$PCC have a lower maximum value and higher RMS. Also, the 95% percentile value is lower (3.11 mm compared to 3.81 mm).

Also, it is worth noting that the correlation coefficient $c_{corr}$ gives a rounded value of 1.00 indicating that a perfect positive correlation between the two input patterns is given. As discussed in Kröger et al. (2022c), the $\mathrm{PCO}_{\mathrm{Up}}$ is usually the most dominating part in PCC. Thus, the different sets of PCC need to be transformed by use of Equation 3.2 to a common PCO before calculating the characteristic values.

Table 3.2 presents the characteristic values of $\Delta\mathtt{PCC}_{\mathtt{real}}$ for GPS L1, L2 frequencies and the respective IF-LC and GF-LC. To properly characterize also small differences, the patterns are transformed beforehand to a common PCO using Equation 3.2, resulting in $\Delta\overline{\mathtt{PCV}}$.

These values mainly reflect the behavior of the differences as it could already be seen in Figure 3.4(b), i.e. GPS L1 and L2 are in a comparable order of magnitude while the differences for the linear combinations are amplified. This is reflected in all characteristic values except the correlation coefficient. It indicates a lower similarity (0.84) of the PCC L1 differences than for the other analyzed frequencies (0.93 – 0.98). Also, it should be noted that the value for the *Spread* changes if a transformation following Equation 3.2 is carried out. While the *Spread* for GPS L1 differences is -2.88 mm in the untransformed case (see Table 3.1, column 3), it gives a value of 0.37 mm for the transformed ones.

The above introduced characteristic values can be used to assess the similarity of various $\Delta$PCC sets, e.g. in regional networks of GNSS stations, to classify these differences. This is further discussed in Section 7.2.1.

**Table 3.2:** Characteristic values of $\Delta\overline{\mathtt{PCV}}_{\mathtt{real}}$ ($(z = 0) \neq 0$) for GPS L1, L2 frequencies and linear combinations.

| **Characteristic Value** | $\Delta\overline{\mathbf{PCV}}_{\mathbf{L1}}$ | $\Delta\overline{\mathbf{PCV}}_{\mathbf{L2}}$ | $\Delta\overline{\mathbf{PCV}}_{\mathbf{IF}}$ | $\Delta\overline{\mathbf{PCV}}_{\mathbf{GF}}$ |
|---|---|---|---|---|
| Maximum [mm] | 4.07 | 4.66 | 13.68 | 6.28 |
| RMS [mm] | 2.16 | 1.87 | 7.81 | 3.75 |
| 95% percentile [mm] | 3.11 | 3.14 | 11.53 | 5.63 |
| Standard deviation [mm] | 1.11 | 0.72 | 2.68 | 1.12 |
| Range [mm] | 6.86 | 4.07 | 17.75 | 7.24 |
| Spread [mm] | 0.37 | -0.35 | 8.36 | 2.49 |
| Correlation Coefficient [-] | 0.84 | 0.98 | 0.93 | 0.96 |

### Image Similarity Measures

Usually, estimated PCC are mapped on a regular grid with a typical step size of 5° for zenith and azimuth angles, as they are depicted in Figure 3.1(a) and 3.3(a). Thus, the differences can be interpreted as a two-dimensional image, whereas the pixel $x_{ij}$ corresponds to the actual zenith $z$ and azimuth $\alpha$-dependent PCC value

$$x_{ij} = \mathrm{PCC}(\alpha_i, z_j). \tag{3.7}$$

In Kröger et al. (2022c), the potential of global image similarity measures as well as feature detection algorithms for comparing PCC sets are presented. As an example for the measure mentioned first, the Structural SIMilarity (SSIM) index is used to compare different PCC sets w.r.t. a reference image, which is in this case a reference set of PCC values. The reader is referred to Wang et al. (2004) for details on the SSIM index and to Kröger et al. (2022c) for details on its application for comparing PCC sets. All in all, the analyses show that the SSIM index is a powerful measure for comparing ΔPCC. Even though, the authors suggest to use the Pearson correlation coefficient instead, since it gives basically the same conclusions using fewer parameters to be set and adjusted.

Also, in Kröger et al. (2022c) the potential of feature detection algorithms for comparing ΔPCC is investigated. As one example, the Speeded-Up Robust Features (SURF) algorithm proposed by Bay et al. (2008) is used to find so-called blobs, i.e. regions with higher ΔPCC. The analysis shows that the blob features are mainly not detected. This is because, on the one hand, the PCC are quite smooth due to the estimation by SH and, on the other hand, fine structures get lost since the PCC values are gridded with a resolution of 5°.

### Analysis of PCO Differences

A first insight into PCC differences can also be reached by analyzing PCO differences. Although PCO, PCV and $r$ should always be treated together, it can give users a helpful insight into the magnitude of the differences, since PCO components are usually the largest components within PCC. The analysis of PCO differences is especially useful if all PCC components, i.e. PCO, PCV and $r$, are strictly separated from each other, e.g. by use of Equation 4.16. In this case, the user can get a first impression to what extent the differences impact topocentric coordinate differences as well as the receiver clock error ΔClock:

$$\begin{aligned} \Delta\mathrm{North} &= \mathrm{PCO}_{\mathrm{North}} \\ \Delta\mathrm{East} &= \mathrm{PCO}_{\mathrm{East}} \\ \Delta\mathrm{Up} &= \mathrm{PCO}_{\mathrm{Up}} \\ \Delta\mathrm{Clock} &= r. \end{aligned}$$

However, for a comprehensive study, all possible processing parameters for GNSS-based positioning, e.g. local satellite distribution and elevation cut-off angle, need to be considered. To this end, a simulative approach has been developed, which is introduced in Section 3.3.2.

#### Analysis of Spherical Harmonic Coefficients and their Differences

Usually, PCC are parametrized by SH and the corresponding SH coefficients are estimated. If the identical approach with same processing parameters were chosen for two different estimations, e.g. application of same normalization factors for Legendre polynomials and same degree and order for SH expansion, the coefficient differences $\Delta$coeff could be analyzed. In principle, this can have two main advantages:

1. Potential uncertainties due to SH synthesis can be revealed, and
2. Easy comparison of different grid sizes or direct inserting of azimuth and elevation angles from visible satellites is possible.

The second point is quite important, since PCC information gets lost if the coefficients are brought by a SH synthesis to the grid. This issue is further discussed in Section 6.5. However, since the SH coefficients are usually not distributed by calibration facilities or publicly available, the analysis of $\Delta$coeff can mostly only be used for internal validation.

However, one possibility would be to exchange the coefficients between the calibration facilities in future (as it is for example done in the gravity field community). If, among others, the normalization factors and exact spherical functions used are reported, only 80 values would have to be exchanged for a SH expansion up to degree and order 8. Usually, with a grid resolution of 5°, $73 \cdot 19 = 1387$ values are required for representing PCV and additional three values for the PCO. The disadvantage, however, is that a straight-forward interpretation and application of PCC information represented by SH-coefficients is not easily possible by users.

## 3.3 Analysis in Observation and Parameter Domain

Currently, there is no strict way how estimated PCC should be analyzed using real GNSS observation data. In principle, two methods exist:

1. Validation in the observation domain, and
2. Validation in the parameter domain.

Both validation strategies have their advantages and challenges, which are elaborated in this section. Generally, the overall challenge is that the pattern information, or especially the pattern differences, are rather small compared to the overall noise in GNSS processing.

### 3.3.1 Observation Domain

As stated in Kallio et al. (2018), the independent validation of PCC values is complicated. If the observation data of a single station is used, e.g. in PPP processing, other dominating error sources are present. Thus, a relative positioning using short baselines should be used. Here, however, PCC of a second antenna from the reference station are introduced so that only the $\Delta$PCC between these two antennas can be assessed. Consequently, different types of antennas should be used so that the patterns are not eliminated by (single- or double-) differencing, see

Section 2.1.4. Hence, the computation of receiver-to-receiver SD for analyzing PCC differences is an appropriate approach. The general proceeding consists of the following steps:

1. Calculation of OMC values for each station separately. Here, the following factors should be considered:
   - PCC for the antenna mounted on the reference station should be adequately taken into account
   - No PCC should be applied to the rover station, where the AUT is mounted
   - To avoid large drifts in observations, an arbitrary height offset $d$ should be applied to the observations of all frequencies on the rover station. It would make sense to use a mean $\mathrm{PCO}_{\mathrm{Up}}$ from all or chosen frequencies. As an alternative, the approximate size of the AUT can be used.
2. Computing receiver-to-receiver SD time series, which only contains $\Delta$PCC between the two antennas, phase ambiguities, a constant initial differential receiver clock error and unmodeled effects/noise.
3. Subtracting an individual integer SD ambiguity $N_k$ from each satellite arc $k$ with taking the respective wavelength $\lambda$ of the signal into account

$$N_k = \mathrm{round}\big(\mathrm{median}(\mathrm{SD}_k)/\lambda\big) \cdot \lambda. \tag{3.8}$$

4. Removing a constant part, which is the median of all SD, from all SD to take the constant differential receiver clock error between the stations into account.

As shown in Kröger et al. (2021), this setup allows analyzing the improvement in terms of standard deviations of SD arcs, when distinct PCC are applied to the observations of the AUT. However, it should be noted that multipath effects remain, which complicates the pure validation of PCC in the observation domain.

Figure 3.5 shows an example from Kröger et al. (2021) for validating PCC in the observation domain. In the example, $\Delta$PCC between a *NOV703GGG.R2 NONE* pinwheel antenna and a geodetic *LEIAR25.R3 LEIT* are analyzed to ensure that the PCC are not largely reduced when computing SD. Since strong multipath effects are present at the stations, an elevation cut-off angle of 15° is applied. In the study, PCC estimated at IfE (method `ROBOT`) are compared with those from University of Bonn (method `CHAMBER`) and values provided by the IGS in the official ANTEX file.

In principle, it can be seen that all curves fit the SD well. Larger deviations to the pattern from University of Bonn can explained by taking PCC from a slightly different antenna (*LEIAX1202GG NONE*), since values for *NOV703GGG.R2 NONE* were not publicly available from the EPN. In general, the GL1C SD are improved in terms of standard deviation on average by 11% (maximum 37%), if PCC estimated by IfE are applied. Additional details and examples for different frequencies can be found in Kröger et al. (2021). In addition, further results from the analysis of PCC in the observation domain are provided in Section 7.1.

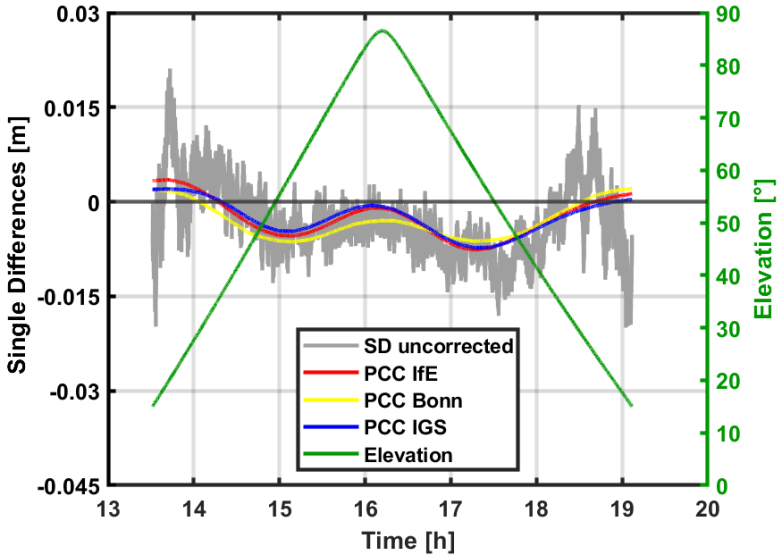


**Figure 3.5:** Uncorrected GL1C SD (PRN12) with color-coded ΔPCC between *NOV703GGG.R2 NONE* and *LEIAR25.R3 LEIT* antenna from different calibration facilities, taken from Kröger et al. (2021).

### 3.3.2 Parameter Domain

The influence of PCC, and especially ΔPCC, on the parameter domain is of main interest for GNSS users and station providers. Consequently, the impact on geodetic parameters, particularly position estimates, should be assessed. Since these estimates are highly correlated with further parameters, e.g. receiver clock errors, tropospheric estimates and phase ambiguities, all parameters need to be analyzed (Kersten et al., 2022). Usually, a relative position algorithm is preferable, so that the majority of the GNSS error budget cancels out. However, in these cases, the PCC of a second antenna are introduced. Moreover, in the case of receiver-to-receiver SD or DD, only the ΔPCC between the two antennas at the different stations remain in the observations. If two antennas with large PCC differences are not selected, the remaining ΔPCC might be lower than the expected noise level. Additionally, the validation process may be affected by other error sources that do not cancel out, such as station-dependent MP effects.

Therefore, it is advisable to carry out two runs of a position algorithm (e.g. PPP or relative positioning), keeping all parameter settings unchanged and exchanging only the input PCC. By computing the differences between the two runs, the impact on all estimated parameters can be assessed. However, a lot of application-specific parameters need to be set so that the resulting influence is only valid for this specific setup. Consequently, a simulative approach has been developed, which aims to standardize application-specific settings. This approach is described in detail in the following section.

#### Simulative Approach

If the impact of ΔPCC should be assessed in the parameter domain, several processing parameters have to be considered. Besides the geographic location and processing time, the chosen processing parameters play a crucial role. This includes, among others, the selected frequencies/systems or linear combinations (see Section 2.1.3), elevation cut-off angle, sampling interval and observation weighting scheme. In order to investigate the impact of ΔPCC in the parameter domain, i.e. topocentric coordinate differences (ΔNorth, ΔEast, ΔUp),

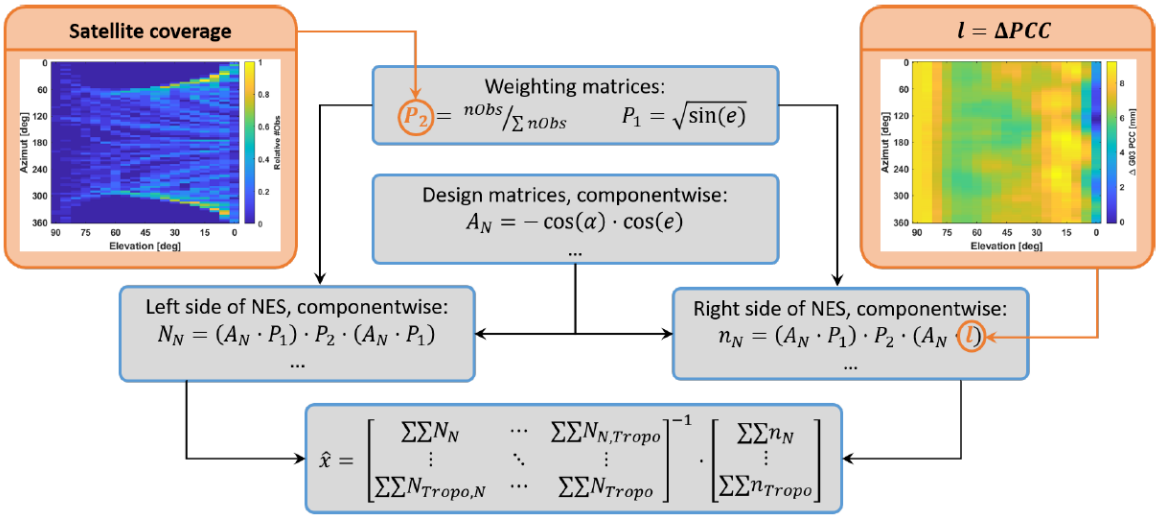


**Figure 3.6:** Flowchart illustrating the main components and steps of the developed simulation approach.

receiver clock error ΔClk and a tropospheric parameter ΔTropo, a standardized simulation approach has been developed (Brekenkamp et al., 2022; Kröger et al., 2022a,b). The general sequence of the approach is depicted in Figure 3.6.

The ΔPCC of the selected frequency, frequencies or linear combinations and the geographic position along with a specific time span, which is crucial for the local satellite distribution weighting scheme, serve as main input. As a result of a LSA, the influence of ΔPCC on the geodetic parameters is obtained – averaged over a specific interval of time $\delta t_\Sigma$.

First, the design matrices $\mathbf{A}$ are set up in a topocentric frame for the North- ($\mathbf{A}_N$), East- ($\mathbf{A}_E$), Up-Component ($\mathbf{A}_U$) as well as for the receiver clock error ($\mathbf{A}_C$) and a tropospheric parameter ($\mathbf{A}_T$)

$$\begin{aligned} \mathbf{A}_N &= \cos(\alpha^k) \cdot \cos(el^k) \\ \mathbf{A}_E &= \sin(\alpha^k) \cdot \cos(el^k) \\ \mathbf{A}_U &= \sin(el^k) \\ \mathbf{A}_C &= 1 \\ \mathbf{A}_T &= \frac{1}{\sin(el^k)}. \end{aligned} \tag{3.9}$$

They are set up with the respective elevation $el^k$ and azimuth $\alpha^k$ angles of the gridded input ΔPCC and are usually filled for the intervals $0° \leq el \leq 90°$ and $0 \leq \alpha \leq 360°$. If the step size of the differential input pattern is 5°, the resulting dimension is $[73 \times 19]$.

The stochastic model for an elevation-dependent weighting scheme reads

$$\begin{aligned} \mathbf{\Sigma_{ll}} &= \sigma_0^2 \cdot diag\left(\frac{1}{\sin^2(el^k)}\right) \\ \mathbf{P_1} &= \mathbf{\Sigma}_{ll}^{-1}, \end{aligned} \tag{3.10}$$

with $\mathbf{\Sigma}_{ll}$ denoting the covariance matrix of the observations $\mathbf{l}$, i.e. ΔPCC, $\sigma_0^2$ is the a priori variance factor and $\mathbf{P_1}$ is the weighting matrix. If unit weighting is chosen for processing, $\mathbf{P_1}$ becomes an identity matrix. Alternatively, there is the option to use a $\sin(el)$ weighting instead of a $\sin^2(el)$ weighting, which results in a change of the denominator in Equation 3.10.

Next, the left side of the NES $\overline{\mathbf{N}}$ can be built componentwise

$$\begin{aligned} \mathbf{N}_{N,N} &= (\mathbf{A_N} \cdot \mathbf{P_1}) \cdot \mathbf{P_2} \cdot (\mathbf{A}_N \cdot \mathbf{P_1}) \\ \mathbf{N}_{N,E} &= (\mathbf{A_N} \cdot \mathbf{P_1}) \cdot \mathbf{P_2} \cdot (\mathbf{A}_E \cdot \mathbf{P_1}) \\ &\dots \\ \mathbf{N}_{T,T} &= (\mathbf{A_T} \cdot \mathbf{P_1}) \cdot \mathbf{P_2} \cdot (\mathbf{A}_T \cdot \mathbf{P_1}), \end{aligned} \tag{3.11}$$

with $\mathbf{P_2}$ denoting a second weighting matrix. It should be noted that all elements are multiplied element-wise, i.e. the size of the input grid is maintained. The weighting matrix $\mathbf{P_2}$ weights the $\Delta$PCC w.r.t. the local satellite distribution. For the selected time span and geographic location, the azimuth, and elevation angles of the visible satellites are calculated. Then, the number of observations are summed up for each bin (e.g. 5° elevation and azimuth angles) and normalized, resulting in the gridded weighting matrix $\mathbf{P_2}$. Here, the chosen sampling rate $\Delta t$ plays a role, since the elevation and azimuth angles per satellite are calculated for $\Delta t$. For the satellite positions, the final orbits are used. As they are usually provided at intervals of 5 min, the satellites' positions are interpolated linearly when a higher sampling rate is selected. Afterward, all elements per component $\mathbf{N}_{i,j}$ are summed up and $\overline{\mathbf{N}}$ is obtained

$$\overline{\mathbf{N}} = \begin{bmatrix} \mathbf{\Sigma\Sigma N}_{N,N} & \dots & \mathbf{\Sigma\Sigma N}_{N,T} \\ \vdots & \ddots & \vdots \\ \mathbf{\Sigma\Sigma N}_{T,N} & \dots & \mathbf{\Sigma\Sigma N}_{T,T} \end{bmatrix}. \tag{3.12}$$

For visualizing the weighting matrix $\mathbf{P_2}$, three different IGS stations have been selected: BAKE (Canada, Northern Hemisphere), BOAV (Brazil, near the equator) and ANTC (Chile, Southern Hemisphere). Figure 3.7 depicts the geographic location of these stations. It is noteworthy that BAKE is situated at a much higher latitude in the Northern Hemisphere compared to ANTC in the Southern Hemisphere. The resulting GPS skyplots as well as the corresponding weighting matrices $\mathbf{P_2}$ for the selected stations on Day Of Year (DOY)091 in 2023 for 24 h ($\Delta t = 5$ min) are shown in Figure 3.8.

It is clearly visible, that parts of the local hemisphere are not covered with satellite observations due to the orbital elements. Especially the inclination, i.e. 55° for GPS satellites, is a key factor here. Thus, high PCC differences at non-covered parts are not transferred to the position domain.

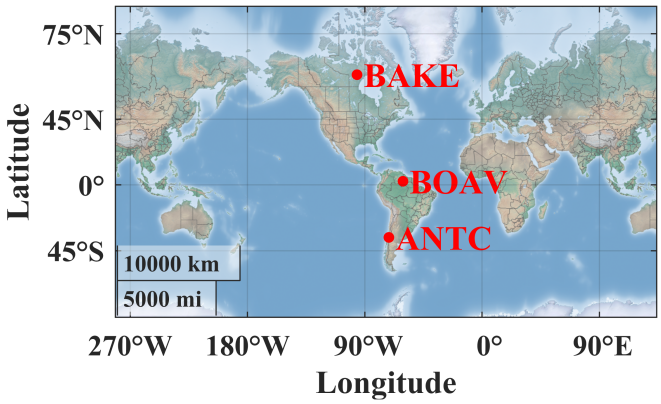


**Figure 3.7:** Selected IGS stations for visualizing weighting matrix $\mathbf{P_2}$.

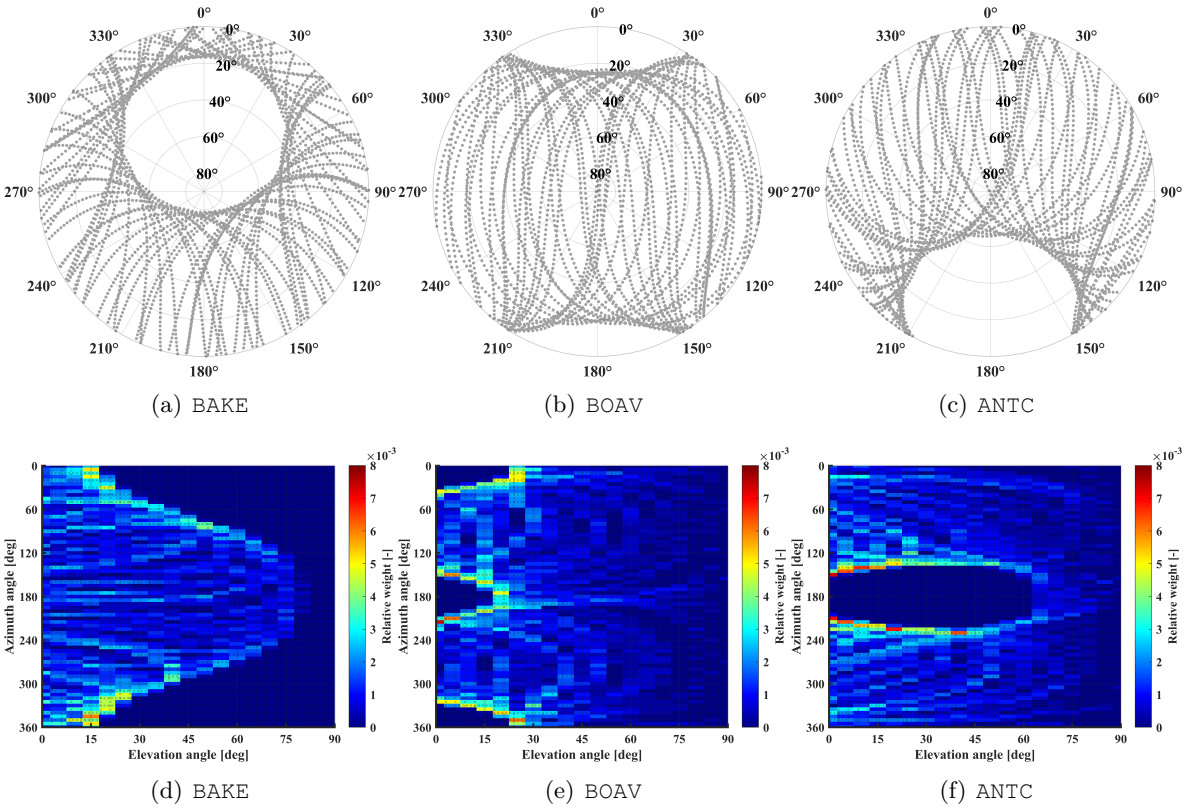


(a) BAKE (b) BOAV (c) ANTC

(d) BAKE (e) BOAV (f) ANTC

**Figure 3.8:** Local satellite distributions for three selected IGS stations: (a) – (c): GPS skyplots and (d) – (f) their corresponding weighting matrices $\mathbf{P_2}$. The results are given for DOY091 (2023) for 24 h with a sampling rate $\Delta t$ of 5 min for the satellites' positions.

Analogously to the left side of the NES, the right side $\overline{\mathbf{n}}$ is set up as

$$\begin{aligned} \mathbf{n}_N &= (\mathbf{A_N} \cdot \mathbf{P_1}) \cdot \mathbf{P_2} \cdot (\mathbf{P_1} \cdot \Delta\mathrm{PCC}) \\ \mathbf{n}_E &= (\mathbf{A_E} \cdot \mathbf{P_1}) \cdot \mathbf{P_2} \cdot (\mathbf{P_1} \cdot \Delta\mathrm{PCC}) \\ &\dots \\ \mathbf{n}_T &= (\mathbf{A_T} \cdot \mathbf{P_1}) \cdot \mathbf{P_2} \cdot (\mathbf{P_1} \cdot \Delta\mathrm{PCC}) \end{aligned} \tag{3.13}$$

resulting in

$$\overline{\mathbf{n}} = \begin{bmatrix} \mathbf{\Sigma\Sigma} \mathbf{n}_N \\ \vdots \\ \mathbf{\Sigma\Sigma} \mathbf{n}_T \end{bmatrix}. \tag{3.14}$$

Next, the NES can be solved for the unknown vector $\hat{\mathbf{x}}$

$$\hat{\mathbf{x}} = \overline{\mathbf{N}}^{-1} \overline{\mathbf{n}}. \tag{3.15}$$

The unknown vector contains the estimated topocentric coordinate differences, receiver clock error and an additional tropospheric parameter, if selected. The estimates are averaged over the selected interval of time $\delta t_\Sigma$. This means that the impact of $\Delta$PCC on the geodetic parameters is either a solution for a longer time period, e.g. one day, or for a higher resolution, e.g. 30 min. Overall, the key to this method is that each element of the observation matrix, specifically the $\Delta$PCC value, is weighted according to the actual local satellite geometry.

Figure 3.9 depicts the impact of $\Delta\mathrm{PCC}_{\mathrm{sim}}$ as well as $\Delta\mathrm{PCC}_{\mathrm{real}}$ for GPS L1, L2 and IF-LC on geodetic parameters at the three IGS stations with the following input/processing parameters:

- 7° elevation cut-off angle
- Processing date and time: 01.04.2023, DOY091 (2023)
- Interval time $\delta t_{\Sigma} = 24\,\text{h}$ (daily solution)
- Sample interval $\Delta t = 5\,\text{min}$
- Weighting scheme: $\mathbf{P_1} = \sin(el)$

The impact of $\Delta\text{PCC}_{\text{sim}}$ is shown in Figure 3.9(a). Since the simulated differences are uniformly distributed over all elevation angles and the impact is averaged over 24 h, the impact remains unchanged between the different stations. As expected, the values for the topocentric impact are consistent with the values of the simulated PCO components: -0.02 mm for the North-component, -0.5 mm for the East-component and -3.5 mm for the Up-component. The differential constant part $\Delta r$ of 4.0 mm is 1:1 reflected in the clock parameter.

Identical results are obtained when the observation period is shortened to half a day, the elevation cut-off angle is increased to 15°, and unit weighting is applied. Thus, it can be stated that a $\sin(el)$ component – which corresponds to a ΔPCO – within the pattern is transferred into the topocentric Up-component, regardless of the local satellite distribution. The same

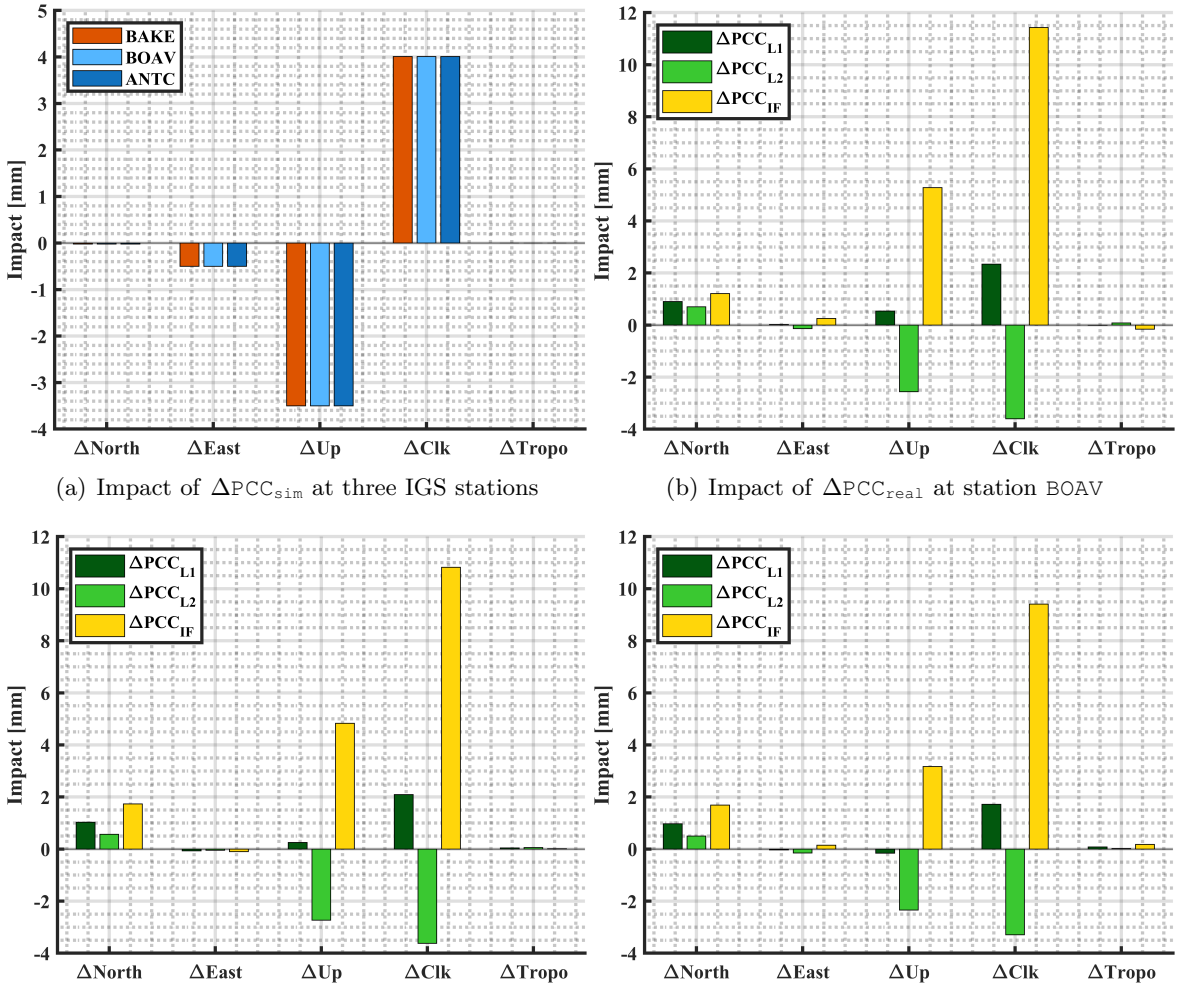


(a) Impact of $\Delta\text{PCC}_{\text{sim}}$ at three IGS stations

(b) Impact of $\Delta\text{PCC}_{\text{real}}$ at station BOAV

(c) Impact of $\Delta\text{PCC}_{\text{real}}$ at station ANTC

(d) Impact of $\Delta\text{PCC}_{\text{real}}$ at station BAKE

**Figure 3.9:** Impact of $\Delta\text{PCC}_{\text{sim}}$ and $\Delta\text{PCC}_{\text{real}}$ at different geographic locations for various frequencies and linear combinations. The geographic location of the stations can be seen in Figure 3.7.

applies to other components within ΔPCC. For example, the constant part corresponds to the receiver clock error, and differences in the horizontal PCO components are reflected in the horizontal topocentric coordinate differences.

Figures 3.9(b) – 3.9(d) depict the impact of $\Delta\mathrm{PCC}_{\mathtt{real}}$ for GPS L1, L2 and IF-LC at the selected stations. Again, two main key factors can be seen. First, the differences are amplified when building linear combination with ΔIF-LC indicating the highest differences. Second, the geographic location plays a crucial role when analyzing the impact of ΔPCC. Even if all processing parameters remain constant (including ΔPCC), the impact on geodetic parameters differs due to the weighting with respect to the local satellite geometry. The highest differences for ΔL1 are present at station BOAV, see Figure 3.9(b). This can be explained by the fact that the highest differences on the pattern level occur at $\approx 15°$ elevation angle and 90° – 270° azimuth angles (see Figure 3.3(a)). When comparing the local satellite distribution in Figure 3.8, it becomes clear that in this region less GPS visibility is given at stations BAKE and ANTC compared to BOAV. Thus, smaller ΔPCC are present at these stations.

Overall, the developed simulation approach serves as a powerful tool for assessing the impact of ΔPCC on geodetic parameters. It allows for straightforward evaluation of effects through forward modeling with varying processing parameters. This represents progress towards standardizing the comparison of different PCC sets. Moreover, it emphasizes the importance of comparing PCC sets at the parameter level rather than the pattern level. However, predicting the impact on geodetic parameters based solely on the pattern is challenging. Specifically, subtle structures within the PCC, particularly PCV, complicate straightforward transfers. Alternatively, the impact can be assessed by applying different PCC sets within a position algorithm utilizing real data.

### 3.3.3 Precise Point Positioning

In order to investigate the impact of ΔPCC on geodetic parameters using real data, differences between two PCC runs can be computed. The only variation between these two processings is the exchange of the receiver antenna PCC values. All other processing parameters remain unchanged. Figure 3.10 depicts the ΔPPP results for station BAKE (averaged over 24 hours) along with the results obtained by the simulation approach. The differences between the two approaches are below 1 mm for all components except the receiver clock error (ΔClk = 1.99 mm). If the highly correlated parameters ΔUp, ΔClk, ΔTropo and ΔAmb are summed up, the differences between the simulation approach and the PPP approach are below 0.03 mm. This indicates that during the PPP runs, parts of the PCC differences are reflected into the estimated float ambiguities. Additionally, differences may arise depending on the strategy used to define the reference point for codephase observations. Generally, if no CPC are applied, two methods can be used: either not considering any additional PCO or applying the carrier-phase PCO. In this case, the latter approach is utilized. For more detailed information, refer to Kersten et al. (2022).

A similar study, which produced comparable results concerning the differences between the simulation and PPP approaches, is presented in Kröger et al. (2022b). Here, the comparison is carried out for three different EPN stations and three different GNSS antennas. The results show again a very good agreement with differences below 0.5 mm. A more detailed study is in addition carried out in Section 7.2.1.

All in all, the comparison between the simulative approach and the PPP analyses shows that the developed standardized simulation approach is a powerful tool to elaborate the impact of ΔPCC on geodetic parameters. Although both strategies are based on a forward propagation, the remaining differences may be due to the following factors:

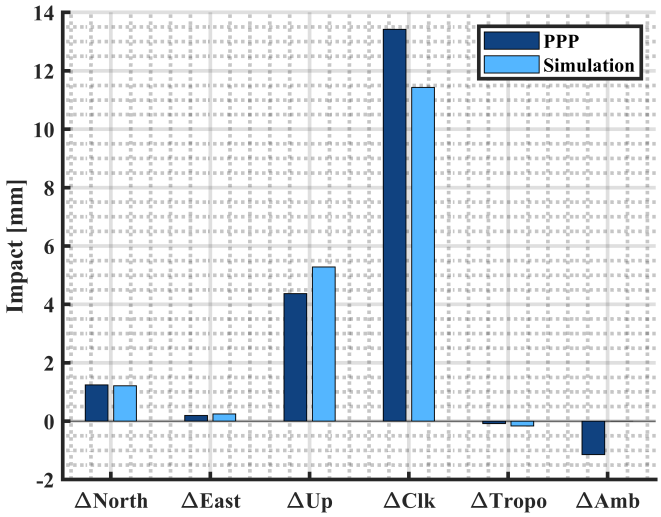


**Figure 3.10:** Impact of ΔPCC on geodetic parameters: comparison between simulation and PPP using real observation data.

- In the case of PPP, $C/N_0$ values are present, which can be used for a different weighting scheme or for an additional cut-off angle
- PPP approaches use an outlier test
- No azimuthal obstruction mask is used in the simulative approach. However, in the case of real data, signals might be blocked
- Ambiguities are not considered in the simulation tool
- Different tropospheric models are used.

# 4

# Developed Methodology for Determining Phase Center Corrections

This section describes the new methodology of absolute receiver antenna calibration developed at IfE. The methodology can be separated in three main components: preparatory work, data acquisition and preprocessing, and estimation of PCC. The preparatory work only needs to be carried out when the used robot is reinstalled on the pillar. While data acquisition is conducted in real-time during the calibration process, data preprocessing and estimation of PCC is done in post-processing. The section closes with a description of different analysis tools to assess the quality of the calibration procedure.

## 4.1 Preparatory Work

In order to precisely and accurately calibrate GNSS receiver antennas, some preparatory work is required before recording the needed raw data. This includes the calibration, leveling, and northing of the robot used for the calibration process. The setup at IfE involves an industrial robot approximately one meter high with five degrees of freedom. Each module can rotate both clockwise and counterclockwise. Two of these modules are used to rotate the AUT horizontally, while the remaining modules are responsible for tilting the AUT.

### Calibration of the Robot

During the calibration of GNSS antennas at IfE, the AUT is rotated and tilted around a nominal fixed point in space (see the red dot in Figure 4.2). It should be noted that since the robot has only five degrees of freedom, maintaining the fixed point while transitioning to a new robot pose is not possible. Any differences between the nominal and actual center of rotation are corrected using a robot model with an accuracy of 0.2 mm Kersten (2014, p. 56). Therefore, the robot must be calibrated by determining the actual arm lengths and load case coefficients.

The calibration of the robot is carried out in a laboratory environment of the Geodetic Institute Hannover (GIH) with stable temperature conditions, where the robot is set up on a tripod, leveled, and a corner cube reflector is mounted at the end of the robot arm, see Figure 4.1. The position of the reflector during different robot poses with different weights attached to the robot are measured with a lasertracker. The lasertracker measurements contain local coordinates along the X, Y, and Z axes, with the coordinate system being that of the lasertracker. In addition, the respective uncertainties, denoted as *U95*, are provided. In accordance with the Guide to the Expression of Uncertainty in Measurement (GUM), *U95*

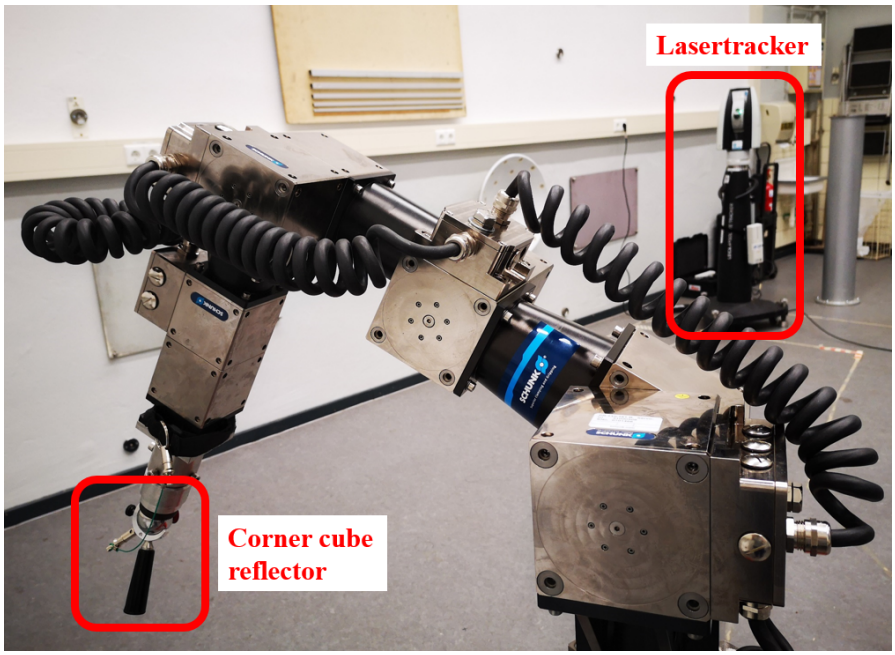


**Figure 4.1:** Calibration of the robot used for antenna calibrations at IfE. Calibration of the robot is carried out in the 3D-Laboratory of the GIH.

is defined as a 95% uncertainty confidence (JCGM, 2008). In total, 156 poses with three different weights (0 kg, 1.56 kg and 4.87 kg) are approached in order to determine also the load case coefficients. Details of the calibration procedure and the respective evaluation can be found in Meiser (2009) and Kersten and Schön (2012, p. 43–51). As of January 2025, the last calibration of the robot was carried out in November 2022.

### Leveling of the Robot

For calibration of GNSS antennas in the field, the robot is mounted on a geodetic pillar (*MSD7*) with known coordinates, as depicted in Figure 4.2. To ensure the correct transfer of the nominal coordinates from the pillar's top level, which is the reference point of the nominal coordinates, to the fixed-point in space marked by a red dot, the robot needs to be leveled. This is achieved by using a digital leveling instrument and a washer with three screws mounted directly on top of the geodetic pillar, so that the robot can be leveled. Details of the leveling procedure can be found in Meiser (2009). Figure 4.2 shows a sketch of the robot mounted on the geodetic pillar. The nominal, geocentric Cartesian coordinates are referred to the top level of *MSD7*. The constant part *const* is determined during the calibration of the robot and contains the length of all robot modules (whole length of the robot) as well as needed adapters and washers. The length $d_{\text{const}}$ describes the distance between the ARP of the AUT and the fixed point in space, marked by a red dot, around which the AUT is rotated and tilted. $d_{\text{const}}$ can be arbitrarily chosen but is usually set to an a priori $\text{PCO}_{\text{Up}}$ component, e.g. the mean $\text{PCO}_{\text{Up}}$ of GPS L1 and L2 frequencies from a type-mean calibration.

### Northing of the Robot

Since PCC are provided for north-orientated GNSS antennas, the orientation towards North has to be ensured during the calibration process. Initially, it is important to establish a defined north direction on the antenna, as detailed in Section 2.2.1. In order to establish a connection

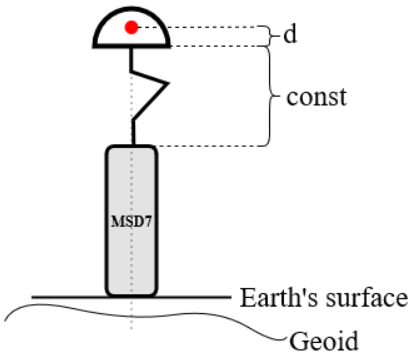


**Figure 4.2:** Sketch of the robot mounted on the geodetic pillar and the fixed point in space (red), around which the robot is tilting and rotating the AUT.

between the antenna's NRP, which corresponds to 0° azimuth in the antenna frame, and the topocentric frame, it is necessary to align the NRP with Geographic North ($N_G$) at the start of the calibration procedure. Due to construction-related constraints, the robot cannot be perfectly aligned with $N_G$. Therefore, the offset between the zero position of the robot, which is the calibration's start pose, and $N_G$ is determined and taken into account. In the following the offset is called North Offset (NO). However, during measurements in the field, the antenna is usually orientated towards Magnetic North ($N_M$) by use of a compass. Even so, these differences might be negligible due to certain facts:

1. PCC are mainly provided with a resolution of 5° steps for azimuth angles so that interpolation errors are present
2. Most GNSS receiving antennas, especially geodetic (reference station) antennas, show rather small azimuthal variations
3. The antenna orientation in the field with a compass is usually not better achievable than approximately 5°.

Since a defined procedure of different calibration institutions for the orientation of the AUT during calibration is currently not publicly available, most of the antenna calibrations were conducted while the antenna was orientated towards $N_G$. However, at present a discussion is ongoing in the framework of the *IGS Antenna Ring Campaign*, called *RingCalVal*. Details on this global initiative are presented in Kersten et al. (2024a).

In order to orient the AUT towards $N_M$, the $N_G$ direction can be determined by conducting a two-face measurement using GNSS data. If the declination (difference angle between $N_G$ and $N_M$) is taken into account, the robot can also be orientated towards $N_M$ so that consequently the resulting PCC are $N_M$ orientated. Since the antenna is orientated in the field with a compass towards $N_M$, this would be a more straight forward strategy. To this end, the declination $\delta_{decl}$ for the geographic position of *MSD7* has been determined by use of an online tool provided by the GeoForschungsZentrum (GFZ) Potsdam[1]. For April 2024, $\delta_{decl} = 3.95°$ so that:

$$\begin{aligned} N_M &= N_G - \delta_{decl} \\ NO = N_M &= 21.5° - 3.95° = 17.55° \approx 17.5°, \end{aligned} \tag{4.1}$$

with $N_G$ being determined when the robot was installed on the pillar.

[1] https://isdc.gfz-potsdam.de/igrf-declination-calculator/

## 4.2 Data Acquisition and Preprocessing

The key steps of data acquisition and preprocessing are illustrated in Figure 4.3. The first part takes place during the calibration process itself in real-time. Subsequently, using the logged raw data, data preprocessing is carried out in post-processing. The resulting dSD then serves as the observation input for estimating PCC.

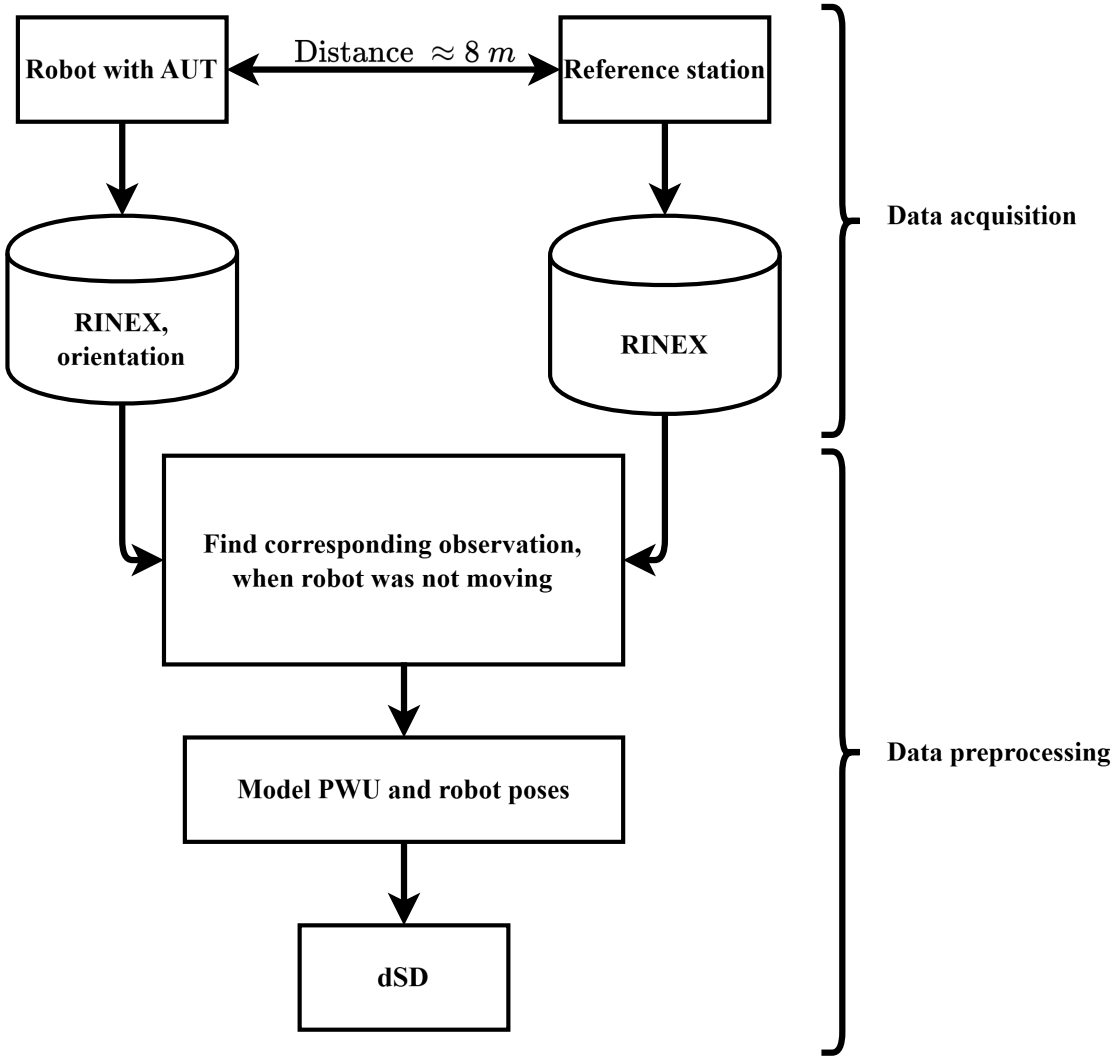


**Figure 4.3:** Flowchart representing the overall process of data acquisition and preprocessing for determining PCC.

### 4.2.1 Data Acquisition

In order to estimate absolute receiver antenna PCC, IfE uses a short baseline common-clock setup. The baseline between the pillar with the mounted robot *MSD7* and the reference station *MSD8* has a length of 8.132 m. A digital model of the calibration facility environment, which has been developed as part of the *MAESTRO* project, is depicted in Figure 4.4 (Breva et al., 2024a). At each end of the baseline, the same type of GNSS receiver is connected to the antenna, which in case of *MSD8* is a geodetic choke ring antenna (*LEIAR25.R3 LEIT*).

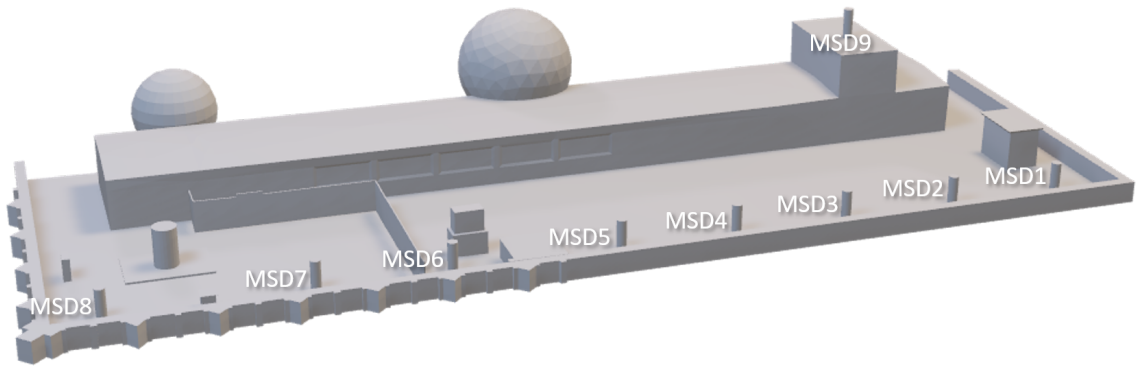


**Figure 4.4:** Digital model of the calibration facility environment at IfE, developed as part of the *MAESTRO* project (Breva et al., 2024a).

During the calibration procedure, the AUT on *MSD7* is tilted and rotated by the robot, to:

1. Avoid that PCC of the AUT cancel out by time-differencing the observations,
2. Uncouple the PCC estimation from the station's surrounding, and
3. Achieve (faster) a dense observation distribution over the whole antenna hemisphere.

The last point is important, since otherwise parts of the antenna hemisphere would not be sensed by any satellite, e.g. in the so-called *north hole* during the *standard* calibration time of approximately 4.5 h.

Figure 4.5 shows the observation distribution for a *standard* calibration for a static antenna depicted by red dots and the tilted and rotated AUT illustrated by black dots. Since AUT's size directly affects the maximum tilting angle, the duration time of a calibration depends, besides the actual satellite geometry, on the AUT dimension. In general, a calibration takes approximately 4.5 h. However, as can be seen in Figure 4.5, the calibration procedure, i.e. the robot poses, is currently optimized for GPS leading to a higher observation density for GPS compared to e.g. Galileo. Additionally, due to the tilting of the AUT, observations with negative elevation angles are also present.

Figure 4.5(c) and Figure 4.5(d) show the number of observations per 5° azimuth bin for GPS and Galileo, respectively. The black bars for the tilted and rotated AUT indicate clearly that in general an equal distribution over the antenna's hemisphere is achieved by tilting and rotating the AUT.

During the data acquisition, the following data is recorded:

- GNSS raw data at both stations
- Robot poses together with GPS timestamps
- Information about start and end time of calibration sets.

Since geodetic receivers are used to log the GNSS raw data, satellite systems, frequencies, sampling rates and (depending on the receiver in use) tracking parameter settings, can be selected according to the application. Typically, a sampling rate of 1 Hz data is chosen for multi-GNSS, multi-frequency data. The role of the used receivers and their settings is discussed in Section 5.4.

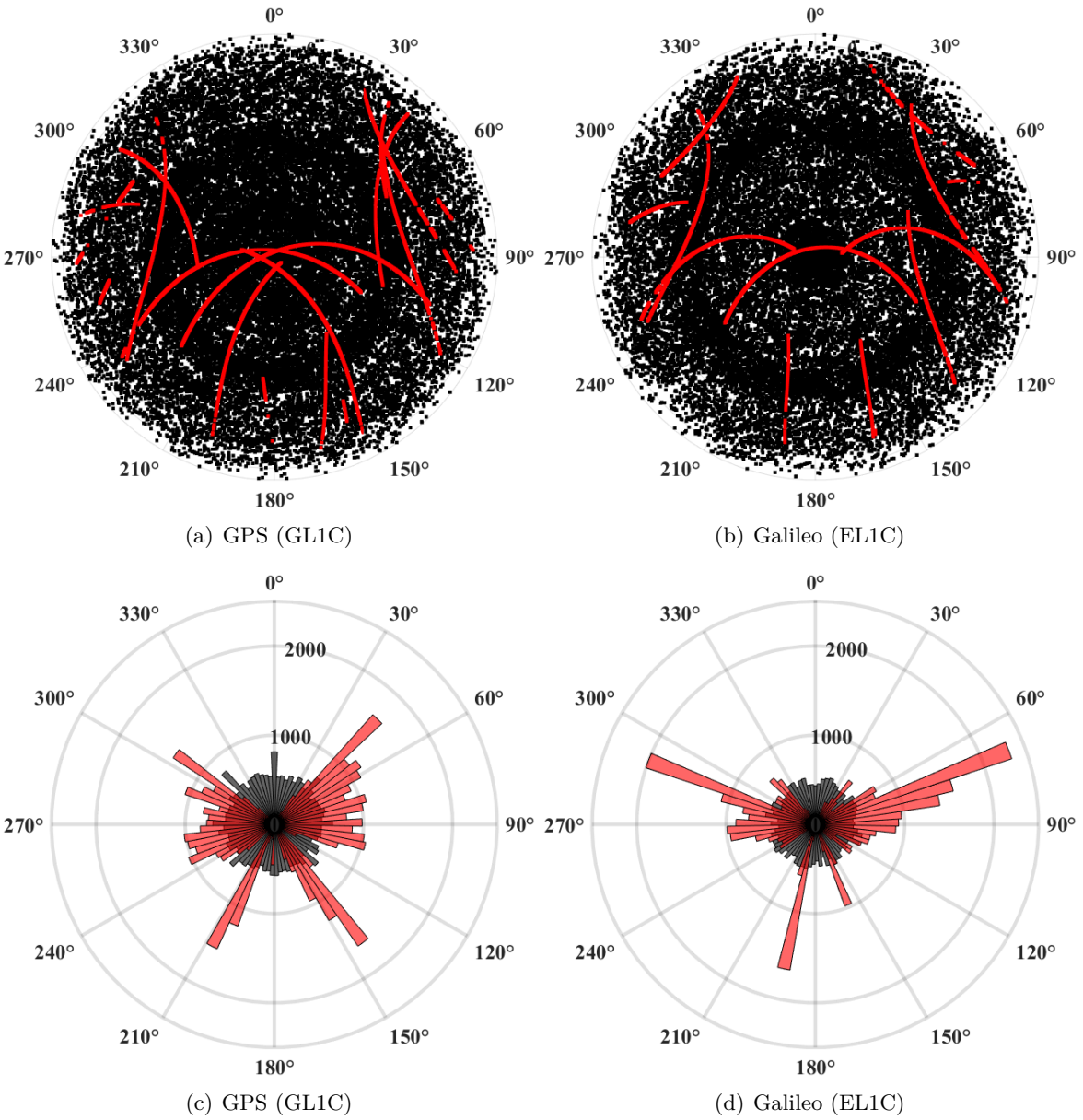


(a) GPS (GL1C)

(b) Galileo (EL1C)

(c) GPS (GL1C)

(d) Galileo (EL1C)

**Figure 4.5:** Distribution (a,b) and number of observations (c,d) of GPS GL1C (a,c) and Galileo EL1C (b,d) during a *standard* calibration (duration ≈ 4.5 h). Red dots and bars depict observations in a static case, black ones when the robot tilts and rotates the AUT.

### 4.2.2 Data Preprocessing

After the calibration process has finished, the binary and proprietary GNSS raw data is converted to RINEX observation files. Along with the satellite positions (e.g. taken from final orbits provided by the IGS), they serve as input for the in-house IfE-GNSS-Toolbox. As a result, the observations of both stations and the azimuth and elevation angles of the satellites in the topocentric frame are available for all signals/systems and epochs. For this, the nominal coordinates of both stations (*MSD7* and the reference station *MSD8*) are required to be in the same reference frame and epoch. These coordinates were determined in 2018 with sub-millimeter accuracy using a local GPS/GLONASS L1 network solution (Koppmann, 2018).

Next, common timestamps at both stations are found where the robot was not moving. To this end, the information about the exact robot poses along with their timestamps are

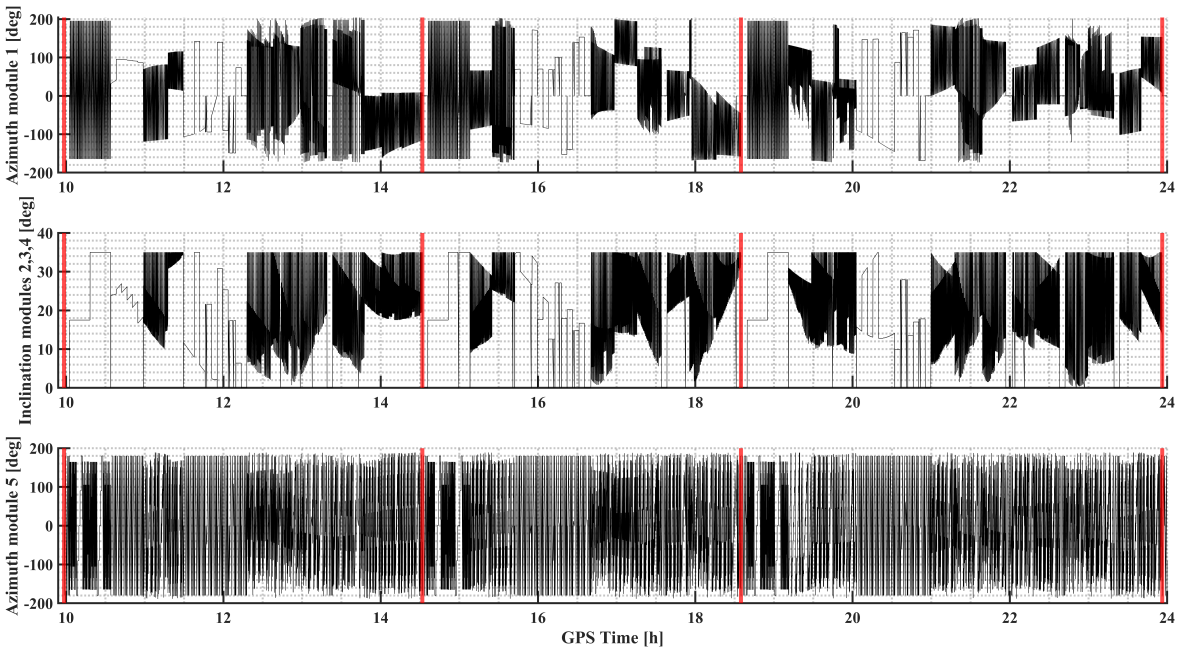


**Figure 4.6:** Robot poses for calibration of a *NOV703GGG.R2* antenna, see Figure 5.1. Red lines separate the three different sets on DOY047, 2023.

imported. Figure 4.6 gives an example of the basic information from this robot procedure file. In addition to the standstill periods, it contains the information about the orientation of the different robot modules. Module 1 and module 5 are horizontal rotating modules, so that consequently, the azimuth angles w.r.t. the North orientation are given. Modules 2, 3 and 4 are tilting modules so that the inclination angle is provided. The red lines in Figure 4.6 separate the different individual calibration sets. As can be seen, the robot poses differ between the respective sets.

Finding of common timestamps is then done by intersecting the observation timestamps of both stations with the timestamps of the stored robot poses. At this step, depending on the chosen processing parameters, several observation masks can already be applied to the observations by either discarding or down-weighting some of them:

- Environmental masks: specific regions in topocentric frame (azimuth and elevation angle-dependent) are removed, e.g. areas with potential high MP error (domes, vertical reflectors)
- Inclination mask: poses of the robot with a specific inclination, e.g. towards a vertical reflector, are removed
- Elevation cut-off angle in topocentric frame for *MSD7* and/or *MSD8*.

The respective observations from station *MSD7* are afterward corrected by the robot model. This includes the nominal arm length and angle offsets of the robot modules, determined as a part of the preparatory work, see Section 4.1. A detailed description of this task can be found in Meiser (2009) and Kersten (2014). Then, the observations are transformed from the topocentric into the antenna frame following the equations provided in Kersten (2014) and further refined in Breva (2025). Figure 4.7 depicts the relation between topocentric and antenna frame. As can be seen, elevation angles in the antenna system can also be negative. Since PCC are usually estimated for the full hemisphere, i.e. $0° \leq el \leq 90°$, this is needed to stabilize the NES at low elevation angles. Section 4.3 and Section 6.3 provide a more detailed discussion on this topic.

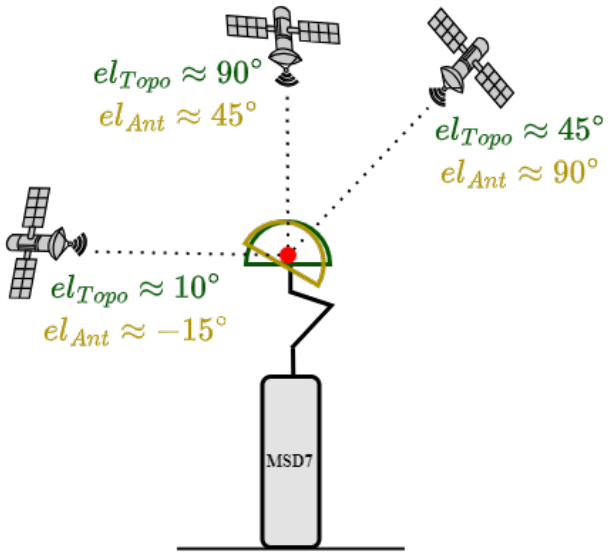


**Figure 4.7:** Relation between topocentric and antenna frame.

After transforming the observations into the antenna frame, an elevation cut-off angle in the antenna frame can be applied. Usually, it is set to $-5°$ and is a trade-off between the quality of possible observations and the loss of important information for the PCC estimation.

Next, receiver-to-receiver SD are formed. Thanks to the short baseline, the distance-specific errors, i.e. the atmospheric refractions due to ionosphere and troposphere, cancel out. In addition, all satellite-specific errors vanish. To further reduce the GNSS error budget, dSD are computed.

Figure 4.8 displays the distribution of the time interval $\Delta$t between two consecutive static epochs, between which dSD are computed. This is illustrated using a calibration set from a *NOV703GGG.R2* antenna. The data shows that the time difference is mostly $\leq 6$ s. However, there are a few instances where the $\Delta$t exceeds 40 s. In these rare cases, the robot was paused while waiting for the next pose instruction from the control software.

To ensure the similarity of observations between two consecutive epochs, dSD with $\Delta t > 6$ s are removed. Consequently, PCC of the static reference antenna as well as the receiver clock error cancel. This is due to the fact that an external frequency standard (Standard Rubidium FS725) with a stability of $< 2 \cdot 10^{-11}$ is connected to the receivers so that the individual

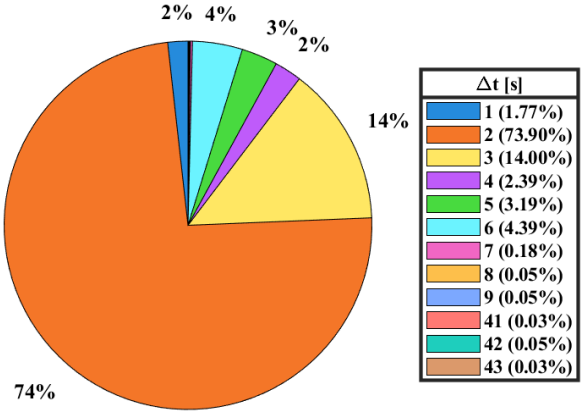


**Figure 4.8:** Distribution of time differences $\Delta$t between consecutive dSD epochs for one calibration set.

receiver clock drift is identical at both receivers (Kersten, 2014). Also, the phase ambiguity term cancels. Since the relative geometry between satellite, antenna and its surrounding does not change in these short time intervals, it is assumed that the static MP effect also cancels. While this assumption can likely be proofed for the static station *MSD8*, remaining MP effects are present for the AUT on *MSD7*. These challenges are further addressed in the joint *MAESTRO* project with the DLR (Breva et al., 2024a).

Since the AUT is tilted and rotated during the calibration procedure, a PWU effect is introduced for the receiving antenna. This effect is not eliminated by time differencing the observations on *MSD7*, unlike at the reference station, and therefore, it needs to be modeled. In the following, the basic algorithm for the PWU model in the case of antenna calibration is shortly demonstrated.

The PWU effect occurs because GNSS satellites transmit RHCP L-band signals. Wave polarization affects the behavior of the electric field vector as it travels from the transmitter to the receiver. Changes in the relative orientation between transmitting and receiving antennas lead to variations in the measured carrier-phase, resulting in the PWU effect (Beyerle, 2009). It is worth noting that the polarization state of the GNSS signal at the receiving antenna deviates from pure RHCP for non-zero off-boresight angles (Wu et al., 1993). However, since the power level of the LHCP signal component is much smaller compared to the RHCP levels, these deviations are negligible for practical purposes, making the assumption of a pure RHCP transmitter valid. The fundamental formulas for calculating correction values needed to account for PWU effects are detailed in Wu et al. (1993) and Beyerle (2009).

In the context of antenna calibration, the necessary adaptations have been implemented by Breva (2025), and a brief summary of these adaptations is provided here. Since time-differenced observations are used, the PWU effect also needs to be taken into account in a time-differenced way, requiring the application of $\Delta$PWU. Through this process, cycle slips occur in the corrected dSD time series (see Figure 4.9(a)). In this dataset, approximately 18% of all observations are affected. To avoid significantly reducing the number of observations, it is preferable to correct the jumps rather than eliminate them. According to Breva (2025), the PWU value should increase when the AUT rotates clockwise from the transmitter's point of view, and decrease for counterclockwise rotations. To determine the relative rotation of the AUT, the azimuth angle (in the topocentric coordinate system) can be time-differenced. Negative values indicate counterclockwise rotations, while positive values indicate clockwise rotations. This method can also be applied to the calculated PWU correction term as described by Beyerle (2009), allowing for the comparison of the resulting values. If differences arise, they indicate cycle slips, which need to be corrected. This correction is achieved by adding or subtracting one wavelength from the previously calculated PWU correction values. The PWU correction, originally in cycles, is then converted into meters by multiplying it by the wavelength of the respective frequency. The resulting dSD time series, which incorporates the corrected PWU values, is depicted in Figure 4.9(b). As clearly shown, the cycle slips are corrected, bringing the dSD in a range of $\pm 2\,\mathrm{cm}$.

Thanks to the measurement setup, differencing strategy and the modeling of the PWU effect, the observations (dSD per satellite $k$) for estimating PCC contain only the PCC of the AUT between the epochs $i$ and noise $\epsilon$, which also might contain remaining MP effects

$$\mathrm{dSD}^k = \mathrm{PCC}^k_{\mathrm{AUT}}(t_{i+1}) - \mathrm{PCC}^k_{\mathrm{AUT}}(t_i) + \epsilon(t_i, t_{i+1}). \tag{4.2}$$

To avoid large outliers in the dSD, a simple threshold method for removing them is applied. The threshold is antenna- and frequency-specific and takes the maximum expectable PCC between two epochs into account. These dSD then serve as input for the estimation process, which is described in detail in the following Section 4.3.

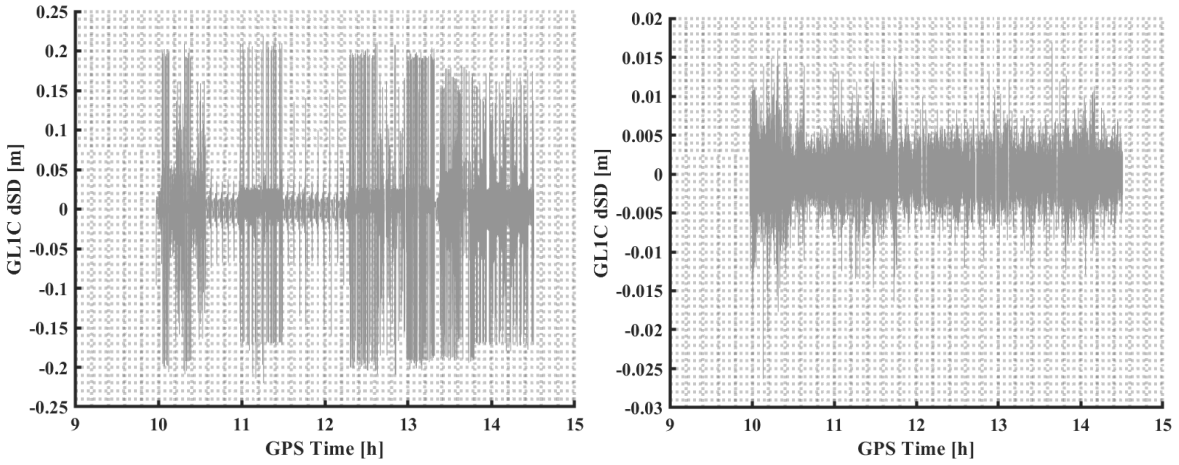


(a) without corrected PWU (b) with corrected PWU

**Figure 4.9:** Comparison of dSD time series without (a) and with (b) corrected PWU correction values. Note the different axes scaling.

## 4.3 Estimation of Phase Center Corrections

This section focuses on the estimation algorithm used to determine PCC. First, the algorithm for determining Hemispherical Harmonics (HSH) coefficients is described in detail, with particular emphasis on the distribution of observations on the antenna hemisphere. This distribution motivates using HSH instead of the more commonly used SH to parametrize PCC. It is then shown how the ANTEX conform output is derived from the estimated PCC, following the format standard. The section concludes with an in-depth explanation of how a PCC set can be divided into its individual components, namely PCO, PCV, and a constant part $r$.

### 4.3.1 Determination of HSH Coefficients

Usually, PCC are parametrized by SH functions with degree up to $m = 12$ and order $n = 12$ (Wübbena et al., 1996; Willi and Guillaume, 2019; Zhou et al., 2023). At this stage, a trade-off has to be made between the number of unknowns, which corresponds to the computational time, and the full representation of the PCC without losing structural information. A more detailed discussion on this is given in Section 6.2. The parametrization of PCC reads

$$\mathrm{PCC}(\alpha^k, z^k) = \sum_{m=1}^{m_{\max}} \sum_{n=0}^{m} \widetilde{P}_{mn}(\cos z^k) \cdot \left( a_{mn} \cdot \cos(n\alpha^k) + b_{mn} \cdot \sin(n\alpha^k) \right), \tag{4.3}$$

where $\widetilde{P}$ denotes the fully normalized Legendre function, $z$ and $\alpha$ the zenith and azimuth angle to the respective satellite $k$ in the antenna frame, and $a_{mn}$ as well as $b_{mn}$ the unknown coefficients which are estimated in a LSA.

SH functions represent orthogonal functions defined on a full sphere. However, in the case of antenna calibration, observations are mostly present on the upper hemisphere. Due to the tilting of the AUT (see Figure 4.7), negative elevation angles are partly present. Figure 4.10 shows the proportion of theoretically possible observations (e.g. before applying any cut-off angle, removing outliers, ...) per GNSS and five degree elevation bin. Observations below $-35°$ elevation angle are not possible due to the antenna size-dependent maximum tilting angle. For all GNSS approx. 85% of the total possible observations lie on the upper hemisphere, i.e. elevation angle $> 0°$. In addition, usually an elevation cut-off angle of $-5°$ in the antenna

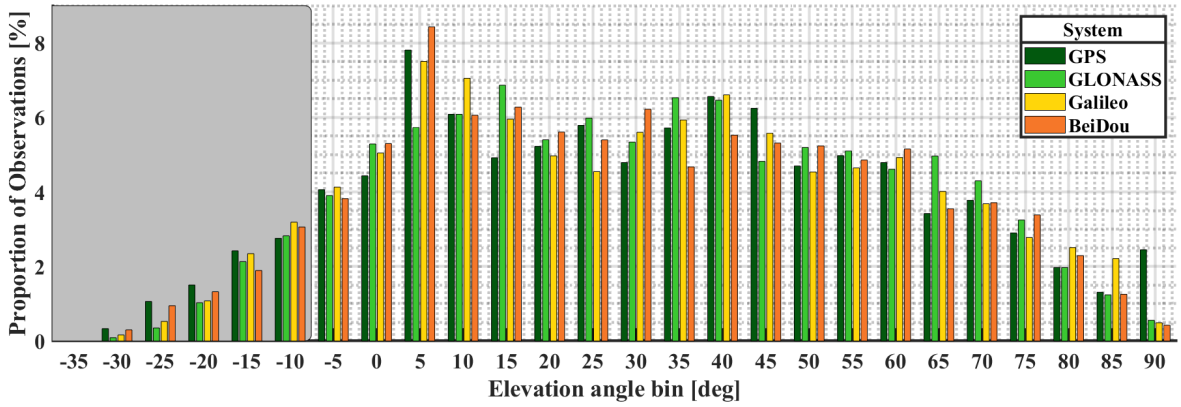


**Figure 4.10:** Proportion of theoretically possible observations in the antenna frame per GNSS and 5° elevation bin. The gray area indicates the typical elevation cut-off angle of -5°, representing observations in this part usually being discarded.

frame is applied, so that possible observations in the gray part in Figure 4.10 are discarded. This observation distribution leads to an ill-conditioned system, so that a small distortion of the observation vector can significantly impact the parameter vector.

To this end, an adapted version of SH called HSH, which serves as a shifted basis of the associated Legendre Polynomials, based on Gautron et al. (2004), is developed. The authors define the shift of the polynomials as a linear transformation of $x$ to $k_1 x + k_2$, with $k_1 \neq 0$. They state that if the polynomials $p_l(x)$ are orthogonal over an interval [a, b], then the shifted polynomials are orthogonal over the new interval $[\overline{a}, \overline{b}]$. Gautron et al. (2004) give the corresponding adaptions and corresponding factors $k_1$ and $k_2$ for the hemisphere. Based on their investigations, the factors for the interval $[\ \overline{a}, \overline{b}]$ for the estimation of PCC are determined. The interval is based on the maximum negative elevation angle and is usually set to $el = -5° = z = 95°$, see also Figure 4.10. Accordingly, the adapted interval reads

$$\begin{aligned} \overline{a} &= \cos(0) \\ \overline{b} &= \cos(\theta_{new}), \theta_{new} = 95° \cdot \frac{\pi}{180°}. \end{aligned} \tag{4.4}$$

By rearranging the equations in Gautron et al. (2004), the factors $k_1$ and $k_2$ can be determined for the chosen maximum negative elevation angle, where a = 1 and b = -1 are taken from Gautron et al. (2004)

$$\begin{aligned} k_2 &= \frac{a \cdot \overline{b} - \overline{a} \cdot b}{\overline{b} - \overline{a}} \\ k_1 &= \frac{a - k_2}{\overline{a}} \\ k_2 &= 1 - k_1. \end{aligned} \tag{4.5}$$

For a maximum negative elevation angle of $-5°$, $k_1$ reads approx. 1.8107. In more specific terms, this means that the argument for $\widetilde{P}$ in Equation 4.3 changes to

$$\widetilde{P}_{mn}(k_1 \cos z^k + k_2), \tag{4.6}$$

so that accordingly the parametrization of PCC by an adapted version of HSH reads

$$\mathrm{PCC}(\alpha^k, z^k) = \sum_{m=1}^{m_{\max}} \sum_{n=0}^{m} \widetilde{P}_{mn}(k_1 \cos z^k + k_2) \cdot \left( a_{mn} \cdot \cos(n\alpha^k) + b_{mn} \cdot \sin(n\alpha^k) \right). \tag{4.7}$$

Equation 4.8 shows the functional model for the LSA. The design matrix $\mathbf{A}$ contains the partial derivatives of Equation 4.7 with respect to the unknowns, see Equation 4.11. The observation vector $\mathbf{l}$ is filled with the dSD

$$\hat{\mathbf{x}} = (\mathbf{A}^{\mathrm{T}}\mathbf{P}\mathbf{A})^{-1} \cdot \mathbf{A}^{\mathrm{T}}\mathbf{P}\,\mathbf{l}. \tag{4.8}$$

The stochastic model reads

$$\begin{aligned} \boldsymbol{\Sigma}_{\mathbf{ll}} &= \sigma_0^2 \cdot \boldsymbol{Q}_{ll} \\ \mathbf{P} &= \boldsymbol{\Sigma}_{ll}^{-1}. \end{aligned} \tag{4.9}$$

with $\sigma_0^2$ being the a priori variance factor, $\boldsymbol{Q}_{ll}$ the cofactor matrix of the observations and $\mathbf{P}$ the weighting matrix. If a unit weighting is selected, $\mathbf{P}$ is the identity matrix ($\mathbf{P} = \mathbf{I}$). The impact of different applied weighting schemes on the estimated PCC is discussed in Section 6.4.

The design matrix $\mathbf{A}$ as well as the weighting matrix (if $\mathbf{P} \neq \mathbf{I}$) is set up epoch-wise for each satellite $k$. Since time-differenced observations are used, $\mathbf{A}$ results from the difference between the design matrices set up individually for each epoch $i$ and epoch $i+1$

$$\mathbf{A} = \mathbf{A}_{i+1} - \mathbf{A}_i. \tag{4.10}$$

$\mathbf{A}$ is filled in each case with the partial derivatives of the function $f$ shown in Equation 4.7. For better readability, the epoch indices $i$ are skipped in Equation 4.11.

$$\begin{aligned} \mathbf{A}_k &= \left[\frac{\partial f}{\partial a_{mn}} \quad \frac{\partial f}{\partial b_{mn}}\right]^{\mathrm{T}} \\ \frac{\partial f}{\partial a_{mn}} &= \cos(m \cdot \alpha) \cdot \widetilde{P}_{mn}(k_1 \cos z^k + k_2) \\ \frac{\partial f}{\partial b_{mn}} &= \sin(m \cdot \alpha) \cdot \widetilde{P}_{mn}(k_1 \cos z^k + k_2) \end{aligned} \tag{4.11}$$

Subsequently, the normal equation matrix $\boldsymbol{N_k}$ for each satellite can be computed

$$\boldsymbol{N_k} = \boldsymbol{A}^{\mathrm{T}}\,\boldsymbol{P}\boldsymbol{A} \tag{4.12}$$

and is then summed up over all satellites

$$\bar{\boldsymbol{N}} = \sum_{k=1}^{k_{Max}} \boldsymbol{N_k}. \tag{4.13}$$

The stacking is carried out in the same way for the right side of the normal equation system

$$\bar{\boldsymbol{n}} = \sum_{k=1}^{k_{Max}} \boldsymbol{A}^{\mathrm{T}}\,\boldsymbol{P}\,\mathbf{l}. \tag{4.14}$$

Finally, the unknowns $a_{mn}$ and $b_{mn}$ can be solved by inverting $\bar{\boldsymbol{N}}$

$$\hat{\boldsymbol{x}} = \bar{\boldsymbol{N}}^{-1} \cdot \bar{\boldsymbol{n}}. \tag{4.15}$$

It is important to ensure that the condition number of $\bar{\boldsymbol{N}}$ is not too high, as this could make the inversion numerically unstable, leading to an unreliable estimation of the unknowns. By using the HSH, a condition number of less than $10^3$ is typically achieved. The impact of

different applied restrictions, which are used to stabilize the NES, on the condition number and the resulting PCC is discussed in detail in Section 4.4.4.

### 4.3.2 ANTEX Conform Output

In order to achieve an ANTEX conform output of the estimated PCC, i.e. gridded values, the estimated unknowns $\hat{\mathbf{x}}$ are inserted into Equation 4.7. The HSH synthesis is carried out by inserting azimuth angles from 0° to 360° and zenith angles from 0° to 90°. At this stage, the resolution of the PCC can be chosen, which is typically a step size of 5° for both angles. The PCC could also be provided for negative elevation angles, which is usually not the case but might be beneficial for e.g. GNSS reflectometry.

The obtained grid comprises PCO components, PCV values as well as a constant part $r$. Since a constant component $d_{\text{const}}$ between ARP and the mean approximated $\text{PCO}_{\text{Up}}$ is subtracted before calibration (see e.g. Figure 4.2), only a $\Delta\text{PCO}_{\text{Up}}$ is contained within the grid so that $d_{\text{const}}$ needs to be added later.

Since usually an (arbitrary) PCO offset is extracted from the PCC values, a second LSA is carried out. In general, several methods exist to separate the PCC into the individual components. A detailed analysis regarding the separation methods is provided in Section 4.3.3. It is shown that the resulting PCC are equal, as long as all individual parts are taken adequately into account and the PCC are estimated for the upper hemisphere.

At IfE, a constant term $r$ is typically estimated and then added to the PCC, fulfilling Equation 2.27. The advantage of estimating $r$ is that it can be omitted if necessary. This is useful, for instance, when no restrictions based on the NES are applied, as discussed in Section 6.3. In such cases, a large $r$ is added to the pattern, causing comparisons of $\Delta$PCC on the pattern level to exhibit significant deviations. Since the difference $\Delta r$ between two PCC sets generally does not affect the position solution itself, but rather the receiver clock error, this approach is appropriate. Also, as discussed in Section 3.1, any addition and subtraction of a constant value to a pattern is a valid transformation.

The separation of PCC into the individual parts is carried out following Equation 4.16.

$$\hat{\boldsymbol{x}} = \begin{bmatrix} \text{PCO}_{\text{North}} \\ \text{PCO}_{\text{East}} \\ \Delta\text{PCO}_{\text{Up}} \\ r \end{bmatrix} = (\boldsymbol{A}^{\text{T}}\boldsymbol{A})^{-1} \cdot \boldsymbol{A}^{\text{T}}\boldsymbol{l} = \boldsymbol{N}^{-1} \cdot \boldsymbol{n} \tag{4.16}$$

Here, the unknown vector $\hat{\mathbf{x}}$ consists of the ($\Delta$)PCO components and $r$. Since usually $\mathbf{P}$ is set to the identity matrix indicating equal weighted and uncorrelated observations, it is neglected in Equation 4.16. However, different weighting schemes do not affect the resulting PCC, as it can be seen in Section 4.3.3. The observation vector $\mathbf{l}$ is filled with the gridded PCC. The design matrix $\mathbf{A}$ reads

$$\mathbf{A} = \begin{bmatrix} \cos(\alpha^i) \cdot \cos(el^i) \\ \sin(\alpha^i) \cdot \cos(el^i) \\ \sin(el^i) \\ -1 \end{bmatrix}^{\mathbf{T}} . \tag{4.17}$$

The design matrix is filled with the respective elevation angles $el^i$ and azimuth angles $\alpha^i$. The step size and their range is defined during the transition from the estimated coefficients to the grid, i.e. by the above described HSH synthesis.

Usually, published PCC values adhere to the constraint that PCV are zero in the zenith

direction (PCV($z = 0$) = 0), commonly referred to as the *zero zenith constraint*. To satisfy this condition, a constraint is incorporated, resulting in an extended NES $\widetilde{\boldsymbol{N}}$ for the left side and $\widetilde{\boldsymbol{n}}$ for the right side

$$\begin{aligned} \widetilde{\boldsymbol{N}} &= \begin{bmatrix} \boldsymbol{N} & \boldsymbol{R}^{\mathrm{T}} \\ \boldsymbol{R} & \boldsymbol{0} \end{bmatrix} \\ \widetilde{\boldsymbol{n}} &= \begin{bmatrix} \boldsymbol{n} & -\boldsymbol{l}(z=0) \end{bmatrix}^{\mathrm{T}}. \end{aligned} \tag{4.18}$$

The restriction matrix $\boldsymbol{R}$ reads

$$\boldsymbol{R} = \begin{bmatrix} 0 & 0 & -1 & 1 \end{bmatrix} \tag{4.19}$$

and fulfills along with the last entry from $\widetilde{\boldsymbol{n}}$ the condition that the PCV are zero at zenith ($z = 0$). The residuals $v$ of the LSA represent the PCV values and can be computed following Equation 4.20

$$\mathbf{v} = \mathbf{A} \cdot \hat{\mathbf{x}} - \mathbf{l}. \tag{4.20}$$

Finally, the constant PCO part and the corresponding PCV are written for the AUT per frequency and GNSS into the ANTEX file. Hereby, $d$ extracted beforehand is added to the $\mathrm{PCO}_{\mathrm{Up}}$ component

$$\begin{bmatrix} \mathrm{PCO}_{\mathrm{North}} \\ \mathrm{PCO}_{\mathrm{East}} \\ \mathrm{PCO}_{\mathrm{Up}} \end{bmatrix} = \hat{\mathbf{x}}(1:3) + \begin{bmatrix} 0 \\ 0 \\ d_{\mathrm{const}} \end{bmatrix}. \tag{4.21}$$

It should be noted that, in contrast to the current ANTEX file published by the IGS (as of January 2025), individual PCC per frequency and GNSS are written into the ANTEX file. Within the publicly available ANTEX file, PCC values are identical for identical frequencies from different GNSS (e.g. G01 and E01). Analyses of differences between identical frequencies from different GNSS are given in Section 5.5.

As discussed in Kröger et al. (2021), it could be beneficial to switch from the currently used frequency specifier (e.g. G01 for GPS L1 or E05 for Galileo E5) to the widely used RINEX observation file specificator. This would bring, among other reasons, mainly two improvements:

1. Consistency of different IGS products/data formats. Especially, since the notation *G01* is also widely used for GPS Pseudo Random Noise (PRN)01 satellite, e.g. in final orbit products.
2. Simplified integration of CPC (also known as GDV) into the ANTEX file, e.g. GC1 for GPS C/A code observations.

Moreover, a more sound comparison between different PCC sets could be carried out if some more metadata would be added into the comment section for each antenna within the ANTEX file. These could include:

- Degree and order of SH/HSH, if SH/HSH expansions are used to parameterize PCC
- Constant part $r$, if it is (partly) extracted from PCC
- Used constrain to separate between PCO, PCV, i.e. *zero zenith constraint* or *Zero mean constraint* (over the whole or a part of the antenna hemisphere)
- Used tracking code/mode of respective frequency following the RINEX observation file specificator, e.g. GL2W (encrypted signal) or GL2L (civil signal)
- Additionally: used receiver type along with PLL and DLL settings

Integrating this metadata into the ANTEX file would require two additional lines per receiver antenna. However, the added metadata would not be particularly beneficial to general users of the ANTEX file. The primary advantage of the more detailed metadata would be for research purposes, as it would enable a more thorough comparison of ΔPCC between different calibration facilities and strategies.

### 4.3.3 Methods to Separate PCC into PCO, PCV and Constant Parts

After transferring the estimated $a$- and $b$-coefficients to a grid by a HSH synthesis, a full separation following Equations 4.16 – 4.21 into PCO, PCV and $r$ is carried out at IfE. During this step, it is also implicitly formulated that the PCV values are zero at zenith (PCV($z$=0)=0). Afterward, the PCC are calculated following Equation 2.27. For certain analyses, it can be beneficial to exclude $r$ from the pattern, as discussed in Section 6.3.

The advantage of this full separation is that it provides an initial insight into potential differences of ΔPCC in the position domain, as further discussed in Section 3.2.2. However, as long as all components are adequately taken into account, several methods can be used to extract constant parts or PCO components from PCC. The differences between the full patterns typically fall within numerical precision, except when HSH synthesis is carried out down to -5° elevation angle, which results in a slightly different PCC pattern.

The different methods for estimating PCO and $r$ components based on gridded PCC are introduced and applied in this section, and the corresponding results are discussed. Figure 4.11 shows the different ways to parametrize the estimation of PCO and $r$ components. The settings of the different runs (= ID) are provided in Tab. 4.1. Since the impact of the chosen resolution is investigated in Section 6.5, it is not further discussed here. In principle, five different settings can be applied:

1. Estimation of a constant part $r$
2. Application of a zero-zenith restriction

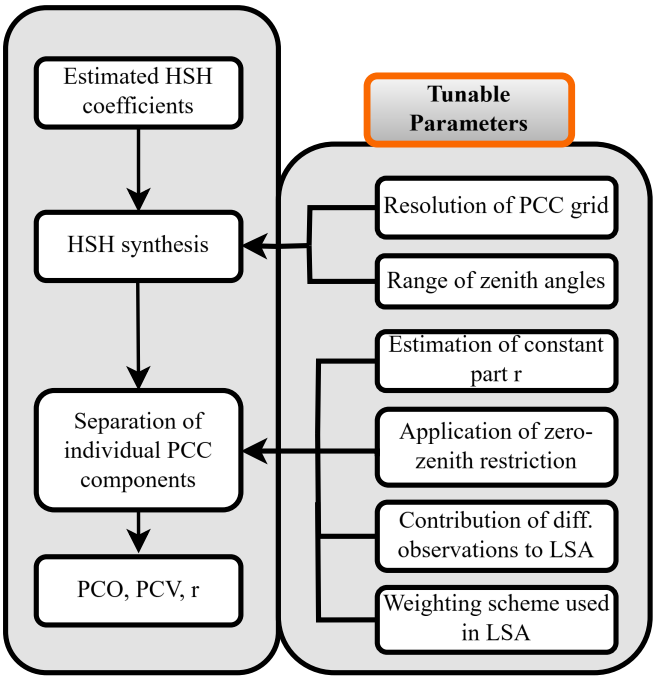


**Figure 4.11:** Tunable parameters for separating PCC into PCO, PCV and constant $r$ components.

3. Application of different weighting schemes for estimating the unknowns, i.e. PCO (and $r$) components
4. Contribution of which observations, i.e. PCC values, to the LSA
5. Strategy for separating PCV from PCC

In addition to the unit weighting, two other weighting models are particularly relevant when selecting the weighting model, which is addressed in case 3. Either the PCC can be weighted w.r.t. their estimated standard deviation $\sigma_{\mathrm{PCC}}$, or it is taken into account that the segments at higher elevation angles cover a smaller area. Based on Fuhrmann et al. (2015), who use this method for MP stacking, the weights are chosen based on the corresponding elevation angle. Consequently, gridded PCC values at 90° elevation angle get the largest weight $w = 1$ and the weight decreases with decreasing elevation angle down to $w \approx 0.2$ at the horizon.

To separate PCV values from PCC, two methods exist. The first method involves using the residuals of the LSA as the PCV values (see Equation 4.20). The second method, known as the two-step approach, involves subtracting the estimated PCO components, which are calculated over a specific elevation angle range, from the input PCC to derive the PCV values. This method is indicated with a † in Table 4.1 and involves the following steps:

1. Estimation of PCO components using Equation 4.16.
2. Calculation of PCV by subtracting the PCO from the PCC, i.e., PCV = PCC - PCO.

To analyze the impact of the different tunable parameters on the resulting PCC, GL1C PCC of a *NOV703GGG.R2 NONE* pinwheel antenna are used as an example. The basic processing parameters for estimating the PCC are listed at the beginning of Chapter 6.

**Table 4.1:** Methods for separating PCC into PCO, PCV and $r$ components. Unless otherwise specified in the column *Remark*, the following basic settings are applied: HSH synthesis is carried out for the full upper hemisphere ($0° \leq el \leq 90°$), i.e. PCC([0° 90°]), and all grid points are contributing to the PCO estimation, i.e. PCO([0° 90°]). Methods denoted with a † us the two-step approach to determine the PCV values.

| **ID** | **Estim.** $r$ | **PCV**$(z=0)$**=0** | **Weighting** | **Remark** |
|---|---|---|---|---|
| A | ✓ | ✓ | unit | standard approach at IfE |
| B | ✓ | - | | |
| C | - | ✓ | | |
| D | - | - | | |
| E | ✓ | ✓ | congruent cells | |
| F | ✓ | - | | |
| G | - | ✓ | | |
| H | - | - | | |
| I | ✓ | ✓ | $\sigma_{\mathrm{PCC}}$ | |
| J | ✓ | - | | |
| K | - | ✓ | | |
| L | - | - | | |
| M | ✓ | ✓ | unit | PCC([-5° 90° ]]), PCO([0° 90°]]) |
| N | ✓ | ✓ | unit | PCC([-5° 90° ]]), PCO([-5° 90° ]]) † |
| O | ✓ | ✓ | unit | PCC([-5° 90° ]]), PCO([0° 90°]]) † |
| P | ✓ | ✓ | unit | PCC([0° 90°]]), PCO([5° 90°]]) † |
| Q | ✓ | ✓ | unit | PCC([0° 90°]]), PCO([10° 90°]]) † |
| R | ✓ | ✓ | unit | neglecting repeated values for z=0° |

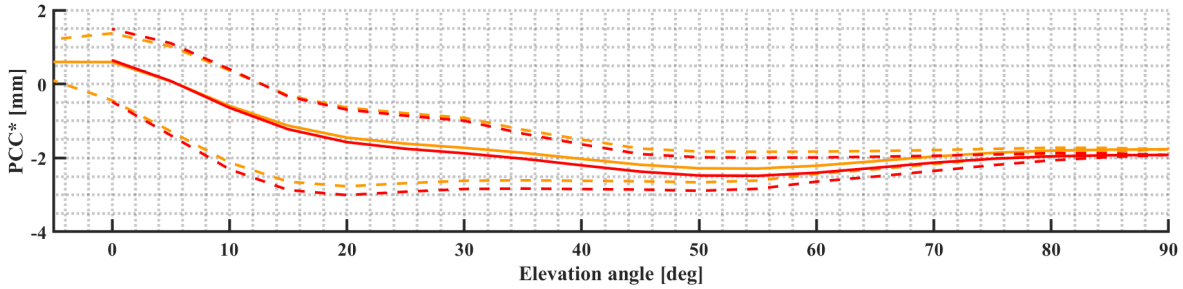


**Figure 4.12:** Illustration of averaged PCC* (see Equation 3.3) per elevation angle, where the individual components were separated using different methods as listed in Table 4.1, before computing PCC*. The orange-colored curve represents case O, which overlaps with cases M and N, while the reddish curve represents case R, overlapping all other cases. Dashed lines represent the minimum and maximum value per elevation angle bin.

First, it can be stated that the ΔPCC between all listed processings are within the range of calculation accuracy, as long as the HSH synthesis is carried out for the upper hemisphere (cases A-L and P-R). In these cases, any of the listed method can in general be used to extract PCO or $r$ components from PCC on a regular grid. This is visualized in Figure 4.12, where the PCC* for all cases are depicted. Since all parts of PCC are consistently considered, the reddish lines lie on top of each other for most of the cases (A-L and P-R). The orange-colored curve shows case O (which lies on top of case M and N). In these processings, PCC are estimated also for negative elevation angles.

The estimated PCO components as well as the constant part $r$ for all cases are shown in Figure 4.13. It can be clearly seen that differences between the methods are present, especially for the Up-component and the constant part. Here, differences up to 2.35 mm for the $\mathrm{PCO}_{\mathrm{Up}}$ (between H and Q) and 1.45 mm for $r$ exist. However, these differences occur because the respective components are considered without the corresponding PCV values. Consequently, they also differ between the different cases, which can be seen in Figure 4.14. It depicts the PCV for all cases, where differences up to almost 1.5 mm are detectable at low elevation angles between the individual cases.

To further evaluate the interaction between different PCC components, Table 4.2 presents the respective values, which are illustrated in Figures 4.13 and 4.14 for cases A-D and O, respectively. According to Equation 2.27, $\mathrm{PCO}_{\mathrm{Up}}$ is added with a negative sign, resulting in correction values of -1.92 mm for an elevation angle of 90°. However, as previously observed, case O (as well as cases M and N) shows a different value.

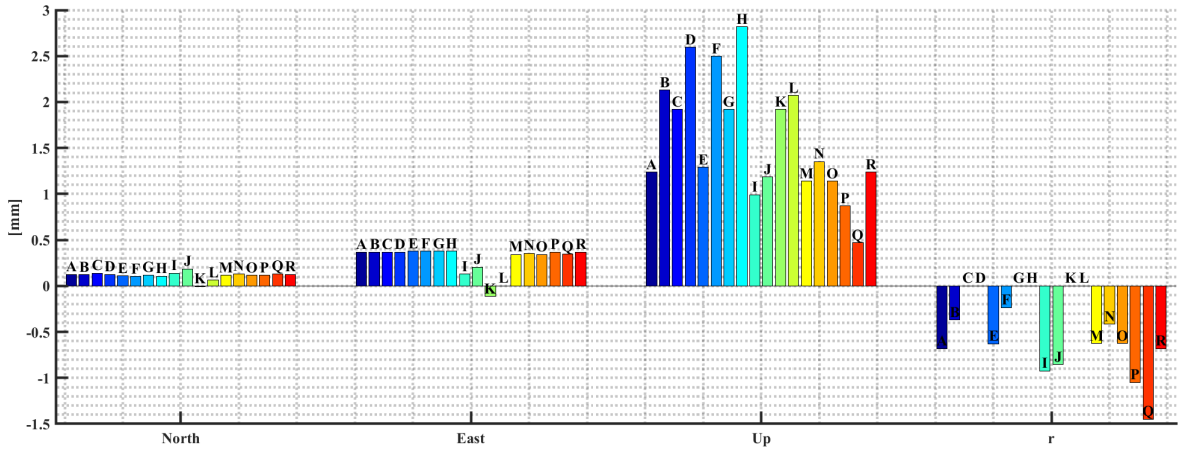


**Figure 4.13:** PCO and $r$ components extracted from PCC by different methods, see Table 4.1.

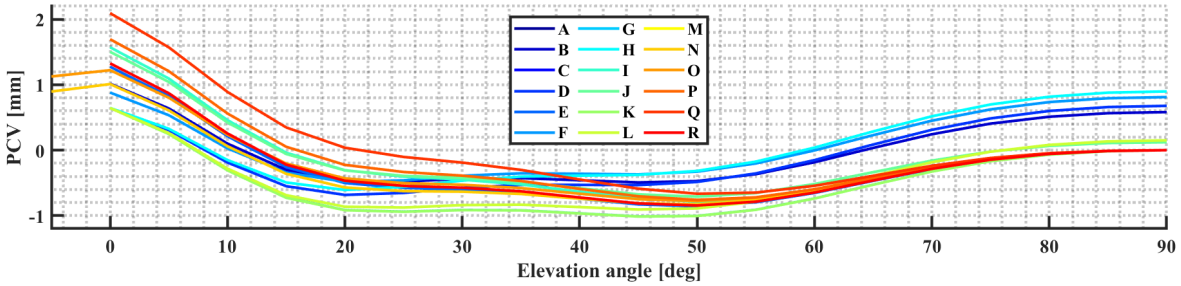


**Figure 4.14:** Pure PCV, separated from PCC using different methods, see Table 4.1. Here, averaged variations per elevation bin are depicted.

**Table 4.2:** PCC values at 90° elevation angle for selected cases, demonstrating different strategies for separating PCC into its individual components.

| ID | $\mathbf{PCO_{Up}}$ | r | $\mathbf{PCV}(el{=}\mathbf{90°})$ [mm] | $\mathbf{PCC}(el{=}\mathbf{90°})$ |
|---|---|---|---|---|
| A | 1.24 | -0.68 | 0.00 | -1.92 |
| B | 2.13 | -0.37 | 0.58 | -1.92 |
| C | 1.92 | 0.00 | 0.00 | -1.92 |
| D | 2.60 | 0.00 | 0.68 | -1.92 |
| O | 1.14 | -0.63 | 0.00 | -1.77 |

This study highlights the importance of consistently considering all components of PCC, namely PCO, PCV, and $r$. Analyzing only the PCO components of two different patterns may lead to misleading conclusions. However, when all components are correctly accounted for, the strategy used to determine PCO, PCV and $r$ from the gridded PCC does not have any significant impact on the PCC, as long as the upper hemisphere is considered.

## 4.4 Quality Analysis of Calibration Procedure

In this section, several analysis tools to assess the quality of the calibration procedure itself are presented. For some of them, the individual design matrices $\mathbf{A}_k$ and weighting matrices $\mathbf{P}_k$ are stored per satellite $k$ during the LSA.

### 4.4.1 Residuals and A Posteriori Variance Factor

The residuals $\mathbf{v}_k$ express how well the observations fit the functional model, and can be computed per satellite $k$ by use of the respective design matrices $\mathbf{A}_k$, the parameter vector $\hat{\mathbf{x}}$ and the observation vector $\mathbf{l}_k$.

$$\mathbf{v}_k = \mathbf{A}_k \cdot \hat{\mathbf{x}} - \mathbf{l}_k \tag{4.22}$$

In an ideal case, the residuals are normal-distributed with a standard deviation related to the observation noise, e.g. 4 mm in the case of ΔSD. Thus, higher residuals indicate unmodeled effects, i.e. the observations do not fit the functional model.

Using the weighting matrix $\mathbf{P}_k$ and the number of observations $n_k$ as well as unknowns $u$, the a posteriori variance factor $\hat{\sigma}_{0k}^2$ can be computed

$$\hat{\sigma}_{0,k}^2 = \frac{\mathbf{v}_k^{\mathrm{T}} \mathbf{P}_k \mathbf{v}_k}{n_l - u_{\hat{x}}}. \tag{4.23}$$

Since $n_k \gg u$, $\hat{\sigma}_{0k}^2$ is usually quite small per satellite $k$. If $\hat{\sigma}_{0k}^2$ is accumulated over all satellites, its value can be compared with the a priori variance factor $\sigma_0^2$. The ratio between $\hat{\sigma}_0^2$ and $\sigma_0^2$ should be approximately 1

$$\frac{\hat{\sigma}_0^2}{\sigma_0^2} \approx 1, \qquad \hat{\sigma}_0^2 = \Sigma_{k=1}^{k_{Max}} \hat{\sigma}_{0,k}^2 = \frac{\Sigma_{k=1}^{k_{Max}} \mathbf{v}_k^{\mathrm{T}} \mathbf{P}_k \mathbf{v}_k}{n_l - u_{\hat{x}}}. \tag{4.24}$$

If this is not the case, $\sigma_0^2$ should be appropriately adjusted in the stochastic model, see Equation 4.9. For instance, if the ratio is less than 1, it indicates that the variance of the observations was assumed too pessimistically, and thus the value for $\sigma_0^2$ can be reduced accordingly. However, this adjustment has no effect on $\hat{\mathbf{x}}$ but significantly impacts the Variance Covariance Matrix (VCM) of the estimated parameters $\mathbf{\Sigma}_{\hat{\mathbf{x}}\hat{\mathbf{x}}}$.

### 4.4.2 Formal Errors

The computation of the formal errors, i.e. the VCM $\mathbf{\Sigma}_{\mathrm{PCC}}$ of gridded PCC values, follows the law of error propagation. Using the notation of Balmino (2009), $\mathbf{\Sigma}_{\mathrm{PCC}}$ reads

$$\mathbf{\Sigma}_{\mathrm{PCC}} = \boldsymbol{Y}^{\mathrm{T}} \cdot \mathbf{\Sigma}_{\hat{\mathbf{x}}\hat{\mathbf{x}}} \cdot \boldsymbol{Y}. \tag{4.25}$$

Here, $\boldsymbol{Y}$ is set up following a HSH synthesis

$$\boldsymbol{Y} = \{\widetilde{P}_{mn}(k_1 \cos z^k + k_2)\cos(n\alpha);\ \widetilde{P}_{mn}(k_1 \cos z^k + k_2)\sin(n\alpha)\} \tag{4.26}$$

and is ordered the same way as the unknown vector $\hat{\mathbf{x}}$

$$\hat{\mathbf{x}} = \{a_{10}, a_{11}, ..., b_{11}, ..., b_{m_{\max},n_{\max}}\}. \tag{4.27}$$

$\mathbf{\Sigma}_{\hat{\mathbf{x}}\hat{\mathbf{x}}}$ indicates the cofactor matrix of the estimated coefficients and results from the multiplication of $\sigma_0^2$ and $\mathbf{Q}_{\hat{\mathbf{x}}\hat{\mathbf{x}}}$

$$\mathbf{\Sigma}_{\hat{\mathbf{x}}\hat{\mathbf{x}}} = \sigma_0^2 \cdot \mathbf{Q}_{\hat{\mathbf{x}}\hat{\mathbf{x}}} = \sigma_0^2 \cdot \bar{\boldsymbol{N}}^{-1}, \tag{4.28}$$

where the a priori variance factor $\sigma_0^2$ is set to the variance of the input dSD.

### 4.4.3 Condition Number of Normal Equation System

As briefly mentioned in Section 4.3, maintaining the condition number of $\bar{\boldsymbol{N}}$ within a moderate range, such as below $10^3$, is crucial for numerical stability during the inversion of $\bar{\boldsymbol{N}}$. The condition number is defined as the ratio of the maximum to minimum singular value of a matrix, which can be determined through Singular Value Decomposition (SVD).

If the condition number is high, the NES becomes unstable, meaning that small errors in the observation vector, and consequently in $\bar{\boldsymbol{N}}$ (refer to Equation 4.15), can critically affect the estimated unknowns. Therefore, it is important to properly stabilize the NES. Several methods for achieving this stabilization and their associated properties are discussed and analyzed in Section 6.3.

### 4.4.4 Closed-loop Simulation

To validate the developed PCC estimation algorithm, a closed-loop simulation can be performed. The overall procedure is shown in Figure 4.15. In this simulation, HSH $a$ and $b$

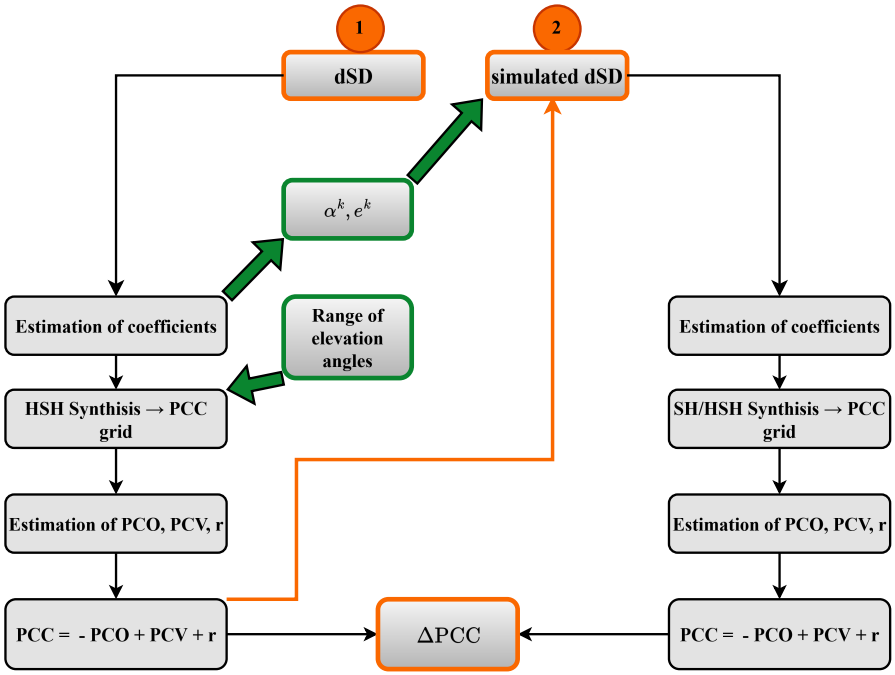


**Figure 4.15:** Flowchart illustrating the overall process of the closed-loop simulation process, detailing each major step of the methodology.

coefficients are estimated using real observation data and *standard* settings. Subsequently, a HSH synthesis is typically carried out to calculate the PCC on a grid, generally with elevation angles ranging from 0° to 90° and a resolution of 5°. From the gridded values, PCO, PCV and the constant part $r$ are estimated, and PCC are calculated and stored in the ANTEX file.

In the closed-loop simulation, these correction values are then imported from the ANTEX file. Simulated observations $\Delta\mathrm{SD}_{\mathrm{sim}}$ are calculated using the robot poses and satellite geometry from the initial calibration. Accordingly, the corrections are calculated on the Line-of-Sight (LOS) vectors for all visible satellites

$$\Delta\mathrm{SD}_{\mathrm{sim}}(t) = \left(-\mathrm{PCO}(t) \cdot \vec{e} + \mathrm{PCV}(t)\right) - \left(-\mathrm{PCO}(t+1) \cdot \vec{e} + \mathrm{PCV}(t+1)\right). \tag{4.29}$$

Several key factors significantly impact the closed-loop process. First, since the estimated PCC values are typically stored in the ANTEX file only for the upper hemisphere (with elevation angles from 0° to 90°), negative elevation angles are not included in the second step of the closed-loop simulation, resulting in unstable PCC estimations at low elevation angles. Additionally, valuable information is lost when PCC values are gridded with a resolution of 5°. Therefore, two recommendations should be followed:

- Store PCC in the ANTEX file with a higher resolution, e.g. 1°, and inclusion of negative elevation angles.
- Avoid applying any observation mask when using simulated observations to ensure that simulated dSD from satellites with negative elevation angles are correctly considered.

To visualize these recommendations, closed-loop simulations with different strategies are conducted. Table 4.3 lists these strategies and their properties. One strategy tested is using a correction value for a -5° elevation angle, even when it is not estimated, by either duplicating the value for 0° or mirroring the value at a 5° elevation angle. Additionally, a method is implemented to directly calculate PCC values by using the actual azimuth and elevation

**Table 4.3:** Strategies for conducting closed-loop simulations to validate the PCC estimation algorithm.

| ID | Elevation Angles | Resolution | Remark |
|---|---|---|---|
| (A) | 0°- 90° | 5° | **Commonly used format** |
| (B) | -5°- 90° | 5° | PCC($el$=0°) used for -5° |
| (C) | -5°- 90° | 5° | Mirrored PCC($el$=5°) used for -5° |
| (D) | -5°- 90° | 5° | PCC estimated down to -5° |
| (E) | -5°- 90° | 1° | PCC estimated down to -5° |
| (F) | - | - | Direct use of azimuth & elevation angles of visible satellites |

angles of visible satellites during the HSH synthesis instead of generating a regular grid. The corresponding modifications are highlighted in green in Figure 4.15.

Regardless of the method used for the closed-loop simulation, simulated observations are considered to estimate PCC using the same steps as the initial calibration run of the closed-loop simulation. Finally, PCC differences on the grid are calculated. If the ΔPCC values are smaller than 0.01 mm, this indicates a well working closed-loop, since PCC are stored with a precision of one-hundredth of a millimeter in the ANTEX file.

Figure 4.16 presents the results of different methods listed in Table 4.3 for GPS and Galileo L1 frequencies. Method (F) results in differences at the level of computational accuracy ($< 10^{-14}$ mm), indicating a perfectly working PCC estimation algorithm, and thus, its results are not shown in the figure.

For the other methods, the observed differences range from -0.15 mm to 0.35 mm, with the largest deviations occurring at low elevation angles. This is particularly evident when negative elevation angles are not included in the ANTEX file or the value for 0° is duplicated. In such cases, method (B) shows identical results to method (A), causing their lines to overlap. If PCC values for -5° elevation angles are included and the results are stored with a 5° resolution in the ANTEX file, as it is the case for (B) - (D), the ΔPCC values in the closed-loop simulation remain higher than the target accuracy. However, setting the resolution to 1° reduces ΔPCC to a maximum of ±0.02 mm. These differences result from rounding when writing values to the ANTEX file, so that it can be stated that method (E) also provides a well working closed-loop simulation.

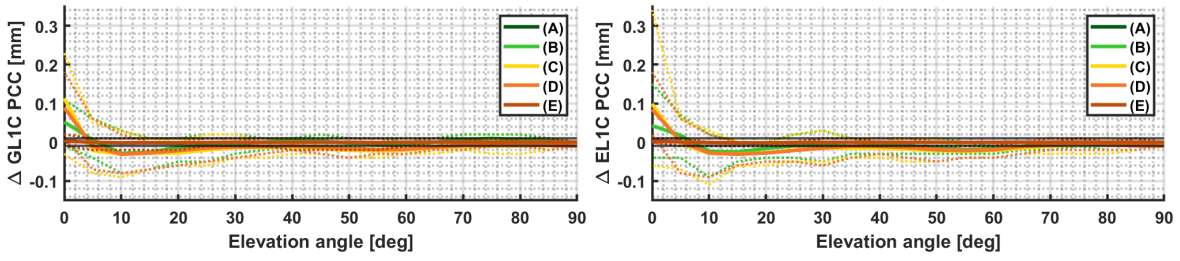


(a) GL1C (b) EL1C

**Figure 4.16:** Averaged ΔPCC values per elevation angle from closed-loop simulations using different strategies. Methods (A) and (B) produce identical results, causing their lines to overlap. Method (F) achieves ΔPCC values within the level of computational accuracy ($< 10^{-14}$ mm) and is therefore not shown. Black lines denote the target accuracy of 0.02 mm.

### 4.4.5 Comparison with External Data

To evaluate the quality of the calibration procedure, it is worthwhile to compare the estimated PCC with external data. Since no ground truth exists, the estimated PCC can be compared with calibration results from other facilities. This is applicable as long as the identical AUT, or at least the same antenna type (but with a different serial number), has already been calibrated in the same configuration, such as with the same ground plate or radome.

In general, the type-mean calibration values published by the IGS in the ANTEX file can be used to carry out the comparison. However, it should be kept in mind that differences between type-mean calibrations and individual calibrations exist, typically ranging from a few millimeters up to a few centimeters, depending on the antenna type and the analyzed frequency or LC (Kersten et al., 2024c; Dawidowicz and Bakuła, 2024). Therefore, possible differences are not only due to variations in the calibration process itself but also due to inherent differences between type-mean and individual calibrations.

Kröger et al. (2024) present possible approaches for selection criteria based on which PCC values from different calibration facilities could be included in the IGS ANTEX file. The presented selection criteria can be used as a benchmark to validate the developed PCC estimation algorithm. The authors state that the impact of $\Delta$PCC on topocentric 3D positions should not exceed a certain threshold. One suggested threshold is 4 mm, which is linked to the expected accuracy for PPP and DD processing. The impact can be assessed by computing $\Delta$PCC with respect to IGS type-mean values and transferring these differences to the position domain, e.g., by using the developed simulation approach introduced in Section 3.3.2. In this context, formal errors, the repeatability of individual calibrations, as well as subdaily variations, need to be considered.

In order to compare estimated PCC with external data, while isolating differences between type-mean and individual calibrations, identical antennas can be calibrated at different calibration institutions. This is exemplified by the global collaboration called *RingCalVal*, involving nine different institutions, as reported in Kersten et al. (2024a,b,c).

# 5

# Estimated Phase Center Corrections

In this section, estimated PCC as well as the quality of the calibration process itself are presented for three different antenna types, see Figure 5.1:

1. **Geodetic pinwheel antenna:** *NOV703GGG.R2 NONE* (#12400040), in the following named `NOV`
2. **Geodetic 3D choke ring antenna:** *LEIAR25.R3 NONE* (#09330001), in the following named `LEI`
3. **Mass-market antenna:** *ANN-MB1 NONE* (#2133-1) mounted on a ground plate, in the following named `UBX`.

For each individual calibration, identical setup and processing parameters have been used. *Septentrio PolaRx5TR* receivers are used to log the raw 1 Hz GNSS data. Besides, the processing steps described in Section 4.2.1 – 4.3 are used. A summary of those is also provided at the beginning of Chapter 6. It should be kept in mind that different satellite geometries and robot poses are present for the different, individual calibrations. Thus, it is not possible to draw direct conclusions about the residuals or standard deviations between different calibrations of different AUTs.



(a) `NOV` (b) `LEI` (c) `UBX`

**Figure 5.1:** Different AUTs mounted on robot. Note that for antenna `UBX` a slightly smaller ground plate has been used for the calibrations presented here.

Section 5.1 presents the estimated PCC and evaluates their quality, while Section 5.2 compares the estimated PCC from different AUT. Section 5.3 documents the repeatability of individual calibrations for the identical NOV antenna. These analyses are followed by investigations of the used receivers (Section 5.4) and evaluations of differences between identical frequencies from different GNSS (Section 5.5), again exemplarily for antenna NOV. The chapter concludes with a comparison of the estimated NOV PCC to external data, specifically publicly available type-mean calibration values.

## 5.1 Estimated PCC of Individual Calibrations

Figure 5.2 illustrates the estimated GL1C PCC for the three antennas using stereographic projections. It is evident that the NOV and LEI antennas have values that strongly depend on the elevation angle. Any further variations are not immediately apparent, which is attributed to large $PCO_{Up}$ components. For the NOV antenna, the $PCO_{Up}$ ranges from 55 mm to 60 mm across all frequencies. Since PCO components are subtracted in the PCC calculation (as noted in Equation 2.2.1), the PCC vary from -61 mm to 5 mm for all frequencies.

For the LEI antenna, the PCC values across all frequencies range from -161 mm to 10 mm, with $PCO_{Up}$ values between 152 mm and 160 mm. In contrast, the UBX antenna displays variations that do not solely depend on elevation angle. The PCC for UBX across all frequencies spans from -2.2 mm to 24 mm.

To effectively present smaller variations, the subsequent analyzes show the estimated PCC for the different antennas and frequencies as PCC*. This means that, following Equation 3.3, a common $PCO_{Up}$ for all frequencies per antenna is subtracted.

In the following, a brief assessment of PCC* for NOV, LEI and UBX along with the quality analyzes of the calibrations is carried out. This includes the analysis of residuals in the topocentric and antenna frame, the analysis of the a posteriori variance factor as well as the formal errors of the gridded PCC. The section closes with a short comparison of the quality parameters of the estimated PCC for the three antennas.

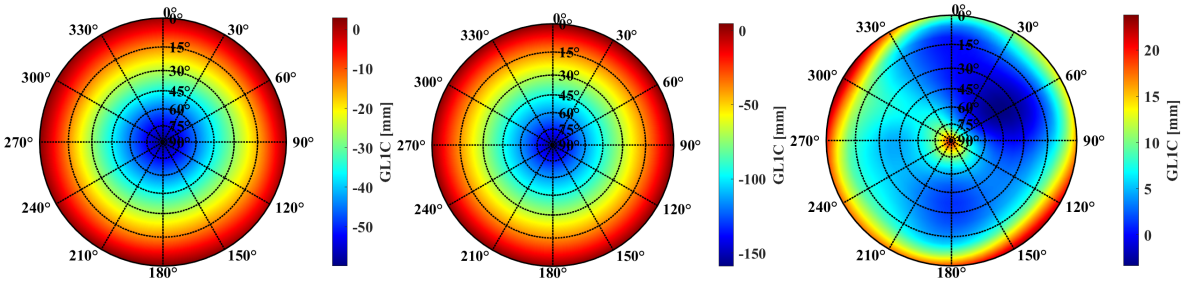


(a) NOV PCC (b) LEI PCC (c) UBX PCC

**Figure 5.2:** Estimated GL1C PCC for antennas NOV, LEI and UBX. Note the different scales for the colorbars.

### Estimated NOV PCC

Figure 5.3 presents the estimated NOV PCC* for four selected GPS and Galileo frequencies using stereographic projections. To highlight the azimuth-dependent variations, a common $PCO_{Up}$ value of $PCO_{Up}$ $\overline{d} = 58.27$ mm is subtracted independently for each frequency. This value corresponds to $d_{const}$, the a priori $PCO_{Up}$ chosen and subtracted before the calibration

process, as illustrated in Figure 4.2. For further PCC* results, the reader is referred to the annex, where in Figure A.1 the PCC* for GPS, in Figure A.2 for Galileo, in Figure A.3 for GLONASS and in Figure A.4 for BeiDou frequencies are presented.

Depending on the frequency, the PCC* variations in Figure 5.3 are in a range of -2 mm to 5 mm. Although the scale of the color-coded PCC* differs for the depicted frequencies (so that small details are visible), a highly similar behavior of the L1 frequencies (GL1C, EL1C) and L5 frequencies (GL5Q, EL5Q), respectively, can be observed. Since PCC are frequency-dependent, as stated in Section 2.2.1, this is expected. A more detailed analysis of $\Delta$PCC between same frequencies from different GNSS is carried out in Section 5.5. For the depicted L1 frequencies, PCC* show positive correction values at low elevation angles and negative values in east-west direction. For the L5 frequencies, a distinct north-south slope is observed. As indicated in Figure 3.2(a), this indicates a larger $\mathrm{PCO}_{\mathrm{North}}$. Specifically, the $\mathrm{PCO}_{\mathrm{North}}$ values for GL5Q and EL5Q are -1.7 mm and -1.6 mm, respectively, whereas for the L1 frequencies, they are less than 0.2 mm.

Figure 5.4(a) depicts PCC* results as mean values per elevation angles for various GPS and Galileo frequencies. PCC* results for GLONASS and BeiDou are illustrated in Figure 5.4(b). In general, a broad number of signals show a comparable behavior: a sharp decline is present in values between 0° and 10° elevation angles, followed by an increase in PCC* up to a 25° elevation angle. Subsequently, there is a slight drop in values until reaching a 40° elevation angle, with little variation observed up to 90° elevation angle. However, some frequencies

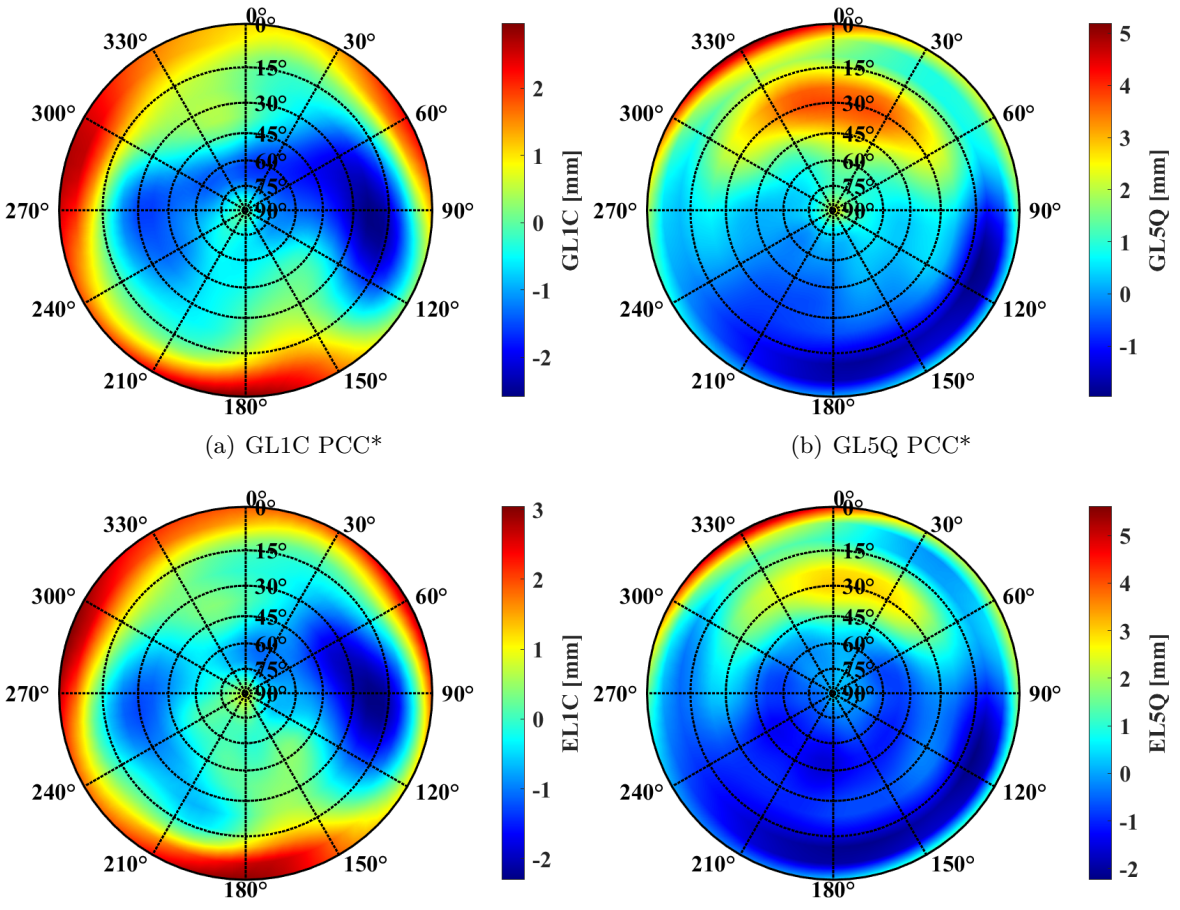


(a) GL1C PCC*

(b) GL5Q PCC*

(c) EL1C PCC*

(d) EL5Q PCC*

**Figure 5.3:** Estimated NOV PCC* for selected GPS and Galileo frequencies. Note the different scales for the color-coded PCC*.

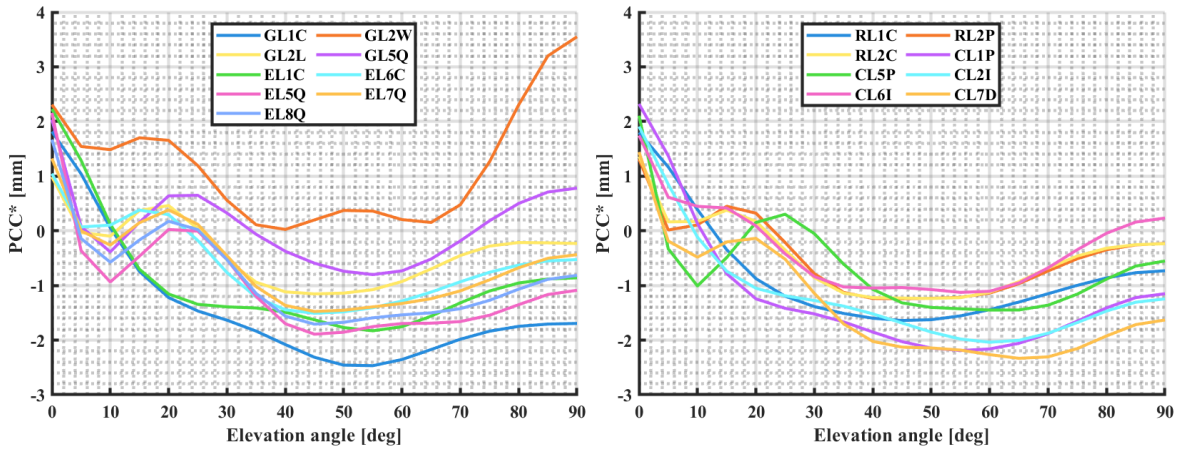


(a) GPS and Galileo PCC* (b) GLONASS and BeiDou PCC*

**Figure 5.4:** Estimated NOV PCC* for various frequencies and systems, represented as mean values per elevation angle.

have another behavior. On the one hand, corrections values for GL2W are larger than those of all other frequencies. On the other hand, certain frequencies (GL2L, RL1C, EL5Q, CL1P, CL7D) show another cluster, i.e. comparable behavior. They show a decrease between 0° and 20° elevation angle, followed by constant variations up to 90° elevation angle.

The clustering of PCC* behavior is primarily due to identical frequencies and, to some extent, frequencies that are close to each other from different signals across various GNSS. This is analyzed in detail in Section 5.5.

Due to the use of FDMA for uniquely assigning GLONASS satellites, it is important to note that the resulting PCC and PCC* are not specifically provided for the center frequency (e.g., 1602 MHz for RL1C, see Section 2.1.2). Instead, they represent an average of the frequencies of the satellites contributing to the PCC estimation. In this context, it should be noted that two GLONASS satellites share the same frequency. As of January 2025, the GLONASS constellation consists of 24 satellites arranged across three orbital planes, with each plane containing 8 satellites, and 2 satellites within each plane sharing the same frequency channel, as detailed in Table 5.1 (GLONASS.IAC, 2025).

Figure 5.5(a) depicts the number of observations contributing to the PCC estimation of RL1C, RL2P and RL2C signals. Apart from a few exceptions, the observation number from the different satellites is equal for the different signals. The maximum difference is six observations in the case of slot number 19.

Figure 5.5(b) shows the differences of the respective resulting wavelengths $\lambda$ w.r.t. the nomi-

**Table 5.1:** Assigned GLONASS frequency channels (Freq. Ch.) to individual satellites (slot number), based on GLONASS.IAC (2025).

| **Orbital Plane 1** | | **Orbital Plane 2** | | **Orbital Plane 3** | |
|---|---|---|---|---|---|
| Slot Nr. | Freq. Ch. | Slot Nr. | Freq. Ch. | Slot Nr. | Freq. Ch. |
| 01 & 05 | 1 | 9 & 13 | -2 | 17 & 21 | 4 |
| 02 & 06 | -4 | 10 & 14 | -7 | 18 & 22 | -3 |
| 03 & 07 | 5 | 11 & 15 | 0 | 19 & 23 | 3 |
| 04 & 08 | 6 | 12 & 16 | -1 | 20 & 24 | 2 |

nal *center* wavelength. The differences lie in a range between $-1.1{\cdot}10^{-3}$ mm to $-0.8 \cdot 10^{-3}$ mm. Since the *nominal* wavelength differences for GLONASS satellites, when taking the individual frequency channels into account, are in a range of 0.0652 mm to 0.0660 mm, these differences are acceptable. Thus, it can be stated that the estimated PCC reflect the frequency-dependent PCC for the respective GLONASS *center* frequencies.

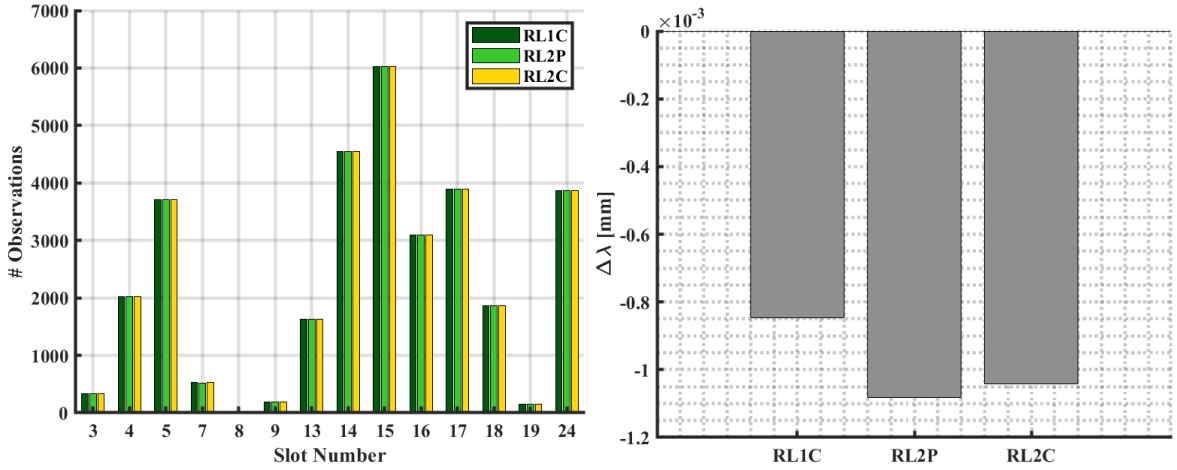


(a) Number of observations per GLONASS satellite and signal

(b) Differences between GLONASS *center* wavelengths and resulting wavelengths

**Figure 5.5:** Analysis of estimated NOV PCC for GLONASS frequencies.

### Quality Assessment of Estimated NOV PCC

In order to assess the quality of the estimated NOV pattern, the metrics introduced in Section 4.4 are used. In the following, the assessment is exemplarily carried out for GL1C, GL2W and EL1C.

Figure 5.6 depicts the GL1C residuals. Overall, the residuals are in a range of ±1 cm with some higher deviations up to ±1.3 cm. If the residual w.r.t the elevation angle in the topocentric frame are analyzed in Figure 5.6(b) it can be seen that they show a smooth behavior within ±6 mm for elevation angles larger than 50°. When analyzing the residuals in the stereographic projection shown in Figure 5.6(c), no unexpected characteristics are observed. As expected, the highest residuals occur at low elevation angles. A cluster of higher residuals is visible only at an azimuth of approximately 240°, likely due to one short satellite arc.

Figure 5.6(d) shows the residuals in a stereographic projection in the antenna frame. Generally, higher residuals appear at lower elevation angles, suggesting a correlation with the antenna's gain pattern (see Figure 2.3). The assumption is that lower gain corresponds to higher residuals.

Figure 5.7 shows the residuals of GL2W. It is apparent that these residuals are significantly larger than those of GL1C, with values exceeding ±3 cm. Notably, unlike GL1C, the residuals remain high across all elevation angles in both topocentric and antenna frames. This implies that the receiver settings used may not have been ideal for tracking GL2W. This conclusion is further supported by the analysis of GL2L residuals, shown in Figure 5.8, which exhibit behavior similar to GL1C, indicating no frequency-dependent issues.

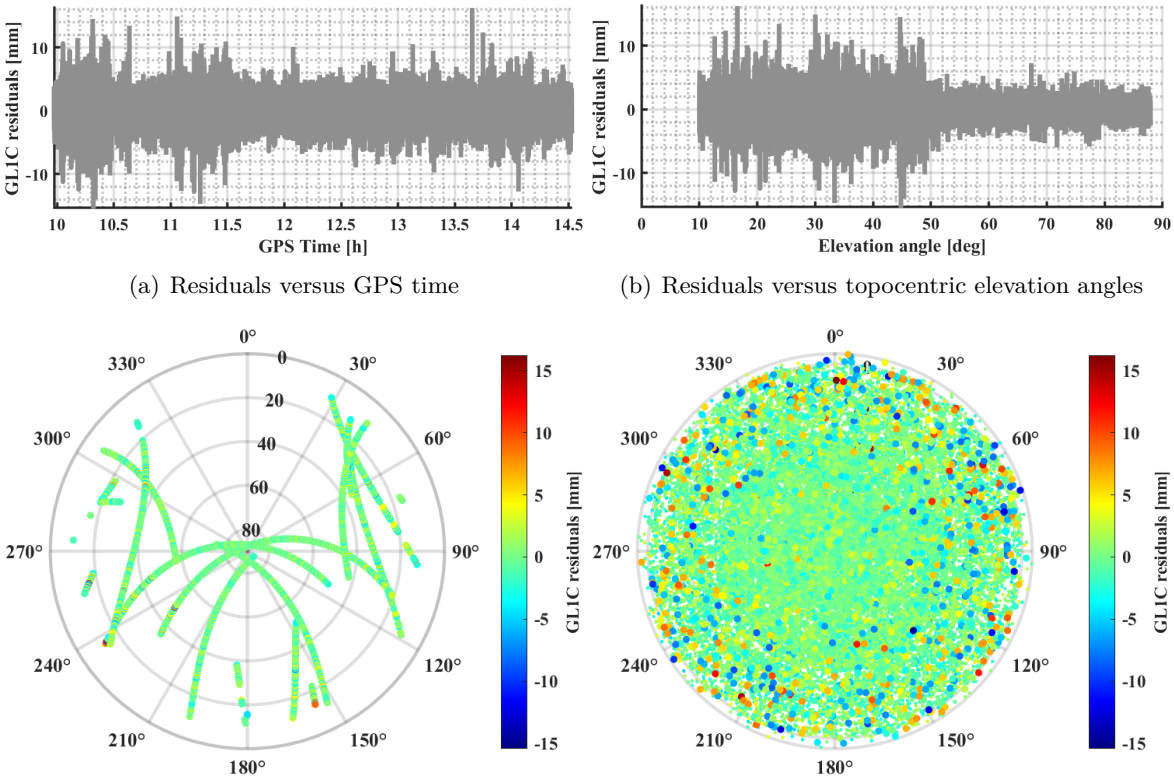


(a) Residuals versus GPS time

(b) Residuals versus topocentric elevation angles

(c) Stereographic projection in topocentric frame

(d) Stereographic projection in antenna frame

**Figure 5.6:** Residuals of estimated NOV GL1C PCC.

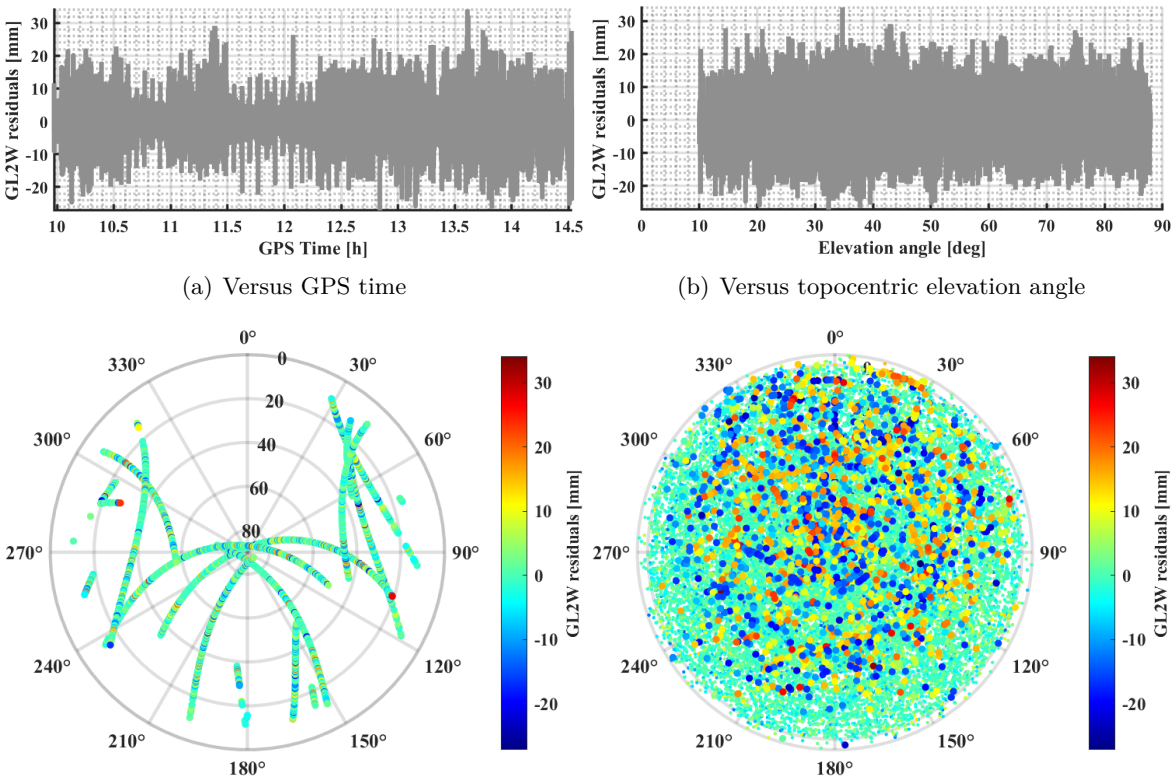


(a) Versus GPS time

(b) Versus topocentric elevation angle

(c) Stereographic projection in topocentric frame

(d) Stereographic projection in antenna frame

**Figure 5.7:** Residuals of estimated NOV GL2W PCC.

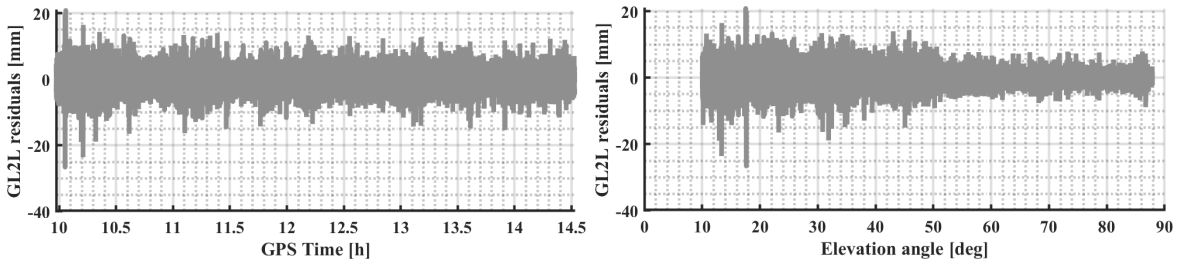


(a) Residuals versus GPS time (b) Residuals versus topocentric elevation angles

**Figure 5.8:** Residuals of estimated NOV GL2L PCC.

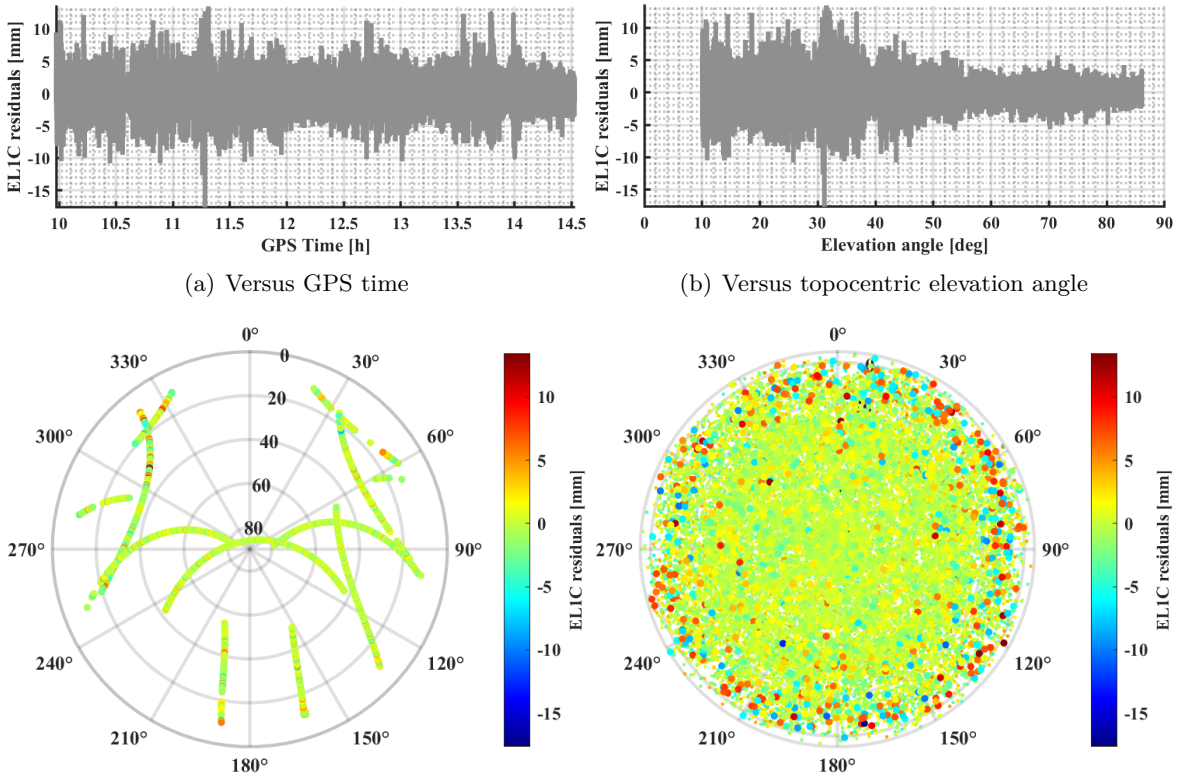


(a) Versus GPS time (b) Versus topocentric elevation angle

(c) Stereographic projection in topocentric frame (d) Stereographic projection in antenna frame

**Figure 5.9:** Residuals of estimated NOV EL1C PCC.

Figure 5.9 illustrates the residuals for EL1C. Overall, they exhibit a very smooth pattern, mostly within a range of ±1.2 cm, with some deviations reaching up to 1.8 cm. A slight correlation with elevation angles can also be observed. In general, the EL1C residuals are comparable to those of GL1C and GL2L.

The conclusions mentioned earlier are also supported by the a posteriori variance factor of the estimated PCC, as shown in Figure 5.10(a). While most $\hat{\sigma}_{\hat{0}}^2$ values range from 2.5 mm$^2$ to 7.5 mm$^2$, the value for GL2W is significantly higher at 27.5 mm$^2$. This metric can therefore be used to evaluate the overall quality of the estimated PCC.

Figure 5.10(b) presents all residuals in a cumulative histogram along with the standard normal distribution N(0,1). For a direct comparison across all frequencies, the residuals are not normalized with respect to $\sigma_0^2$; instead, they are provided in the figure legend. It is evident that GL2W generally shows the largest residuals, as indicated by the flattest curve for this

frequency. However, the maximum residual is observed for the turquoise-colored frequency RL1C, where two large peaks from different PRNs exceed the 4 cm level.

Figure 5.11 illustrates the standard deviations $\sigma$ of the estimated NOV PCC. The average value for each elevation bin across all azimuth angles is shown with solid lines, while dashed lines represent the minimum and maximum $\sigma$ for each bin. It is evident that there is minimal variation over the azimuthal range. To calculate $\sigma$, the relevant values of $Q_{\hat{x}\hat{x}}$ are multiplied by the variance of the input dSD $\sigma_0^2$. Consequently, the standard deviation for GL2W is the highest. The other frequencies exhibit similar behavior, with higher $\sigma$ at low and high elevation angles due to the reduced number of available observations, as depicted in Figure 4.10. Overall, the standard deviations range from 0.05 mm to 0.35 mm, indicating a precise PCC estimation.

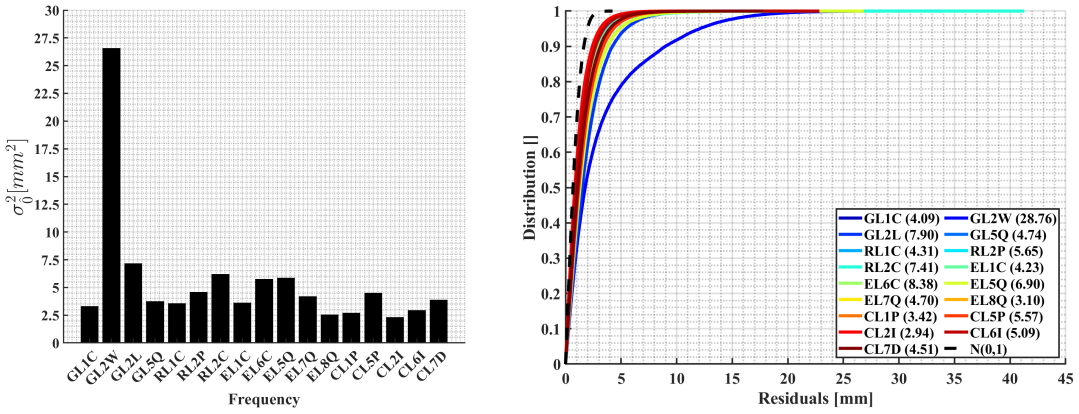


(a) A posteriori variance factor $\hat{\sigma}_0^2$ (b) Unnormalized residuals

**Figure 5.10:** Quality metrics of estimated NOV PCC.

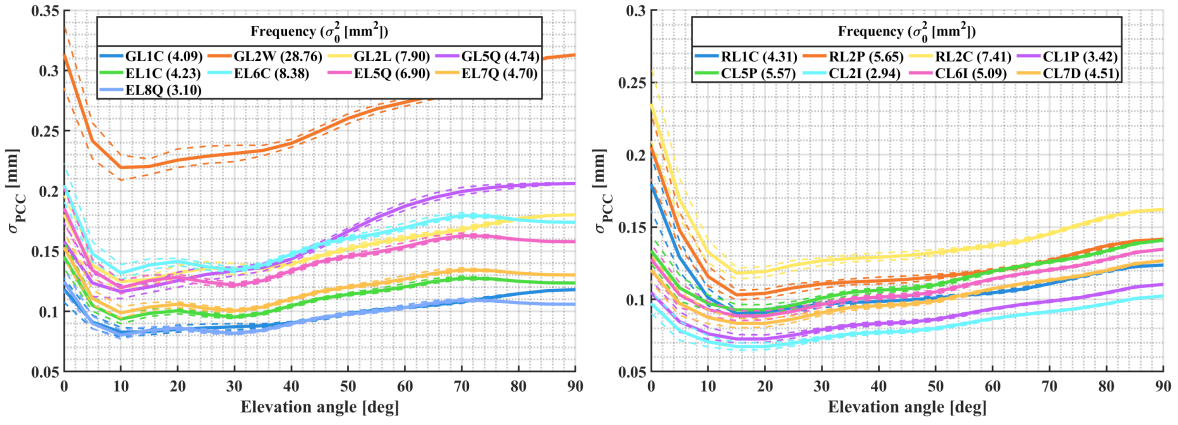


(a) GPS and Galileo frequencies (b) GLONASS and BeiDou frequencies

**Figure 5.11:** Averaged formal errors per 5° elevation angle for estimated NOV PCC. Note the different y-axes scales.

## Estimated LEI PCC

This subsection provides the estimated LEI PCC*, with $\overline{d}$ =160.19 mm subtracted from all frequencies. Figure 5.12 displays the PCC* exemplarily for selected GPS and Galileo frequencies. For further results, the reader is referred to the annex, where in Figure A.5 the PCC*

for GPS, in Figure A.6 for Galileo, in Figure A.7 for GLONASS and in Figure A.8 for BeiDou frequencies are presented.

The similarity between identical frequencies from different GNSS systems is noticeable. For GL1C and EL1C, positive PCC values of approximately 1.5 mm are observed at high elevation angles, transitioning to negative values of approximately -3.5 mm at mid-elevation angles. In contrast, GL5Q and EL5Q exhibit PCC values of around -6 mm at high elevation angles, which gradually decrease to about 1 mm at an elevation of 15°, before increasing to approximately 8 mm near the horizon.

Compared to NOV, there are fewer recognizable variations across azimuth angles. This may suggest that larger $PCO_{Up}$ components remain in the PCC. Due to its overall large magnitude, significant $PCO_{Up}$ differences occur between the individual frequencies. However, since a common value of $\overline{d} = 160.19$ mm was subtracted from all frequencies, larger $PCO_{Up}$ components persist in the PCC.

Figure 5.13 illustrates the LEI PCC as a function of elevation angles across all estimated frequencies. Two main clusters are apparent. The frequencies of the upper L-Band, i.e. GL1C, EL1C, RL1C, CL2I and CL1P, present wave-shaped PCC* with minimal absolute values at 90° elevation angle. All other frequencies exhibit a different behavior, where positive correction values are present at the horizon and in zenith direction and negative values around 30° and 40° elevation angles. This already shows clearly the frequency-dependent characteristic of PCC.

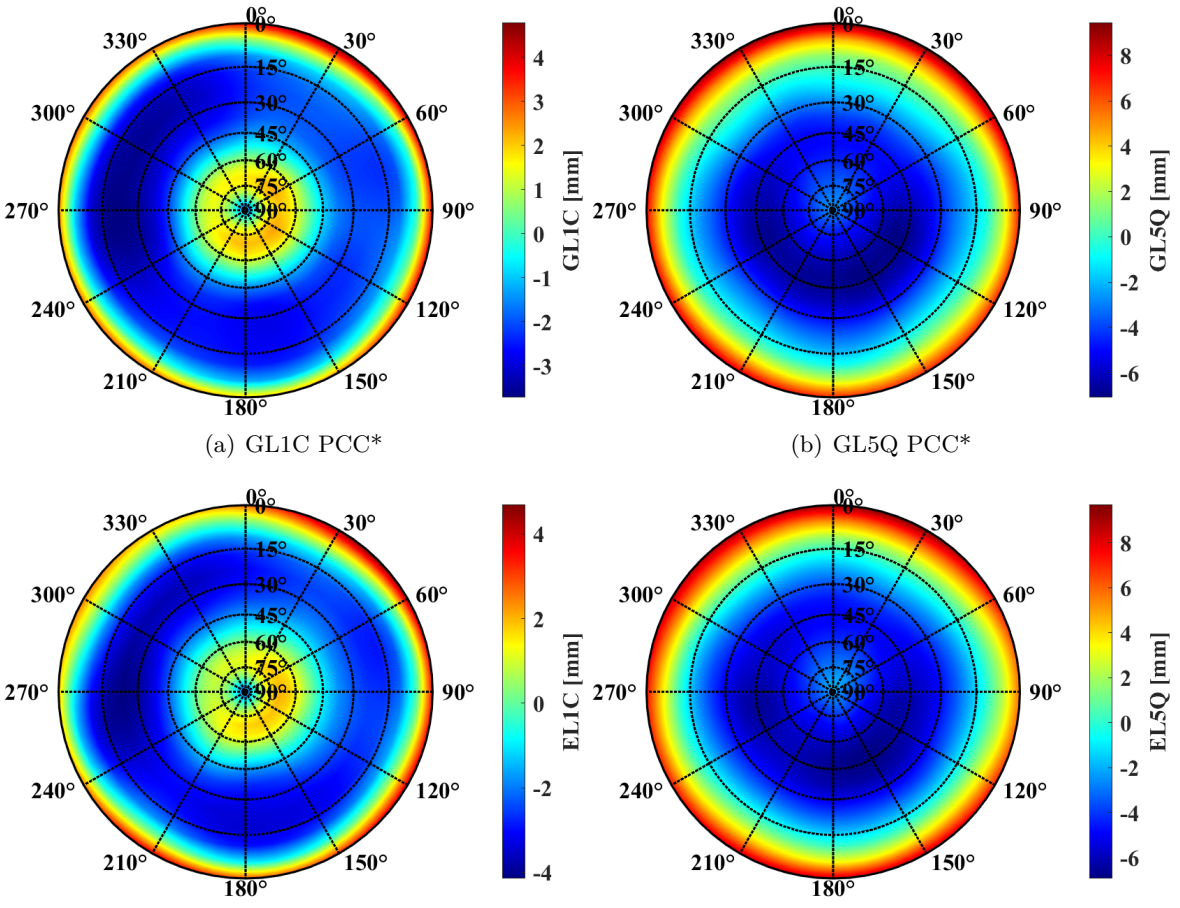


(a) GL1C PCC*

(b) GL5Q PCC*

(c) EL1C PCC*

(d) EL5Q PCC*

**Figure 5.12:** Estimated LEI PCC* for selected GPS and Galileo frequencies. Note the different scales for the color-coded PCC*.

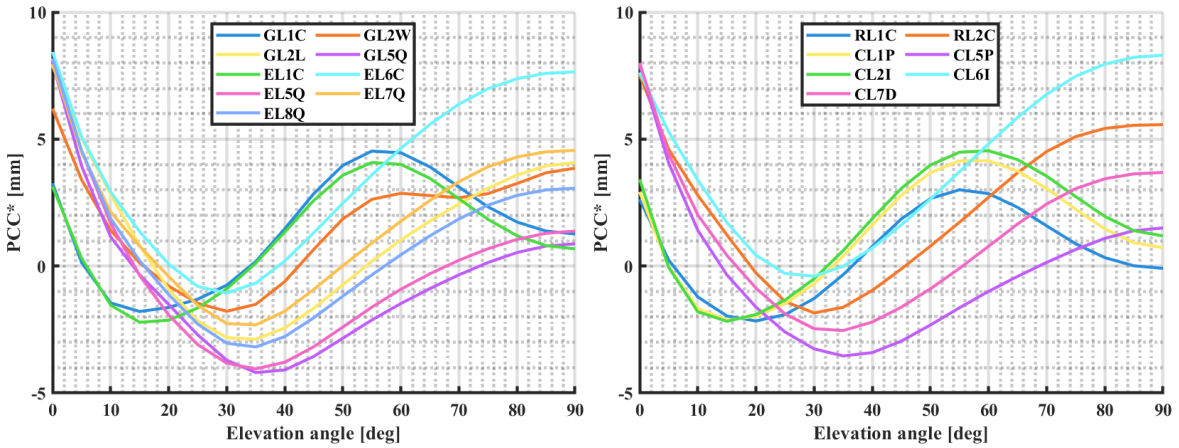


(a) GPS and Galileo PCC* (b) GLONASS and BeiDou PCC*

**Figure 5.13:** Estimated LEI PCC* for various frequencies and systems, represented as mean values per elevation angle.

## Quality Assessment of Estimated LEI PCC

Since the quality assessment of the estimated LEI PCC generally leads to the same conclusions as for the NOV antenna, only the residuals for GL1C are presented here. The results for GL2W and EL1C can be found in the appendix in Figure B.1 and Figure B.2, respectively.

Figure 5.14 presents the GL1C residuals. The data generally demonstrates a smooth pattern

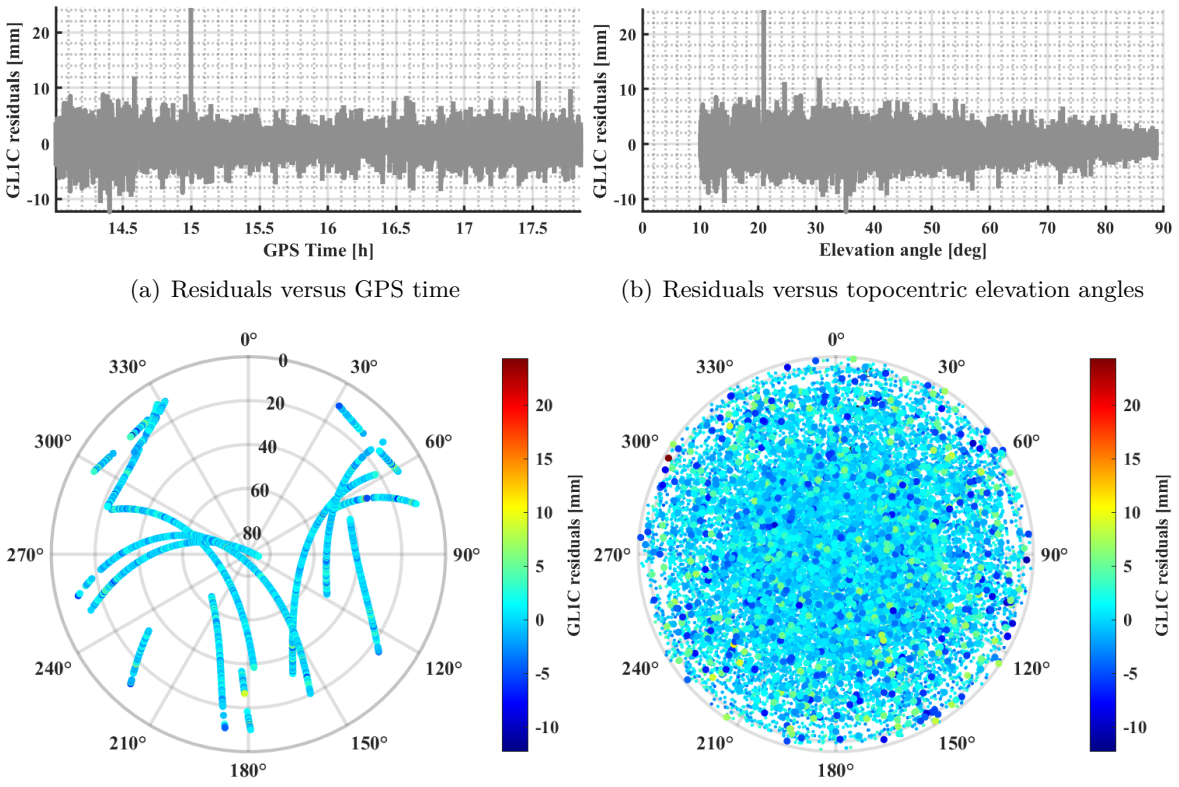


(a) Residuals versus GPS time (b) Residuals versus topocentric elevation angles

(c) Stereographic projection in topocentric frame (d) Stereographic projection in antenna frame

**Figure 5.14:** Residuals of estimated LEI GL1C PCC.

with a notable exception at 15 h GPS time, where the residual reaches 2.4 cm. Overall, the residuals lie within a ±1 cm range. However, a comparison of the residuals in the antenna frame using the stereographic projection, shown in Figure 5.14(d), to those of the NOV-antenna, illustrated in Figure 5.6(d), reveals that unlike NOV, the LEI residuals do not exhibit a clear correlation with the elevation angle in the antenna frame.

Figure 5.15(a) depicts the a posteriori variance factors. The large GL2W residuals are reflected by $\hat{\sigma}_0^2$. Overall, the results align closely with those obtained for NOV. This similarity is also evident in Figure 5.15(b), which displays the residuals in a cumulative histogram. It is important to note that the residuals are not normalized by $\hat{\sigma}_0^2$, allowing for the detection of different noise levels. Figure 5.16 shows the formal errors. Similar behavior to NOV can be observed, although the formal errors are slightly larger for LEI. Notably, for GLONASS and BeiDou frequencies, larger values are apparent at both low and high elevation angles. This is linked to the number of available observations within specific elevation angle bins. Additionally, the maximum tilting angle during data acquisition had to be set lower for LEI compared to NOV due to the antenna height, as discussed in Section 4.2.1. This adjustment can result in fewer available observations in certain elevation angle bins.

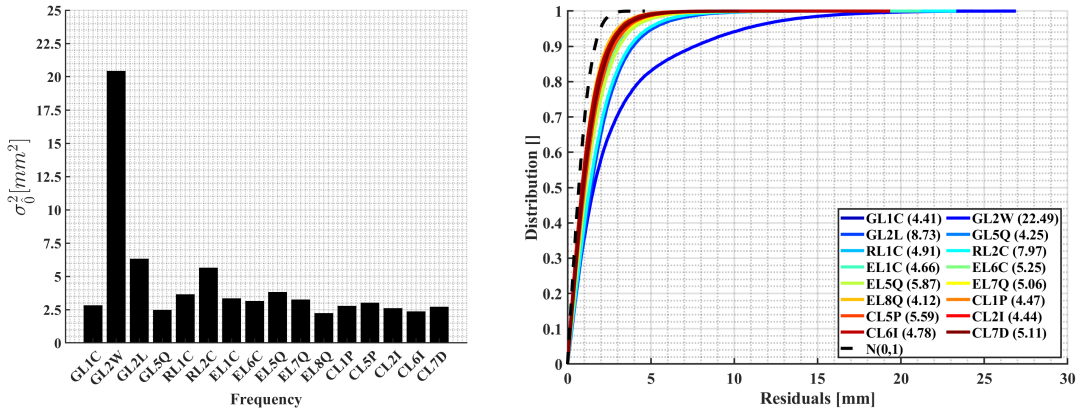


(a) A posteriori variance factor $\hat{\sigma}_0^2$ (b) Unnormalized residuals

**Figure 5.15:** Quality metrics of estimated LEI PCC.

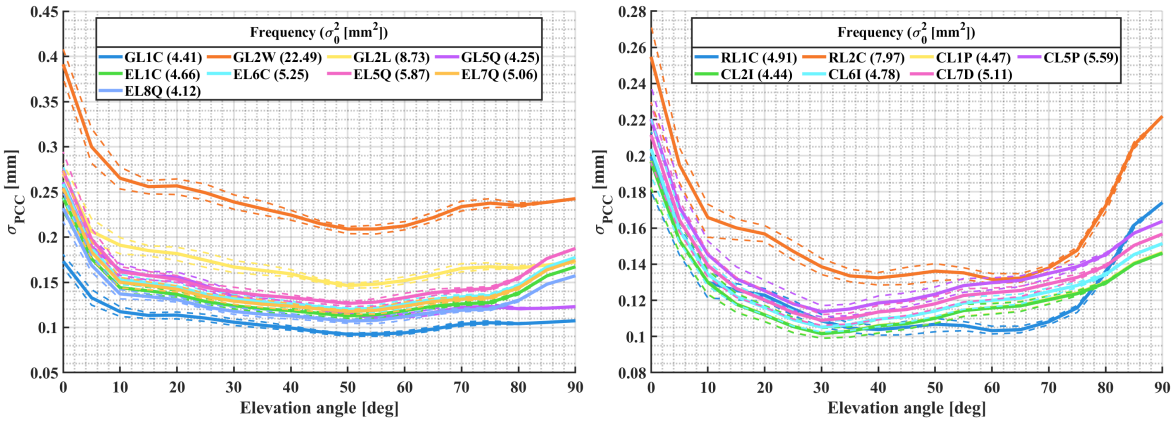


(a) GPS and Galileo frequencies (b) GLONASS and BeiDou frequencies

**Figure 5.16:** Averaged formal errors per 5° elevation angle for LEI PCC. Note the different y-axes scales.

### Estimated UBX PCC

Figure 5.17 shows the UBX PCC results for selected GPS and Galileo frequencies. Additional results can be found in the annex, specifically in Figure A.9 and Figure A.10. This antenna displays noticeable azimuthal variations, even without subtracting a common $PCO_{Up}$ component. For GL1C and EL1C frequencies, an almost uniform pattern across the azimuthal angles is observed. In contrast, for GL5Q and EL5Q frequencies, a northeast-southwest slope is visible. Overall, the full PCC range from approximately -5 mm to 25 mm, which is significantly smaller than those observed for NOV and LEI. This difference can be linked to the dimensions of the antennas, as illustrated in Figure 5.1.

Additionally, it is remarkable that the resulting $PCO_{Up}$ value for UBX is negative for all signals. Unlike NOV and LEI, the value at a 90° elevation angle is positive, a phenomenon likely generated by the used ground plate. Figure 5.18 displays the averaged PCC per 5° elevation angle for GPS and Galileo frequencies. It is clear that all observations from the L1-band (GL1C, EL1C, GL1L) as well as from the L5 band (GL5Q, EL5Q) exhibit highly similar behavior. It should be noted that this mass-market antenna is only capable to process frequencies from the L1 and L5 band.

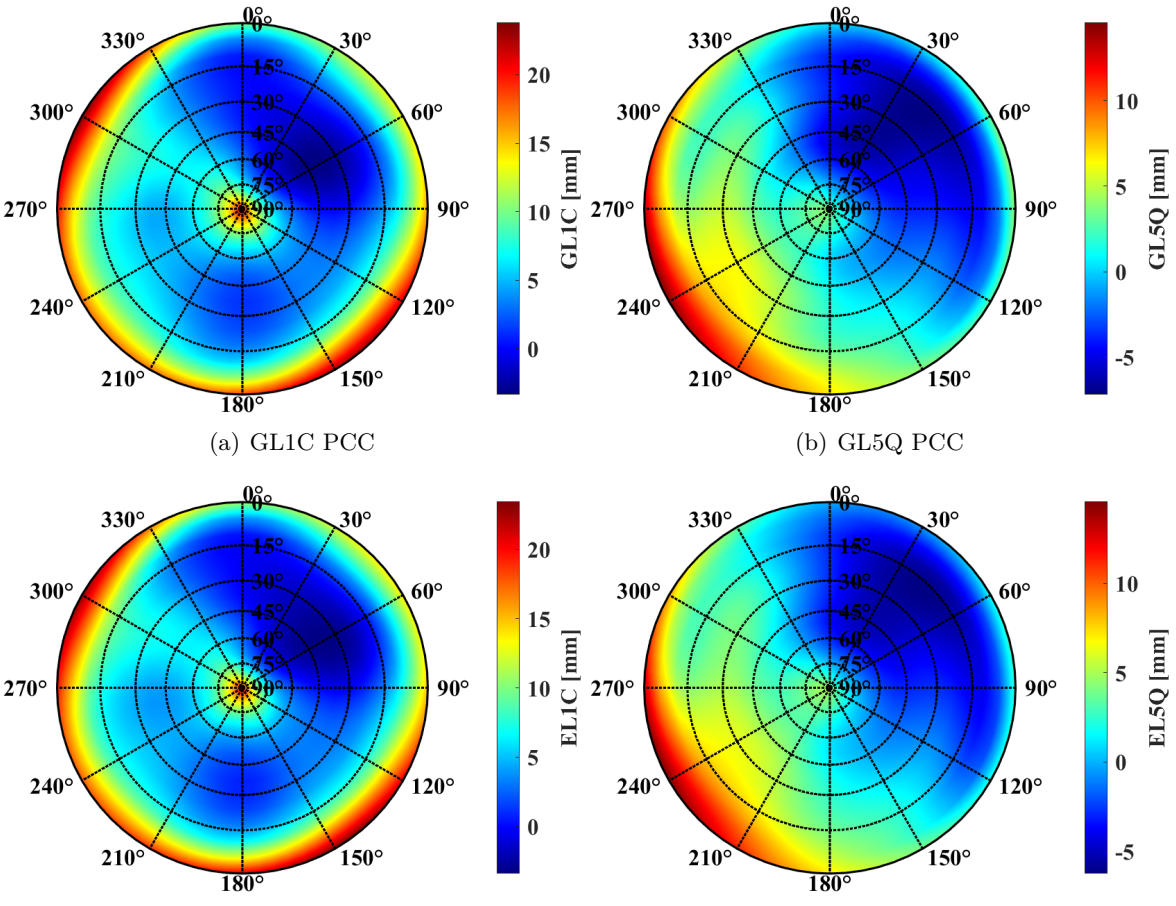


(a) GL1C PCC (b) GL5Q PCC

(c) EL1C PCC (d) EL5Q PCC

**Figure 5.17:** Estimated UBX PCC for selected GPS and Galileo frequencies.

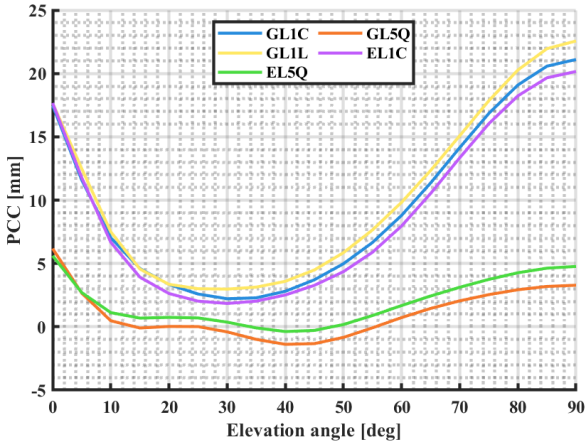


**Figure 5.18:** Estimated UBX PCC for GPS and Galileo frequencies represented as mean values per elevation angle.

### Quality Assessment of Estimated UBX PCC

Figure 5.19 shows exemplarily the GL1C residuals of estimated UBX PCC. For EL1C, the respective residuals can be found in the annex in Figure B.3. The residuals exhibit a higher magnitude compared to those of NOV and LEI, with a larger amount of high peaks. The residuals reach up to ±5 cm in magnitude, showing a slight elevation-dependent behavior. Notably, higher residuals also appear at mid-elevation angles, specifically between 40° and 50°. In Figure 5.19(d), which shows the residuals in the antenna frame using a stereographic projection, it is clear that the highest residuals occur at low elevation angles.

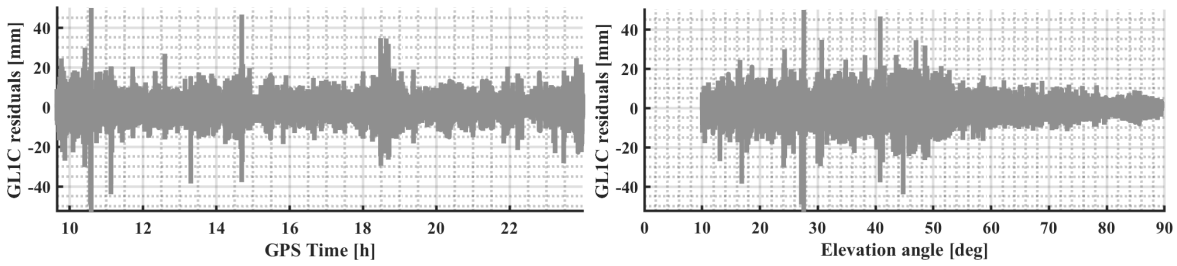


(a) Residuals versus GPS time




(b) Residuals versus topocentric elevation angles

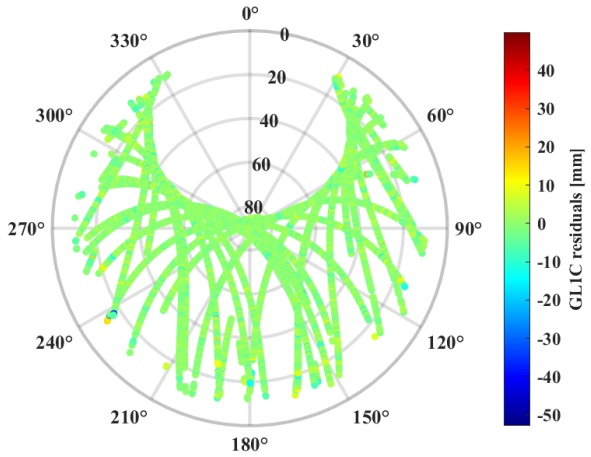


(c) Stereographic projection in topocentric frame

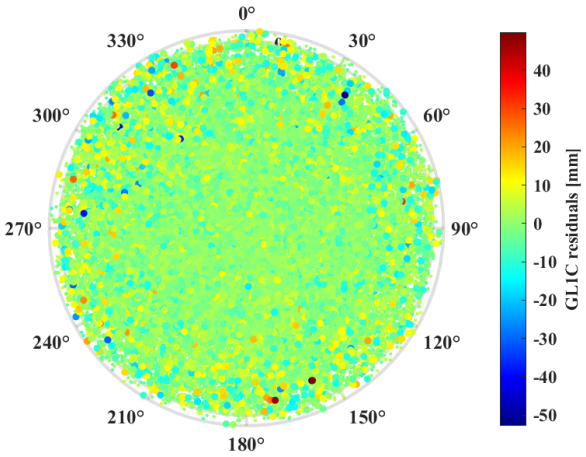


(d) Stereographic projection in antenna frame

**Figure 5.19:** Residuals of estimated UBX GL1C PCC.

Overall, since UBX is a mass-market antenna, its ability to suppress any remaining MP effects is limited, which could explain the higher residuals. Therefore, a longer calibration period was chosen for this antenna to potentially average out these effects.

The higher residuals are clearly evident in the a posteriori variance factor, as shown in Figure 5.20(a), and in the cumulative histogram of unnormalized residuals in Figure 5.20(b). The a posteriori variance factor is larger compared to the values for NOV and LEI antennas. While $\hat{\sigma}_0^2$ for these antennas is mostly less than 3 mm$^2$, the values for UBX range from 6 mm$^2$ to 9.5 mm$^2$. This increase is also reflected in the significantly larger values of $\sigma$ (see Figure 5.21), compared to the formal errors from NOV and LEI. The increase results from the larger variances of the input dSD data.

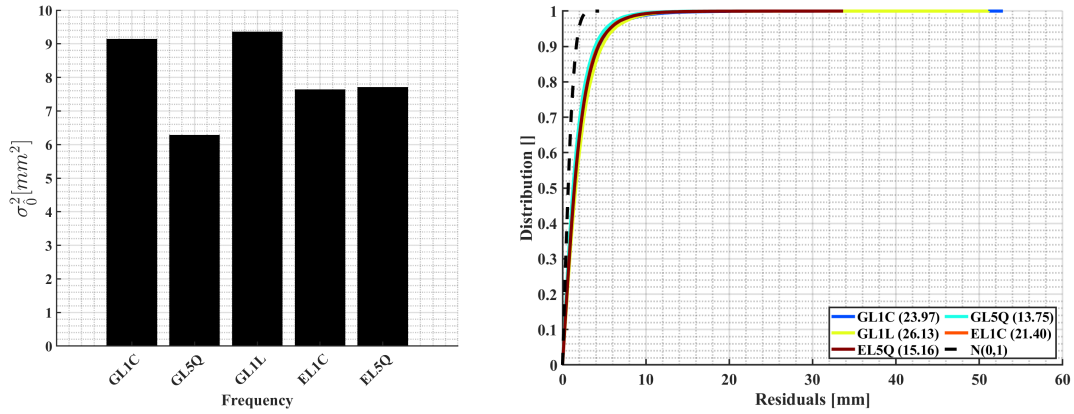


(a) A posteriori variance factor $\hat{\sigma}_0^2$ (b) Unnormalized residuals

**Figure 5.20:** Quality metrics of estimated UBX PCC.

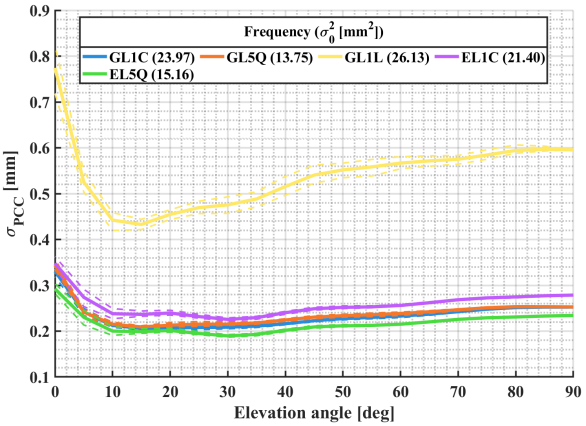


**Figure 5.21:** Averaged formal errors per 5° elevation angle for UBX PCC.

## 5.2 Comparison of Estimated PCC of Different AUTs and their Quality

In this section, the main findings concerning the estimated PCC for the three different AUTs, see Figure 5.1, are briefly compared. Figure 5.22 illustrates an example of the input dSD along with the estimated PCC* for the GL1C frequency band. The gridded PCC* values are calculated using the unit LOS vectors of all visible satellites, considering their azimuth and elevation angles in the antenna frame. Notably, since the AUT rotates around a fixed

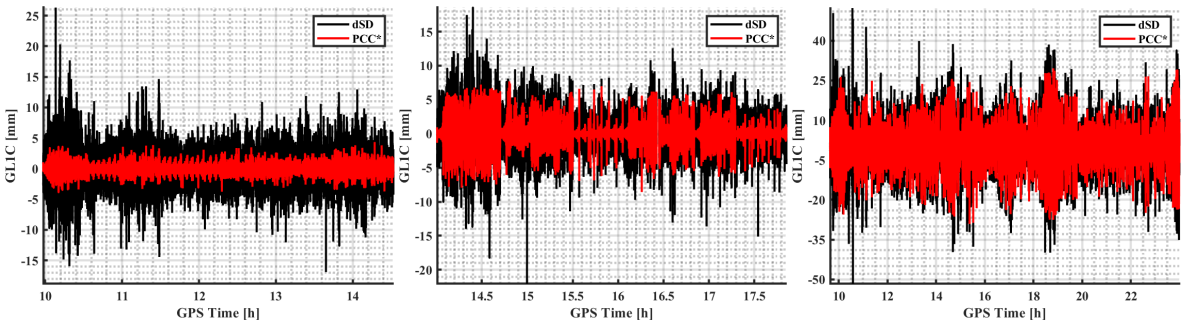


(a) NOV, $d_{\text{const}} = 58.27\,\text{mm}$ (b) LEI, $d_{\text{const}} = 160.19\,\text{mm}$ (c) UBX, $d_{\text{const}} = 12.85\,\text{mm}$

**Figure 5.22:** Comparison between estimated GL1C PCC* and input observations for all three antennas. Note the different axes scales.

point in space and not around the ARP, the observations are reduced by the distance $d_{\text{const}}$, as depicted in Figure 4.2. Consequently, the estimated PCC values are also reduced by the chosen a priori PCO $d_{\text{const}}$, resulting in PCC*. Due to varying $d_{\text{const}}$ values across different antennas, the magnitude of the dSD cannot be directly compared between the antennas; instead, comparisons should be made between different types of observations or between the ratio of dSD and PCC*. In the case of GL1C, in general the PCC* follows the pattern of the dSD, particularly for LEI. However, there are noticeable discrepancies between PCC* and dSD, reaching up to 4 cm for the UBX antenna, which is directly reflected in the corresponding residuals.

Figure 5.23 illustrates the respective quantities for GL2W. As previously analyzed, unexpectedly high residuals are evident after the PCC estimation for NOV and LEI. The formal error graphics reveal that the input variance of the dSD was significantly higher for GL2W, which is confirmed by the data presented in the figure. For both antennas, unusually high peaks are noticeable.

Figure 5.24 depicts the quantities for EL1C. As it was already visible for the depicted residuals and in the variance of the dSD, for all antennas a comparable behavior compared to GL1C is detectable.

Overall, the comparison indicates that the ratio between the dSD and the estimated PCC* is smallest for the LEI antenna across all the frequencies shown. Given that the input dSD theoretically includes only pattern information along with remaining MP effects and noise, it is ideal for this ratio to be minimal. The observed correlation between the antenna's quality

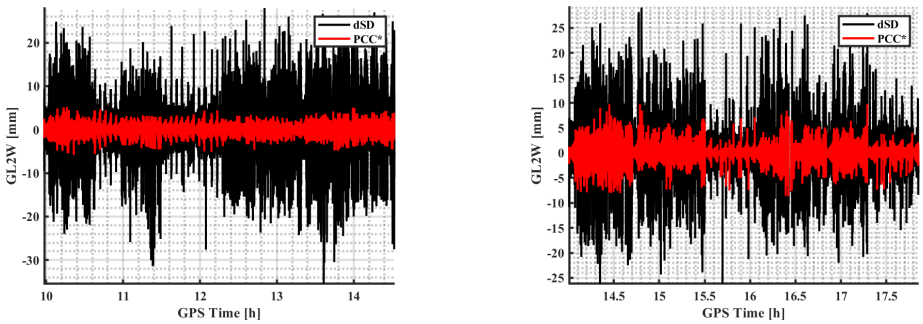


(a) NOV, $d_{\text{const}} = 58.27\,\text{mm}$ (b) LEI, $d_{\text{const}} = 160.19\,\text{mm}$

**Figure 5.23:** Comparison between estimated GL2W PCC* and input observations for NOV and LEI (UBX does not support L2). Note the different axes scales.

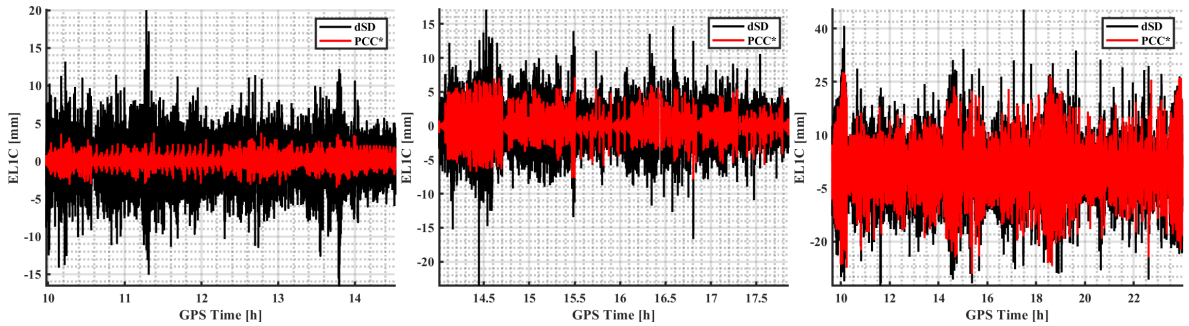


(a) NOV, $d_{\text{const}} = 58.27\,\text{mm}$ (b) LEI, $d_{\text{const}} = 160.19\,\text{mm}$ (c) UBX, $d_{\text{const}} = 12.85\,\text{mm}$

**Figure 5.24:** Comparison between estimated EL1C PCC* and input observations for all investigated antennas. Note the different axes scales.

class and the ratio of input observations to the estimated pattern suggests insights into the antenna's MP suppression capability. This conclusion is further supported by the ratio of the a posteriori variance factors relative to the variance of the dSD, as depicted in Figure 5.25.

In order to assess the MP suppression capability of the different AUT, Figure 5.26 depicts the MP-LC, calculated by use of Equation 2.14. Since UBX supports only L1/L5 frequencies, the MP-LC is calculated using GC1C, GL1C and GL5Q observations. Since time-differenced observations are used, the MP-LC is depicted as ΔMP-LC, too. The MP-LC is provided for the antenna at the reference station *MSD8* (which is the identical *LEIAR25.R3 LEIT* for all three calibrations), and the AUT.

When analyzing the results at *MSD8*, it becomes clear that the MP effect is reduced due to time-differencing. Thus, the assumption made in Section 4.2.2 can be proofed to some extent. Except for some larger peaks during the calibration of UBX (see Figure 5.26(e)), the ΔMP-LC vary between ±2 m. Due to the involvement of one codephase observation in the MP-LC, the linear combination lies in the expected range of observation noise.

In the case of the AUT, time-differencing also reduces the variations in the MP-LC. Notably, this process decreases some higher deviations, resulting in an overall reduction of the ΔMP-LC compared to the original MP-LC. However, two considerations must be noted. Firstly, as the

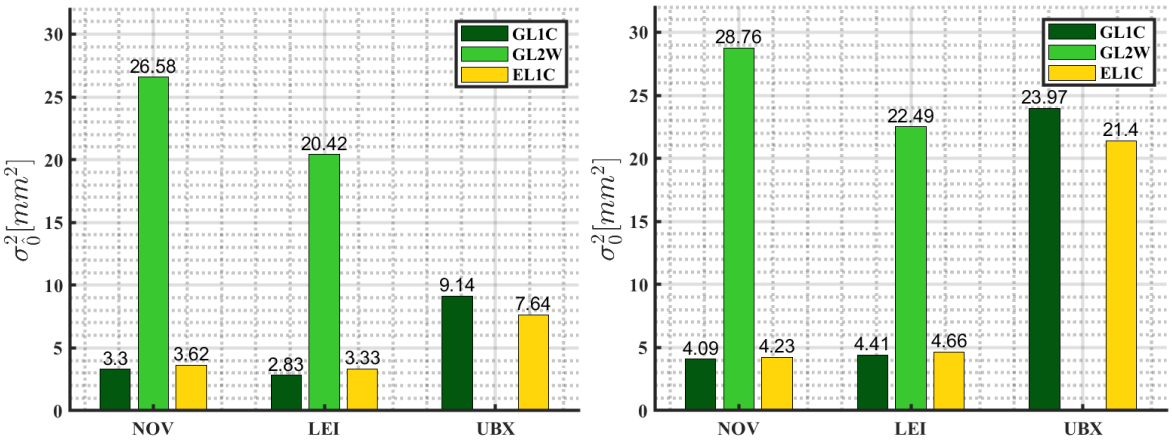


(a) A posteriori variance factor $\hat{\sigma}_{\hat{0}}^2$ (b) Variance of dSD

**Figure 5.25:** Comparison of a priori variance factors and variance of input dSD among NOV, LEI, and UBX PCC for selected frequencies. Note that UBX is a L1/L5 antenna, so that no values for GL2W are available.

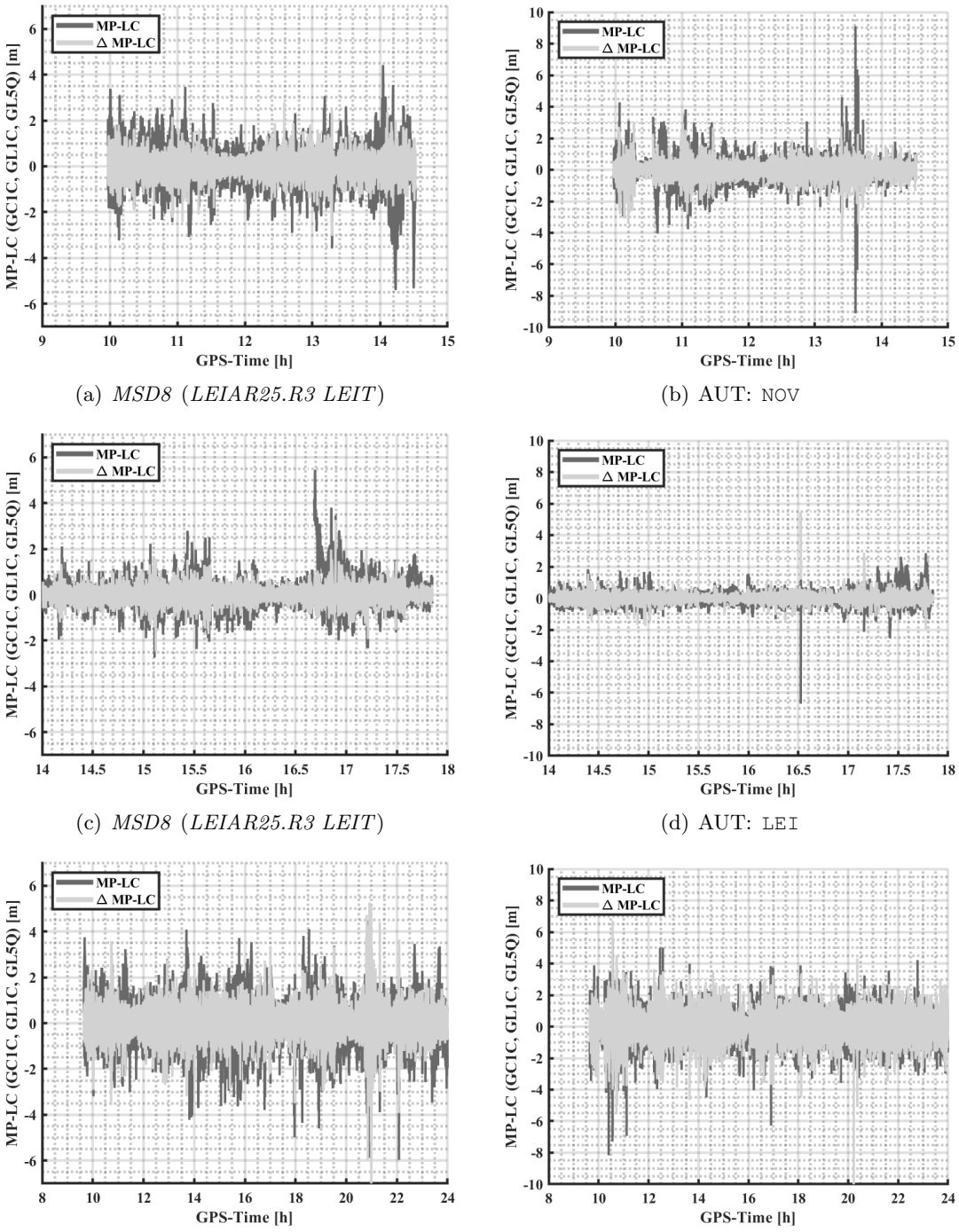


(a) *MSD8* (*LEIAR25.R3 LEIT*) (b) AUT: NOV

(c) *MSD8* (*LEIAR25.R3 LEIT*) (d) AUT: LEI

(e) *MSD8* (*LEIAR25.R3 LEIT*) (f) AUT: UBX

**Figure 5.26:** MP-LC and ΔMP-LC for the three investigated AUTs and the antenna mounted on the reference station *MSD8*. Note the different scales between AUT and *MSD8*.

pose of the robot changes, assuming static MP becomes less likely, since time differentiation does not eliminate these affects caused by the movements. Thus, effects caused by the robot itself might play a role, here. Secondly, because CPC are not applied and the effect does not cancel due to the tilting and rotating of the AUT (similar to the PCC), these effects remain present within the ΔMP-LC. Nonetheless, its magnitude typically remains below the overall noise level.

The overall magnitude and variations of the ΔMP-LC among the AUTs align with expec-

tations based on antenna class and their MP suppression capabilities. The geodetic 3D-choke ring antenna LEI presents the smallest MP-LC and ΔMP-LC, followed by the geodetic pinwheel antenna NOV. The mass-market antenna UBX shows the highest ΔMP-LC and MP-LC. Although the a posteriori variance factor and the variance of the dSD shown in Figure 5.25 are provided for single frequencies, the conclusions drawn from the ΔMP-LC for the AUTs are consistent with these quantities.

It is worth noting that in general ΔMP-LC can also be used as an observation input to estimate CPC, as demonstrated in Breva (2025). This approach allows for CPC estimation without additional data from a reference station, so that also the noise is reduced by a factor of $\sqrt{2}$ in comparison to dSD. However, PCC for both carrier-phase observations are required, and the PWU effect needs to be modeled. Since Breva (2025) successfully uses MP maps to down-weight or exclude observations likely to suffer from MP, that method is effective. As a result, theoretically, the ΔMP-LC should contain only the CPC information of the AUT, along with noise and any remaining unmodeled effects.

## 5.3 Repeatability of Individual Calibrations

This section analyzes the repeatability of individual calibrations with identical receivers. In total, seven different PCC sets for the NOV antenna, connected to a *Septentrio PolaRx5TR* receiver, with *standard* processing parameters are calculated and the differences between all possible combinations for all frequencies are formed. The assumption is that ΔPCC between two sets are smaller when the distribution of observations on the antenna hemisphere is more similar. This is influenced by the relative antenna-satellite geometry within the antenna frame, so that the corresponding robot poses play an important role, too.

First, the similarity of the individual sets is analyzed based on GPS daytime, calibration length, and robot poses. This analysis leads to a comparison of the number of available observations per set and frequency. Using the calculated ΔPCC for all sets and frequencies, three notable case examples are chosen. For these cases, the ΔPCC are studied in more detail, considering the differences themselves, the distribution of observations across the antenna hemisphere, the condition number of the NES, and the a priori variance factor as well as the distribution of the residuals after the LSA. Since GLONASS uses FDMA to uniquely assign satellites, it transmits at different frequencies. Consequently, the estimated PCC are more dependent on the specific satellites contributing observations to the estimation algorithm. Therefore, the resulting *mixed* wavelength for three GLONASS frequencies and all seven sets are briefly demonstrated.

### Number of Observations and Executed Robot Poses

Figure 5.27 shows the calibration time for the seven sets, recorded on DOY047 and DOY048 in year 2023. While sets 1 and 5, 2 and 6 as well as 7 and 3 have an overlapping time period between the two consecutive days, this is not the case for set 4. If there are almost identical calibration periods for two sets on two consecutive days (with an offset of 23:56:04 h), in theory the same satellite constellation is present for GPS. However, due to the partly randomized tilting and rotating of the AUT, this is only the case in the topocentric- and not in the antenna-frame. Thus, the observation distribution is equal only to some extent for GPS frequencies. Consequently, it is not expected that the corresponding estimated PCC show a higher similarity for the above-mentioned calibration pairs.

The partial randomization of the robot poses is shown in Figure 5.28, which depicts the

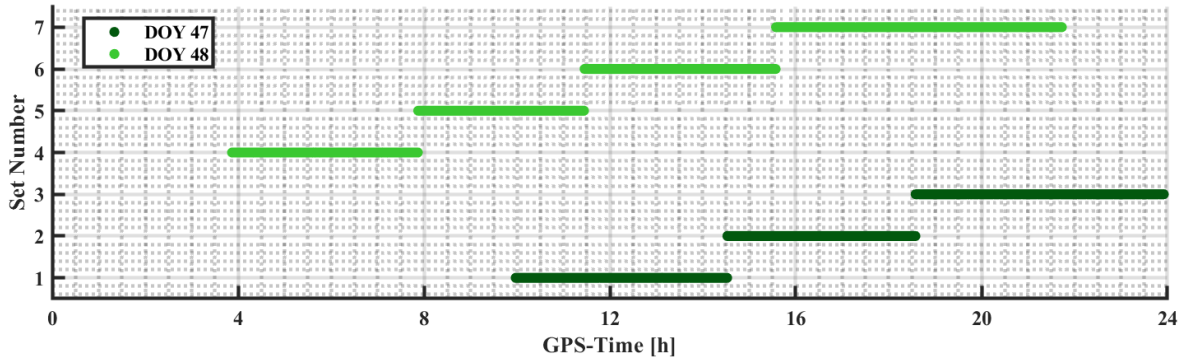


**Figure 5.27:** Calibration times of the seven individual sets on DOY047 and DOY048 in year 2023 (16/02/2023 and 17/02/2023).

robot poses for all seven individual calibration sets separated by red lines. A more closed-up view for the first three sets is also visible in Figure 4.6. It can be seen that the robot approaches different poses during the calibration sets but also similar movement patterns can be recognized. The azimuth angle of module 1 (shown in the top figure) serves as an example, where in this case the AUT is always rotated from −164.5° in 30° steps to an azimuth angle of 195.5°, afterward in 60° steps to−164.5°, followed by rotations of 90° to 195.5°. Nonetheless, the poses differ further on in the calibration process so that usually a different sensing of the antenna hemisphere is given for all GNSS – even if adjusted calibration times taking the sidereal orbit repetition times into account are used.

It is worth noting that a longer calibration brake between set 3 and 4 is present. This is due to general internal evaluation routines so that satellite coordinate jumps at day boundaries are avoided. However, for the specific application *antenna calibration* the errors for the satellite positions cancel out by use of dSD.

The exact calibration durations and the number of observations per frequency and individual set are depicted in Figure 5.29. As expected, the longer the calibration takes, the more

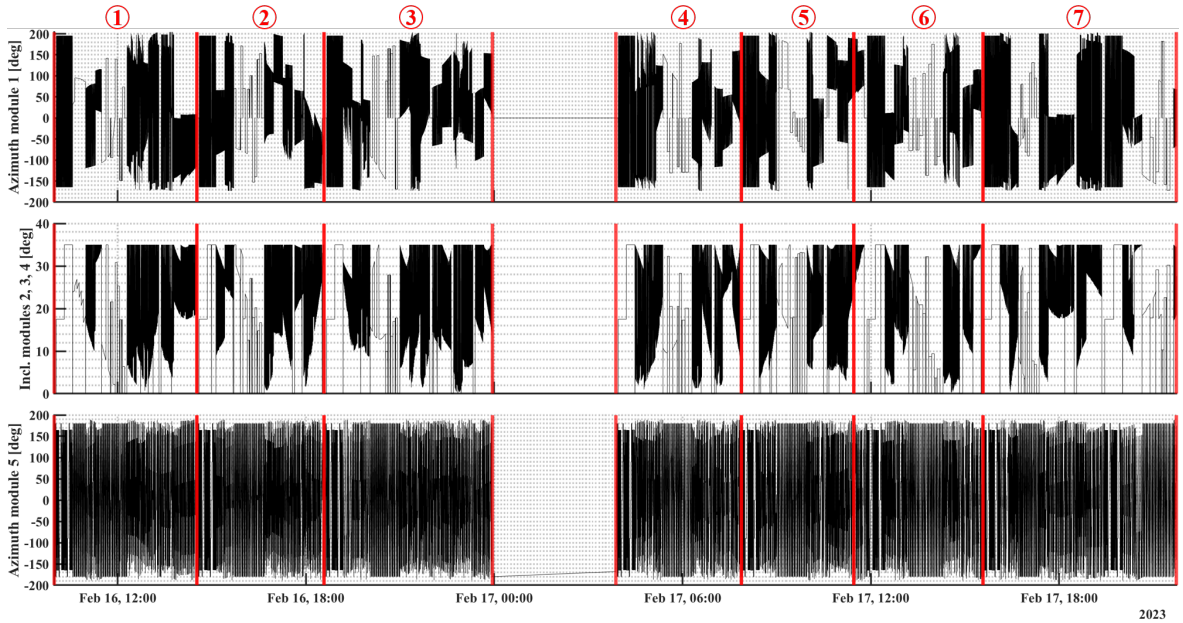


**Figure 5.28:** Robot poses for all seven individual calibration sets, which start and end times are illustrated by red lines.

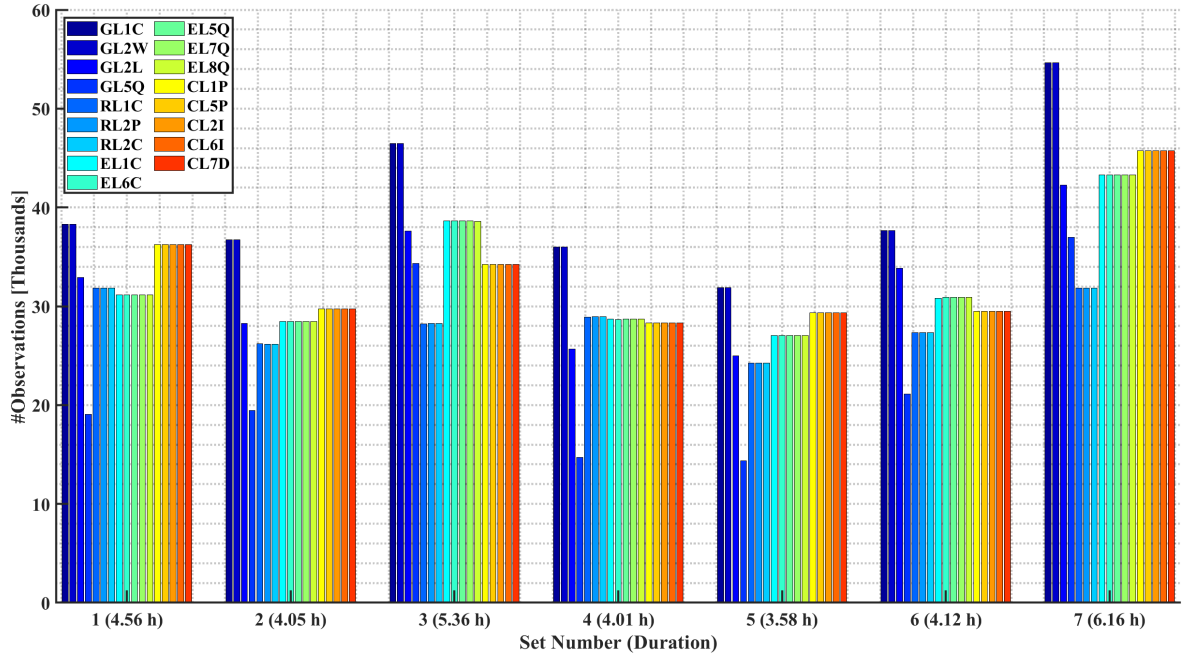


**Figure 5.29:** Number of used observations per calibration set and frequency.

observations are available. However, the number of observations does not increase linearly with the calibration duration, which can be derived from the number of observations per hour. For example, the shortest set 5 for GL1C contains 8906 observations per hour, while the longest set 7 has only 8871 observations per hour. This can also be observed for the other sets and frequencies.

Since only GPS satellites from block IIF and III/IIIF (as of July 2023 in total 18 operational satellites) transmit the GL5Q signal, it has the lowest number of observations. Also, fewer observations are present for GL2L compared to GL1C and GL2W, since this signal is transmitted in total by 25 satellites, while the full GPS constellation consists of 31 operational satellites (GPS.GOV, 2024). Moreover, it can be seen from Figure 5.29 that most observations are present for GL1C and GL2W, followed by BeiDou and Galileo signals.

### Selection and Analysis of Case Examples

Due to the overwhelming number of possible set combinations and signals, only three different combinations, further addressed as (A), (B), and (C), are exemplarily analyzed:

(A) Signal GL1C: Differences between sets 5 and 7, as this is where the largest differences in the number of observations for all signals and set combinations exist

(B) Signal GL5Q: Differences between sets 5 and 7, as set 5 has the overall fewest observations

(C) Signal RL1C: Differences between sets 1 and 7, as this variant has the smallest overall difference in the number of observations (only 8).

Figure 5.30 shows the absolute $\Delta$PCC for three frequencies (GL1C, GL5Q, RL1C) and all possible set combinations in cumulative histograms. The above defined cases are highlighted by black lines. Interestingly, case (A) shows the lowest PCC differences over all combinations, i.e. highest repeatability, although the highest differences in the amount of available observations

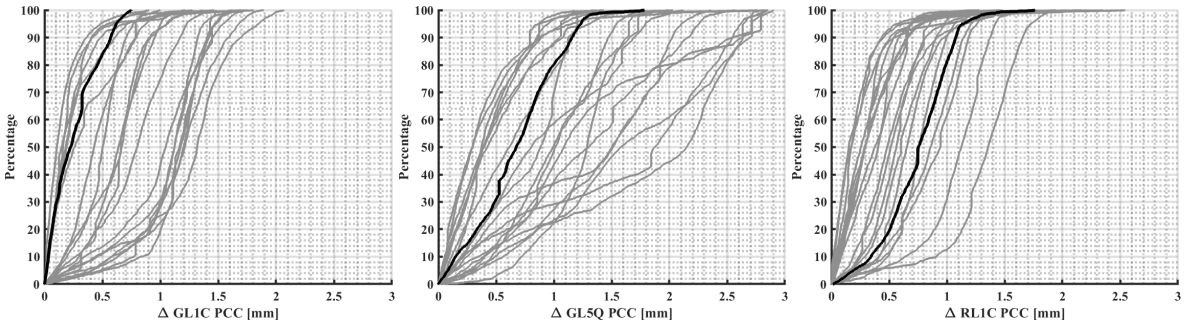


(a) Case (A) (b) Case (B) (c) Case (C)

**Figure 5.30:** Cumulative histogram of absolute values of ΔPCC for all possible set combinations. Black curves indicate the specified three cases.

is present. Here, the maximum ΔPCC is at 0.75 mm, while the maximum differences for (B) and (C) reads 1.78 mm and 1.76 mm, respectively.

To visualize the behavior of the differences, mean ΔPCC per elevation angle for the defined cases are depicted in Figure 5.31. In addition, the minimum and maximum values per elevation angle over all azimuth angles are indicated by dashed lines. In general, it can be seen that the differences over the azimuth angles (dashed lines) increase with decreasing elevation angle. Also, an offset in zenith direction can directly be observed. All in all, the PCC differences which only depend on the elevation angle show only few variations over the whole hemisphere.

To further analyze the correlation between the number of available observations and ΔPCC, the difference number of observations per 5° elevation bins, calculated as the mean value over all corresponding azimuth bins, is depicted along with the ΔPCC in Figure 5.32. It is observed that the difference in number of observations is the smallest for case (C), where the value differs by less than 20 at most. Apart from this, no direct correlation between the differences in the number of observations and the magnitude of the ΔPCC can be drawn.

Figure 5.33 illustrates the absolute difference of the number of available observations per 5° elevation and azimuth bin, so that the differences of the observation distribution on the antenna hemisphere gets visible. For all cases, the highest differences in the number of available observations occur at mid-elevation ranges. Especially for case (A), a yellowish-reddish circle

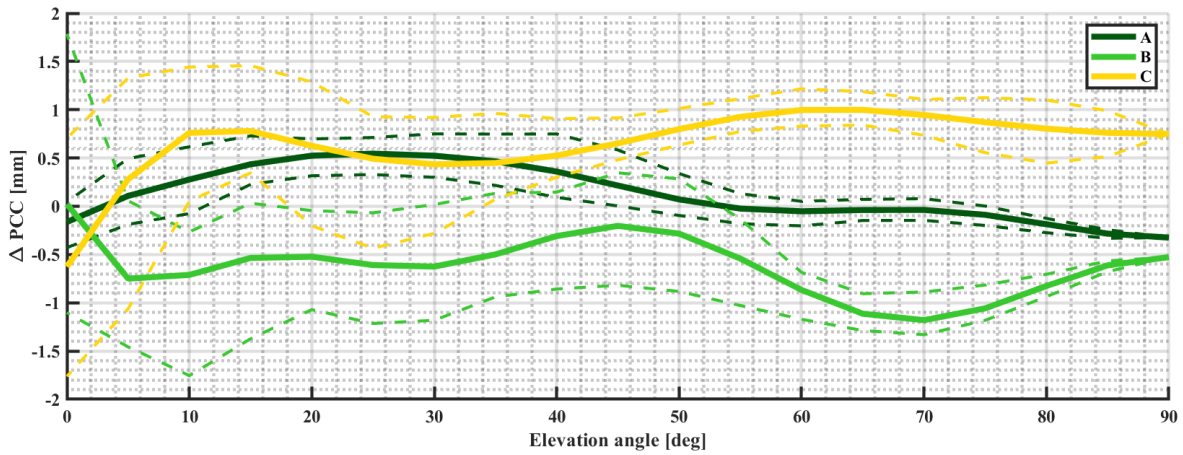


**Figure 5.31:** ΔPCC for the defined cases, shown as mean differences per elevation angle, with minimum and maximum values per bin illustrated as dashed lines.

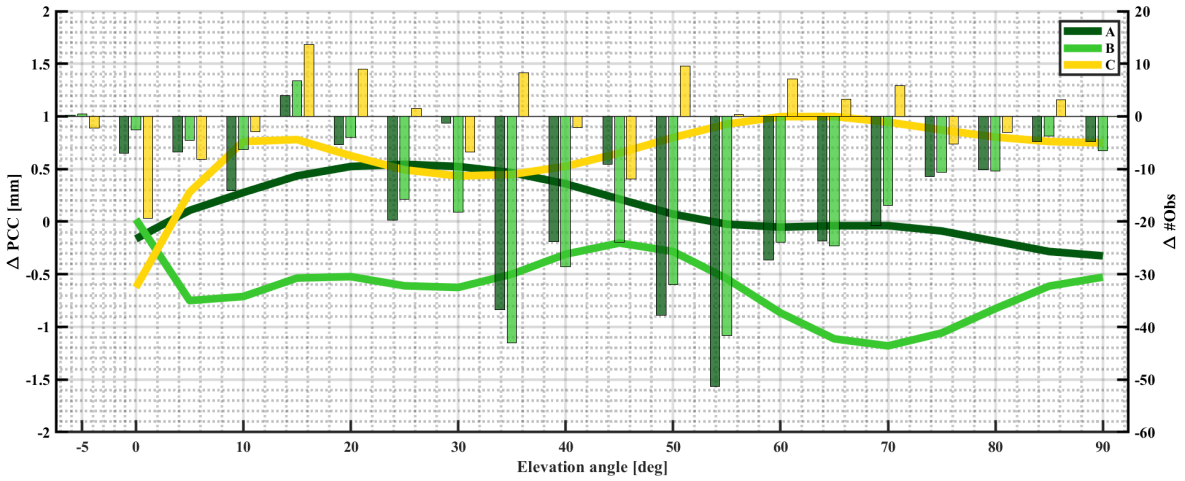


**Figure 5.32:** ΔPCC presented as mean differences per elevation angle (left y-axis), along with differences in available observations per 5° elevation angle bin (right x-axis) for the defined cases.

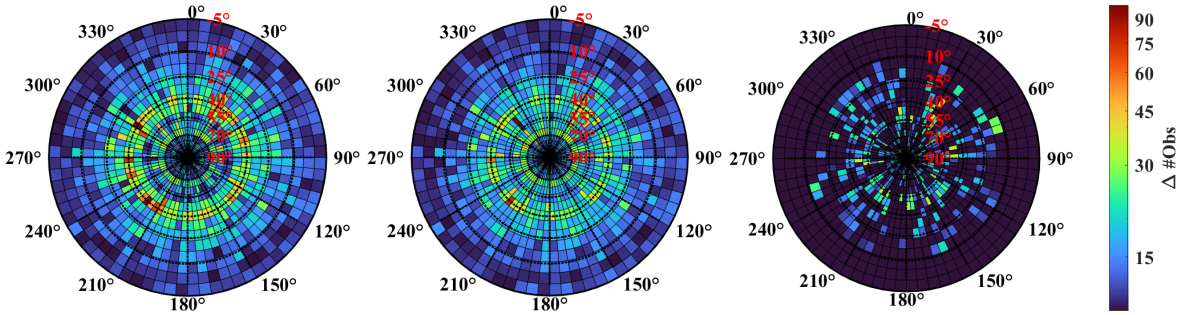


(a) Case (A) (b) Case (B) (c) Case (C)

**Figure 5.33:** Distribution of differences in the number of observations for the three defined cases, displayed as stereographic projections.

at 40° elevation angles can be clearly be seen. For case (C), the absolute difference is especially low at low elevation angles (dark blue). However, no direct correlation between the differential observation distribution and the ΔPCC, as depicted in Figure 5.31, is identifiable.

### Quality Parameters after Least-Squares Adjustment

To assess certain quality parameters after the LSA for the three defined cases, the condition number of the NES, illustrated in Figure 5.34(a), the a posteriori variance factors $\hat{\sigma}_0^2$, shown in Figure 5.34(b), and the distribution of the residuals after the LSA, depicted in Figure 5.35, are analyzed.

In the case of the condition numbers, no clear correlation to the respective PCC differences is observable. However, since a similar number of observations is present for case (C) with a comparable distribution over the antenna hemisphere (see Figure 5.33), the condition number is also comparable. For $\hat{\sigma}_0^2$, a conclusion for the three defined cases w.r.t. the maximum ΔPCC can be drawn: the more similar $\hat{\sigma}_0^2$ between the two sets is, the smaller the maximum ΔPCC is, see Figure 5.34(b).

To further investigate, the difference in $\hat{\sigma}_0^2$ values ($\Delta\hat{\sigma}_0^2$) between two sets is compared to the maximum value of ΔPCC for five frequencies and all possible set combinations, as shown in Figure 5.34(c). Unlike in Figure 5.34(b), no clear correlation is observed between these

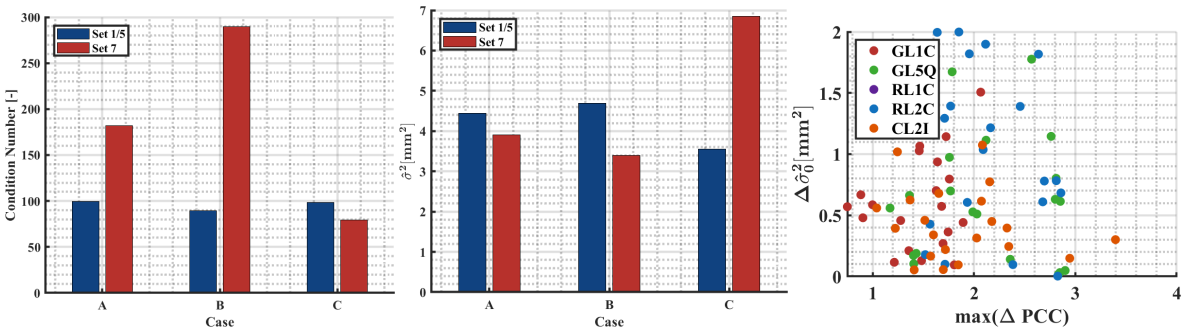


(a) Condition number (b) A posteriori variance factor $\hat{\sigma}_0^2$ (c) $\Delta\hat{\sigma}_0^2$ vs. max(ΔPCC)

**Figure 5.34:** Illustration of quality parameters after LSA to compare similarity of different PCC sets: (a) Condition number of NES, and (b) a posteriori variance factor $\hat{\sigma}_0^2$ for the three defined cases. Figure (c) depicts $\Delta\hat{\sigma}_0^2$ vs. ΔPCC for five selected frequencies and all possible combination sets.

two measures. However, it is noteworthy that the highest $\Delta\hat{\sigma}_0^2$ values are observed for RL2C, with maximum ΔPCC values ranging from 1.5 mm to 2.6 mm. Conversely, a maximum ΔPCC value of 3.4 mm corresponds to a $\Delta\hat{\sigma}_0^2$ of 0.3 mm$^2$.

It should be noted that $\sigma_0^2$ is set to 1 for these analyses. The outcomes are not significantly impacted if $\sigma_0^2$ is changed to the variance of the input observations. Additionally, potential correlations are investigated by analyzing the dependence of the ratio between $\hat{\sigma}_0^2$ or $\Delta\hat{\sigma}_0^2$, and other characteristic values of ΔPCC, such as the RMS and standard deviation of ΔPCC (see Section 3.2.2). No clear correlations are detectable in these analyses.

To further analyze the residuals, Figure 5.35 presents the distribution of residuals for the three defined cases using cumulative histograms. $\sigma_0^2$ is set to 1, allowing for easier comparison of the distributions among different cases. In case (A), the distributions between set 5 and set 7 are very similar, which is not observed in case (C) between set 1 and 7. Since $\sigma_0^2$ is set to 1, it can be assumed that the input dSD are more similar between the two sets in case (A). This is indicated by the dSD variance differences, which are 0.57 mm$^2$ for case (A), 1.67 mm$^2$ for case (B), and 3.69 mm$^2$ for case (C). In these scenarios, it can be concluded that greater similarity in the input dSD leads to higher PCC repeatability, resulting in smaller ΔPCC values. This effect is also reflected in the a posteriori variance factor shown in Figure 5.34(b).

To summarize, the analysis conducted in this section indicates that the similarity between two PCC sets, as estimated from individual sets, is influenced not only by the distribution of observations on the antenna hemisphere but also significantly by the quality of those observations.

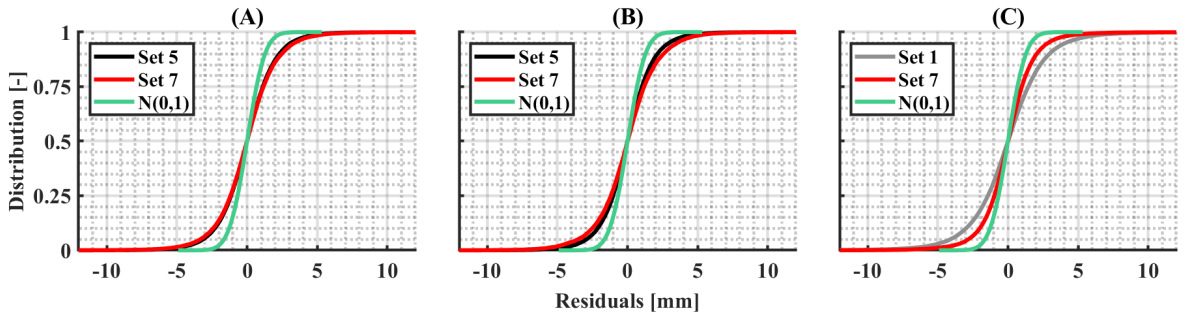


**Figure 5.35:** Cumulative histogram of unnormalized dSD residuals for the above defined cases: left (A), middle (B) and right (C). In addition, the standardized normalized distribution N(0,1) is depicted.

### Analysis of GLONASS Frequencies

A special focus should also be placed on the repeatability of GLONASS frequencies. Since the FDMA technique is used to uniquely assign the satellites, the resulting PCC depend on the ratio of observations from different satellites and, consequently, different frequencies. Figure 5.36 depicts the differences of the resulting *mixed* wavelength to the respective GLONASS *center* wavelength for all sets and all three GLONASS frequencies. The wavelength differences of the individual GLONASS frequency channels are in a range of 0.0652 mm to 0.0660 mm. The dashed line indicates these values. Considering these values, the estimated GLONASS PCC are appropriate, particularly for sets 1, 2, and 4 to 7. Details for set 1 can also be found in Figure 5.5(b).

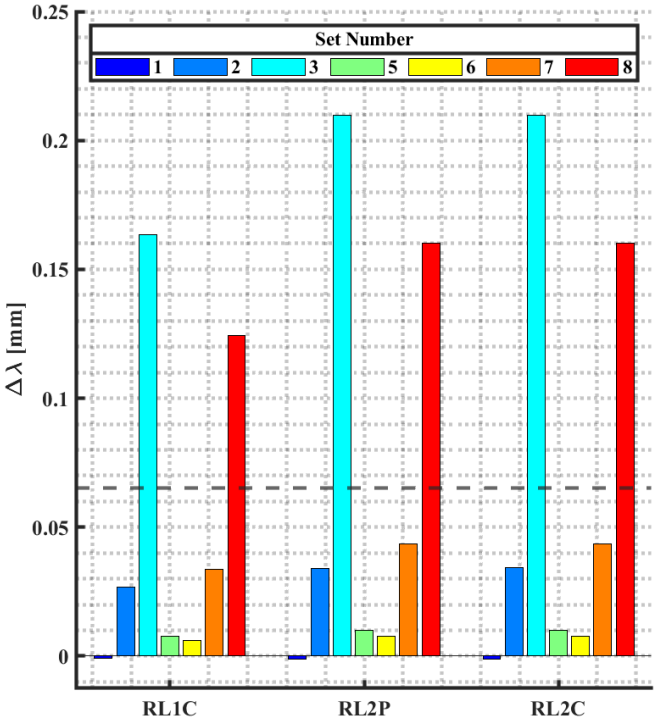


**Figure 5.36:** Differences of *mixed* GLONASS frequencies to the respective *center* frequency. The dashed line indicates the $\Delta\lambda$ between the individual GLONASS frequency channels.

## 5.4 Repeatability with Different Receivers

For the estimation of PCC, geodetic receivers are used to log raw GNSS data from the reference antenna and the AUT. Since the used antenna-receiver combination affects the observations, it also influences the PCC estimation. Additionally, the receiver settings itself impact the obtained observations (as written into the RINEX observation file). In order to investigate the impact of the receiver, an experiment following the sketch depicted in Figure 5.37 has been carried out. In total, three different receiver types were connected to both antennas, leading into two zero-baseline setups. A calibration of a *NOV703GGG.R2 NONE* antenna from May 21, 2024 (DOY142) serves as data set. In the following, the analyses are carried out exemplarily for GPS L1/L5 and Galileo E1 frequencies. It is important to note that inter-receiver dSD are computed between identical receiver types. This approach ensures that no additional receiver-specific hardware biases are introduced to the observations.

First, the resulting PCC estimated by different receivers are analyzed. These results are

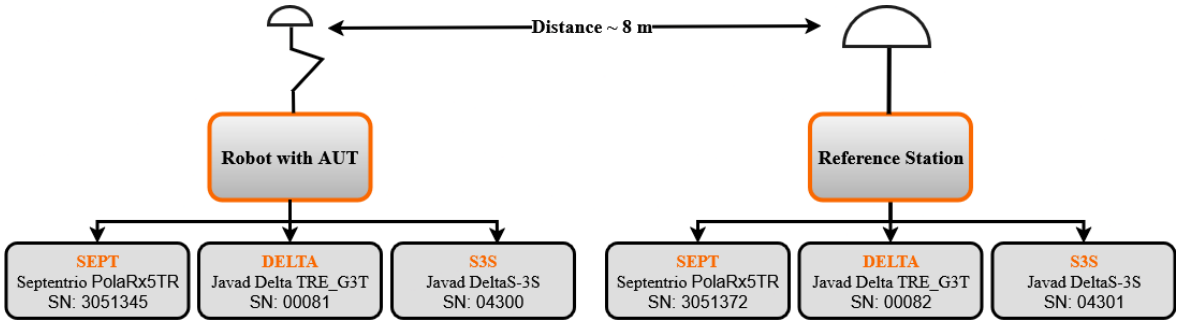


**Figure 5.37:** Measurement setup used to analyze the PCC estimation repeatability with different receivers.

further examined by comparing the respective input observations for the PCC estimation algorithm, as well as by analyzing the residuals and a posteriori variance factors after the LSA.

### PCC Differences

Figure 5.38 shows PCC* and ΔPCC for GL1C. A constant $PCO_{Up}$ offset $\overline{d}$ of 58.27 mm has been subtracted from the PCC, as described in Equation 3.3. The mean values per elevation angle, illustrated in Figure 5.38(a), demonstrate the overall behavior of PCC*. The estimated PCC* from all receivers exhibit similar behavior. At low elevation angles ($el < 10°$), the PCC* estimated with SEPT receivers show higher negative values for the azimuthal variations, indicated by the dashed lines. This becomes evident when analyzing ΔPCC in Figure 5.38(b). Overall, the differences are generally smaller than ±1 mm, and the mean differences per elevation angle show only minor variations.

Figure 5.39 depicts the results for GL5Q/GL5X frequencies. As summarized in Table 5.2 for GPS and Galileo frequencies and in Table 5.3 for the sake of completeness for GLONASS and BeiDou frequencies, the different receivers may track signals using different modulation types. While for GPS L1 frequency all used receivers track GL1C, it differs for GPS L5 and Galileo frequencies. Receiver SEPT tracks the GL5Q and EL1C signals, whereas the *Javad*

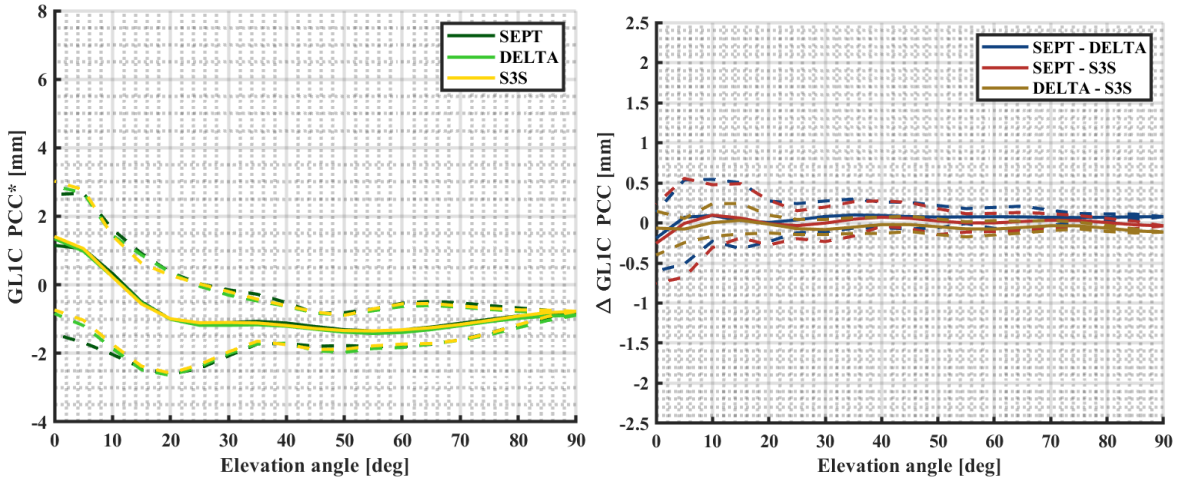


(a) PCC* (b) ΔPCC

**Figure 5.38:** Impact of different receivers on estimated GL1C PCC, presented as averaged PCC* and averaged ΔPCC per elevation angle. Dashed lines represent the minimum and maximum values per bin.

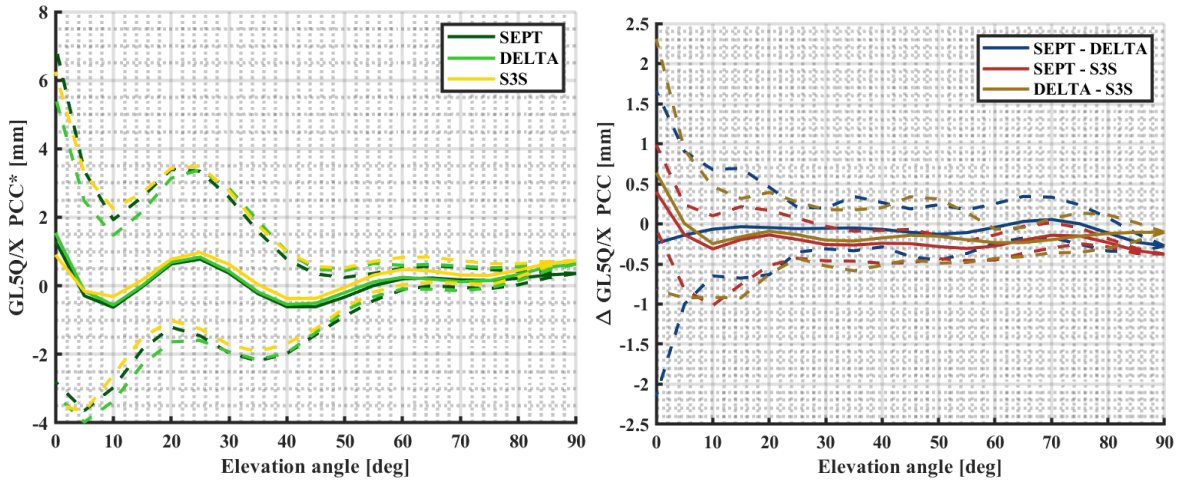


(a) PCC* (b) ΔPCC

**Figure 5.39:** Impact of different receivers on estimated GL5Q/GL5X PCC, presented as averaged PCC* and averaged ΔPCC per elevation angle. Dashed lines represent the minimum and maximum values per bin.

receivers, DELTA and S3S, track the GL5X and EL1X signals, respectively. Thus, for these cases higher differences between the individual receiver PCC estimations are expectable.

In this analysis, the differences are in a range of ±2.5 mm, with the highest differences occurring at low elevation angles. Interestingly, this is also observable between DELTA and S3S, which both track GL5X signals.

For EL1C/EL1X PCC estimates, as illustrated in Figure 5.40, ΔPCC has a range between -1.20 mm and 2.0 mm. It is worth noting that DELTA has an offset in zenith direction compared to SEPT and S3S of 0.49 mm and 0.60 mm, respectively. This offset then leads to the clearly

**Table 5.2:** Overview of GPS and Galileo frequencies tracked by different receivers. Characters indicate the tracking loop, as described in IGS (2023).

| | Receiver Shortcut | | | | Receiver Shortcut | | |
|---|---|---|---|---|---|---|---|
| **GPS** | SEPT | DELTA | S3S | **Galileo** | SEPT | DELTA | S3S |
| GL1 | C | C | C | EL1 | C | X | X |
| GL1 | L | – | – | EL5 | Q | X | X |
| GL2 | W | W | W | EL6 | Q | – | X |
| GL2 | L | X | X | EL7 | Q | – | X |
| GL5 | Q | X | X | EL8 | Q | – | X |

**Table 5.3:** Overview of GLONASS and BeiDou frequencies tracked by different receivers. Characters indicate the tracking loop, as described in IGS (2023).

| | Receiver Shortcut | | | | Receiver Shortcut | | |
|---|---|---|---|---|---|---|---|
| **GLONASS** | SEPT | DELTA | S3S | **BeiDou** | SEPT | DELTA | S3S |
| RL1 | C | C | C | CL1 | P | – | X |
| RL1 | – | P | P | CL2 | I | – | I |
| RL2 | C | C | C | CL5 | P | – | X |
| RL2 | – | P | P | CL6 | I | – | I |
| RL3 | – | – | X | CL7 | I | – | I |

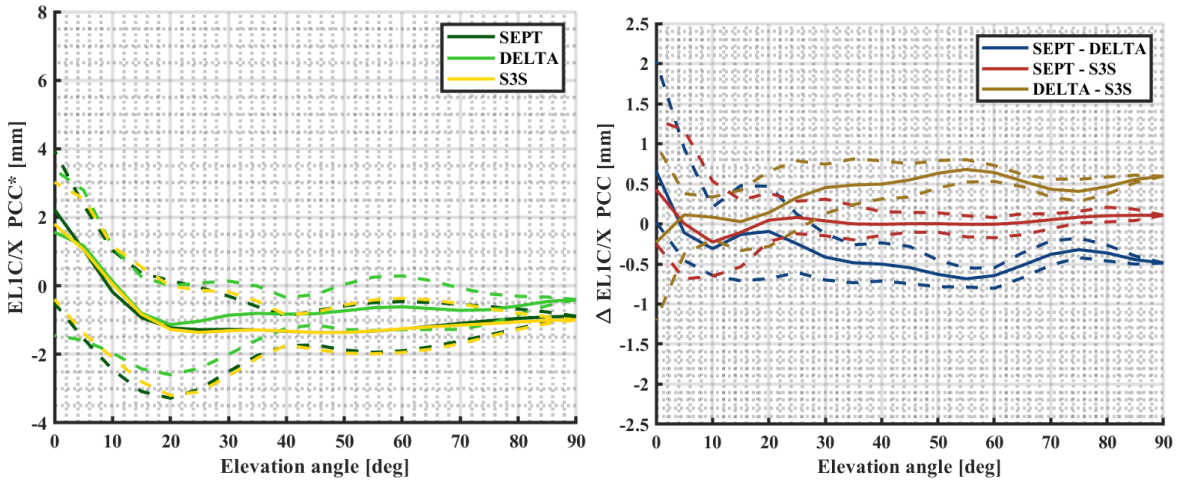


(a) PCC* (b) ΔPCC

**Figure 5.40:** Impact of different receivers on estimated EL1C/EL1X PCC, presented as averaged PCC* and averaged ΔPCC per elevation angle. Dashed lines represent the minimum and maximum values per bin.

recognizable level differences in ΔPCC shown in Figure 5.40(b). In contrast, the estimated patterns of SEPT and S3S show a high consistency, with mean differences per elevation angle smaller than 0.23 mm. However, at low elevation angles, the differences dependent on elevation and azimuth angles, are exceeding the 1 mm level.

In conclusion, for the investigated antenna-receiver combinations and the analyzed frequencies, the ΔPCC values are at most 2.5 mm. While mean PCC* per elevation angle show generally good agreements, larger discrepancies occur across azimuth angles, particularly at low elevation angles. These findings are generally consistent with the results presented by Kröger et al. (2021), where the difference patterns between estimated PCC using a *Javad Delta TRE_G3T* and a *Septentrio PolaRx5TR* receiver with a *LEIAR25.R3 LEIT* antenna were analyzed. In that study, the differences for the L1 and L5 frequencies of GPS and Galileo are below 1.2 mm, with the largest differences also occurring for GPS L5.

### Comparison of Input Observations and Residuals

To further investigate the impact of the different receivers, the respective input dSD for the LSA and the resulting residuals after the LSA are analyzed. Figure 5.41 depicts these values for GL1C. Overall, the dSD values for SEPT show the smallest variations, followed by S3S and DELTA. However, some observations from SEPT show large dSD values, exceeding ±2 cm. In the case of the two *Javad* receivers (DELTA and S3S), it is noticeable that peaks often occur simultaneously, although the magnitude is often higher for DELTA. This visual assessment is supported by the statistical values presented in Table 5.4, where the variances of the dSD are listed. The dSD from SEPT have a variance $\sigma^2$ of 4.03 mm$^2$, while $\sigma^2 = 6.45\,\text{mm}^2$ for S3S and $\sigma^2 = 6.54\,\text{mm}^2$ for DELTA.

Figure 5.41(b) illustrates the GL1C residuals. A behavior similar to that of the dSD is observed. It is worth noting that at certain epochs, no observations contribute to the PCC estimations. These are typically extended time spans with no available observations, see Figure 5.41(a). This absence of observations can result from longer standstill periods of the robot that are discarded (as seen in Figure 4.8) or from short satellite arcs. The overall comparable behavior of the residuals w.r.t. the input dSD is also reflected in the a posteriori variance factors, which are provided in Table 5.5.

Figure 5.42 illustrates the dSD and residuals for GL5Q/GL5X. Similar to the GL1C frequency, the DELTA dSD show the highest variations, which are even more pronounced here. Consequently, the variance of the dSD is also very high at $7.52\,\mathrm{mm}^2$. For SEPT, $\sigma^2 = 4.74\,\mathrm{mm}^2$, which is slightly higher than for GL1C. Meanwhile, the variance of S3S dSD is lower at $5.11\,\mathrm{mm}^2$. However, the a posteriori variance factor is smaller for SEPT compared to S3S, as shown in Table 5.5.

Figure 5.43 presents the time series for EL1C/EL1X. The overall dSD variations are smaller for all receivers compared to the other frequencies, which is also reflected in the corresponding statistical values. Besides, the previously mentioned conclusions also apply here.

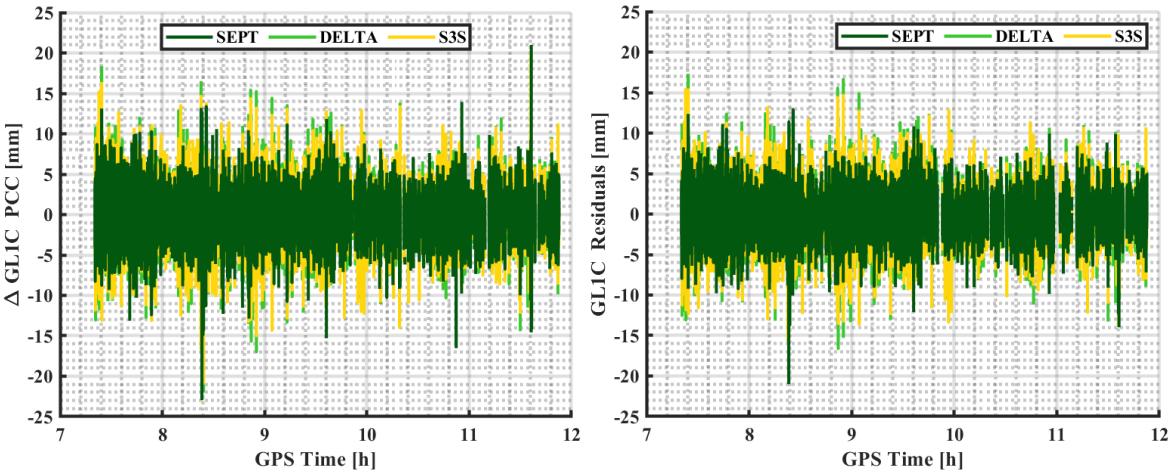


(a) dSD (b) Residuals

**Figure 5.41:** Input dSD and residuals after GL1C PCC estimation with different receivers.

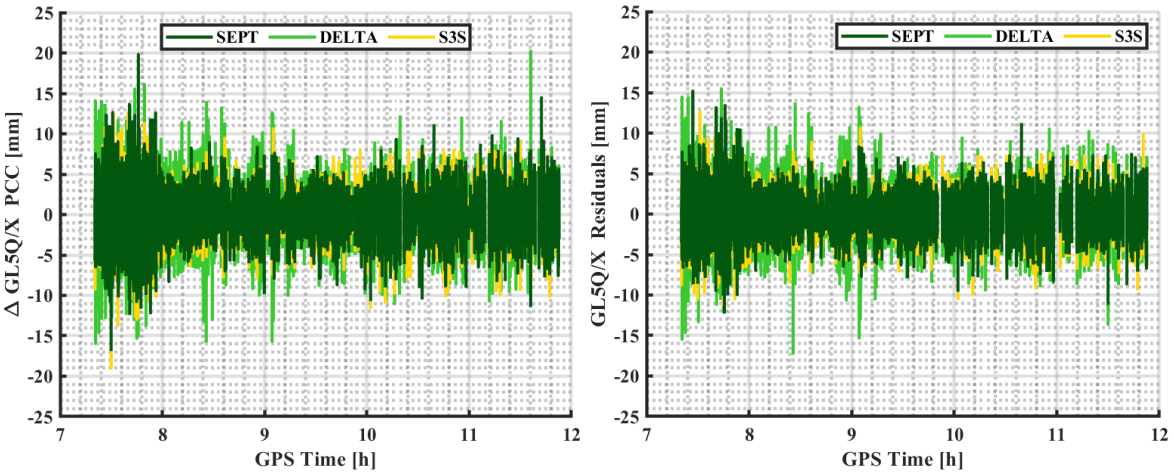


(a) dSD (b) Residuals

**Figure 5.42:** Input dSD and residuals after GL5Q/GL5X PCC estimation with different receivers.

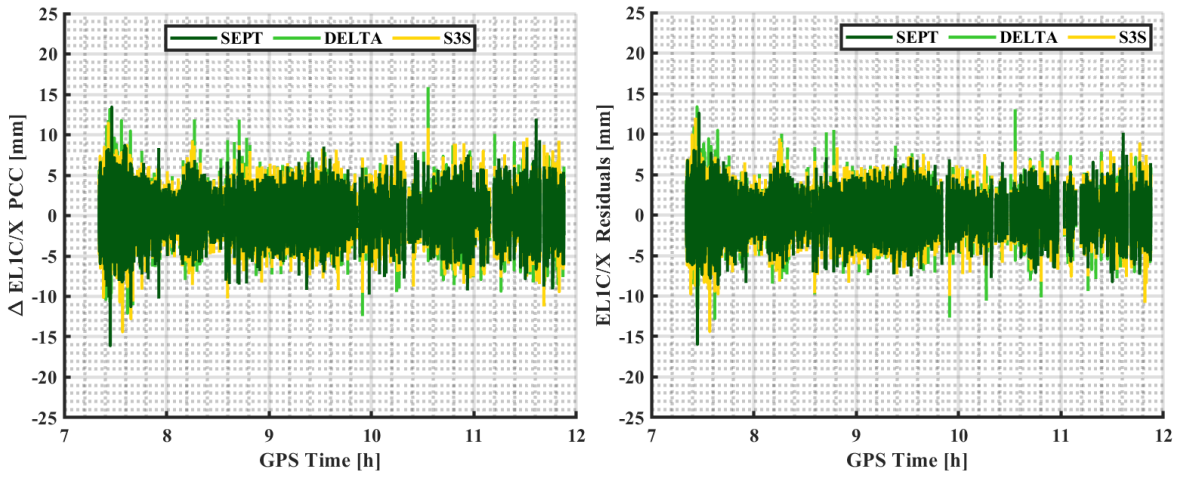


(a) dSD (b) Residuals

**Figure 5.43:** Input dSD and residuals after EL1C/EL1X PCC estimation with different receivers.

**Table 5.4:** Variances of input dSD for different receivers and selected GPS and Galileo frequencies.

| | SEPT | DELTA | S3S |
|---|---|---|---|
| | [mm$^2$] | | |
| GL1C | 4.03 | 6.54 | 6.45 |
| GL5Q/X | 4.74 | 7.52 | 5.11 |
| EL1C/X | 3.14 | 4.57 | 3.79 |

**Table 5.5:** A posteriori variance factors of estimated PCC by different receivers for selected GPS and Galileo frequencies.

| | SEPT | DELTA | S3S |
|---|---|---|---|
| | [mm$^2$] | | |
| GL1C | 3.55 | 6.04 | 5.97 |
| GL5Q/X | 3.88 | 6.50 | 4.25 |
| EL1C/X | 2.71 | 4.08 | 3.40 |

## 5.5 Differences between Identical Frequencies from Different GNSS

In this section, differences between identical frequencies from different GNSS are analyzed. Additionally, two cases are examined where PCC values are estimated for the same frequency and the same GNSS, but with different tracking modes. Specifically, these cases are G02 (GL2W and GL2L) and R02 (RL2P and RL2C).

First, ΔPCC values are analyzed on the pattern level using graphical methods and numerical measures introduced in Chapter 3. Following that, the impact on geodetic parameters is assessed using the developed simulation approach, which is detailed in Section 3.3.2.

Since PCC is theoretically frequency-dependent, it is assumed that providing a single set of PCC values for identical frequencies across different GNSS would be sufficient, as this is currently handled in the newest ANTEX files. However, as discussed in Kröger et al. (2021), geodetic receivers process carrier-phase measurements from different GNSS to a certain extent differently. This includes, among others, the corresponding tracking loop parameters, i.e. PLL and DLL. Consequently, differences between identical frequencies from different GNSS can occur, as observable in Section 5.1.

### Differences on Pattern Level

Figure 5.44 illustrates the differences between identical frequencies from different GNSS for the NOV antenna. The smallest differences (ΔPCC $< 1$ mm) occur for Δ(RL2P - RL2C) be-

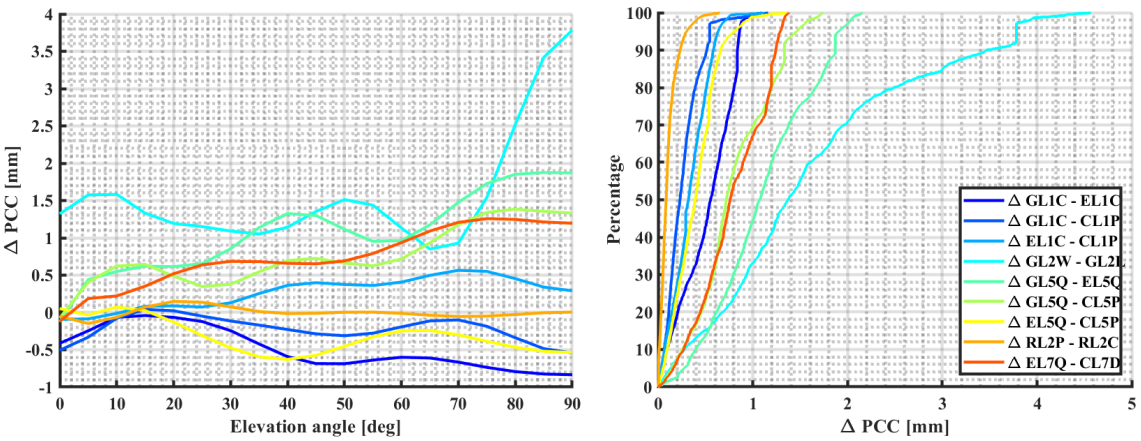


(a) Averaged ΔPCC per elevation angle

(b) Cumulative histogram of absolute ΔPCC

**Figure 5.44:** NOV ΔPCC between identical frequencies from different GNSS.

cause the same GLONASS satellites transmit these frequencies, leading to identical geometry and observation distribution over the antenna hemisphere. For the other frequency pairs, the differences are below 2.2 mm, except for Δ(GL2W - GL2L). In this case, the maximum difference between the two GPS signals with different tracking modes is 4.6 mm. As detailed in Section 5.1, GL2W exhibits unexpectedly high dSD with the *Septentrio* receiver (specific settings), leading to higher residuals after the LSA. This is not the case for GL2L; refer to Figure 5.7 for GL2W and Figure 5.8 for GL2L. The larger differences between GL2W and GL2L can be attributed to the noisy input observations and a 14% difference in the number of available observations between the two frequencies, as shown in Figure 5.29.

The above-mentioned reasons explain the higher differences, which are in accordance with the results presented in Kröger et al. (2021). In that study, the results obtained by identical *Septentrio* receivers with another AUT (*LEIAR20 LEIM*) are analyzed. Along with the characteristic values of the study carried out in this work, the values from Kröger et al. (2021) are listed in Table 5.6. It is visible, that the characteristic values describing the ΔPCC reflect the differences quite well.

**Table 5.6:** NOV ΔPCC between identical frequencies (from different GNSS). In addition, the results presented in Kröger et al. (2021) are listed in the last column.

| **ΔPCC** | **Max** | **Std** [mm] | **RMS** | **Δ#Obs** | **Kröger et al. (2021)** [mm] |
|---|---|---|---|---|---|
| GL1C - EL1C | 1.09 | 0.32 | 0.58 | 7173 | max < 1.0 |
| GL1C - CL1P | 1.16 | 0.22 | 0.31 | 2085 | |
| EL1C - CL1P | 1.12 | 0.27 | 0.38 | 5088 | |
| GL2W - GL2L | 4.57 | 1.13 | 1.94 | 5407 | max < 4.2 |
| GL5Q - EL5Q | 2.15 | 0.57 | 1.21 | 12064 | max < 1.0 |
| GL5Q - CL5P | 1.74 | 0.46 | 0.88 | 17155 | |
| EL5Q - CL5P | 1.35 | 0.32 | 0.45 | 5091 | |
| RL2P - RL2C | 0.65 | 0.14 | 0.14 | 0 | |
| EL7Q - CL7D | 1.38 | 0.43 | 0.86 | 5086 | max < 2.3 |

### Impact on Geodetic Parameters

In order to assess the impact of the ΔPCC on geodetic parameters, the developed simulation approach is used. The basic processing parameters are stated in Section 3.3.2. Here, the impact is calculated for three consecutive days in April 2024 for station BAKE, located in Canada (see Figure 3.7). In principle, a single frequency mode is used. However, for cases where two different GNSS are involved, e.g. Δ (GL1C - EL1C), both satellite geometries from the involved GNSS systems are used. In these cases, two different clock errors, for each system, are estimated.

Figure 5.45 illustrates the results for all cases as the norm of topocentric coordinate differences. In addition, Figure 5.46 shows exemplarily the results for all geodetic parameters for Δ(GL1C - EL1C), Δ(GL2W - GL2L) and Δ(RL2P - RL2C), respectively.

The results in Figure 5.45 reflect in principle the order of magnitude of each case, which can be seen in Figure 5.44. While Differences Δ(GL2W - GL2L) have the highest impact on the position solution, Δ(RL2P - RL2C) and Δ(GL1C - CL1P) show the lowest impact. All in all, the magnitudes are slightly smaller compared to the differences on the pattern level. This is due to the fact that parts of the differences are mapped into the receiver clock error and the tropospheric zenith delay, which are not visualized in Figure 5.45. It is worth noting that especially for Δ(GL2W - GL2L) highly comparable variations across the different days are present. This is due to the sidereal orbit repetition time of GPS, as further addressed in Section 7.2.2.

The results presented in Figure 5.46 underline the impact of the selected cases on the individual geodetic components separately. The impacts for all three cases range from -4 mm to 2 mm. Notably, the topocentric Up-component and the receiver clock error are the most affected across all cases. A clear correlation between the estimated receiver clock error(s) and the Up-component is evident. The effect on the horizontal topocentric coordinate differences and the tropospheric parameter are largely smaller. It is also observable that variations over the processed time span of three days are present. This underlines again that the actual processing time (and therefore the local satellite distribution) plays a crucial role.

In addition, it can be stated that the differences at the pattern level only reflect to some extent the order of magnitude the ΔPCC have in the parameter domain. For example, ΔPCC (GL1C - EL1C) shows differences at maximum of 1.09 mm at the pattern level. However, the maximum in the position domain, i.e. the Up-component, is higher with at maximum 1.5 mm. This is due to the fact that the differences are summed-up over the interval of 30 min, see

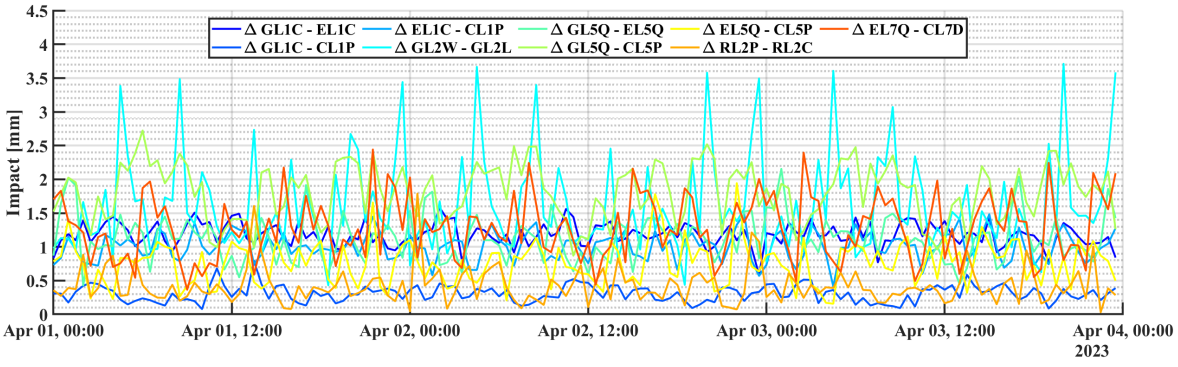


**Figure 5.45:** Impact of ΔPCC between identical frequencies (from different GNSS) on position solutions using the developed simulation approach. Results are depicted as the norm of 3D topocentric coordinate differences.

Section 3.3.2. This underlines again the need to compare the impact of ΔPCC on geodetic parameter rather than only analyzing the differences on the pattern level.

Overall, for these specific analyses (including the ΔPCC, as well as the particular geographic location and processing parameters), the impact on the position domain is relatively small. For instance, in the case of PPP, it remains below the expected position accuracy. Therefore, in this specific scenario, using a single frequency-dependent PCC set for various GNSS is sufficient.

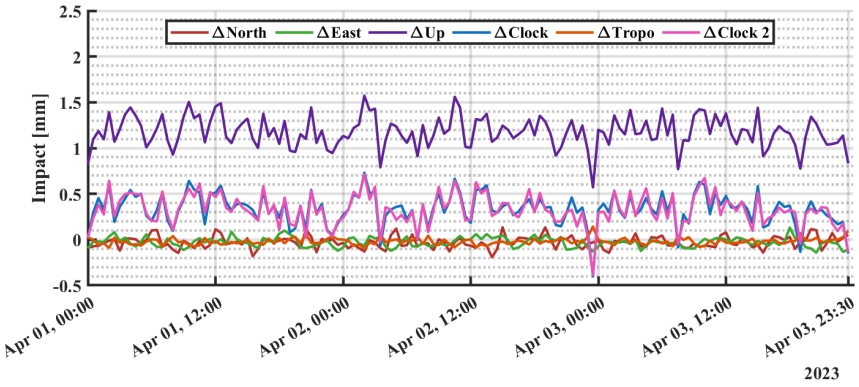


(a) Δ (GL1C - EL1C)

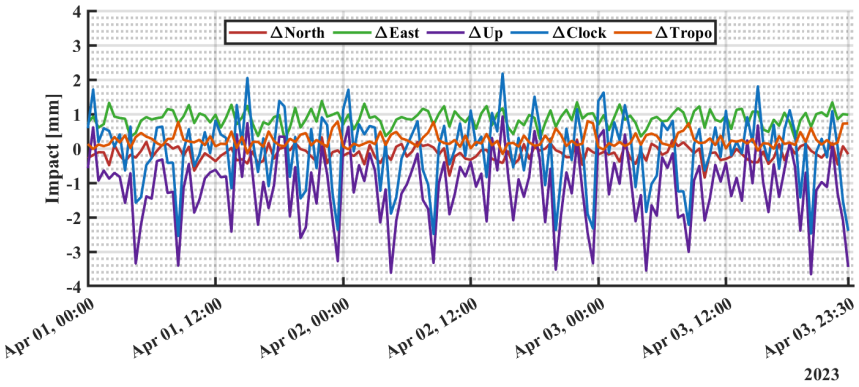


(b) Δ(GL2W - GL2L)

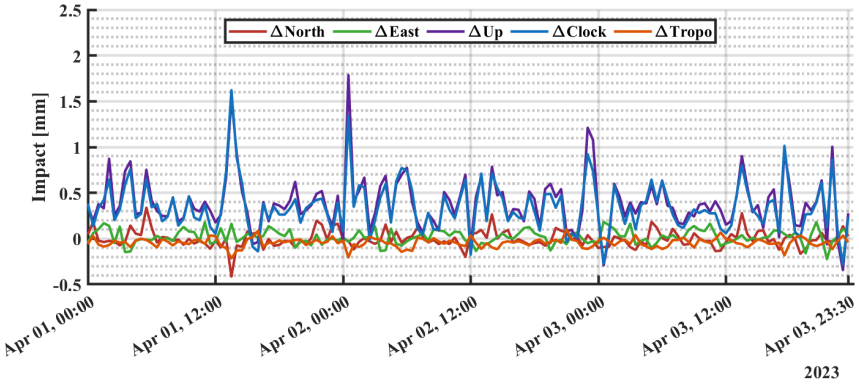


(c) Δ(RL2P - RL2C)

**Figure 5.46:** Impact of ΔPCC between identical frequencies (from different GNSS) on geodetic parameters. Note the different scales for the y-axes.

## 5.6 Comparison to Type-mean Calibration Values

In order to briefly compare the estimated NOV PCC with external data, differences with respect to the type-mean calibrations, published in the file *igs20_2343.atx*, are computed and illustrated in Figure 5.47. It can be seen that ΔPCC ranges overall from -4 mm to 3 mm, while the mean differences per elevation angle (solid lines) are smaller, predominantly falling within the range of ±1.5 mm. The standard deviations of ΔPCC range from 0.60 mm for EL8Q to 1.20 mm for RL1C. It is also noteworthy that offsets occur at a 90° elevation angle, which can be attributed to differences in the $PCO_{Up}$ and/or constant parts $r$.

The observed differences are generally within a typical order of magnitude when comparing individual calibrations with type-mean calibrations, even when different types of AUT are considered. For instance, Tupek et al. (2024) examine the estimated GPS PCC for the *LEIAX1202GG NONE* compared to IGS type-mean values. They found that the maximum difference for the L1 frequency is 2.31 mm, whereas the differences for the L2 frequency are greater, at 3.60 mm. Additionally, Dawidowicz et al. (2021) notes that for two different geodetic antennas, the ΔPCC remains within 2 mm. However, deviations exceeding 2 mm are observed at both high elevation angles (70° to 90°) and low elevation angles (0° to 10°).

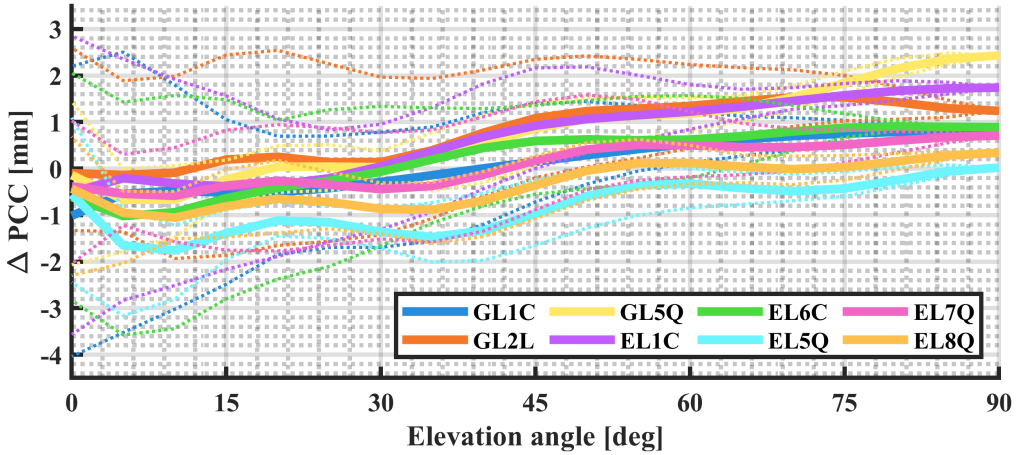


(a) GPS and GALILEO ΔPCC

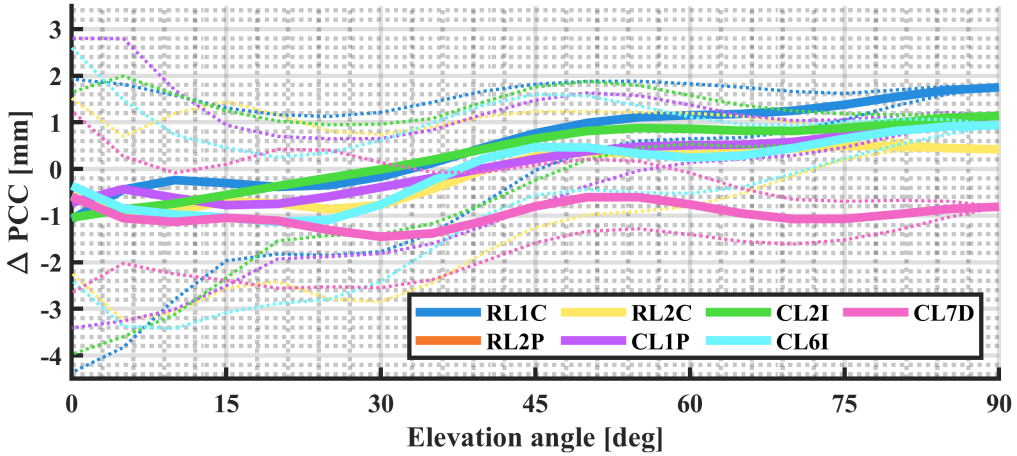


(b) GLONASS and Beidou ΔPCC

**Figure 5.47:** Comparison of estimated NOV PCC with type-mean calibrations from the file *igs20_2343.atx*.

# 6

# Variation of Processing Parameters

During the entire processing chain of the calibration procedure, several parameters can be set, which have a different impact on the estimated PCC. Figure 6.1 depicts the general antenna calibration procedure along with the parameters, which can be modified at the respective stages. In this subsection, the impact of the different processing parameters' settings are discussed. Unless otherwise stated, these *standard calibration* parameters are used for the investigations:

- AUT: *NOV703GGG.R2 NONE*
- Calibration time and length: DOY47 (2023), one single set with a duration of $\approx 4.5$ hours.
- *Septentrio PolRx5TR* receivers with standard receiver settings (DLL bandwidth = 0.25 Hz, PLL bandwidth = 15 Hz).
- Topocentric elevation cut-off angle = 5° and elevation cut-off angle in the antenna frame = −5°.
- Detection and removing outlier strategy: simple threshold method deleting dSD > 60 mm.
- HSH with degree and order 8 (denoted as HSH(8,8)) used to parametrize PCC, no further restrictions applied on the level of the NES.
- Observation weighting scheme: equal weighting ($\mathbf{P} = \mathbf{I}$).
- Resolution of PCC grid: 5° zenith and 5° azimuth angles steps.
- PCV, PCO and $r$ are separated with restriction that PCV=0 at zero zenith.
- PCC are calculated following Equation 2.27, including the constant part $r$.

The selected parameters are then varied in the following sections.

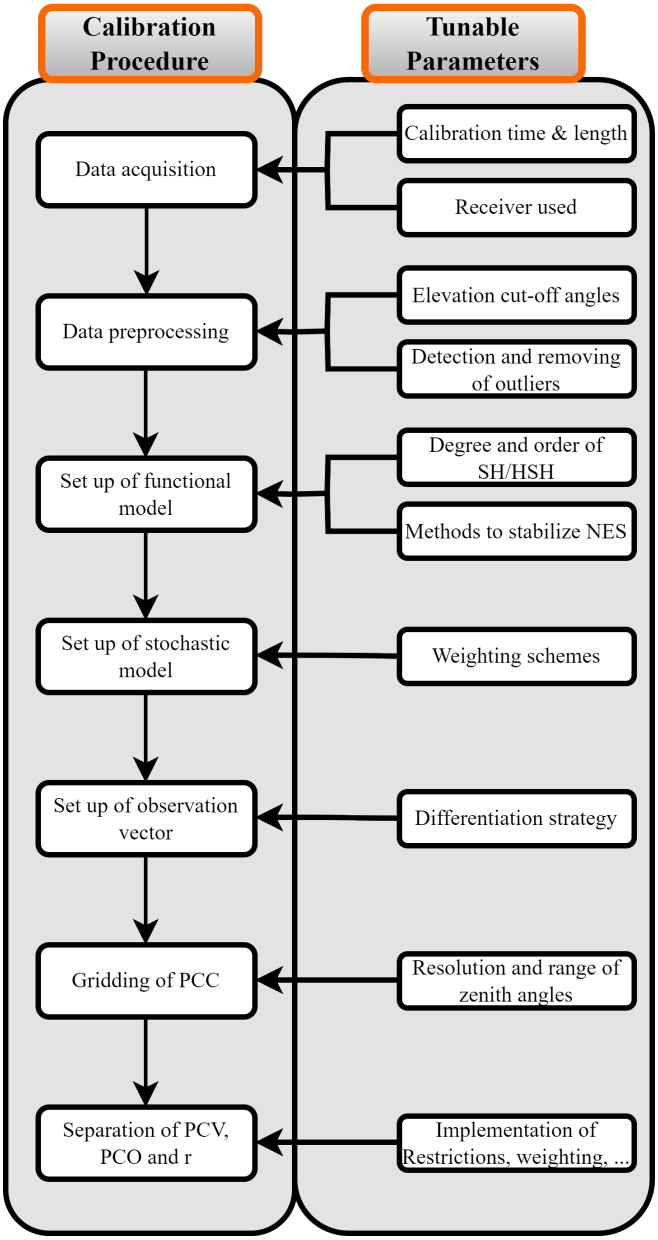


**Figure 6.1:** Flowchart illustrating the calibration procedure, highlighting adjustable parameters.

## 6.1 Calibration Time and Length

To investigate the influence of calibration time and length in detail, an experiment was performed using identical robot poses and utilizing the same GPS constellation as closely as possible. To this end, an initial robot calibration was carried out (set 1). Next, the actual used robot poses were extracted, and a sequence script was written to run at the GPS sidereal repeatability time. Since absolute timestamps could not be used, the experiment was repeated as accurately as possible (set 2). As the calibration was carried out on the following day, set 2 is set to start 236 s earlier than set 1 started. This would take the mean sidereal repetition time into account. However, as stated in Dilssner (2007), the individual GPS satellites have individual repetition times. At the end, the analysis shows that set 2 started 234 s earlier than set 1, so that an offset of $\approx 2$ s w.r.t. the nominal mean sidereal GPS repetition time is present.

Finally, a third calibration with the identical robot poses but during another time period were carried out, namely set 3. For all calibrations, the identical equipment was used: SEPT receivers and NOV antenna as the AUT.

The analyses of calibration time and length involve examining and comparing input observations across different sets. This also includes assessing differences in observation distribution. The section closes with a comparison of the estimated PCC.

### Evaluation of Input Observations and their Distribution

Figure 6.2 illustrates the dSD for all three sets for frequencies GL1C, GL5Q and EL1C versus the GPS time. Figure 6.3 also presents these time series w.r.t. the robot pose index. The expectation is that dSD of GL1C and GL5Q would be most similar between set 1 and set 2, due to (almost) sidereal repeatability and the same robot poses. However, this similarity is not immediately obvious from the graphs. For instance, there are high dSD values for GL1C around 8:30 GPS time (epoch $\approx 1500$), which do not appear in the other sets. These visual observations are supported by the standard deviations shown in Table 6.1. For example, GL1C reveals greater similarity in standard deviations between set 2 and 3 than GL1C does between set 1 and set 2.

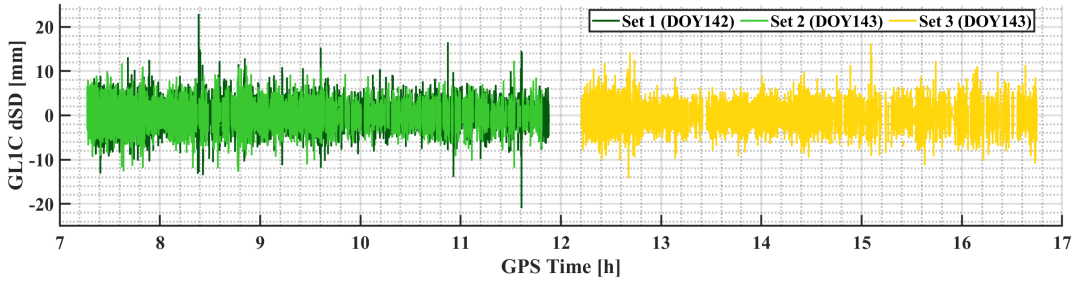


(a) GL1C

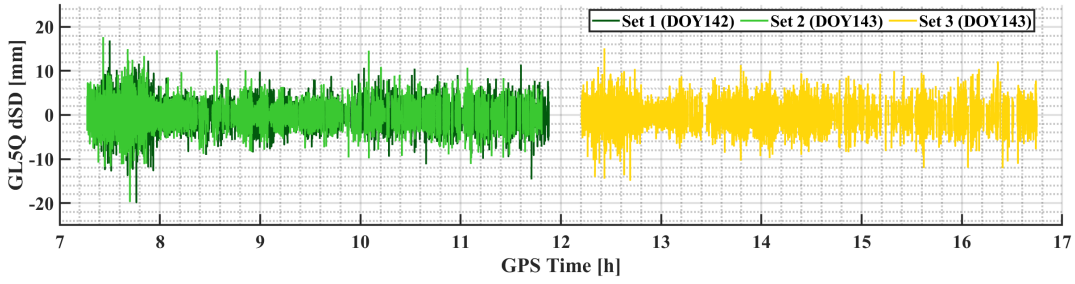


(b) GL5Q

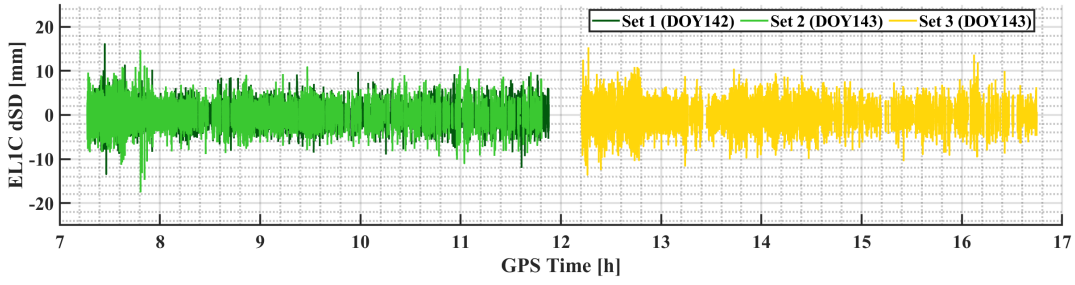


(c) EL1C

**Figure 6.2:** Input dSD versus GPS time for calibrations with identical robot poses. Sets 1 and 2 are conducted with the same GPS satellite constellation as far as possible, considering sidereal repetition time.

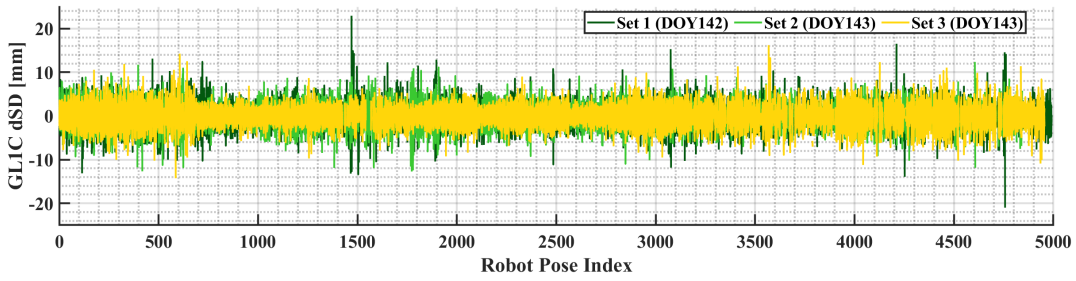


(a) GL1C

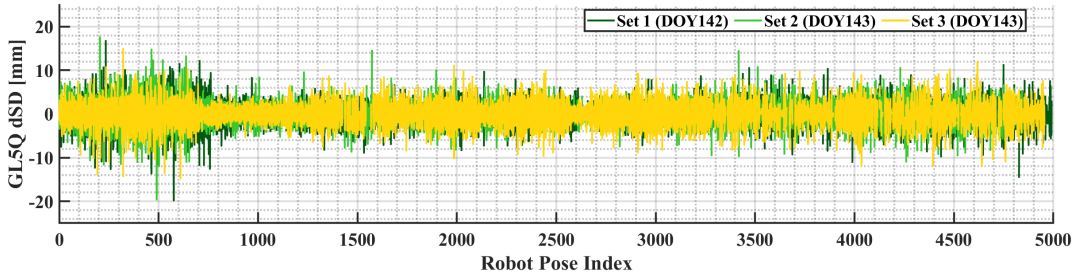


(b) GL5Q

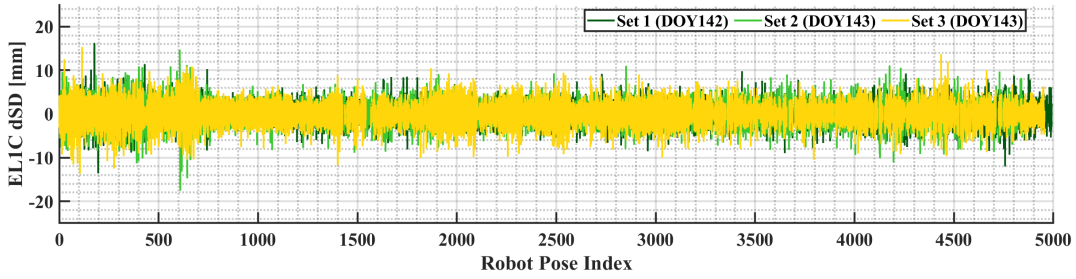


(c) EL1C

**Figure 6.3:** Input dSD versus robot pose index for calibrations with identical robot poses. Sets 1 and 2 are carried out using the GPS satellite constellation that is as similar as possible, taking into account the sidereal time of repetition.

Figure 6.4 illustrates the differences in observation distribution within the antenna system compared to set 1. As shown, the differences for GL1C and GL5Q between sets 1 and 2 are remarkably small, with maximum differences of 13 and 11, respectively (refer to Table 6.2). As expected, the differences in observation distribution for EL1C, as well as the differences between sets 2 and 3, are more pronounced across all frequencies. This indicates that the calibrations carried out have been successful in producing a highly comparable geometry within the antenna system. This similarity is not immediately apparent through visual inspection of the observations.

**Table 6.1:** Standard deviations $\sigma$ of input dSD.

| | **GL1C** | **GL5Q** | **EL1C** |
|---|---|---|---|
| | $\sigma$ [mm] | | |
| Set 1 | 2.01 | 2.18 | 1.77 |
| Set 2 | 1.90 | 2.12 | 1.88 |
| Set 3 | 1.87 | 2.17 | 2.03 |

**Table 6.2:** Maximum number of observation differences within each 5° azimuth and elevation bin.

| | **GL1C** | **GL5Q** | **EL1C** |
|---|---|---|---|
| | max($\Delta$ # Obs) | | |
| $\Delta$(1 - 2) | 13 | 11 | 44 |
| $\Delta$(1 - 3) | 37 | 33 | 75 |

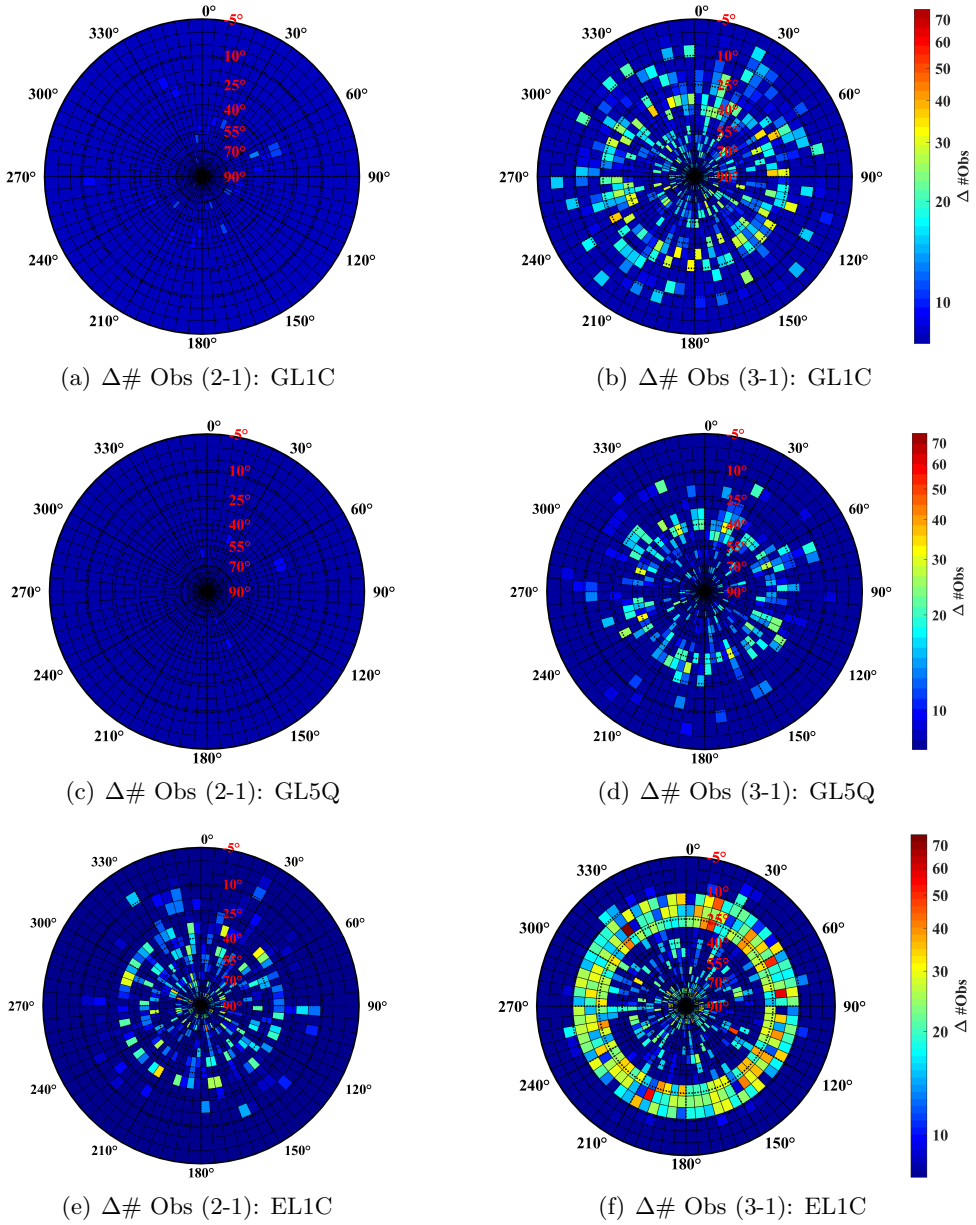


(a) Δ# Obs (2-1): GL1C

(b) Δ# Obs (3-1): GL1C

(c) Δ# Obs (2-1): GL5Q

(d) Δ# Obs (3-1): GL5Q

(e) Δ# Obs (2-1): EL1C

(f) Δ# Obs (3-1): EL1C

**Figure 6.4:** Differences in the number of observations for selected GPS and Galileo frequencies. First column: Differences between set 2 and set 1. Second column: Differences between set 3 and set 1.

### Comparison of Estimated PCC

Figure 6.5 shows the resulting PCC* (according to Equation 3.3, where a mean $PCO_{Up}$ of 58.27 mm has been subtracted from the PCC) and ΔPCC relative to set 1. It is evident that, across all frequencies, averaged variations per elevation angle indicate a higher similarity between sets 1 and 2 than between sets 2 and 3. However, at low elevation angles, the differences between sets 1 and 2, particularly when azimuthal variations are considered, are greater compared to Δ(1 - 3).

These findings align with the results from the analysis of individual repeatability conducted in Section 5.3. The key factor for achieving high agreement between individual calibration sets is not only the actual observation distribution across the antenna hemisphere but the quality of the observation data.

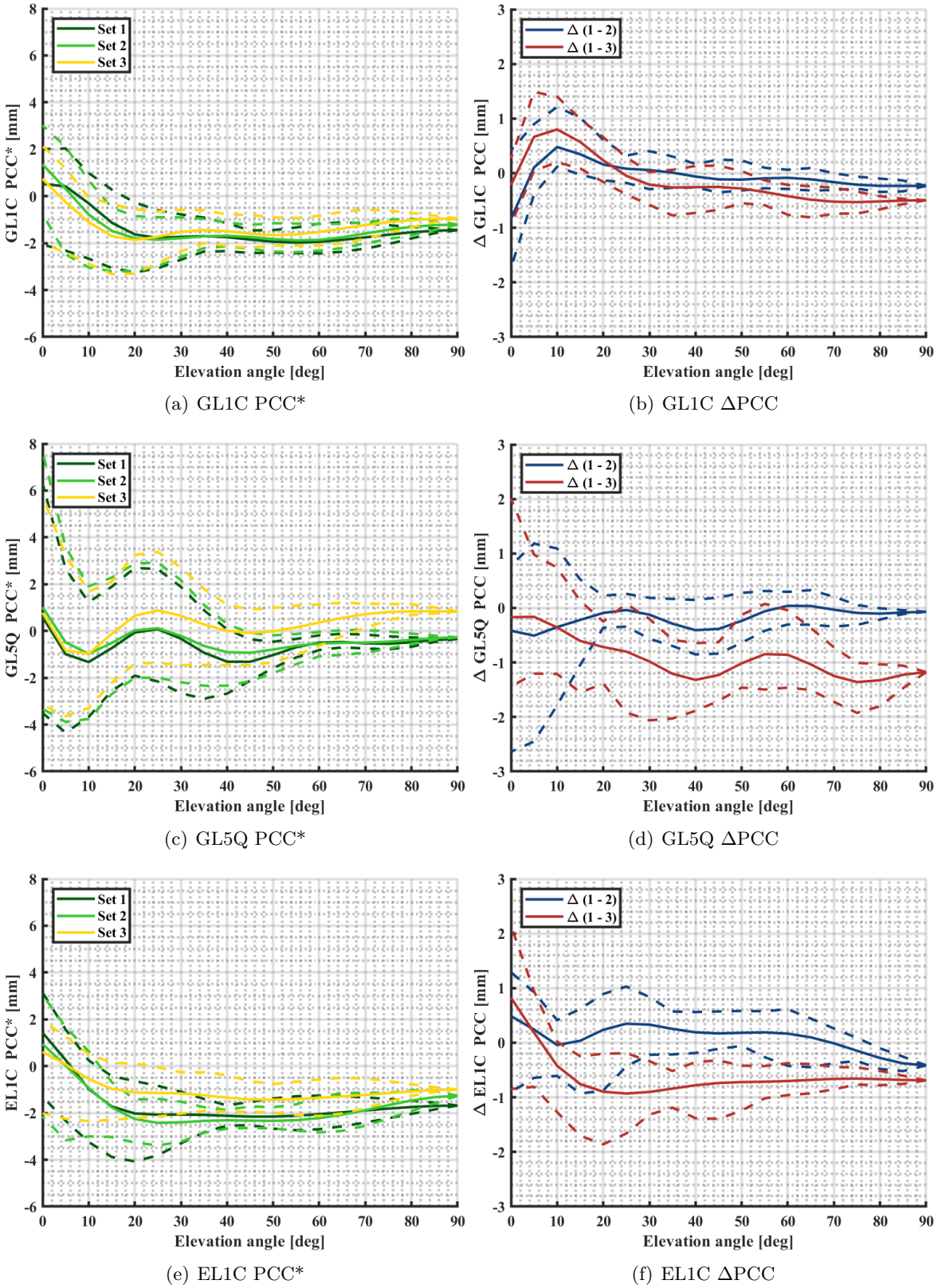


(a) GL1C PCC*

(b) GL1C ΔPCC

(c) GL5Q PCC*

(d) GL5Q ΔPCC

(e) EL1C PCC*

(f) EL1C ΔPCC

**Figure 6.5:** Averaged PCC* and ΔPCC per elevation angle between all calibration sets, used to analyze the impact of calibration time and length on resulting PCC.

## 6.2 Degree and Order of Hemispherical Harmonics

In this section, the influence of the selected degree $m$ and order $n$ of the HSH, denoted as HSH($m$,$n$), on the estimated PCC is analyzed. To this end, PCC are estimated using HSH up to degree $m = 12$ and order $n = 12$, while all other processing parameters remain unchanged. First, the total number of unknowns to be estimated and the condition number of NES for each HSH($m$,$n$) are briefly discussed. Next, the differences in the PCO components and constant parts $r$ are investigated. Afterward, averaged PCC* per elevation angle are shown. In order to reveal small azimuthal variations, SVD of selected HSH($m$,$n$) is carried out. The section closes with an assessment of the impact of the ΔPCC on geodetic parameters.

### Number of Unknowns and Condition Number

Figure 6.6(a) depicts the number of a- and b-coefficients to be estimated in a stacked bar plot, so that the total number of unknowns can directly be observed, too. On the x-axis, the corresponding HSH($m$,$n$) with continuous increasing $m$ and $n$ are given. In general, the number of unknowns increases with increasing $m$ and $n$. Since per definition coefficients b($m$,0) can not be estimated (Hofmann-Wellenhof and Moritz, 2006), the number of unknown a-coefficients is higher than b-coefficients. This also explains the reason for the small number of unknowns, which occur at each HSH($m$,0). Since the computational time increases with increasing number of unknowns, it is important to balance between a full representation of PCC, computational time and no overparameterization.

To get a first understanding of specific coefficients, Table 6.3 lists them along with their interpretation. For instance, if HSH(1,0) is selected, only the $\mathrm{PCO}_{\mathrm{Up}}$ component is estimated. Moreover, estimating PCC with $n$ set to 0 results in PCC that depend solely on elevation angles, thus excluding azimuthal variations. The factors $k_1$ and $k_2$ are introduced to shift the associated Legendre Polynomials (as detailed in Section 4.3). This means the listed coefficients do not directly represent the corresponding PCO components. Instead, these factors need to be properly considered. Typically, this modification is made during the HSH synthesis.

In order to analyze the impact of the selected $m$ and $n$ on the condition number of the NES, i.e. cond($\bar{\boldsymbol{N}}$), Figure 6.6(b) depicts the condition number as a function of $m$ and $n$. It can be seen, that the condition number increases with the total number of unknowns.

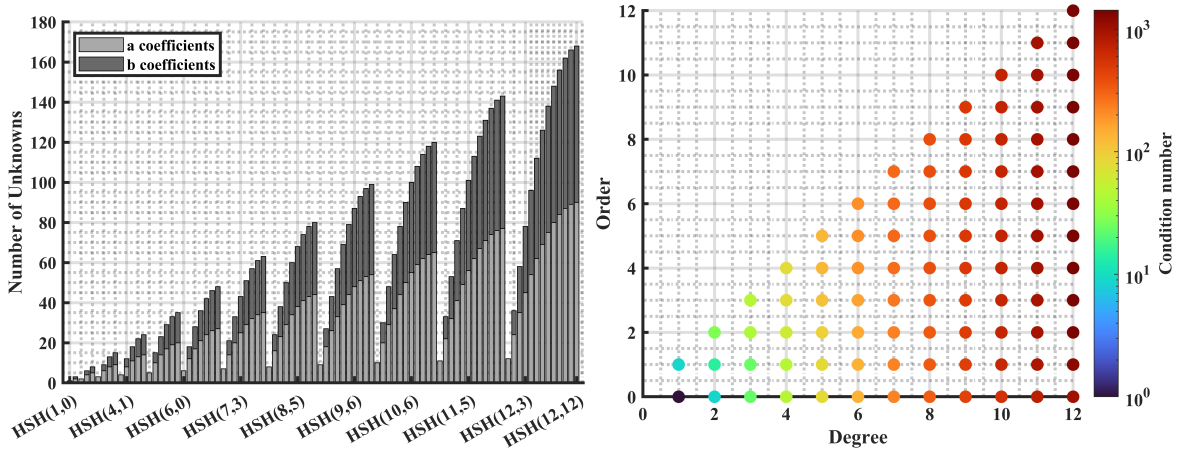


(a) Number of unknowns to be estimated

(b) Condition number of NES

**Figure 6.6:** Properties of PCC estimations with varying degrees and orders for HSH expansions.

**Table 6.3:** Interpretation of estimated HSH coefficients.

| Coefficient | Interpretation | Remark |
|---|---|---|
| $a_{00}$ | constant part $r$ | usually not estimated |
| $a_{10}$<br>$a_{11}$<br>$b_{11}$ | $\mathrm{PCO}_{\mathrm{Up}}$<br>$\mathrm{PCO}_{\mathrm{North}}$<br>$\mathrm{PCO}_{\mathrm{East}}$ | consideration of HSH factors needed |
| $a_{n0}$ | PCC only depending on elevation angles | |

A stronger increase can be observed for increasing $m$, whereas the condition number is not strongly impacted by $n$.

### PCO Differences and Averaged PCC per Elevation Angle

To get a first insight into the results of the 90 processings, the estimated GL1C PCO and constant parts $r$ after the full separation from the PCV, applying Equation 4.16 are depicted in Figure 6.7. Since the $a_{00}$ coefficient is usually not estimable, it is not present in the following graphics.

It can be seen that $\mathrm{PCO}_{\mathrm{North}}$ and $\mathrm{PCO}_{\mathrm{East}}$ (see Figure 6.7(a), 6.7(b)) are (almost) zero if $n = 0$. In this case, only variations dependent on elevation angles are estimated. Since the $\mathrm{PCO}_{\mathrm{Up}}$ (see Figure 6.7(c)) is only dependent on elevation angles, a change of the estimate is also only visible if $m$ changes. Moreover, the high correlation between $\mathrm{PCO}_{\mathrm{Up}}$ and $r$ can be observed. All in all, the PCO differences between the different processings is with maximum -1.2 mm rather small.

In order to get a more deep insight into the behavior of the different estimated PCC, Figure 6.8(a) depicts the averaged PCC* per elevation angle for all 90 processings. In order to make the variability between the individual processings more visible, a common $\mathrm{PCO}_{\mathrm{Up}}$ $\overline{d} = 58.27\,\mathrm{mm}$ is subtracted from all values using Equation 3.3. It should be noted that the depicted values illustrate the overall behavior of PCC* so that higher PCC* do not indicate a worse performance.

In general, it can be seen that comparable degree and order show a similar behavior, i.e. blueish and reddish curves have a very comparable course. It is worth noting, that some curves show a higher divergent. To this end, selected HSH with specific degree and order are depicted in Figure 6.8(b). Here, it can clearly be seen that HSH(1,0) leads to a totally different PCC*. This was expected since no horizontal parts are estimated. Moreover, HSH(5,0) shows a slightly different behavior. This is also evident in Figure 6.7(c), where a different estimated $\mathrm{PCO}_{\mathrm{Up}}$ is visible. HSH with $m \geq 6$ (e.g. HSH(6,0), HSH(8,5), ...) demonstrate another behavior. They do not show an overall smooth decrease of PCC* with increasing elevation angle.

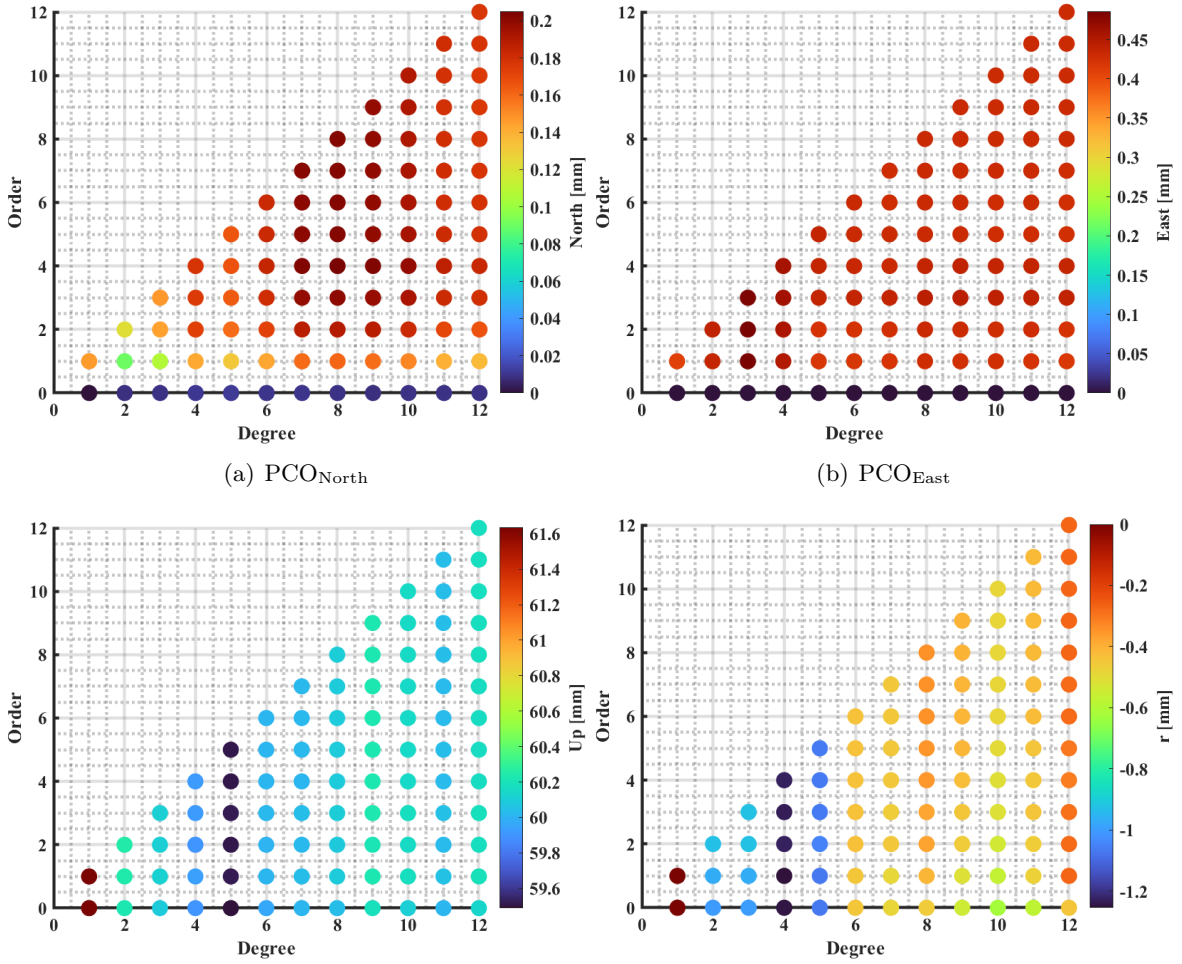


(a) $\mathrm{PCO}_{\mathrm{North}}$ (b) $\mathrm{PCO}_{\mathrm{East}}$

(c) $\mathrm{PCO}_{\mathrm{Up}}$ (d) constant part $r$

**Figure 6.7:** Estimated GL1C PCO and $r$ components using different degrees and orders for HSH expansions. Note the different scales for the colorbars.

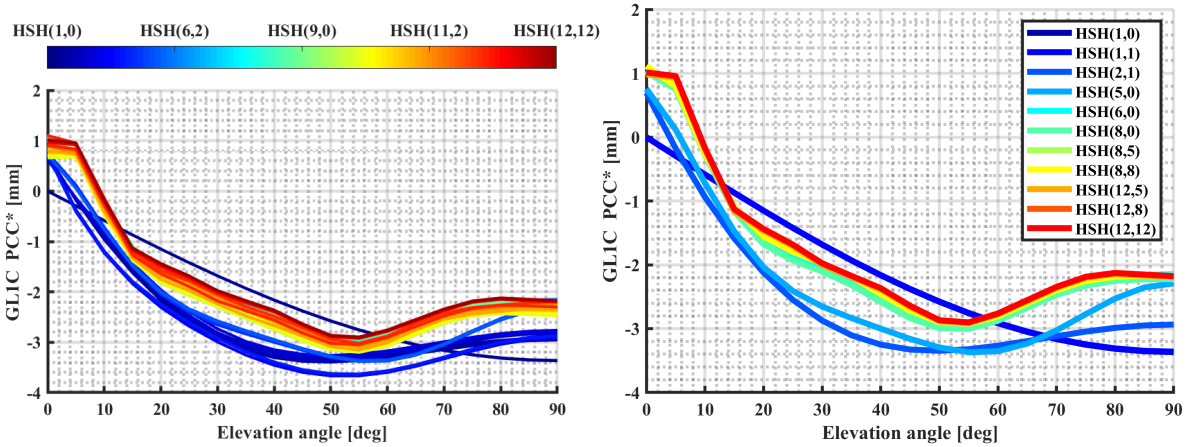


(a) For all processed HSH expansions (b) For selected degree and order

**Figure 6.8:** Averaged PCC* per elevation angle, estimated with different degree and orders for HSH expansions.

### Singular Value Decomposition of PCC

In order to get a more deep insight into the structure of the different PCC – including azimuthal variations – SVD of the different patterns is carried out. According to Kröger et al. (2022c), SVD can be used to express ΔPCC or in this case PCC as the product of the three matrices **U**, **S** and **V**. Matrix **S** contains the singular values $s_i$ on the main diagonal

$$\mathbf{PCC} = \mathbf{U} \cdot \mathbf{S} \cdot \mathbf{V}^{\mathrm{T}} = \sum_{i=1}^{i_{\max}} \mathbf{u}_i \cdot s_i \cdot \mathbf{v}_i^{\mathrm{T}} = \sum_{i=1}^{i_{\max}} \mathbf{M}_i. \tag{6.1}$$

The results of SVD applied to simulated ΔPCC, along with a discussion of pros and cons of the methodology, are available in Kröger et al. (2022c). Generally, the authors suggest that SVD can be used to identify and characterize distinct structures within the PCC. It provides an approximation of the PCC data matrix through the Frobenius norm, with the rectangular data matrix serving as a hemisphere map. It should be noted that each grid point contributes equally to the Frobenius norm, although grid points at lower elevation angles represent a larger area of the spherical segment. This represents a common drawback of the standard mapping method for PCC (Kröger et al., 2022c).

In the following, SVD results for selected HSH($m$,$n$) are analyzed. The SVD of the respective PCC is carried out for $i_{\max} = 5$, in addition a remaining class containing the sum of all remaining non-zero $\mathbf{M}_i$ is calculated.

Figure 6.9 shows the results for HSH(1,0), HSH(1,1), and HSH(2,1). For HSH(1,0), only $\mathbf{M}_1$ contains information, specifically the $\mathrm{PCO}_{\mathrm{Up}}$ component. In the case of HSH(1,1), the horizontal PCO components are also estimated, which involve the coefficients $a_{11}$ and $b_{11}$, as listed in Table 6.3. For HSH(1,1), $\mathbf{M}_1$ and $\mathbf{M}_2$ contain PCC information. While $\mathbf{M}_1$ clearly displays the $\mathrm{PCO}_{\mathrm{Up}}$ component, $\mathbf{M}_2$ particularly illustrates the $\mathrm{PCO}_{\mathrm{North}}$ and $\mathrm{PCO}_{\mathrm{East}}$ components. Refer to Figure 3.2 for a separate depiction of how offsets in the north and east directions appear. In the case of HSH(2,1) further PCC structures are estimated, so that $\mathbf{M}_3$ contains these additionally information.

It is worth noting, that only $\mathbf{M}_1$ shows significant structures when $n$ is 0. This implies that $\mathbf{M}_1$ typically represents the structures of the PCC that depend solely on elevation angles. As shown in Figure 6.9, the graphics for $\mathbf{M}_1$ closely correspond to the overall PCC, such as in Figure 5.2. Consequently, HSH($m$,0) are not presented here.

Since higher degree and order of HSH shows only very small varieties between the estimated PCC, the SVD results are not depicted in detailed here. Exemplarily, Figure 6.10(a) illustrates ΔPCC between HSH(8,8) and HSH(8,5), where the differences remain within a range of ±0.1 mm. An interesting pattern becomes apparent in these differences, with positive and negative values alternating evenly across the antenna hemisphere. This pattern likely correlates with the number of zero crossings associated with each HSH($m$,$n$).

Additionally, Figure 6.10(b) shows ΔPCC between several pairs: HSH(12,12) and HSH(8,5), HSH(8,8), HSH(12,5), and HSH(12,8). These combinations have been chosen based on their frequent use in PCC estimation at different calibration institutions, as shown in Table 2.6. The differences observed are generally below 1 mm, and for averaged PCC per elevation angle, they are even below ±0.2 mm. Notably, ΔPCC values, which also vary with azimuth angle (indicated by dashed lines), increase as the elevation angle decreases. Moreover, the more similar the HSH expansions are, the smaller the differences in ΔPCC. For instance, the smallest differences occur between HSH(12,12) and HSH(12,5).

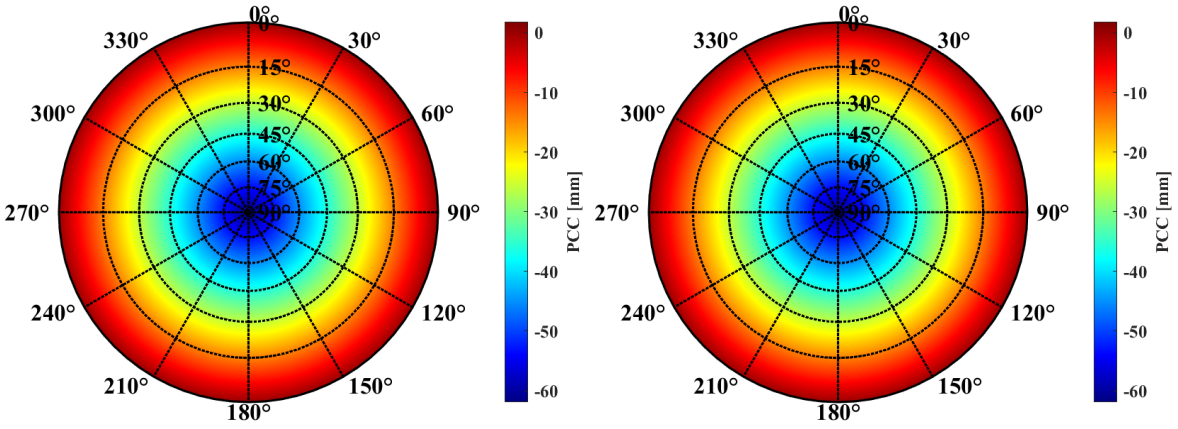


(a) HSH(1,0): $\mathbf{M}_1$




(b) HSH(1,1): $\mathbf{M}_1$

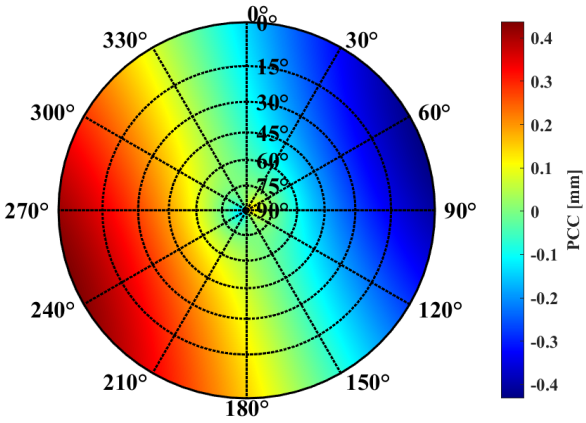


(c) HSH(1,1): $\mathbf{M}_2$

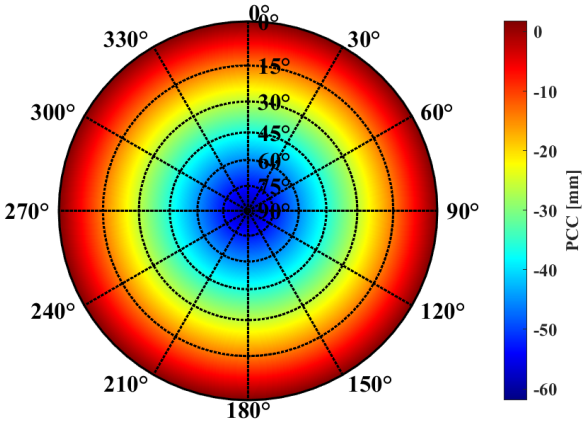


(d) HSH(2,1): $\mathbf{M}_1$

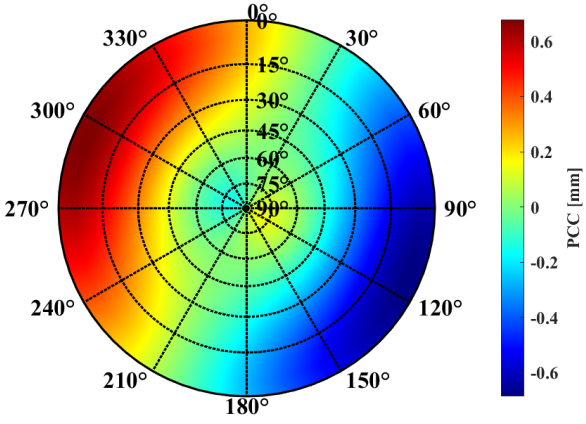


(e) HSH(2,1): $\mathbf{M}_2$

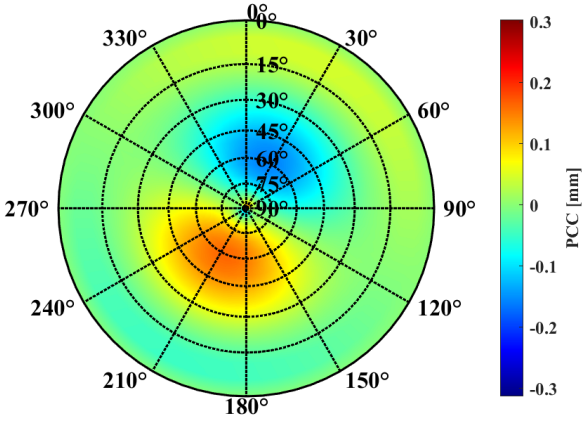


(f) HSH(2,1): $\mathbf{M}_3$

**Figure 6.9:** Stereographic projections of $\mathbf{M}_i$ matrices resulting from SVD of PCC, estimated using different HSH expansions: HSH(1,0), HSH(1,1), and HSH(2,1). Note the different colorbar scales.

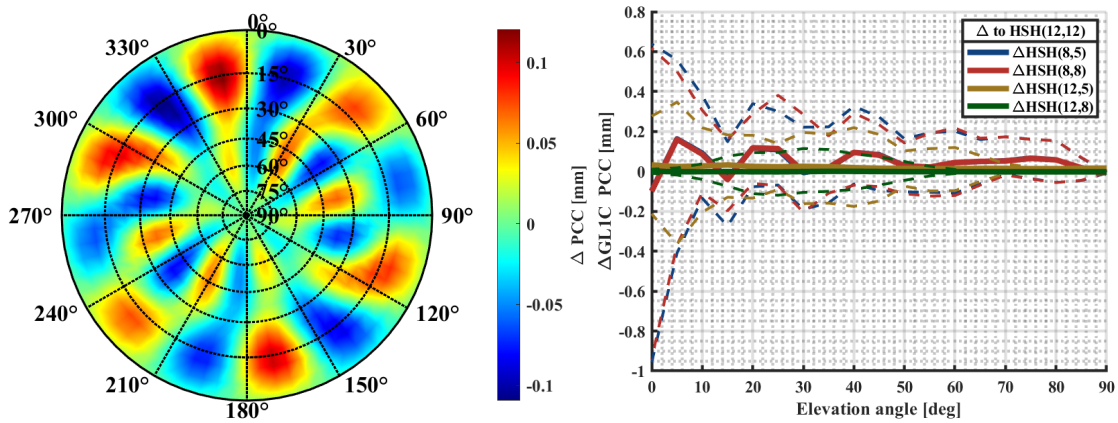


(a) Stereographic projection of ΔPCC (HSH(8,8) - HSH(8,5))

(b) Averaged ΔPCC per elevation angle bin relative to HSH(12,12)

**Figure 6.10:** Illustration of ΔPCC between different PCC parametrizations using various HSH expansions.

### Impact on Geodetic Parameters

To assess the impact of the ΔPCC on geodetic parameters, the developed simulation approach is used. The basic processing parameters are specified in Section 3.3.2. The impact is evaluated for three consecutive days in April 2024 at station BAKE, located in the Northern Hemisphere, as shown in Figure 3.7. The ΔPCC input is based on the differences between the HSH(12,12) and selected examples. Their average PCC* per elevation angle is presented in Figure 6.8(b). The results for each HSH run are averaged over the observation period, with the minimum and maximum values across all three days depicted in Figure 6.11.

It is evident that as the degree and order of the HSH increase, both the magnitude of the mean values and the range of the values decrease. This observation is expected, given that

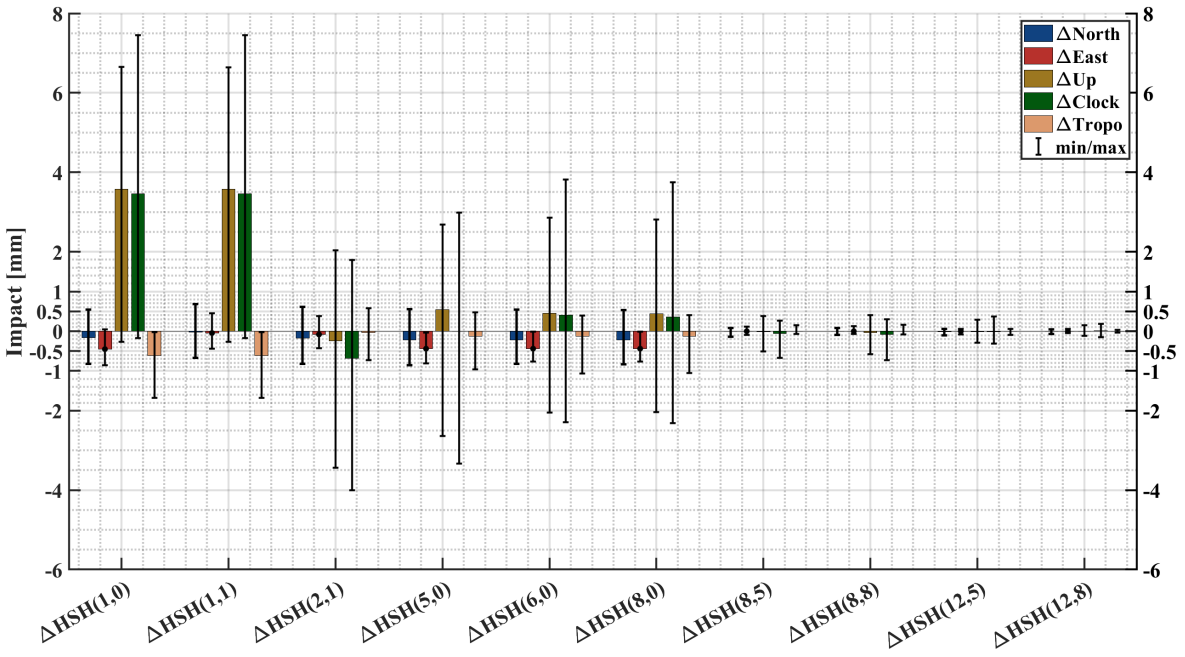


**Figure 6.11:** Impact of PCC estimated using different degrees and orders in the HSH expansion. Differences are calculated relative to HSH(12,12), and the impact is averaged over three days. In addition, minimum and maximum values are presented, too.

differences are computed with respect to HSH(12,12). The highest deviations are seen in ΔHSH(1,0) and ΔHSH(1,1) for ΔUp and ΔClock, reaching up to 7.5 mm. This trend is also illustrated in Figure 6.7(c) and Figure 6.7(d), where $PCO_{Up}$ and $r$ display a different order of magnitude for HSH(1,0) and HSH(1,1) compared to estimates with higher degrees and orders. Nevertheless, due to the summation of effects across all visible satellites and the summation interval $\delta t_\Sigma$ of 5 min, the overall magnitude of the impact is higher.

Usually, PCC are estimated using SH/HSH with $m > 8$ and $n > 5$, up to $m = n = 12$, as shown in Table 2.6. For these cases and the chosen settings, the impact is less than ±0.7 mm (including both minimum and maximum values), indicating that the degree and order used for SH or HSH do not significantly affect the estimated geodetic parameters since this impact is smaller than the expected absolute position accuracy achievable with methods like PPP.

## 6.3 Methods to Stabilize the Normal Equation System

Usually, PCC are parametrized by SH, which are defined for a full sphere. However, since reliable observations can only be measured in the upper antenna hemisphere, as for example depicted in Figure 4.10, the observation distribution is restricted to that region and subsequently the NES is poorly conditioned, when no further restrictions or adaptions are made. As introduced in Section 4.3, the algorithm developed in this work uses an adapted version of HSH to stabilize the NES. In this section, the developed method (A) is compared with further approaches:

(B) SH without applying further restrictions/adaptions on the basis of the NES

(C) SH are transformed to a three-quarters sphere

(D) SH are transformed to a hemisphere

(E) SH-coefficients with an odd index sum (e.g. $a_{21}$, $b_{21}$, $a_{30}$) are restricted to zero as they express the anti-symmetry between the upper and lower hemisphere.

For the different methods, Equation 4.3 changes accordingly. Equation 4.7 provides the adaption made for case (A). No further adaptions of Equation 4.3 are made for case (B). For (C) and (D), the term $\widetilde{P}_{mn}(\cos z^k)$ in Equation 4.3 changes to $\widetilde{P}_{mn}(f \cdot \cos z^k)$, where $f = 1.75$ for (C) and $f = 2$ for (D).

The detailed formulas for (E) are given in Kröger et al. (2021). Basically, the formulas for case (B) are used and after the stacking of the individual $\mathbf{N}$ matrices, the NES is extended with restrictions that ensures that the above-mentioned coefficients are restricted to zero. This means that after summing up $\boldsymbol{N_k}$ over all satellites $k$ (see Equation 4.13), an extended NES $\widetilde{\boldsymbol{N}}$ is set up

$$\widetilde{\boldsymbol{N}} = \begin{bmatrix} \bar{\boldsymbol{N}} & \boldsymbol{R}^{\mathrm{T}} \\ \boldsymbol{R} & \mathbf{0} \end{bmatrix} \tag{6.2}$$

with $\boldsymbol{R}$ being the restriction matrix and

$$\widetilde{\boldsymbol{n}} = \begin{bmatrix} \bar{\boldsymbol{n}} \\ \mathbf{0} \end{bmatrix} \tag{6.3}$$

for the right side. By inverting $\widetilde{\boldsymbol{N}}$, the NES is solved for the unknowns $a_{mn}$ and $b_{mn}$

$$\hat{\boldsymbol{x}} = \widetilde{\boldsymbol{N}}^{-1} \cdot \widetilde{\boldsymbol{n}}. \tag{6.4}$$

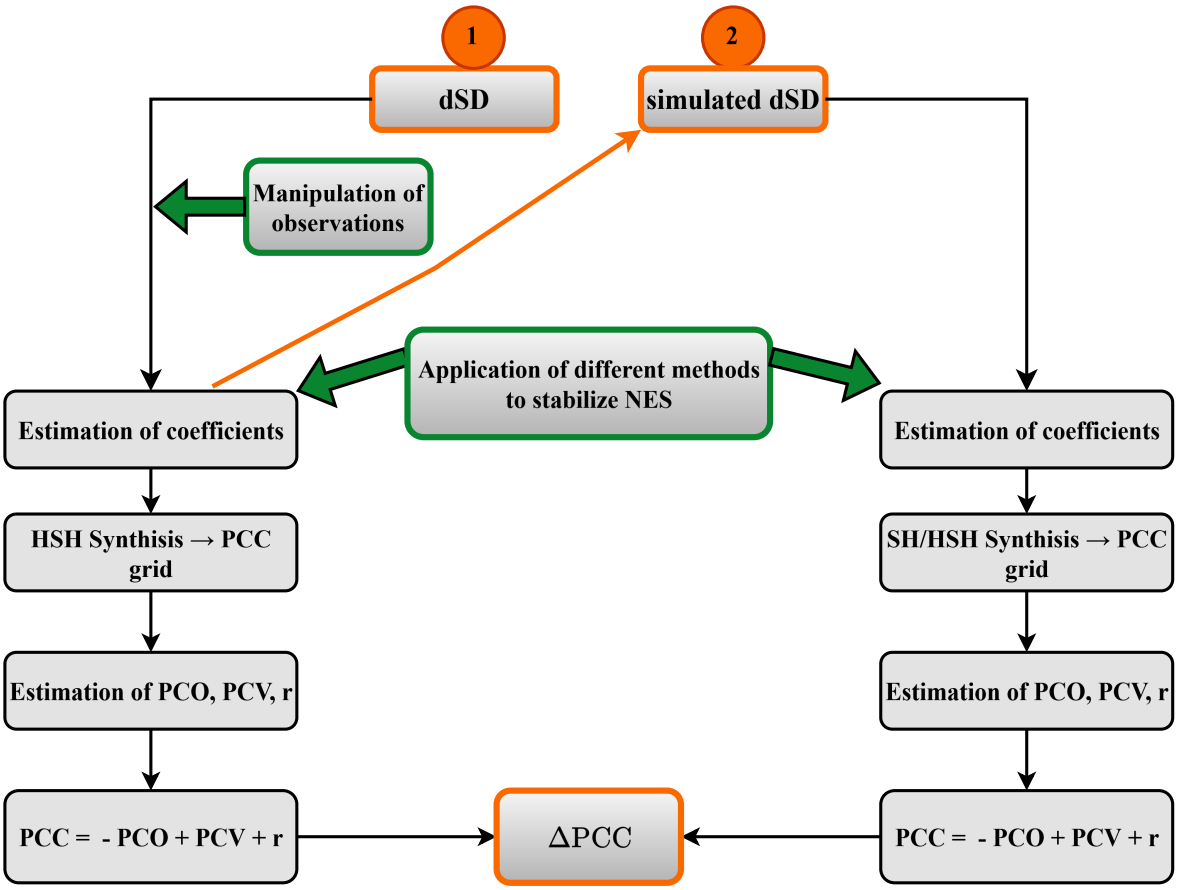


**Figure 6.12:** Flowchart illustrating the analysis strategy for investigating the impact of stabilization methods on the NES within the PCC estimation algorithm.

To provide a detailed analysis of the different methods, this section is organized in the following way. First, the condition number of the (extended) NES is studied for all methods and ΔPCC is analyzed for all cases w.rt. the newly developed method (A). Subsequently, the quality parameters of the estimated PCC, including the formal errors and distribution of residuals are presented. Following this, closed-loop simulations are performed according to the sequence outlined in Section 4.4.4, with simulated dSD generated directly from the estimated coefficients, ensuring that simulated observations for negative elevation angles are included. These simulations are performed using real dSD observations with and without the addition of white noise. The section concludes with an analysis of the stability of the methods presented. This includes assessing the impact of a significant outlier added to the observations on the estimated PCC, as well as the effect on the estimated PCC when observations from a specific satellite are excluded.

Figure 6.12 illustrates the overall procedure for analyzing various methods used to stabilize the NES. First, real dSD data are used to estimate SH/HSH coefficients. Following the synthesis, PCO, PCV, and the constant components $r$ are extracted from the generated grid using Equation 4.16. Subsequently, PCC are computed in accordance with Equation 2.27. Due to the introduction of a large constant offset $r$ into the PCC, some analyses are performed without including $r$. Simulated observations are generated directly from the coefficients, and the same processing steps are repeated with these observations, allowing for a comparison of the resulting PCC. The green-highlighted boxes in Figure 6.12 indicate the steps where methods for stabilizing the NES are applied and where the real observations are manipulated.

### Condition Number and PCC Differences

The key parameter to investigate is the condition number of the (extended) NES. The lower the number, the more stable the NES. Table 6.4 lists the condition numbers for the different cases and selected frequencies. It can be clearly seen that case (B) without any applied adaptions shows the highest condition number, followed by case (E). The overall lowest condition number is reached with method (D). However, the differences between (A), (C) and (D) are rather small (at maximum 91 between (A) and (D) for signal RL1C).

In order to visualize the differences w.r.t. to the in this work newly implemented case (A), Figure 6.13 shows exemplarily the PCC differences from all cases to case (A), i.e. (A) - (B), etc., for GL1C and CL2I. The differences are depicted as mean variations per elevation angles, and dashed lines indicate additionally the minimum and maximum values per elevation bin over all azimuth angles.

Since in the case of (B) a large constant offset $r$ is introduced to the PCC, $r$ is subtracted from the pattern here. As discussed in Section 3.1, it is valid to subtract any constant part from PCC. Thus, this is a valid strategy. For the sake of completeness, $r$ is provided in Table 6.5 for all cases and investigated frequencies. It can be seen, that in general the absolute value of $r$ is below 2 mm. However, for case (E) $r$ is up to -10 mm and for (B) even up to 4.5 m.

**Table 6.4:** Condition numbers of NES for various frequencies and stabilization methods.

| | **GL1C** | **GL5Q** | **EL1C** | **RL1C** | **CL2I** |
|---|---|---|---|---|---|
| (A) | 90 | 95 | 98 | 117 | 80 |
| (B) | $6 \cdot 10^{10}$ | $5 \cdot 10^{10}$ | $6 \cdot 10^{10}$ | $7 \cdot 10^{10}$ | $6 \cdot 10^{10}$ |
| (C) | 29 | 54 | 33 | 39 | 31 |
| (D) | 22 | 44 | 19 | 26 | 26 |
| (E) | 11665 | 13374 | 14481 | 16321 | 8159 |

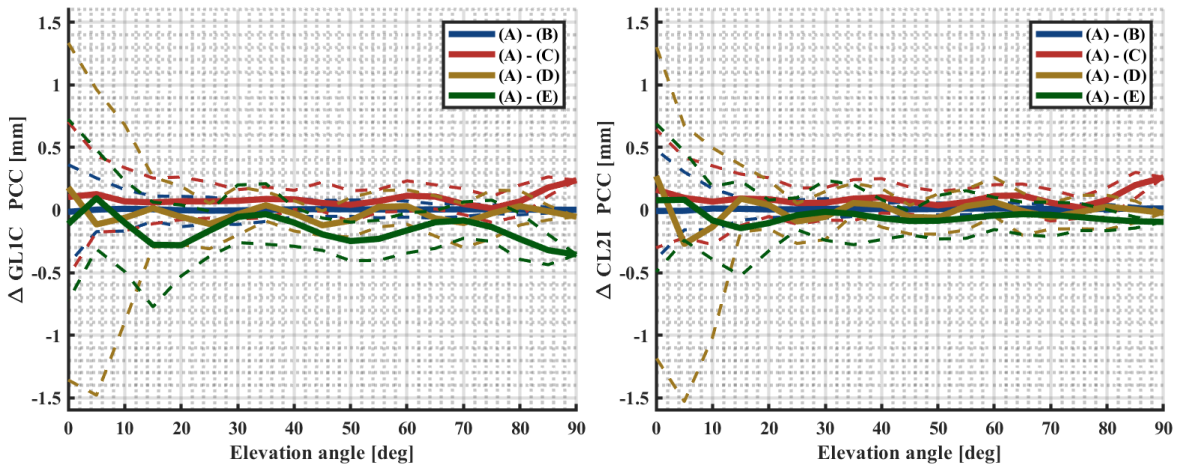


(a) GL1C (b) CL2I

**Figure 6.13:** Comparison of PCC estimated using different stabilization methods with respect to method (A), represented as mean differences per elevation angle. Dashed lines indicate the minimum and maximum differences per elevation angle.

**Table 6.5:** Constant $r$ values subtracted from PCC, estimated with various stabilization methods, to facilitate improved comparison between different PCC sets.

| | **GL1C** | **GL5Q** | **EL1C** | **RL1C** | **CL2I** |
|---|---|---|---|---|---|
| | | | [mm] | | |
| (A) | -0.93 | -0.98 | -1.08 | -0.84 | -0.97 |
| (B) | -220.37 | 4536.19 | -842.12 | 1456.68 | 380.62 |
| (C) | 1.55 | 0 | 0.95 | 1.02 | 1.25 |
| (D) | 1.80 | -0.04 | 1.21 | 1.27 | 1.49 |
| (E) | -5.04 | -9.84 | -4.11 | -5.52 | -5.88 |

In general, the deviations depicted in Figure 6.13 are in the range of approximately ±1.5 mm. Two specific characteristics for both frequencies can directly be observed. First, as seen at an elevation angle of 90°, differences in $\mathrm{PCO}_{\mathrm{Up}}$ are introduced. This is evident because $r$ is subtracted, and a *zero zenith* constraint is applied, as described in Equation 4.19. Thus, the only remaining component at 90° elevation angle is the $\Delta\mathrm{PCO}_{\mathrm{Up}}$. Second, azimuthal variations, indicated by the dashed lines, increase with decreasing elevation angles. The maximum differences are present for (A) - (D), where the values exceed the -1.5 mm level.

Another interesting behavior can be found for (A) - (E). Here, an oscillation in the differences, even amplified when the minimum and maximum values per bin are considered, is observable. This is probably due to introducing restriction on the level of the NES. To further analyze this, Figure 6.14 depicts the GL1C ΔPCC for (A) - (B) and (A) - (E) as stereographic projections. In order to highlight the differences in the pattern structure, no equal scales for the colorbars are used. In Figure 6.14(a), the differences are in a range of -0.4 mm to +0.3 mm. The highest absolute differences are present at low elevations. This is in accordance with Figure 6.13(a). In Figure 6.14(b), the differences of case (E) w.r.t. (A) are illustrated. Due to the introduced restrictions, the pattern differences show a clear oscillation, visually identifiable by regular stripes. These are alternating either colored yellowish, which indicates a positive difference of $\approx 0.2$ mm, or bluish, which indicates a negative difference of $\approx -0.4$ mm. Again, the highest differences are present at low elevation angles. This is due to the before mentioned fact that observations are mainly present at the upper hemisphere, although the SH are valid for all full sphere. Thus, the estimation in these regions is unstable.

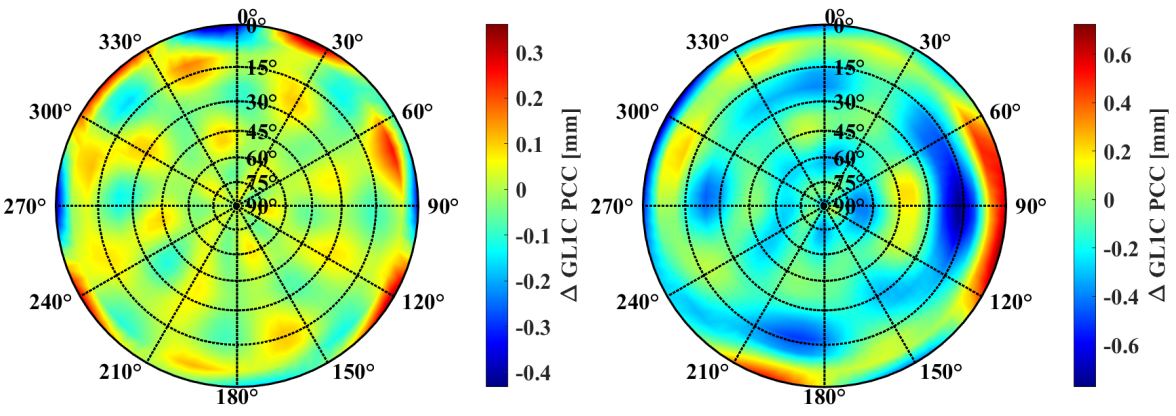


(a) (A) - (B) (b) (A) - (E)

**Figure 6.14:** ΔGL1C PCC resulting from PCC estimations using different methods to stabilize the NES, depicted as stereographic projections. Note the different colorbar scales.

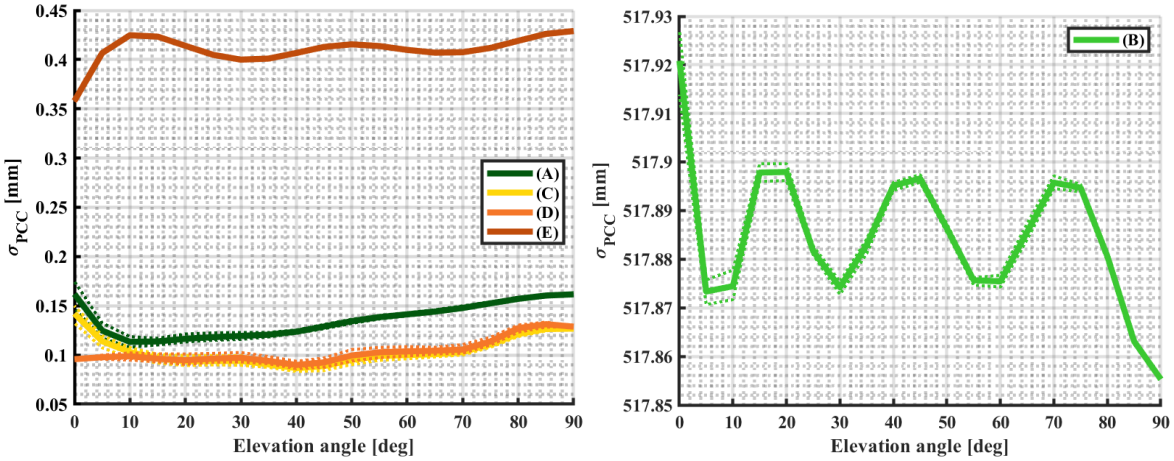


(a) cases: (A), (C), (D), (E) (b) case (B)

**Figure 6.15:** Averaged standard deviations $\sigma$ per elevation angle bin of estimated GL1C PCC using different stabilization methods, with $\sigma_0^2 = 4.01\,\text{mm}^2$ for all methods. Note the different scales for the y-axes.

### Quality Parameters

One important reason why the condition number of the NES should be within a moderate range, e.g. $< 1000$, is that otherwise a meaningful computation of the standard deviation $\sigma$ of the estimated PCC is not feasible. Figure 6.15 depicts the obtained standard deviations, averaged over the azimuth angles, for all five methods. The values are calculated using Equations 4.25 to 4.28, with $\sigma_0^2 = 4.01\,\text{mm}^2$. Since method (B) is in a completely different range, its values are depicted in Figure 6.15(b). Here, standard deviations up to almost 51.8 cm can be seen. The other methods show a $\sigma$ in a range of 0.08 mm up to 0.43 mm. The smallest standard deviations are present for case (C) and (D), whereas method (C) shows higher values at low elevation angles. It is worth noting that method (A) has similar standard deviations to (C) at low elevation angles, but larger values compared to (C) at mid and high elevation angles. For method (A), the lowest $\sigma$ values occur at mid-elevation angles. In addition, Figure 6.15 depicts the minimum and maximum standard deviations per elevation angle bin. It is evident that the variations within the azimuthal range are very small (less than 0.015 mm). All in all, a clear correlation between the magnitude of the standard deviations and the condition number of the NES is observable, compare with the condition numbers listed in the first column of Table 6.4.

To further address the unique characteristics of the selected methods, which can be used to stabilize the NES, the residuals and residual differences w.r.t. case (A) are presented in Figure 6.16. The residuals are for GL1C and CL2I and in each case in a range of $\pm 2$ cm, whereas the GL1C residuals are slightly higher than those of the CL2I frequency. Since the residuals are not normalized based on the variance of the input dSD, this reveals again that CL2I dSD have a smaller variance compared to the GL1C dSD ($2.94\,\text{mm}^2$ and $4.01\,\text{mm}^2$, respectively).

When the residual differences w.r.t. to case (A) in Figure 6.16(c) and Figure 6.16(d) are studied, it can be clearly seen that method (A) and (B) perform similarly. The highest residual differences are present between case (A) and (D) with a magnitude of $\pm 3$ mm. Here, a correlation can be observed between the differential robot poses across two epochs. Specifically, larger changes in pose tend to correspond with larger residual differences, particularly with large inclinations of the AUT. In case (D), where the SH are transformed to a hemisphere,

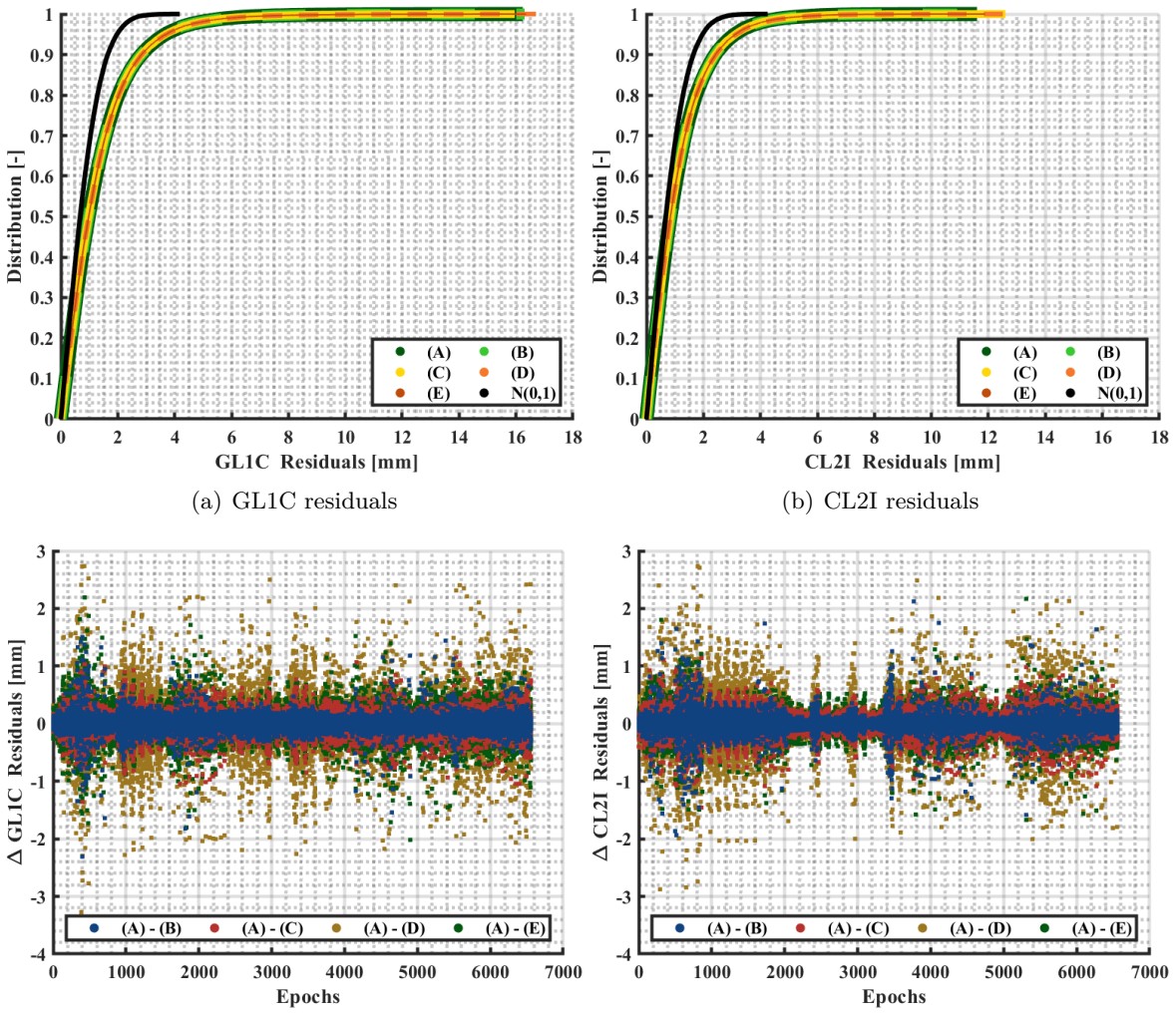


(a) GL1C residuals

(b) CL2I residuals

(c) GL1C Δ residuals

(d) CL2I Δ residuals

**Figure 6.16:** Residuals and Δ residuals with respect to method (A) from closed-loop simulations, validating different methods to stabilize the NES.

the absence of negative elevation angles — which are incorporated by inclinations — might contribute to instability in the estimation.

The analysis results concerning the residual differences are in accordance with the estimated PCC, visually shown as ΔPCC in Figure 6.13. Since the residuals are overall of the same order of magnitude, no direct conclusions from the calculated a posteriori variance factors $\hat{\sigma}_0^2$ can be drawn. This is also because the redundancy number is very high due to the large number of observations. Over all cases and frequencies, $\hat{\sigma}_0^2$ is between 2.29 mm$^2$ and 3.94 mm$^2$.

Figure 6.17 illustrates the ratio of $\hat{\sigma}_0^2$ to $\sigma_0^2$, which is of particular interest. The ratio is quite similar across all cases and frequencies. However, case (D) consistently shows the highest ratio across all frequencies. Among the different frequencies, EL1C exhibits the highest values, whereas CL2I shows the lowest. This deviation is attributed to the different dSD variances. It should be noted that unit weighting is applied in these analyses.

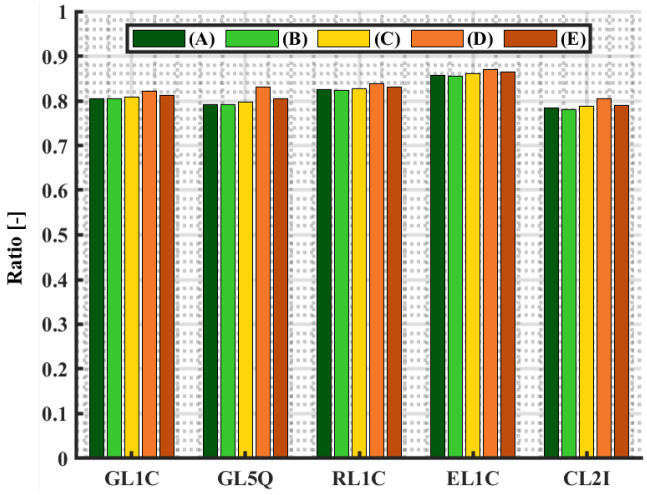


**Figure 6.17:** Ratio of $\hat{\sigma}_0^2$ to $\sigma_0^2$ for different methods to stabilize the NES.

### Closed-loop Simulations

To further verify the different methods, a closed-loop simulation is performed for each method following the sequence introduced in Section 4.4.4 with 1000 runs. Since only the observation vector $\mathbf{l}$ is changed in the closed-loop simulation, the geometry equals for all runs. For all frequencies, the differences between the PCC estimated with real dSD and the simulated ones are at maximum $10^{-15}$ mm, indicating a well-working PCC estimation algorithm. However, for case (B), the maximum difference is in the order of $10^{-7}$ mm. Since PCC are provided in the ANTEX file to the hundredth of a millimeter, this is still below the significance level but indicating differences in the closed-loop procedure.

To validate the different methods, white noise is added to the simulated dSD and a closed-loop simulation is performed. Since the noise of carrier-phase observations can be assumed to be 1% of the wavelength (which is $\approx$ 2 mm for GL1C) and this noise is amplified by a factor of 2 in the case of dSD (see Section 2.1.4), white noise with a standard deviation of 4 mm has been added to the simulated dSD. Since constant parts are cancelled out by time-differencing, the mean value of the added noise is set to zero.

Figure 6.18 shows exemplarily the simulated dSD for PRN01 along with the real observations and the simulated observations, on which the white noise has been added. It can be seen, that the real dSD show lower variations compared to the simulated observations with added white noise. This is also reflected in the respective standard deviations $\sigma$ of these time series, which

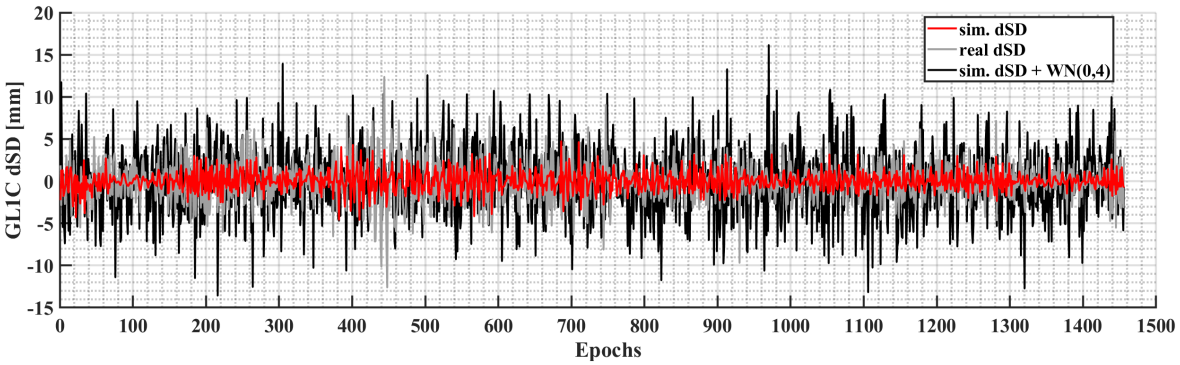


**Figure 6.18:** Simulated dSD, real dSD, and simulated dSD with added white noise characterized by $\sigma$=4 mm and $\mu$=0 mm (WN(0,4)) for PRN01.

reads $\sigma = 1.13\,\text{mm}$ for the simulated observations, $\sigma = 2.33\,\text{mm}$ for real dSD and $\sigma = 4.03\,\text{mm}$ for the modified, simulated dSD. This demonstrates that the receivers used (along with the measurement setup) provide a noise level lower than the 2 mm typically expected according to the rule of thumb. Consequently, in the following analysis, white noise with a standard deviation of 2.2 mm is used, i.e., WN(0,2.2), which represents the maximum $\sigma$ of the dSD across all frequencies. A fixed value has been chosen for all frequencies to ensure consistent comparison among them.

Figure 6.19 presents the closed-loop results for GL1C in terms of absolute maximum deviations, standard deviation of ΔPCC, and mean ΔPCC. In this study, 1000 runs are conducted using identical white noise sequences (WN(0,2.2)), with characteristic values of the ΔPCC calculated for each run. Since the ΔPCC for case (B) are of a significantly different magnitude, their values are displayed separately. As mentioned earlier, this difference is due to the introduction of a large constant offset $r$ into the pattern.

The results indicate that the addition of white noise with a standard deviation of 2.2 mm results in an impact of less than 1.65 mm on the absolute maximum deviation across all cases except for case (B), where differences of up to 2 m occur. In terms of standard deviation, case (B) performs similarly to other cases, as the standard deviation $\sigma$ of ΔPCC is independent of $r$ (see Table 3.1).

Overall, cases (A), (C), and (D) present similar characteristic values for ΔPCC, whereas

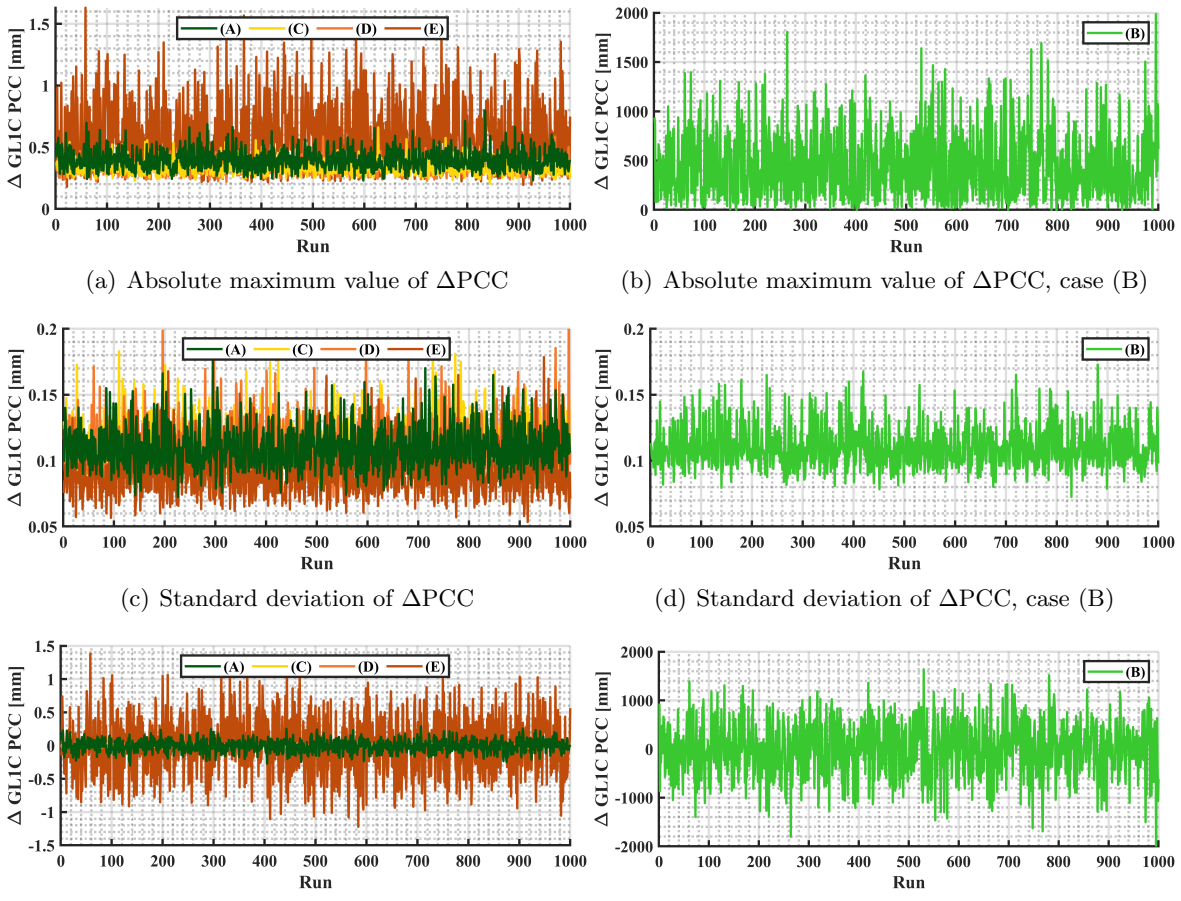


(a) Absolute maximum value of ΔPCC

(b) Absolute maximum value of ΔPCC, case (B)

(c) Standard deviation of ΔPCC

(d) Standard deviation of ΔPCC, case (B)

(e) Mean value of ΔPCC

(f) Mean value of ΔPCC, case (B)

**Figure 6.19:** Results of closed-loop simulations with added identical white noise sequences to the simulated GL1C dSD in terms of maximum, absolute deviations, standard deviations and mean ΔPCC. The characteristic values are calculated individually for each ΔPCC per run. Note the different y-axes scales.

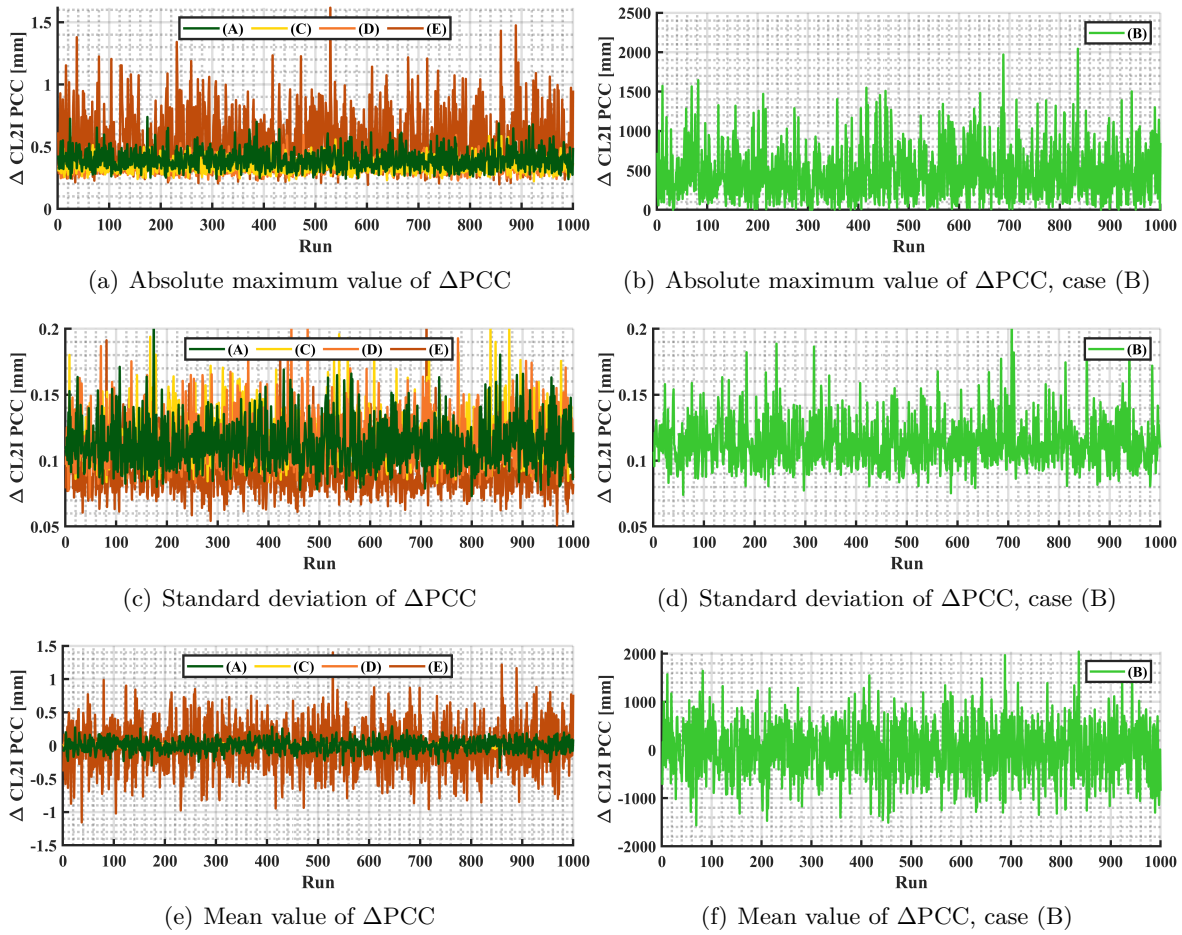


(a) Absolute maximum value of ΔPCC

(b) Absolute maximum value of ΔPCC, case (B)

(c) Standard deviation of ΔPCC

(d) Standard deviation of ΔPCC, case (B)

(e) Mean value of ΔPCC

(f) Mean value of ΔPCC, case (B)

**Figure 6.20:** Results of closed-loop simulations with added identical white noise sequences to the simulated CL2I dSD in terms of maximum, absolute deviations, standard deviations and mean ΔPCC. The characteristic values are calculated individually for each ΔPCC per run. Note the different y-axes scales.

case (E) shows higher values, particularly noticeable in the maximum and mean value of ΔPCC. The lower standard deviation in case (E), compared to the other cases, implies the introduction of a constant component in the pattern, as $\sigma$ is independent of $r$.

Figure 6.20 presents the results for CL2I. Overall, the effect of the added white noise on the observations is similar to that observed for GL1C, but slightly less pronounced. To directly compare the results from both frequencies, the absolute ΔPCC values are shown in Figure 6.21 using a cumulative histogram. In this comparison, the constant component $r$ is not included in the individual PCC, making it possible to compare with case (B) as well. The results demonstrate that the differences are smaller than 1 mm for all cases, with all cases performing similarly, except case (D), which performs slightly worse.

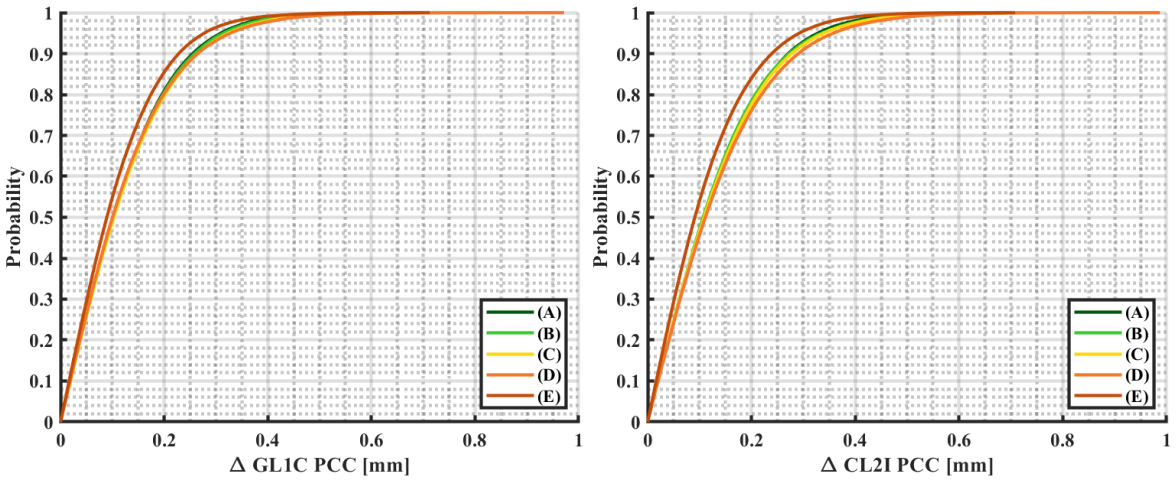


(a) Absolute GL1C ΔPCC (b) Absolute CL2I ΔPCC

**Figure 6.21:** Results of closed-loop simulations with added identical white noise sequences to simulated GL1C and CL2I dSD, depicted as absolute ΔPCC values in cumulative histograms.

To further analyze the outcomes of the closed-loop simulation, Figure 6.22 depicts the GL1C ΔPCC for one single run and all methods. Since white noise has been added to the observations, no clear behavior can be derived from the stereographic projections. For all methods (and this specific run), the differences are in a range of ±1 mm. In some cases, the highest differences are present at high elevation angles (see Figure 6.22(c)), in other cases at low elevation angles (see Figure 6.22(e)) and partly in both regions.

More detailed analyses of the extent to which observation noise impacts the estimation of CPC and PCC are presented in Breva et al. (2024b). Here, not only the effect of Gaussian white noise with different standard deviations is analyzed, but the noise behavior of dSD is

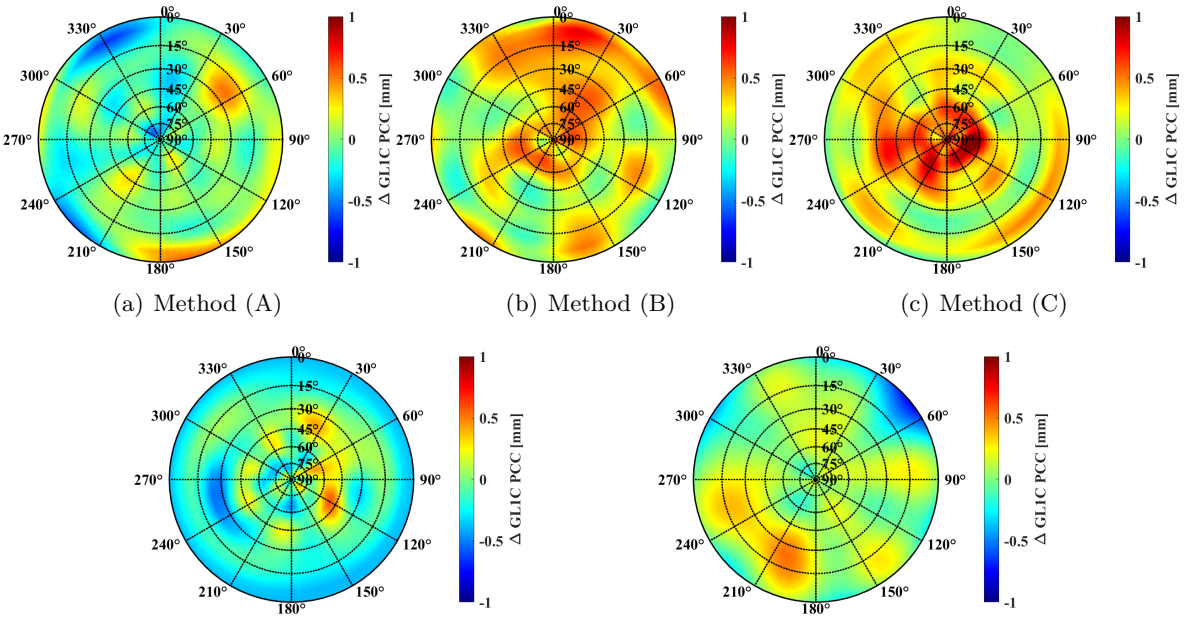


(a) Method (A) (b) Method (B) (c) Method (C)

(d) Method (D) (e) Method (E)

**Figure 6.22:** Stereographic projections of Δ GL1C PCC resulting from one single closed-loop simulation with identical white noise sequences.

also reproduced by consideration of the respective $C/N_0$ values. The main findings are that white noise with the same magnitude as the pattern itself results in 17% declined estimation outcome and that the use of a $C/N_0$ based noise model can reproduce real dSD convincingly.

### Resilience of Methods to Stabilize NES

Two further analyses of the stability of the different methods are performed below:

1. A large outlier of 3 cm is added to the observations
2. Observations from the satellite that provides the largest number of observations for the PCC estimation are excluded.

For the first case, a *leverage observation* is determined so that a clear influence on the estimated pattern can be seen. *Leverage observations* are data points that have a high influence on the estimation results. A disturbance of these observations can have a high impact on the parameters to be estimated (Niemeier, 2008).

To determine the *leverage observations*, a projection matrix, so-called *Hat-Matrix* $\boldsymbol{H}$ is computed

$$\boldsymbol{H} = \mathbf{A}(\mathbf{A}^{\mathrm{T}}\mathbf{A})^{-1}\mathbf{A}^{\mathrm{T}}. \tag{6.5}$$

Since in this work the NES is stacked with the individual $\mathbf{N}_k$ matrices per satellite $k$, resulting in $\bar{\boldsymbol{N}}$ (see Equation 4.13), only the individual $\mathbf{A}_k$ matrices exist. Thus, the Hat-Matrix is computed satellite-wise

$$\boldsymbol{H}_k = \mathbf{A}_k\bar{\boldsymbol{N}}^{-1}\mathbf{A}_k^{\mathrm{T}}. \tag{6.6}$$

An observation is a *leverage observation*, if $h_{k,ii}$, which is the i-th diagonal element of $\boldsymbol{H}_k$, is large. For the investigations carried out here, the maximum value of all individual $h_{k,ii}$ is chosen. The *leverage observation* is determined using $\bar{\boldsymbol{N}}$ from method (B) so that no restrictions are applied. For frequency GL1C, $\max(h_{ii}) = 0.09381$. This is significantly larger than the mean value $\bar{h}$

$$\bar{h} = \mathrm{mean}(h_{ii}) = \frac{u}{n_k} = \frac{80}{38318} \approx 0.00208, \tag{6.7}$$

which according to Huber (1981) can also be calculated from the ratio of the number of unknowns $u$ to the number of observations $n_k$. Thus, the determined observation (PRN06, epoch 1749) can be clearly classified as a *leverage observation*. The corresponding dSD as well as the modified observation, with an added offset of 30 mm, are depicted in Figure 6.23. It

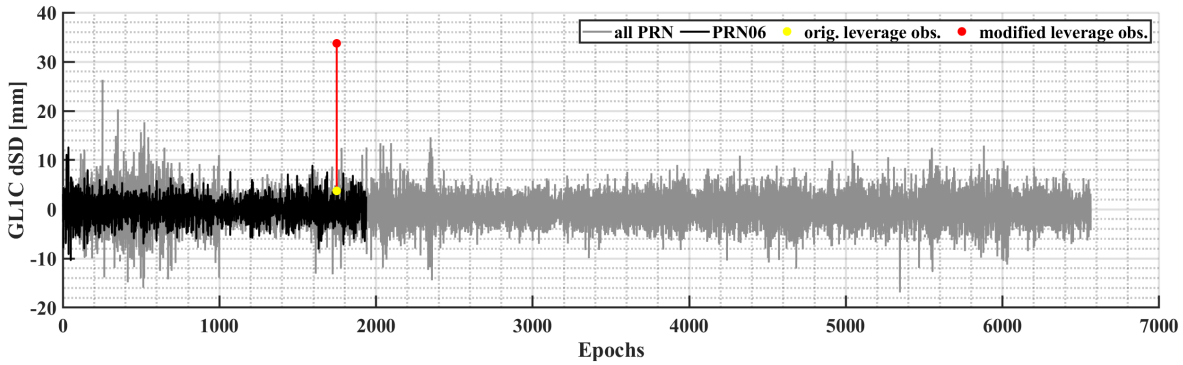


**Figure 6.23:** Overlapping representation of original dSD time series with highlighted *leverage observation* from PRN06 and the corresponding modified *leverage observation* with an added offset of 3 cm.

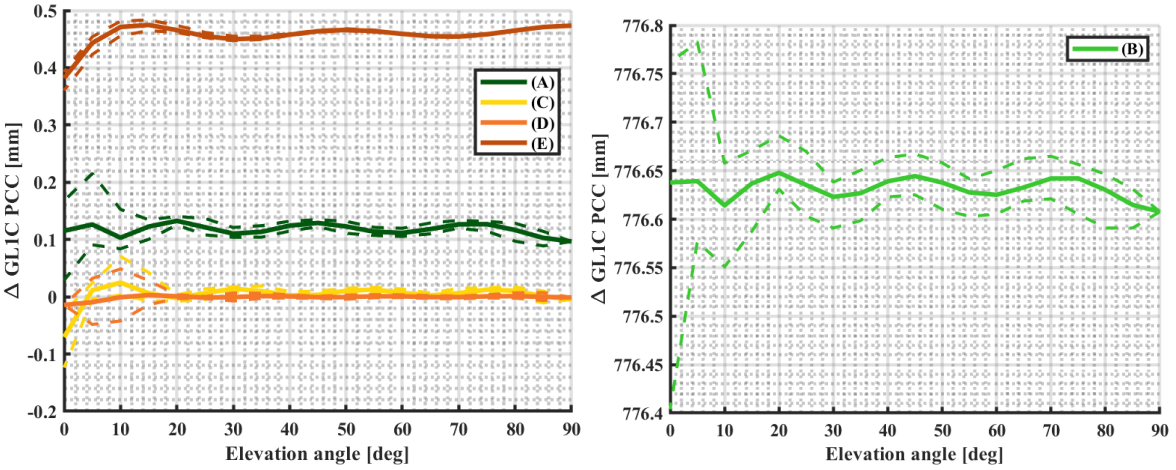


(a) cases: (A), (C), (D), (E) (b) case (B)

**Figure 6.24:** GL1C ΔPCC represented as averaged differences per elevation angle bin, from a closed-loop simulation where a 30 mm outlier was added to the determined *leverage observation*. Note the different y-axes scales.

can be seen that the value of the *leverage observation* is not particularly large compared to the other observations of PRN06, nor to all other gray-color-coded dSD.

Figure 6.24 depicts the result of the closed-loop simulation with the modified *leverage observation* for frequency GL1C and all methods. Due to the different order of magnitude, the results of method (B) are again displayed separately. Here, differences are in a range of 776.4 mm to 776.8 mm, due to a large constant part $r$ within the pattern. For all other cases, ΔPCC are between -0.2 mm and 0.5 mm. A clear correlation between the respective condition numbers (see Table 6.4) and the magnitude of the closed-loop simulation results can be observed. The higher the condition number, the higher the maximum deviations. This underlines again the need to appropriate stabilize the NES.

The closed-loop results of the study, in which all observations from the satellite with the most observations are deleted, are shown in Figure 6.25. In total, 6274 observations from PRN12 (≈ 16% of all available observations) are deleted. Again, method (B) is displayed separately. It is worth noting that, except for method (E), the behavior of the differences is quite similar among the methods. Although method (B) exhibits a large offset compared to the other methods, its variation patterns are similar to those of methods (A), (C), and (D). Overall, except for method (B), the differences fall within a range ±0.3 mm. Therefore, it is not surprising that PCC estimates from different calibration sets (each with different satellite geometry) can vary by up to 3 mm (see for example Figure 5.30).

## 6.4 Weighting Schemes

In a first step, a unit weighting for the stochastic model has been applied for estimating the PCC presented in Section 5.1. This means that the same weights are applied to all observations and that uncorrelated observations are assumed, i.e. $\mathbf{P} = \mathbf{I}$.

However, if resulting residuals in Section 5.1 are analyzed, a slight elevation-dependent behavior can be observed. Also, since in general the signal quality can be assessed by the respective $C/N_0$ values, $C/N_0$-dependent weighting schemes are expedient and thus widely

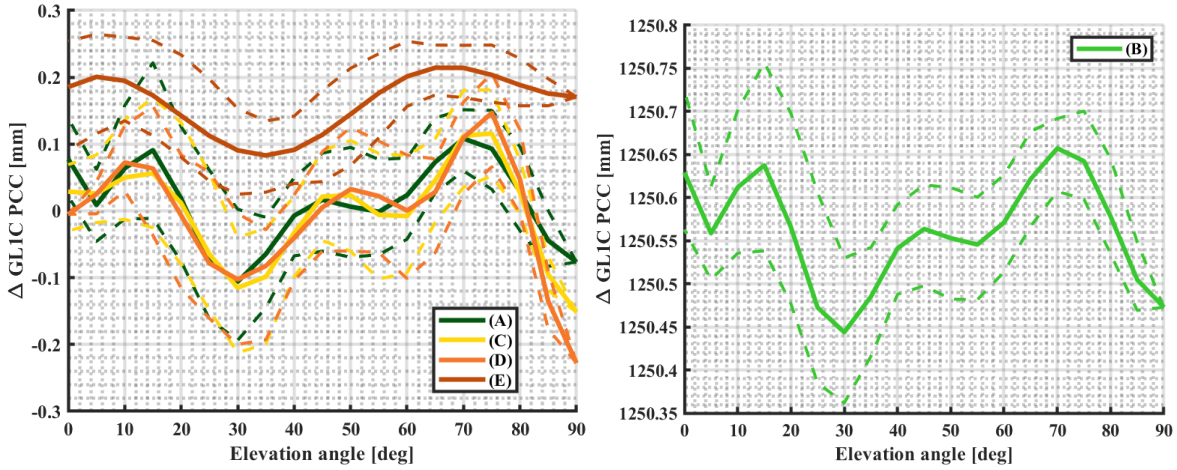


(a) cases: (A), (C), (D), (E) (b) case (B)

**Figure 6.25:** GL1C ΔPCC represented as averaged differences per elevation angle, from a closed-loop simulation where approximately 16% of all observations (6274 observations from PRN12) were removed. Note the different y-axes scales.

used. Therefore, the impact of two specific weighting schemes on estimated PCC and the corresponding quality parameters are analyzed in the following:

1. Elevation-dependent weighting
2. $C/N_0$-dependent weighting.

In order to take dependencies between $C/N_0$ values and elevation angles from both receivers and both epochs, which contribute to the dSD, into account, two weighting schemes have been developed. For both of them, PCC with a unit weighting have been estimated first and afterward been subtracted from dSD.

To take the respective noise level into account, an antenna-receiver and signal specific constant $a_\sigma^2$ is empirically determined. The target value is that the time series best approximated follows the standard normal distribution, i.e.

$$\frac{(dSD - PCC)}{\sigma} \sim \mathcal{N}(0,1). \tag{6.8}$$

After determining $a_\sigma^2$, the two weighting schemes can be set up, where each follows the law of error propagation in the way that the uncertainties from both stations and both epochs are taken into account, i.e. the respective variances are summed-up. The variance ${\sigma_n^k}^2$ for satellite $k$ at epoch $n$ for the elevation-dependent weighting scheme reads

$${\sigma_n^k}^2 = a_\sigma^2 \cdot \Bigg( \underbrace{\frac{1}{\sin(el^k_{AUT,n})} + \frac{1}{\sin(el^k_{AUT,n+1})}}_{el^k \text{ in antenna frame of AUT}} + \underbrace{\frac{2}{\sin(el^k_{Ref,n})}}_{el^k \text{ ref. station}} \Bigg), \tag{6.9}$$

taking elevation angles of the AUT in the antenna frame for epoch $n$ and $n+1$ (due to the time differencing), and of the reference station for both epochs into account. Since the elevation angle at the static reference station maximum changes 0.36° between consecutive epochs, it can be simplified into one term.

The formula for the advanced $C/N_0$-dependent weighting is given in Equation 6.10. Instead of weighting observations w.r.t their elevation angles, the respective $C/N_0$ values in [dB-Hz]

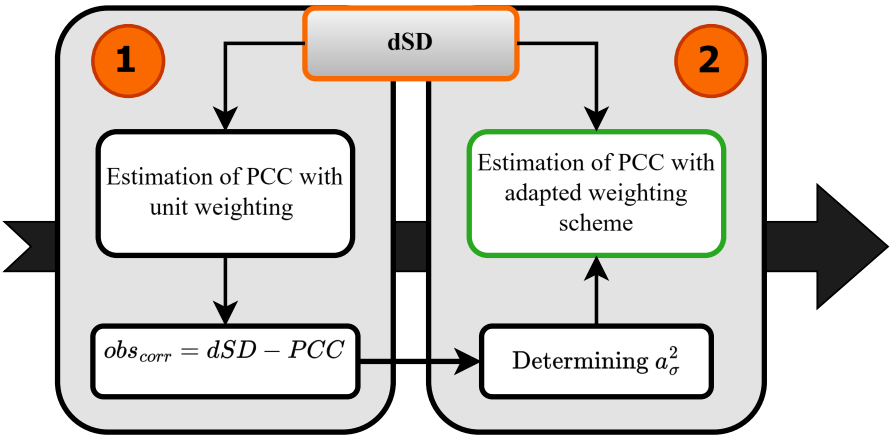


**Figure 6.26:** Flow chart for developing and applying different weighting models for PCC estimation.

for both epochs $n$, $n+1$ and stations *Ref*, AUT are considered

$$\sigma_n^{k\,2} = a_\sigma^2 \cdot \left(10^{-\frac{C/N_0{}^k_{AUT,n+1}}{10}} + 10^{-\frac{C/N_0{}^k_{AUT,n}}{10}} + 10^{-\frac{C/N_0{}^k_{Ref,n}}{10}} + 10^{-\frac{C/N_0{}^k_{Ref,n+1}}{10}}\right). \tag{6.10}$$

The stochastic model of the LSA for estimating the PCC reads accordingly

$$\mathbf{P} = diag\left(\frac{1}{\sigma_n^{k\,2}}\right). \tag{6.11}$$

The general process of the application of different weighting schemes for PCC estimation is conclusively depicted in Figure 6.26. In the following, the determination of the noise factors $a_\sigma^2$ is explained, followed by the analysis of PCC estimated with different weighting models. Next, the quality parameters of the estimated PCC are assessed and evaluated. Additionally, the impact of the used receiver connected to the AUT, is examined.

### Determination of Noise Factors

This section briefly summarizes the determination of $a_\sigma^2$ for the elevation-dependent weighting scheme for frequency GL1C, using antenna NOV (and a *Septentrio PolaRx5TR* receiver). Fig-

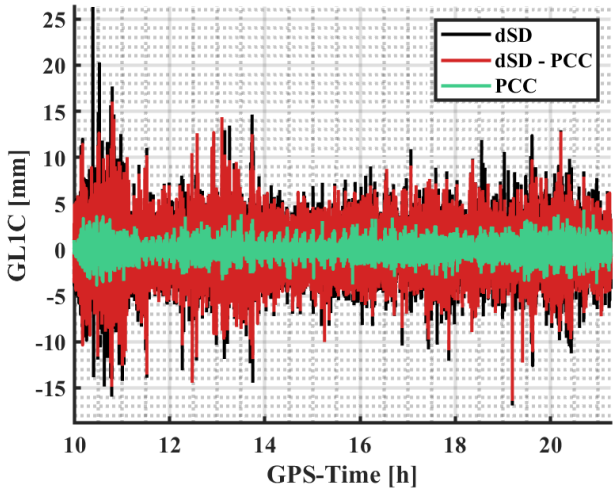


**Figure 6.27:** Illustration of input dSD time series used to determine noise factors $a_\sigma^2$.

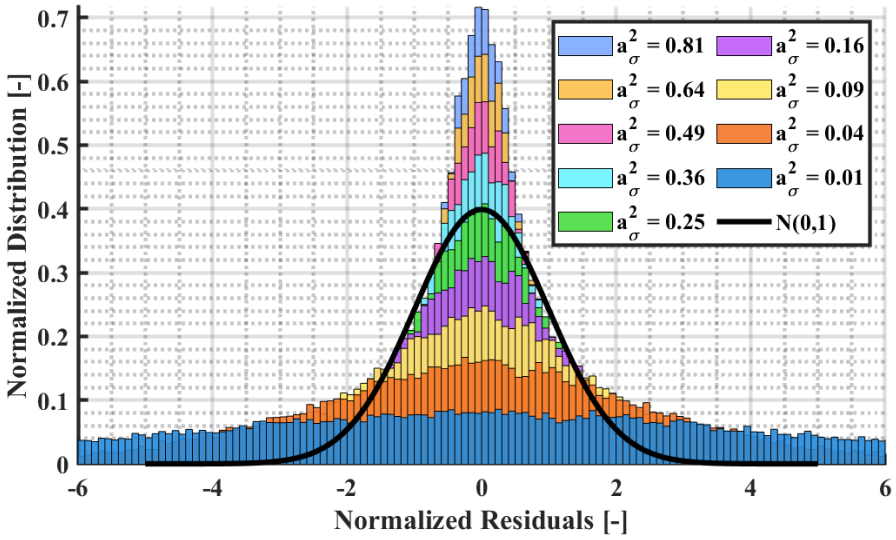


**Figure 6.28:** Normalized residuals for different values of $a_\sigma^2$. The coefficients $a_\sigma^2$ are expressed in mm$^2$.

ure 6.27 illustrates the input dSD, the estimated PCC using a unit weighting and the resulting dSD with subtracted PCC. The latter one, depicted in red, serves as input for determining $a_\sigma^2$. Figure 6.28 shows the resulting normalized residuals for varying $a_\sigma^2$. It can be nicely seen that with $a_\sigma^2 = 0.25\,\text{mm}^2$, the normalized residuals follow the standard normal distribution best. Following this sequence, $a_\sigma^2$ is determined for both weighting schemes, and all frequencies for specific antenna-receiver combinations.

Table 6.6 presents the determined noise factors for the mentioned antenna-receiver combination for GPS and Galileo frequencies, as well as both weighting schemes. Table 6.7 lists the corresponding factors for GLONASS and BeiDou frequencies. The determined factors for the elevation-dependent weighting schemes appear to be very similar across the different frequencies, except for GL2W. As detailed in Section 5.1, this discrepancy is connected to the higher observation noise of the dSD. Contrarily, for $a_\sigma^2$ related to the C/N$_0$-dependent weighting scheme, GL2W does not stand out when compared to other frequencies. Instead, GLONASS frequencies demonstrate the highest values in this context.

**Table 6.6:** Determined noise factors $a_\sigma^2$ for elevation-dependent and C/N$_0$-dependent weighting schemes for GPS and Galileo frequencies (AUT: NOV, receiver: *Septentrio PolaRx5TR*).

| **Frequency** | **Noise factor $a_\sigma^2$** Elev [mm$^2$] | C/N$_0$ [$10^4$] [$\frac{\text{mm}^2}{\text{Hz}}$] |
|---|---|---|
| GL1C | 0.25 | 2.56 |
| GL2W | 3.61 | 3.14 |
| GL2L | 0.64 | 2.56 |
| GL5Q | 0.36 | 3.24 |
| GL1L | 0.25 | 1.96 |
| EL1C | 0.36 | 1.69 |
| EL6C | 0.49 | 2.89 |
| EL5Q | 0.49 | 2.89 |
| EL7Q | 0.36 | 2.89 |
| EL8Q | 0.25 | 3.24 |

**Table 6.7:** Determined noise factors $a_\sigma^2$ for elevation-dependent and C/N$_0$-dependent weighting schemes for GLONASS and BeiDou frequencies (AUT: NOV, receiver: *Septentrio PolaRx5TR*).

| **Frequency** | **Noise factor $a_\sigma^2$** Elev [mm$^2$] | C/N$_0$ [$10^4$] [$\frac{\text{mm}^2}{\text{Hz}}$] |
|---|---|---|
| RL1C | 0.36 | 4.41 |
| RL2P | 0.49 | 4.00 |
| RL2C | 0.64 | 4.84 |
| CL1P | 0.25 | 1.96 |
| CL5P | 0.36 | 2.89 |
| CL2I | 0.16 | 2.56 |
| CL6I | 0.25 | 3.61 |
| CL7D | 0.36 | 2.89 |

### PCC Estimated with Different Weighting Models

Figure 6.29 shows ΔPCC for antennas NOV, LEI, and UBX across selected GPS and Galileo frequencies. The differences relative to the estimated PCC using unit weighting are calculated. Generally, the differences are within the range of ±1 mm. Also, a highly comparable behavior between the advanced elevation-weighting and advanced $C/N_0$ weighting schemes is visible. This indicates that with both developed weighting strategies very similar PCC are estimated. However, larger deviations between these two schemes occur for azimuthal variations, shown with dashed lines, especially at low elevation angles.

Significant differences between unit weighting and the developed weighting schemes are in particular present for antenna LEI for frequency GL5Q, so that it is also depicted with another y-axis scale in Figure 6.29(e). In this case, differences range from -4 mm to approximately 0 mm. A pronounced elevation-dependent behavior is observed, indicating a $\Delta PCO_{Up}$ component, as illustrated in Figure 3.4(a) for a simulated case.

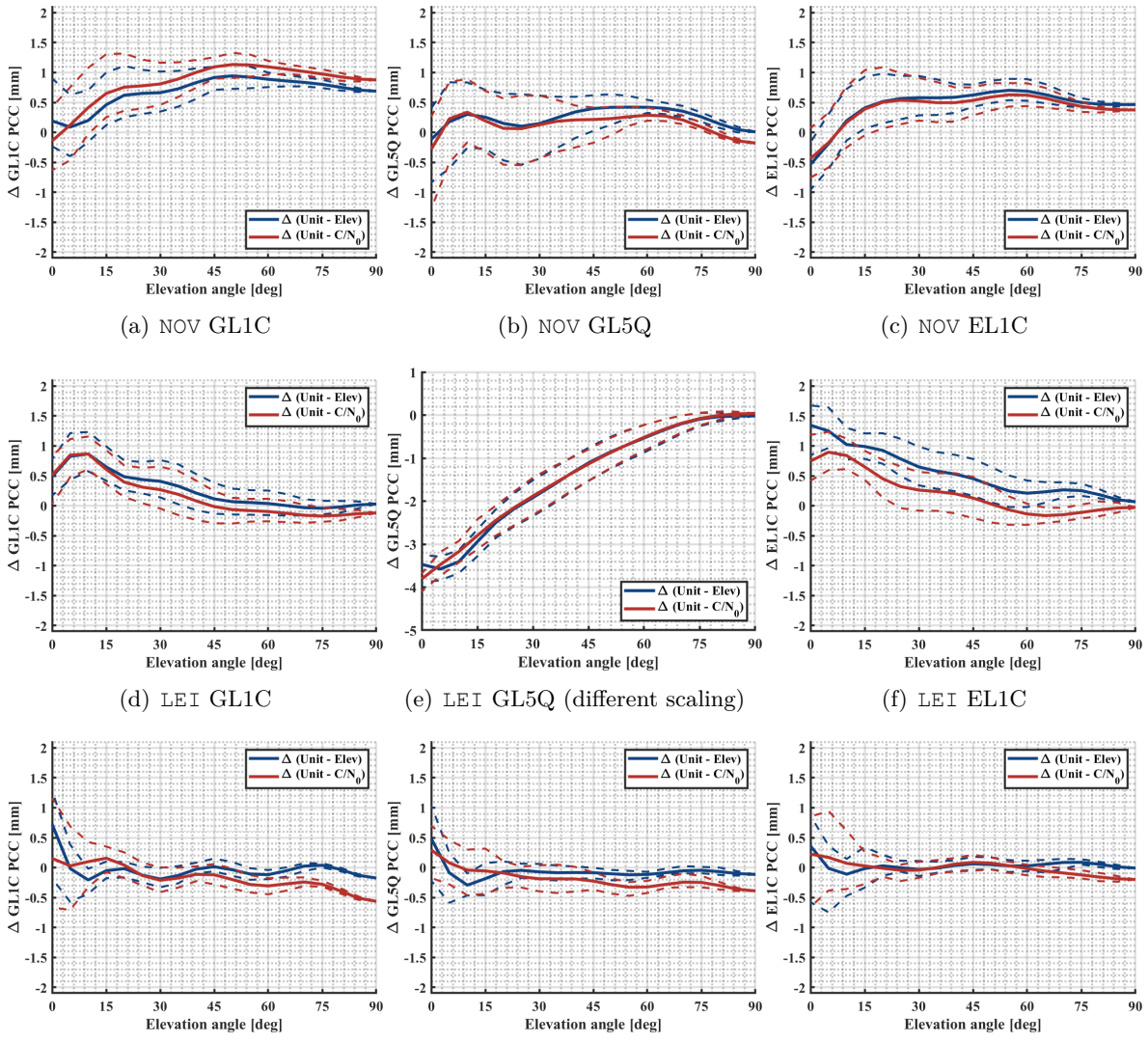


(a) NOV GL1C (b) NOV GL5Q (c) NOV EL1C

(d) LEI GL1C (e) LEI GL5Q (different scaling) (f) LEI EL1C

(g) UBX GL1C (h) UBX GL5Q (i) UBX EL1C

**Figure 6.29:** Averaged PCC differences per elevation angle bin between PCC estimated with unit-weighting and developed weighting schemes for three AUTs and selected GPS and Galileo frequencies.

### Quality Parameters of PCC Estimated with Different Weighting Models

In order to further assess the impact of the applied weighting scheme for PCC estimation, the quality parameters introduced in Section 4.4 are investigated. This includes the analysis of the condition number of the NES, the a posteriori variance factors, the residuals as well as the formal errors of the estimated PCC.

Table 6.8 lists the condition number exemplarily for GL1C for different AUTs and weighting schemes. If another weighting scheme than the unit weighing is applied, the condition number is increased by a factor of up to seven. Nonetheless, it is still in a moderate range, especially compared to the condition numbers when no specific method to stabilize the NES is applied (see Table 6.4 listing the condition numbers for different methods to stabilize the NES).

In Table 6.9, the a posteriori variance factors $\hat{\sigma}_0^2$, again for GL1C, are provided. It can be nicely seen, that it is largely reduced by applying one of the developed weighting schemes, which is especially an improvement for UBX. Figure 6.30 presents cumulative histograms of normalized, absolute GL1C residuals for each of the three antennas and the weighting schemes being studied. Additionally, the figure includes the standard normal distribution N(0,1) and unit weighting schemes using two different $\sigma_0^2$ for normalization: $\sigma_0^2 = 1\,\mathrm{mm}^2$ and $\sigma_0^2$ set to the variance of the input observations. It is observed that either adapting $\hat{\sigma}_0^2$ to the variance of the dSD or using other weighting schemes causes the normalized residuals to closely follow a normal distribution. However, some residuals have higher values than those in a standard normal distribution. The $C/N_0$-dependent weighting scheme aligns more closely with the standard normal distribution compared to the elevation-dependent weighting scheme. Overall, these findings are supported by $\hat{\sigma}_0^2$ listed in Table 6.9. Additionally, using a unit weighting and setting $\sigma_0^2$ to the variance of the input observations is also an effective strategy.

Figure 6.31 shows the formal errors of GL1C PCC when using different weighting schemes. Generally, similar results are obtained across different schemes. However, with unit weighting, the formal errors are higher at high elevation angles and lower at low elevation angles compared to other schemes, consistent across all three AUT. Typically, one would expect PCC to be more precise estimated at higher elevation angles due to better observation quality. Still, when considering only the geometry, such as the number of observations per elevation angle shown in Figure 4.10, the formal errors obtained by a unit weighting closely correspond to this trend.

Using one of the developed weighting schemes, GL5Q PCC for LEI shows a noticeably different pattern compared to unit weighting, as illustrated in Figure 6.29(e). Therefore, Figure 6.32 shows the respective distribution of normalized residuals and formal errors. Interestingly, there is no significant difference in quality parameters between LEI GL5Q and LEI GL1C. Similarly, when comparing GL5Q for NOV or UBX, the values are unremarkable. The same applies when analyzing the $\hat{\sigma}_0^2$ and the condition number of the NES.

**Table 6.8:** Comparison of GL1C condition numbers for different AUTs and weighting schemes.

| AUT | Unit | Elev | $C/N_0$ |
|---|---|---|---|
| | | [-] | |
| NOV | 90.38 | 600.59 | 415.87 |
| LEI | 111.24 | 775.76 | 555.81 |
| UBX | 114.41 | 782.24 | 493.20 |

**Table 6.9:** Comparison of GL1C $\hat{\sigma}_0^2$ for different AUTs and weighting schemes.

| AUT | Unit | Elev | $C/N_0$ |
|---|---|---|---|
| | | [$\mathrm{mm}^2$] | |
| NOV | 3.30 | 1.43 | 1.07 |
| LEI | 2.83 | 1.04 | 1.04 |
| UBX | 9.14 | 1.06 | 1.07 |

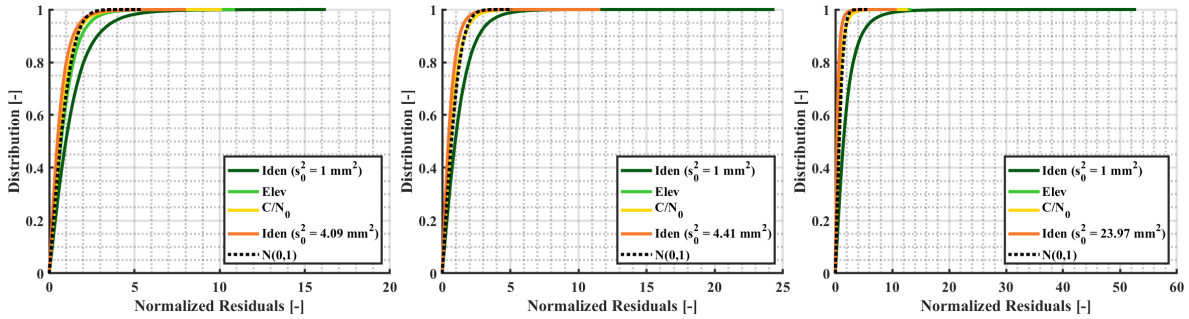


(a) AUT: NOV (b) AUT: LEI (c) AUT: UBX

**Figure 6.30:** Cumulative histograms showing the absolute and normalized GL1C residuals for three different antenna types, using various weighting schemes. Note the different scales.

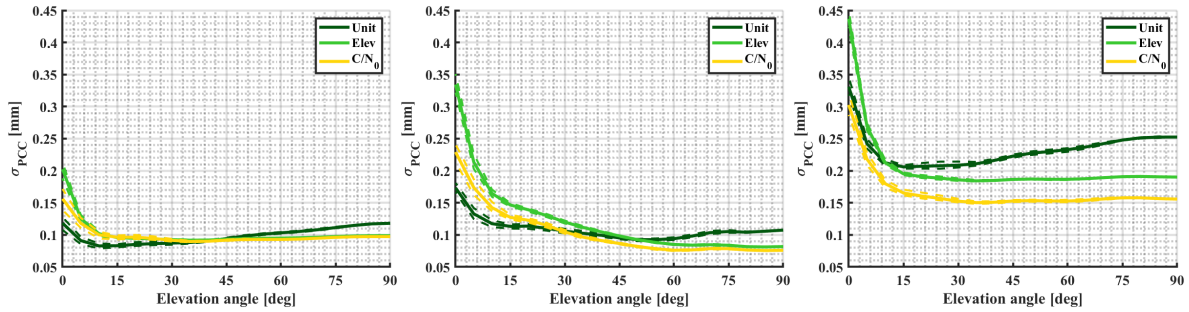


(a) NOV GL1C (b) LEI GL1C (c) UBX GL1C

**Figure 6.31:** Averaged formal errors per elevation angle bin of GL1C PCC estimated using different weighting schemes.

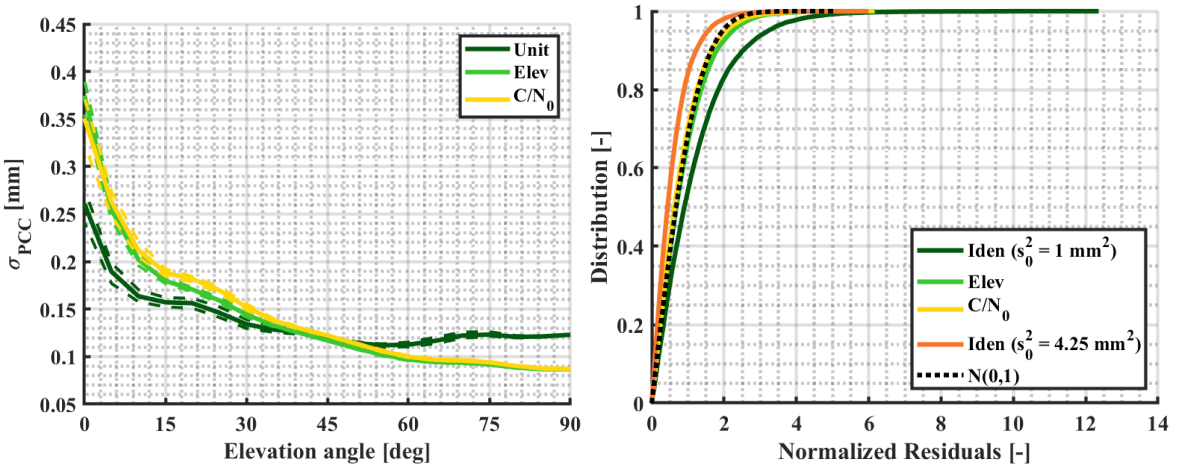


(a) Formal errors (b) Distribution of normalized residuals

**Figure 6.32:** Averaged formal errors per elevation angle bin (a), and cumulative histogram of absolute normalized residuals (b) of GL5Q PCC for LEI, estimated using different weighting schemes.

### Impact of Used Receiver

As discussed in Section 2.1.2 and analyzed in Section 5.4, the used receiver (settings) can influence the observations and, consequently, the estimated PCC. Different receivers, when connected to the same AUT, show different levels of observation noise, as seen in the residuals shown in Figure 5.41. This suggests that each receiver has its own distinct noise characteristics. The analyses in this section are performed using the same data set referenced in Section 5.4 (AUT: NOV, receivers: SEPT, DELTA, and S3S, as illustrated in Figure 5.37).

Table 6.10 presents the determined coefficients for the different antenna-receiver combinations for selected GPS and Galileo frequencies. As expected, different noise factors $a_\sigma^2$ are determined for the different receivers. A part from that there is no clear correlation between the types of receivers and the values obtained. Specifically, Table 5.2 indicates that receivers DELTA and S3S track the GL5X and EL1X frequencies, while receiver SEPT tracks GL5Q and EL1C. It could have been expected that DELTA and S3S show greater similarity in $a_\sigma^2$ compared to SEPT, but this is not observable.

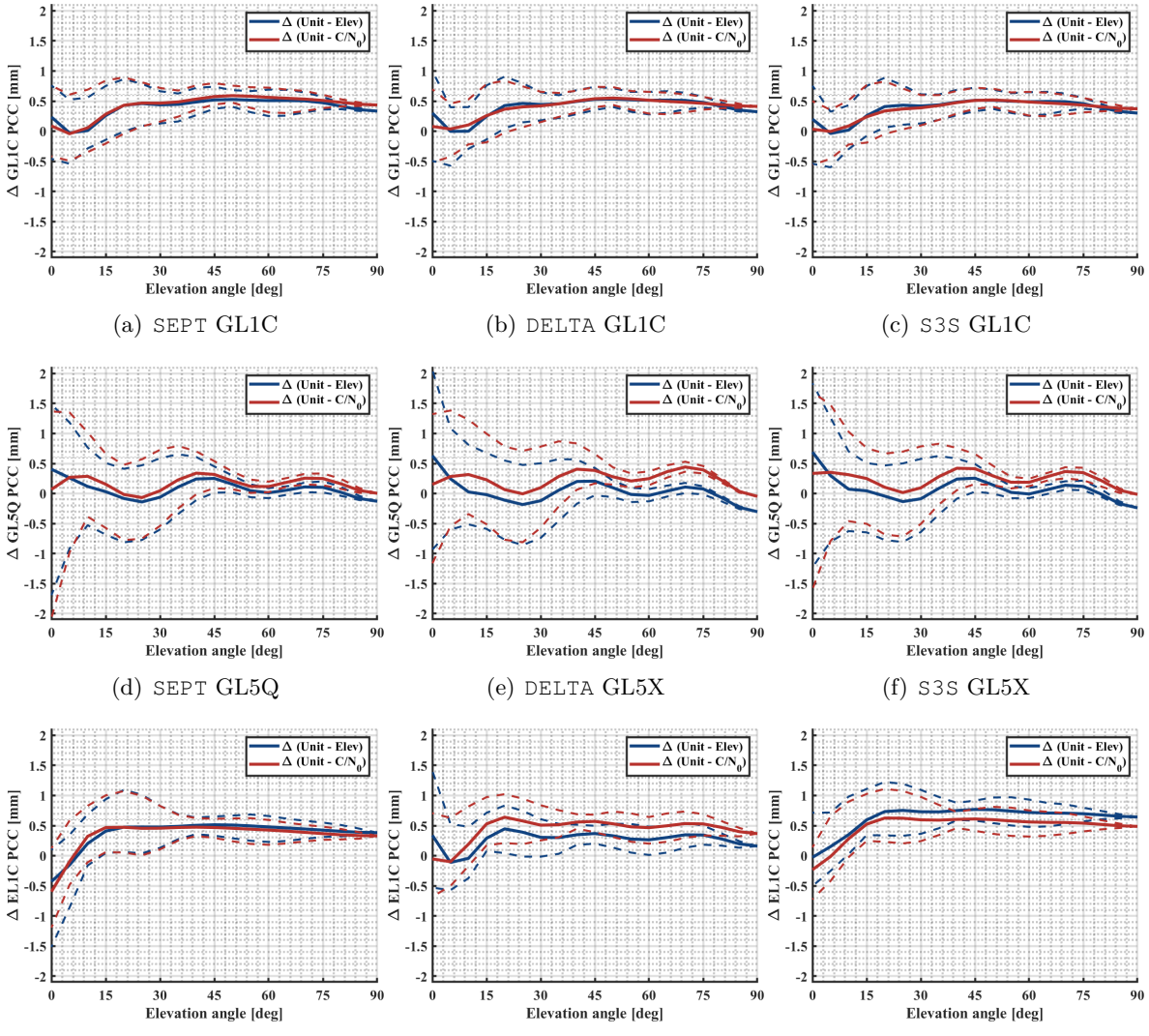


(a) SEPT GL1C (b) DELTA GL1C (c) S3S GL1C

(d) SEPT GL5Q (e) DELTA GL5X (f) S3S GL5X

(g) SEPT EL1C (h) DELTA EL1X (i) S3S EL1X

**Figure 6.33:** Averaged PCC differences per elevation angle bin between PCC estimated with unit-weighting and developed weighting schemes for different antenna-receiver combinations and selected GPS and Galileo frequencies. The NOV antenna is used for all combinations.

**Table 6.10:** Determined noise factors $a_\sigma^2$ for different antenna-receiver combinations using the identical AUT – a *NOV703GG.R2 NONE*.

| | $\mathbf{a_\sigma^2}$ **Elev** | | | $\mathbf{a_\sigma^2}$ C/N$_0$ [$10^4$] | | |
|---|---|---|---|---|---|---|
| | SEPT | DELTA | S3S | SEPT | DELTA | S3S |
| | [mm$^2$] | | | [$\frac{\text{mm}^2}{\text{Hz}}$] | | |
| **GL1C** | 0.36 | 0.64 | 0.64 | 2.56 | 4.41 | 4.00 |
| **GL5Q/X** | 0.49 | 0.81 | 0.49 | 4.41 | 10.2 | 8.41 |
| **EL1C/X** | 0.36 | 0.49 | 0.36 | 1.69 | 4.41 | 4.41 |

Figure 6.33 illustrates the variation in the estimated ΔPCC for different receivers compared to the PCC estimated with unit weighting. The mean differences per elevation angle are shown when applying the elevation- or C/N$_0$-dependent weighting model, using the coefficients from Table 6.10. It can be observed that the differences between the various receivers are relatively small ($\leq 1$ mm). The largest deviations occur for GL5Q/X and EL1C/X. In these instances, differences in ΔPCC with respect to unit weighting become apparent at low elevation angles, particularly for azimuthal differences, which are shown by dashed lines.

#### Closing Remarks

It is worth noting that different noise factors are determined for different calibration sets, even when using the same antenna-receiver combination. This is evident when comparing the values from Table 6.10 for receiver SEPT with those from Table 6.6. The largest differences occur for frequency GL5Q in the C/N$_0$-dependent weighting scheme. However, in general, noise factors can always be determined for a specific calibration set. This can be conducted, as done above, by first estimating PCC with unit weighting, then subtracting these PCC from the dSD time-series, determining the noise factors, and performing a second LSA with one of the weighting schemes (see Figure 6.26).

Alternatively, the officially published type-mean calibration in the ANTEX file of the respective antenna (if available) can be used to create simulated observations (see Section 4.4.4) and subtract them from the dSD to obtain the coefficients for the designated calibration set. This approach is less time-consuming; however, it does not take into account the influence of the specific receiver used, which has been shown to have an impact.

## 6.5 Grid Resolution

Usually, estimated PCC are provided with a grid size of 5° azimuth- and 5° elevation angles in the ANTEX file. Between these 5° sample points, the actual correction value that is applied to the observations, is then bi-linearly interpolated with respect to the azimuth and elevation angle of the visible satellites (see Equation 2.28). However, important information could be lost if the grid resolution is set too low. To this end, the impact of different PCC grid resolutions for different scenarios are analyzed within this section. For the comparison of different resolutions, one set of HSH coefficients with standard settings (see beginning of Chapter 6) is estimated. They are inserted into Equation 4.3 with azimuth and zenith angles defined by the respective resolutions. Next, PCV, PCO and $r$ are separated and PCC are computed following Equation 2.27.

To analyze the effects of different grid resolutions, the study begins with a comparison of

the separated PCO and constant components from the PCC, as well as an evaluation of PCC differences on the grid. Subsequently, the impact is analyzed in one static scenario and two kinematic scenarios - one involving open-sky conditions and the other an urban environment.

### Impact on the Grid

Figure 6.34 depicts the averaged ΔPCC per elevation angle along with the minimum and maximum value per bin. Here, the correction values between the sampling points, e.g. 2° or 5° steps, are bi-linearly interpolated, i.e. a re-sampling is carried out. It can be clearly seen, that all ΔPCC per chosen resolution are zero at the sampling points as marked by dots. Between these sampling points ΔPCC values vary between -0.8 mm and 0.6 mm, with larger deviations occurring as the resolution difference increases. However, the mean values per elevation angle are smaller, ranging from -0.5 mm to 0.2 mm. It should be noted that differences at the sampling points occur if the constant part $r$ is not correctly accounted for, meaning it is not added to the PCC. In such cases, the offset at the sampling points is precisely equal to $\Delta r$.

Figure 6.35 depicts PCO and $r$ differences w.r.t. the 1° resolution, which is assumed to be the nominal solution. It can be seen that the differences increase with a higher resolution, that $r$ and $\mathrm{PCO}_{\mathrm{Up}}$ show the same differences for all cases and that the horizontal PCO components, i.e. ΔNorth and ΔEast show smaller absolute variations ($< 0.1$ mm). It is worth noting that $r$ is typically added to the pattern according to Equation 2.27. Since the PCO is added with a negative sign, $\mathrm{PCO}_{\mathrm{Up}}$ is effectively the same in all cases because of the expression: -PCO + $r$. Overall, the differences in PCO and $r$ between the different resolutions are relatively small, with a maximum of 0.5 mm. However, these differences are still significant because the values are specified to the hundredth of a millimeter in the ANTEX file.

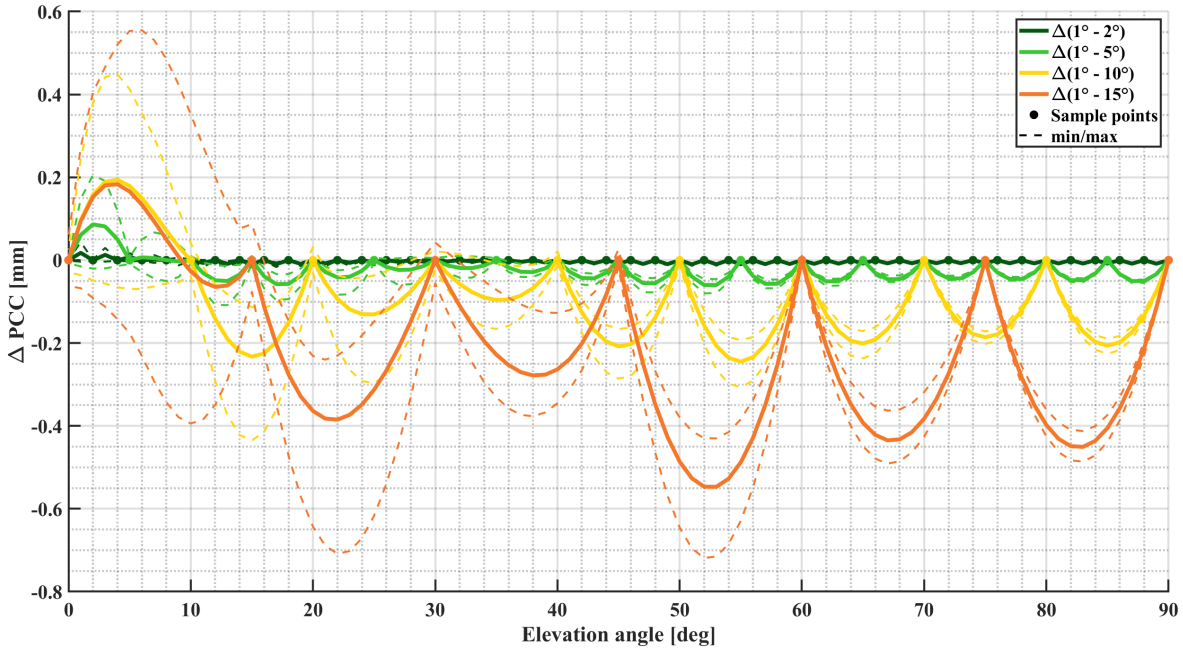


**Figure 6.34:** Influence of PCC grid resolution on bi-linearly interpolated correction values (re-sampling), presented as mean ΔPCC per elevation angle bin. Dashed lines indicate the minimum and maximum deviations.

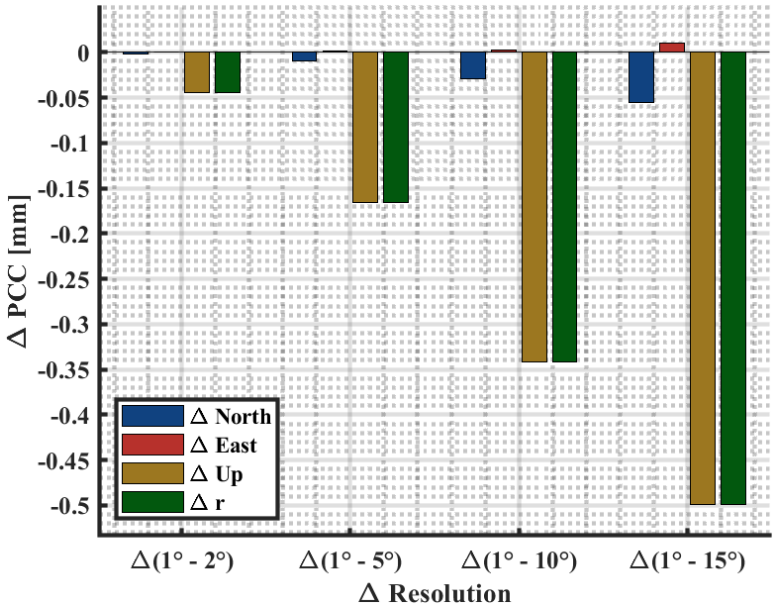


**Figure 6.35:** Influence of different PCC grid resolutions on estimated PCO and constant $r$ parts.

### Impact in a Static Scenario

In order to assess the interpolation error of the different grid resolutions for a real world scenario, the satellite distribution of station BAKE with a sampling rate of $\Delta t = 5\,\text{min}$ is taken (see Figure 3.8(a)). Each PCC set is used to calculate correction values for the respective LOS unit vectors, which would be applied to the observations, see Equation 2.28. The PCC differences between the different resolutions are depicted in Figure 6.36. Again, as expected, the differences w.r.t the 1° solution increase with a higher grid resolution. While for $\Delta(1° - 2°)$ the maximum difference is below 0.04 mm, it reaches almost 0.7 mm in the case of $\Delta(1° - 15°)$ (note the different scales of the colorbars). However, these rather small differences can be explained as follows. The most dominant part in PCC is the $\text{PCO}_{\text{Up}}$ component so that a clear elevation-dependent behavior can be observed, see Figure 5.2. Since the elevation angle of satellites changes in average $\approx 2°/5\,\text{min}$, the interpolation error is within the given sampling rate of 5 min and in the static case rather small. Moreover, the highest differences occur at low elevation angles and have most probably a lower impact since they might be either down-weighted in a position solution algorithm or even discarded due to an elevation cut-off angle of e.g. 7°.

In order to assess the impact on geodetic parameters at station BAKE, the simulation approach introduced in Section 3.3.2 is used. Figure 6.37 depicts the results for $\Delta(1° - 5°)$ for three consecutive days in April 2023, with the following parameter settings are:

- 7° elevation cut-off angle
- Sample interval $\Delta t = 30\,\text{s}$
- Interval time $\delta t_\Sigma = 30\,\text{min}$
- $\sin el$-dependent weighting.

The resulting differences reach at maximum 0.9 mm for the Up- and clock parameter, while differences for the horizontal components as well as for the tropospheric parameter vary around $\pm 0.2\,\text{mm}$. Since the impact is summed up over $\delta t_\Sigma$ and a higher sampling rate $\Delta t$ is used, the differences are slightly higher than those illustrated in Figure 6.36(b). Nonetheless, the

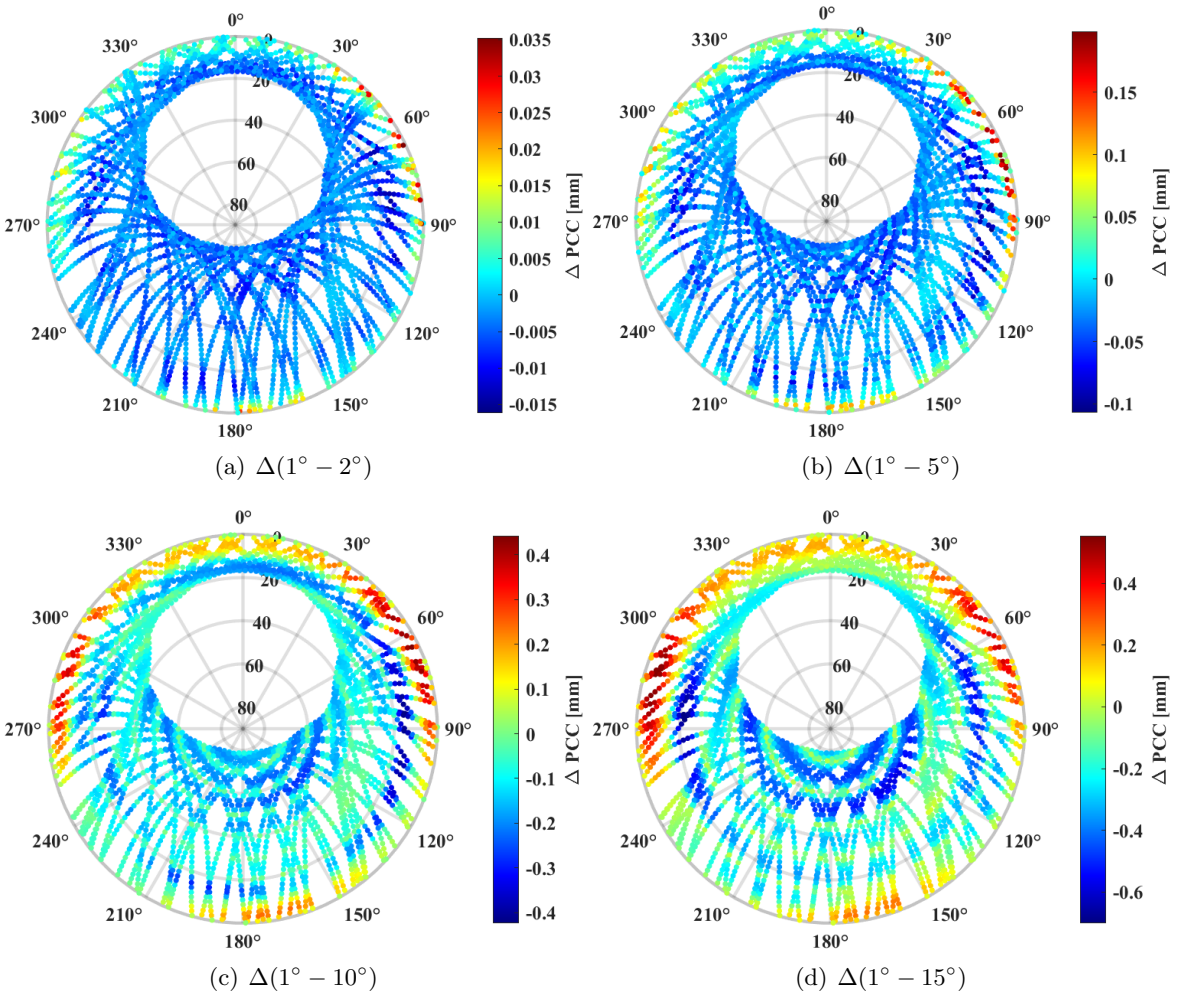


(a) $\Delta(1° - 2°)$ (b) $\Delta(1° - 5°)$

(c) $\Delta(1° - 10°)$ (d) $\Delta(1° - 15°)$

**Figure 6.36:** Stereographic projections depicting the impact of different PCC resolutions on LOS correction values. Note the different scales for the colorbar.

differences can be assumed to be insignificant in an absolute positioning approach (e.g. PPP), since other error sources are dominating. Thus, a PCC grid resolution of 5° can be assumed to be sufficient for the analyzed case.

### Impact in Kinematic Scenarios

In order to analyze the impact of a higher sampling rate as well a faster change of the satellite geometry, data of two kinematic experiments are used. Details of the `open-sky` and `urban` experiment are described in Kulemann and Schön (2023), the respective trajectories are shown in Figure 6.38. The duration of the `open-sky` experiment is approximately 30 minutes (10 consecutive rounds) and of the `urban` scenario 90 minutes. 10 Hz data of the *Javad* (#0046) receiver is used. However, for the analyses carried out here, the used receiver-antenna combination does not play a role, since only the respective satellite geometry and heading information of the vehicle is needed. Since PCC are provided for a north-orientated antenna (see also discussion in Section 4.1), the LOS unit vectors need to be rotated properly.

In order to depict the results independently of a constant part $r$ within the computed LOS correction and to visualize the effect for all visible satellites and epochs, a LSA using Equation 4.16 is carried out. In this way, the impact of the different resolutions/methods

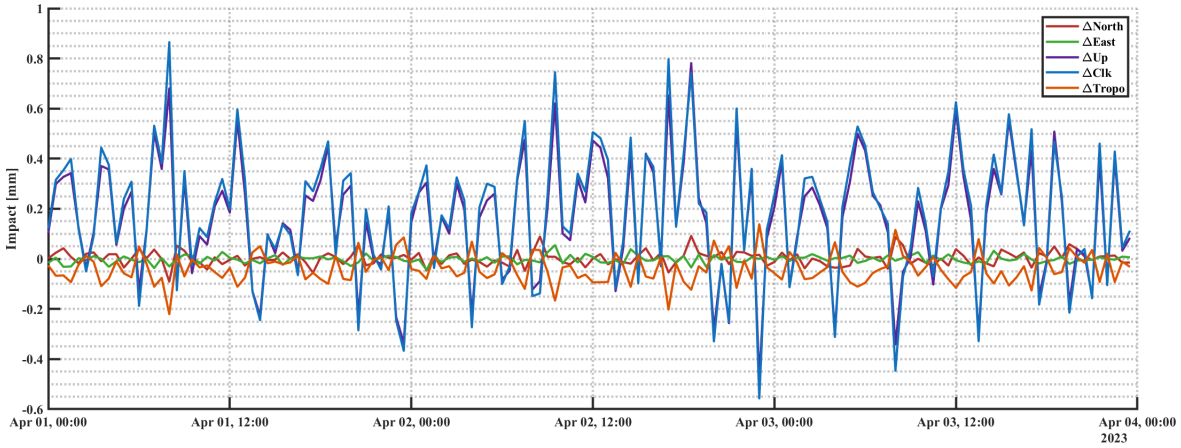


**Figure 6.37:** Impact of different PCC grid resolutions ($\Delta(1° - 5°)$) on geodetic parameters using the developed simulation approach.

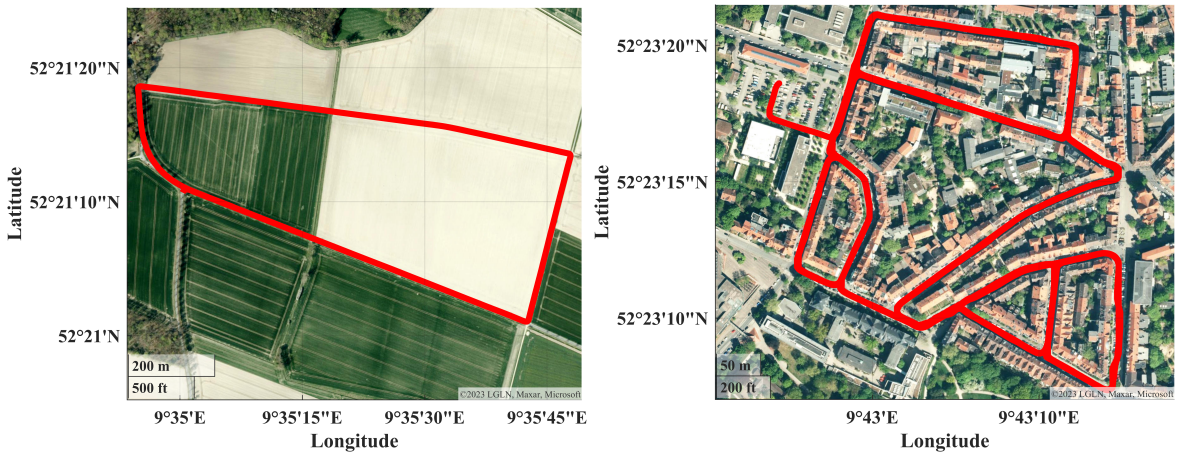


(a) `open-sky` scenario (b) `urban` scenario

**Figure 6.38:** Kinematic trajectories based on Kulemann and Schön (2023) used to analyze the impact of PCC grid resolutions on position estimates.

on topocentric coordinate differences can be assessed. The design matrix $\mathbf{A}$ is filled with the rotated azimuth and elevation angles of all visible satellites $k_{max}$ per epoch $n$. For the stochastic model, identical variances and uncorrelated observations are assumed ($\mathbf{P} = \mathbf{I}$). The observation vector $\mathbf{l}$ is filled with the differences of the computed LOS corrections *corr* per satellite $k$ and reads for differences between the grid resolutions $x_{res} = \{1°, 2°, 5°, 10°, 15°\}$ and the *direct* method

$$\mathbf{l}_n = \begin{bmatrix} corr^{k=1}_{n,\Delta(x_{res}-direct)} \\ \dots \\ corr^{k_{max}}_{n,\Delta(x_{res}-direct)} \end{bmatrix}. \tag{6.12}$$

Figure 6.39(a) shows the `open-sky` results of the *direct* methods as 3D position differences w.r.t the different grid resolutions in a cumulative histogram. All differences are smaller than 0.8 mm, and for $\Delta 1°$ even below 0.01 mm. Thus, it can be stated that for the given data set, the grid resolution/method has no significant impact since other error sources dominate the resulting position error. Figure 6.39 depicts how $\Delta 15°$ differs along the driven trajectory. The differences reach their maximum in the southern part and their minimum in the western side of the experimental area. This is related to the number of visible satellites, i.e. how many

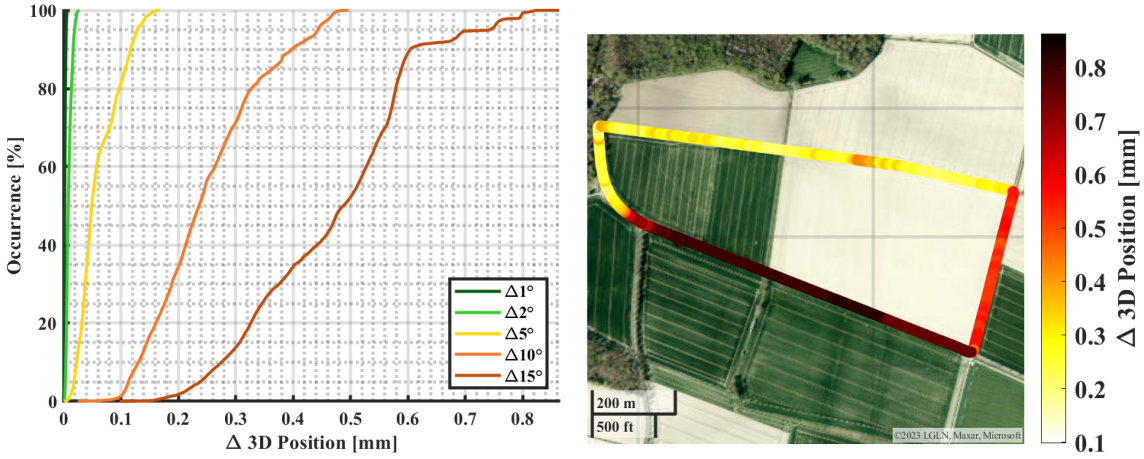


(a) Cumulative histogram (b) $\Delta 15°$ along the trajectory

**Figure 6.39:** Analyses of different PCC grid resolutions on 3D topocentric position estimates for the `open-sky` experiment, shown as absolute differences w.r.t. the *direct* method.

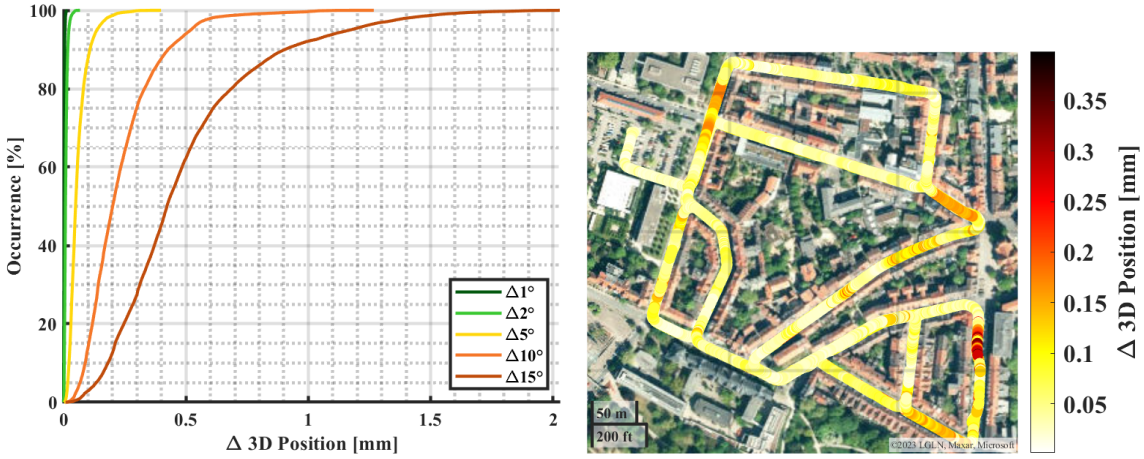


(a) Cumulative histogram (b) $\Delta 5°$ along the trajectory

**Figure 6.40:** Analyses of different PCC grid resolutions on 3D topocentric position estimates for the `urban` experiment, shown as absolute differences w.r.t. the *direct* method.

LOS differences per epoch contribute to the LSA. Since in the western part trees are partly obstructing the trajectory, the total error in the position domain is smaller.

The results for the `urban` scenario are visualized in Figure 6.40. In approximately 16% of all epochs, no solution could be calculated due to the urban canyon caused by narrow streets and densely built-up area. No solution can be calculated if less than four satellites are visible or if the Position Dilution Of Precision (PDOP) value is higher than 50. The maximum differences with $\Delta = 2.03\,\text{mm}$ are present between the 15° resolution and the *direct* method ($\Delta 15°$). For $\Delta 1°$ differences are smaller than 0.02 mm and for $\Delta 5°$ smaller than 0.40 mm. Since 5° is the standard resolution in ANTEX files, these differences are depicted along the trajectory in Figure 6.40(b). The lowest differences occur in the western part at a parking spot, where the car was not moving and low Dilution Of Precision (DOP) values are present. Since there was no movement, the grid size played a secondary, resulting in smaller overall differences.

All in all, it can be summarized for the conducted analyses that the usually used resolution of 5° provided for PCC are sufficient – even for high rate data and kinematic cases.

## 6.6 Summary

In this section, the findings from the previous sections are briefly summarized to provide an overview of the impact of individual investigations on estimated PCC. Table 6.11 highlights the impact in terms of maximum ΔPCC at the pattern level, as well as the influence on the position domain. However, this is only a brief overview as many details need to be considered, which are addressed and discussed in the respective sections. For instance, different datasets with varying receivers are used, and different frequencies from different GNSS are analyzed.

Generally, the maximum ΔPCC at the pattern level is $< 3$ mm, except for GL2W, where dSD and residuals also show significantly higher values compared to other frequencies. The largest differences arise when investigations involve different calibration sets, as seen in cases (A) and (D). It is shown that the key factor is the varying observation quality, rather than the different observation distribution on the antenna hemisphere. This is also reflected in (B), where the receiver impacts the dSD, while the observation distribution remains the same.

The smallest impact on PCC is observed with varying degrees and orders for HSH (case E), as well as with different grid resolutions, as long as the state-of-the-art practices are followed. For case (E), this means that a degree of at least 8 and an order of at least 5 are selected (see Table 2.6, which lists the degrees and orders used by different calibration facilities). In case (H), when a grid resolution of 15° is chosen instead of the *direct* method, where available azimuth and elevation angles are directly inserted into Equation 4.7, higher differences in the position domain can occur, especially in a kinematic scenario. However, with the typical grid resolution of 5°, the differences are smaller than 0.5 mm.

**Table 6.11:** Summary of impacts on PCC: Maximum differences at the pattern level and influences on the position domain based on various investigation scenarios.

| ID | Investigation | Section | Pattern Level | Pos. Domain | Remark |
|---|---|---|---|---|---|
| (A) | Repeat. of inidv. calibrations | 5.3 | $< 3$ mm | - | All sets for GL1C, GL5Q, RL1C |
| (B) | Repeat. with diff. receivers | 5.4 | $< 2$ mm | - | 3 receivers & 3 frequencies |
| (C) | Diff. between identical frequencies from diff. GNSS | 5.5 | $< 2.2$ mm | $< 2.6$ mm | GL2W/GL2L: $< 4.6$ mm, $< 3.5$ mm |
| (D) | Calibration time & length | 6.1 | $< 3$ mm | - | - |
| (E) | Degree & order for HSH | 6.2 | $< 1$ mm | $< 0.7$ mm | On position domain higher for HSH($< 8$,$< 5$) |
| (F) | Methods to stabilize NES | 6.3 | $< 1.5$ mm | - | - |
| (G) | Weighting schemes | 6.4 | $< 1.5$ mm | - | - |
| (H) | Grid resolutions | 6.5 | $< 0.8$ mm | $< 2$ mm | $< 0.5$ mm for 5° res. |

# 7

# Analysis of Phase Center Correction Values for Geodetic Applications

This chapter analyzes PCC for geodetic applications and validates different sets of PCC within the observation domain. In Section 7.1, estimated PCC are validated using real data and both, SD and dSD methods. Section 7.2 explores PCC values in the parameter domain, utilizing the simulation approach developed in Section 3.3.2. This includes assessing the impact on GNSS reference stations in Section 7.2.1 and analyzing effects of $\Delta$PCC on GNSS position time series in Section 7.2.2, with a particular focus on satellite geometry influences. Furthermore, location dependency is evaluated in Section 7.2.3. The chapter concludes by evaluating the effects of different PCC sets on GNSS-based frequency.

## 7.1 Observation Domain

In this section, the estimated NOV PCC are validated in the observation domain using two different approaches. First, the analysis focuses on the improvement in standard deviations when applying PCC to the SD time series of a short baseline. Secondly, the estimated PCC are applied to the dSD during a calibration process to evaluate the enhancement of the corrected observations.

### 7.1.1 Single Differences

The estimated NOV PCC are validated in the observation domain, using real observation data. As stated in Section 3.3.1, the independent validation of PCC in the observation domain is challenging. As suggested, a short baseline approach based on receiver-to-receiver SD is used here to validate different PCC sets. The processing used here follows the general proceeding listed in Section 3.3.1.

A measurement from February 8, 2019 at IfE serves as data set. The pillars *MSD5* and *MSD6* were used here, see Figure 4.4. Since only the differential pattern remains in the SD observations, a LEIAR25.R3 LEIT was used on *MSD6*, the pattern of which is significantly larger than that of NOV. Figure 5.2 can be used as a comparison of the patterns, although the radome (specified as *LEIT*) leads to slightly different calibration values for the *Leica* antenna in this experiment. Multi-GNSS, multi-frequency 1 Hz data was recorded.

Figure 7.1 shows the measurement set up. The stations form a baseline with a length of 7.504 m. At both stations, *Javad Delta TRE_G3T* receivers are used and linked to a common external frequency standard, forming a common-clock short baseline setup. From the figure it

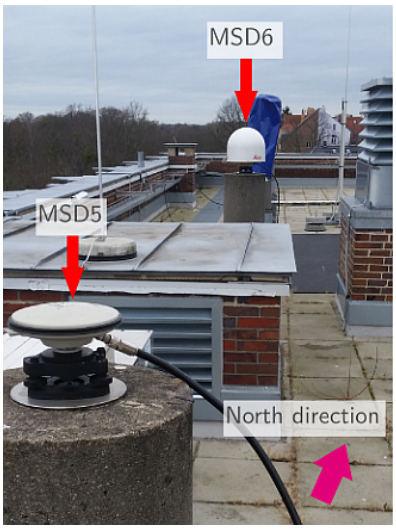


**Figure 7.1:** Measurement setup for validating estimated NOV PCC in the observation domain using a short baseline, common-clock configuration (Kröger et al., 2021).

can already be seen that MP effects might occur which complicate the validation. Especially the ventilation shaft on the right between both stations and the metallic surfaces can cause large MP effects.

In contrast to the results presented in Kröger et al. (2021), where the identical data set has been used, PCC at the reference station are held constant in this study. This is done to facilitate the validation of various patterns at the rover station and to minimize the effect of mixing, when PCC sets at both stations are exchanged. However, this approach has a drawback: the observed differences are relatively small. This is because a $PCO_{Up}$ of 58.27 mm is applied to the observations at the rover station beforehand to prevent large drifts. As can be seen in Section 5.1 for NOV, the $PCO_{Up}$ represents the most significant component of the PCC, and the subtracted value closely matches the $PCO_{Up}$ ($\pm 2$ mm), leading to the applied pattern having a relatively small effect. This small effect complicates the validation, particularly since additional error sources, such as MP effects, might superimpose the impact of the applied PCC set.

Given these challenges, only selected satellite arcs for GL1C and EL1C are presented here as examples. At the rover station *MSD5*, in total five PCC sets are successively applied to the observations:

(A) **IfE**: individual calibration, PCC estimated with the algorithm developed in this work

(B) **IfE (Geo++)**: individual calibration, PCC estimated with Geo++ routines at IfE

(C) **IfE (ASR)**: individual calibration, PCC estimated with the algorithm described in Kröger et al. (2021)

(D) **Geo++ (igsR3)**: type-mean calibration from the ANTEX-file *igsR3_2077.atx*

(E) **Geo++ (IGS20)**: type-mean calibration from the ANTEX-file *IGS20.atx*.

All the PCC sets are determined by method ROBOT (see Section 2.2.3) and are reduced by the identical $PCO_{Up}$ component of 58.27 mm. While sets (A)–(C) are individual calibrations but determined by different calibration algorithms, (D) and (E) are type-mean calibrations of the NOV antenna. Since the maximum GL1C $\Delta$PCC between cases (D) and (E) is 1.99 mm, only minor differences in the observation domain are expected. It is worth noting that the

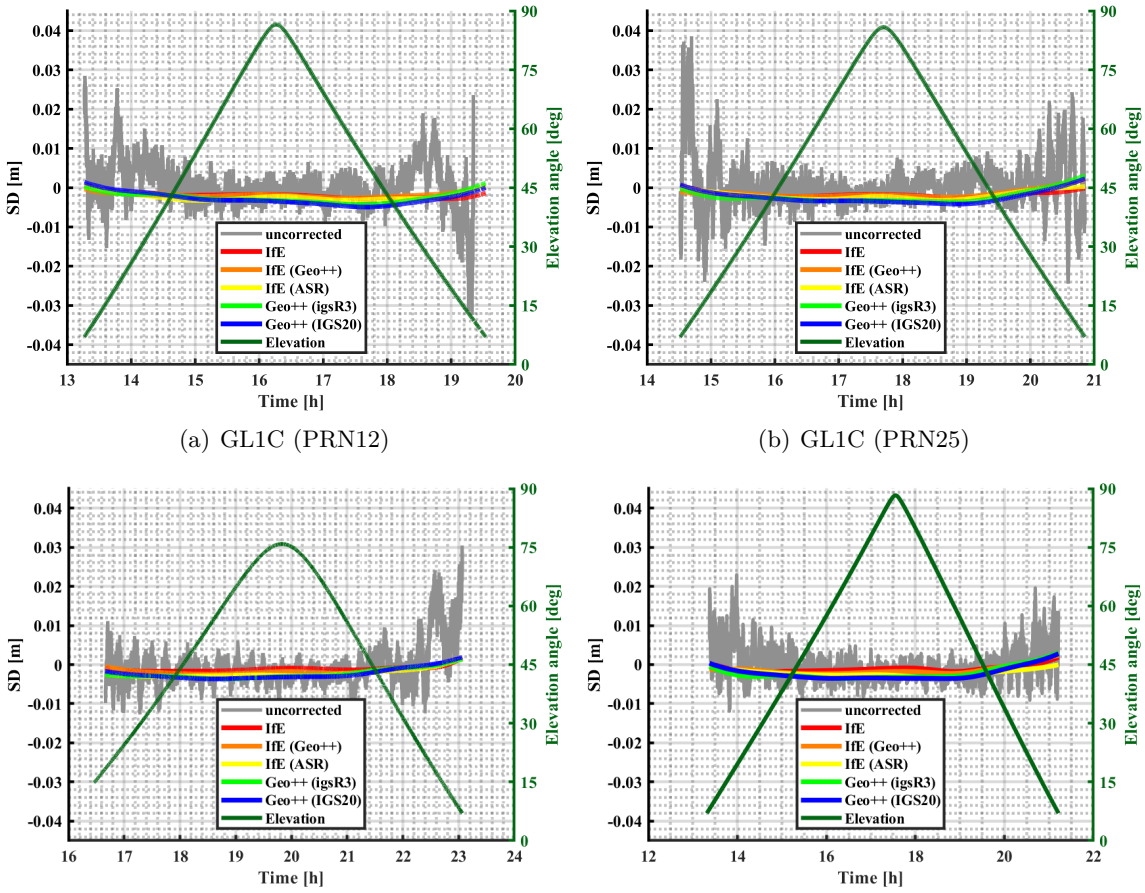


(a) GL1C (PRN12) (b) GL1C (PRN25)

(c) EL1X (PRN21) (d) EL1X (PRN27)

**Figure 7.2:** Resulting SD time series along with different PCC correction values for GL1C and EL1X frequencies, shown for two satellite arcs in each case.

validation strategy, among the measurement setup itself, is dependent on the used processing parameter, especially on:

- Applied PCC set for the antenna at the reference station
- Used a priori $\mathrm{PCO}_{\mathrm{Up}}$, which is applied beforehand to the observations
- Elevation cut-off angle
- Minimum satellite arc length.

In the following, an individual calibration is used (and kept fixed across the different calibration runs) for the `LEIAR25.R3 LEIT` antenna mounted on the used reference station. An elevation cut-off angle of 7° and a minimum satellite arc length of 300 epochs are selected.

Figure 7.2 shows the resulting SD time series along with the different correction values computed on the unit LOS vector. Two satellite arcs with a long visibility for GL1C and EL1X are shown exemplarily. The computed SD are in the range of ±1 cm in the majority, with some higher deviations at lower elevation angles. These effects are most probably linked to MP effects, which complicated the evaluation of the different PCC sets. In general, all calculated corrections fit quite well the time series. However, some small deviations between the different cases are observable. To evaluate the potential improvements achieved by applying the different correction values to the observations, Table 7.1 presents the improvements in terms of the mean standard deviations of corrected SD, achieved by using various PCC sets

**Table 7.1:** Improvements achieved by applying different GL1C correction values to SD time series, evaluated in terms of the overall mean and maximum improvement for a single satellite arc using a 7° elevation cut-off angle. **I** indicates the application of individual PCC, and **II** indicates the use of type-mean PCC for the reference station antenna.

| | | **(A)** | **(B)** | **(C)** | **(D)** | **(E)** |
|---|---|---|---|---|---|---|
| **I** | mean [%] | 1.27 | 1.19 | 0.92 | 0.99 | 1.06 |
| | max [%] | 6.95 | 6.97 | 9.39 | 9.05 | 9.32 |
| **II** | mean [%] | 1.33 | 1.10 | 0.76 | 0.50 | 1.03 |
| | max [%] | 8.02 | 7.22 | 5.6 | 5.83 | 9.16 |

over all satellite arcs, along with the maximum improvement observed for a single satellite arc. Additionally, the impact of changing the PCC set at the reference station is illustrated. Table 7.1 provides the improvements for two scenarios:

- Scenario **I**: individual PCC applied at the reference station
- Scenario **II**: type-mean PCC applied at the reference station.

The results indicate a difference between both scenarios, demonstrating that the validation is influenced by the PCC applied at the reference station. In both scenarios, an improvement is consistently observed, regardless of which pattern is used. However, these improvements are relatively small, ranging from 0.5% to 10%. The limited improvement is attributable to the minor pattern differences between the stations, especially since the a priori $PCO_{Up}$ has already been considered for the *uncorrected* SD at the rover station *MSD5*.

For case (A), the method developed in this thesis results in the highest mean improvement for both scenarios. Nevertheless, the maximum improvement for a single satellite arc is sometimes larger when using one of the other patterns. For the satellite arcs displayed in Figure 7.2, an improvement for case (A) of 1.5% is achieved for PRN12 and 2.3% for PRN25.

To evaluate how the chosen elevation cut-off angle affects the validation strategy, Table 7.2 presents the mean improvements for various cut-off angles, applying individual calibrations for the antenna at the reference station. The values show that the improvements depend on the selected elevation cut-off angle. Nevertheless, an improvement is generally observed, except in cases (C) through (E), where the standard deviation is slightly increased. Generally, the improvement decreases as the cut-off angle is lowered to 5° or 0°. In these scenarios, the validation strategy faces limitations, likely due to the increased presence of MP effects.

To summarize, this section demonstrates that validating PCC is challenging. The conclusions drawn are influenced not only by the measurement setups but also by the PCC set applied at the reference station and the general processing parameters.

**Table 7.2:** Impact of different elevation cut-off angles on the mean improvement of SD time series, with the application of an individual PCC set for the antenna at the reference station. Partly, no improvement is observable, as indicated by "-".

| | **cut-off** | **(A)** | **(B)** | **(C)** | **(D)** | **(E)** |
|---|---|---|---|---|---|---|
| **mean [%]** | 0° | 0.52 | 0.44 | 0.23 | 0.16 | 0.08 |
| | 5° | 0.54 | 0.47 | 0.25 | 0.2 | 0.12 |
| | 7° | 1.27 | 1.19 | 0.92 | 0.99 | 1.06 |
| | 10° | 1.11 | 1.27 | 0.61 | 0.89 | 1.16 |
| | 15° | 0.52 | 0.75 | - | – | - |

### 7.1.2 Time-differenced Single Differences

A recently implemented alternative validation method involves evaluating estimated PCC in the observation domain by using data from a calibration procedure. Using dSD as observations offers advantages, such as largely eliminating the influence of the reference station, as discussed in Section 4.3. To elaborate on this validation method, the estimated NOV pattern is used to generate simulated observations, following the strategy outlined in Section 4.4.4. Since dSD used for PCC estimation theoretically contain only PCC and remaining errors like MP, the standard deviation of the dSD time series should decrease when appropriate PCC are applied.

Figure 7.3 illustrates the improvement in the dSD time series by means of the mean standard deviation of the *corrected* dSD, when different PCC sets are applied. Note that the NOV PCC from *IfE* were determined based on set 1, so that the largest improvement is expected here. However, mean improvements between 0.5% and 6.5% are also seen with other calibration sets when individual calibrations are considered. Apart from *IfE*, the other sets (*IfE (Geo++)* and *IfE (ASR)*) are independent calibrations carried out on different dates. When type-mean calibrations are applied, the standard deviation mostly increases, indicating a negative improvement. Since all individual calibrations were conducted at the same location as the validation data set itself, it is possible that the calibration values are not entirely separated from the station environment, potentially making it to some extent to a station calibration (incorporating, for instance, MP effects).

Although this approach is promising, further investigation is necessary. Specifically, validating other individual calibration sets carried out at different facilities is needed. Future work could be based on the data set recorded as part of the *RingCalVal* project (Kersten et al., 2024a,b). Moreover, considering negative elevation angles is essential. However, since they are not available for most of the other tested calibration sets, they have not been included in this analysis.

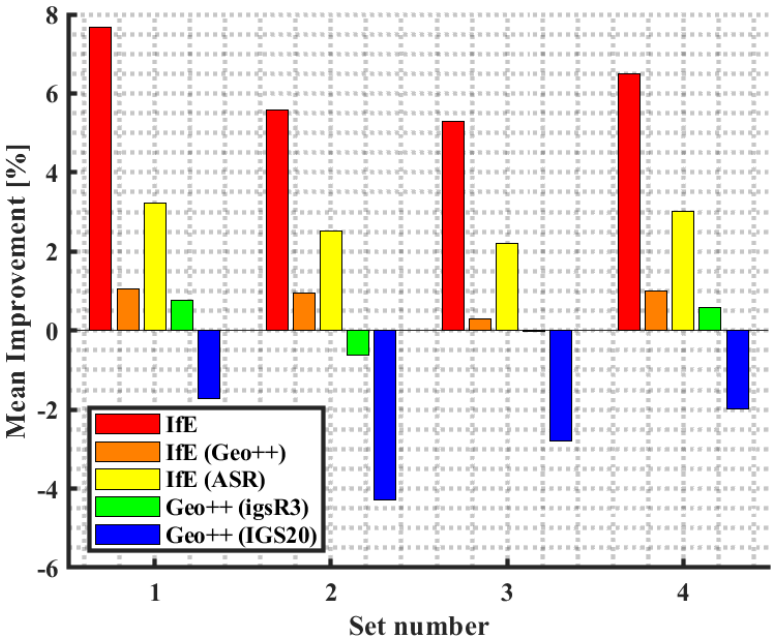


**Figure 7.3:** Improvements achieved by applying different GL1C correction values to dSD time series during a calibration procedure. The improvement is evaluated in terms of the mean standard deviation of the dSD.

## 7.2 Parameter Domain

This section examines the impact of different PCC sets in the parameter domain. To achieve this, the simulative approach described in Section 3.3.2 is utilized to evaluate the impact of ΔPCC on GNSS reference stations, on position time series over a period of three years and on geographic locations. Additionally, the impact on GNSS-based frequency transfer is assessed by applying different PCC sets to both SD and PPP differential receiver clock time series.

### 7.2.1 GNSS Reference Stations

In order to assess the impact of ΔPCC on GNSS reference station, in total 17 stations as part of the EPN are selected. Individual receiver antenna calibrations are available for all these stations, both calibrations determined by method `CHAMBER` and `ROBOT`. Thus, it can be analyzed how a switch from one calibration set to the other affects geodetic parameters, e.g. topocentric coordinate differences. Since the impact using real data at these stations is analyzed in detail in Kersten et al. (2022), the developed simulation approach (see Section 3.3.2) is applied here and compared with the results presented in Kersten et al. (2022).

Figure 7.4 shows the distribution of 16 of the 17 stations. In addition to these stations, which are all located in Germany, station `ISTA`, which is located in Istanbul, Turkey, is also analyzed. For the analyses, the identical processing parameters as in Kersten et al. (2022) are used, so that the respective results can be compared:

- Processing date: January, $8^{\text{th}}$ 2019
- GPS and GLONASS L1/L2 IF-LC
- 24 hrs with a sampling rate of 30 s
- Elevation cut-off angle of 8°
- Elevation-dependent weighting $(1/\sin(el))$.

Figure 7.5 illustrates the impact of varying PCC sets on topocentric position estimates and

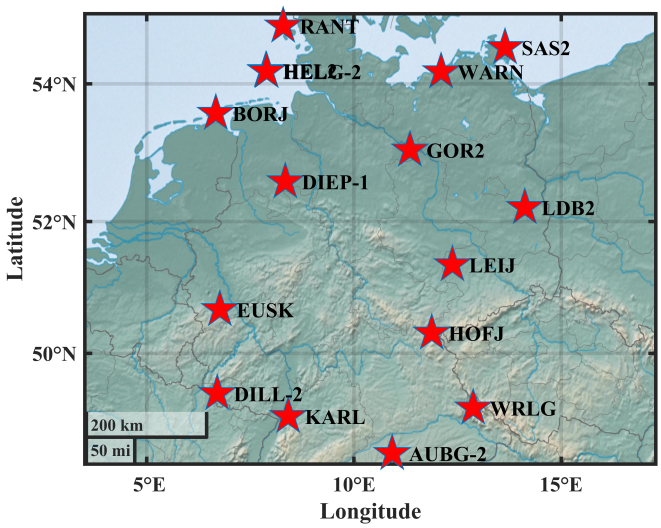


**Figure 7.4:** Distribution of 16 of 17 stations used for analyzing the impact of ΔPCC on reference station. In addition to these stations located in Germany, station `ISTA` located in Istanbul, Turkey, is additionally considered.

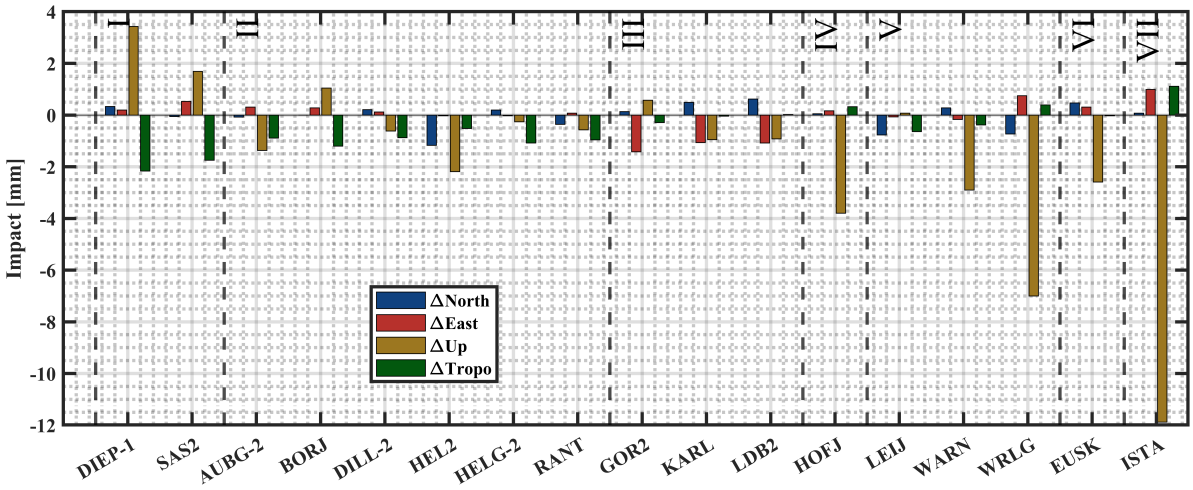


**Figure 7.5:** Impact of varying individual PCC calibrations, either obtained from method `ROBOT` or method `CHAMBER`, on geodetic parameters.

a tropospheric parameter. The estimated receiver clock errors (one for each GNSS) are not presented here, as they are typically of a different order of magnitude. Generally, changes in the PCC set have the largest impact on the topocentric Up-component, with a magnitude of -6.5 mm for station *WRLG* and -12 mm for station *ISTA* being clearly visible. In Kersten et al. (2022), the difference patterns are categorized into seven groups based on the characteristic values of ΔPCC (see Section 3.2.2). The corresponding group numbers are also provided in Figure 7.5 with Roman numerals. Notably, for stations in group III, a relatively high impact on the East-component is detectable.

To compare the results from the simulation approach with the PPP processed real data, Figure 7.6 shows the differences relative to the values presented in Kersten et al. (2022). The results from the developed simulation approach reflect a high degree of similarity to the analysis conducted with real data in Kersten et al. (2022), with most differences below ±0.5 mm. Possible reasons for these deviations are discussed in Section 3.3.2. Notably, differences to Kersten et al. (2022) that exceed the 0.5 mm threshold occur primarily in the Up-component and the tropospheric parameter.. It is important to note the high correlation between these two parameters and the receiver clock error.

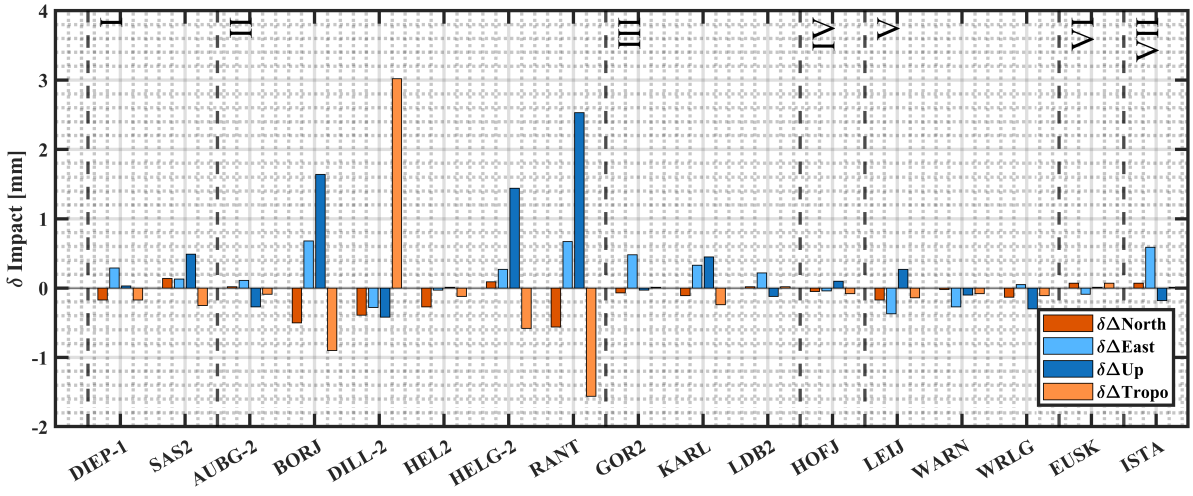


**Figure 7.6:** Differences between the results of the simulation approach and the PPP-processed real data concerning the impact of varying PCC sets on geodetic parameters.

The presented results clearly demonstrate that the developed simulation approach is a powerful tool for assessing the impact of ΔPCC on geodetic parameters. This approach shows that applying different PCC sets as correction values to observations can affect the position solution by more than 1 cm. However, in most cases, the impact remains within a range of ±2 mm, although the topocentric Up-component is occasionally affected by up to 4 mm.

### 7.2.2 GNSS Coordinate Time Series

To evaluate the impact of ΔPCC on geodetic parameters, the difference pattern $\Delta\mathtt{PCC}_{\mathtt{real}}$, which is introduced in Section 3.2 and depicted for GL1C and GL2W in Figure 3.3, is employed. The same PCC set is used throughout, and the impact on geodetic parameters is analyzed by varying the geographic location, interval time, and sampling rate. The various scenarios are outlined in Table 7.3, and the station locations are shown in Figure 3.7. In addition to the processing parameters listed, the following basic settings are used for all six processings:

- Processing time: January, 1st 2021 to December, 31th 2023
- GPS L1/L2 IF-LC
- Elevation cut-off angle of 7°
- Elevation-dependent weighting.

Figure 7.7 presents the results for all scenarios obtained using the developed simulation approach. Overall, the impact is greatest on the receiver clock error (up to 15 mm), followed by the Up-component (up to 8 mm). The impact on the horizontal components and the tropospheric parameter is less than 2 mm. The overall magnitude aligns with the maximum ΔPCC observed at the pattern level, which reaches nearly 14 mm, as shown in Figure 3.4(b).

Additionally, Figure 7.7 clearly shows that, as expected, the time series exhibit greater variability with shorter interval times. For instance, when the impact is assessed every 3 hours, as illustrated in Figures 7.7(a), 7.7(e), and 7.7(f), the highest variations are observed, regardless of the geographic location. Here, noticeable variations with repeatable patterns are also evident. This effect is investigated in more detail in Section 7.2.2.

To analyze the time series further, Figure 7.8 illustrates the impact as mean values over the time series, along with minimum and maximum values. It is evident that the mean value remains highly consistent for the same station BAKE, even when different sampling rates and interval times are processed (scenarios (A) - (D)). However, the variations significantly increase with shorter interval times, while the impact of increasing the sampling rate from 5 min (case (B)) to 30 s (case (C)) is relatively minor. This is because the average change in satellites' elevation angle is about 1° every 2.5 min. Since the PCC are provided with a resolution of 5°, the same grid points mainly contribute to the LSA in both cases (B) and (C), resulting in only small differences between these scenarios.

When comparing scenarios (A), (E), and (F), where only the geographic location is varied,

**Table 7.3:** Varying processing parameters used to assess the impact of ΔPCC on geodetic parameters.

| | **(A)** | **(B)** | **(C)** | **(D)** | **(E)** | **(F)** |
|---|---|---|---|---|---|---|
| Station | | BAKE | | | ANTC | BOAV |
| Interval Time | 3 h | 24 h | 24 h | 12 h | 3 h | 3 h |
| Sampling Rate | 5 min | 5 min | 30 s | 5 min | 5 min | 5 min |

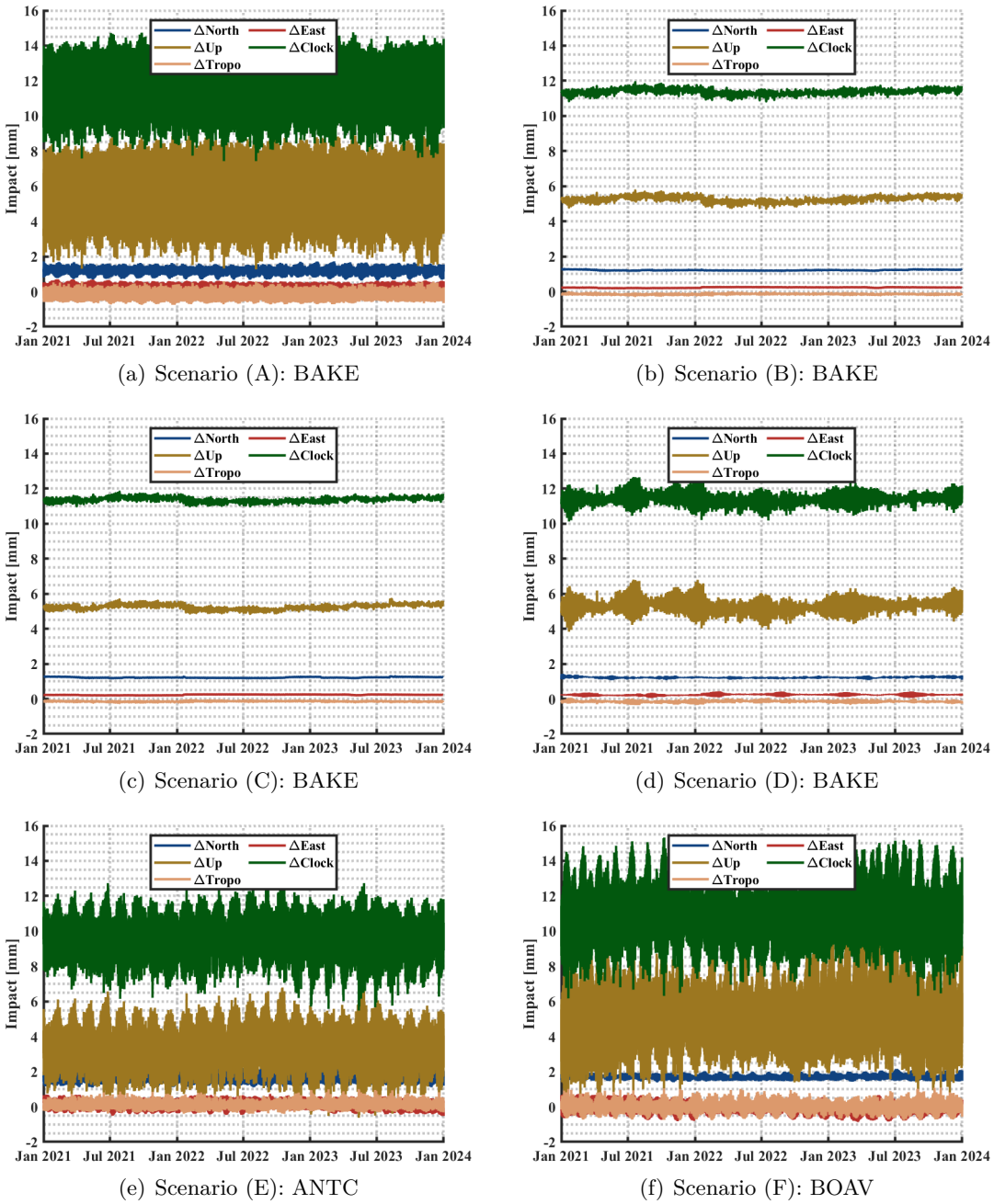


(a) Scenario (A): BAKE

(b) Scenario (B): BAKE

(c) Scenario (C): BAKE

(d) Scenario (D): BAKE

(e) Scenario (E): ANTC

(f) Scenario (F): BOAV

**Figure 7.7:** Impact of ΔPCC on geodetic parameters with varying processing parameters (see Table 7.3). The impact is presented over a three-year time span.

it is observed that the impact of the ΔPCC on the geodetic parameters shows a maximum variation of 2 mm for the Up-component and the receiver clock error. While the impact on these parameters is reduced for scenarios (E) and (F) compared to (A), the impact on the North-component shows a slight increase of less than 1 mm. The location-dependency is further addressed in Section 7.2.3.

The above carried out analyses emphasize the importance of considering geographic location and observation period (both affecting the sensing of the ΔPCC by the satellites) when comparing different PCC sets. Therefore, a suitable approach to assess the impact of ΔPCC on geodetic parameters is to use a shorter interval time and account for variations, rather than computing a daily solution with an interval time of 24 h.

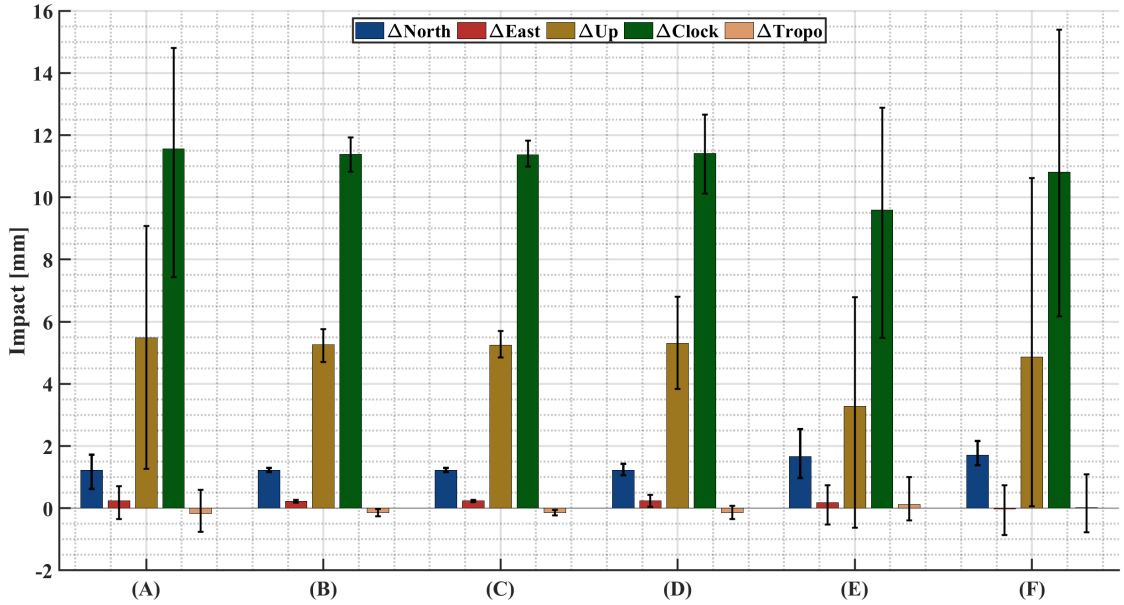


**Figure 7.8:** Impact of ΔPCC on geodetic parameters with varying processing parameters (refer to Table 7.3). The impact is averaged over a three-year period, illustrating the range of variations observed.

### Influence of Satellite Geometry

To analyze the repeatable variations detectable in Figure 7.7 for scenarios with an interval time of 3 h, a Fourier transformation is performed to reveal the frequency components from the Up-component. Figure 7.9(a) shows the obtained frequencies in cycles per day for scenario (A). It is evident that the highest amplitudes occur at approximately 2 cycles per day, followed by 1 and 3 cycles per day. Converting these cycle lengths into hours results in periods of 11 h 58 min, 23 h 56 min, and 7 h 58 min. The first two periods are directly related to the GPS orbital periods. GPS is designed to complete two orbital periods within Earth's sidereal rotation period of 23 h 56 min, resulting in an orbital period of 11 h 58 min. Notably, the revealed variations would differ for multi-GNSS processing, as GLONASS has an orbital period of 11 h 16 min, BeiDou 12 h 53 min, and Galileo 14 h 05 min (Hugentobler and Montenbruck, 2017).

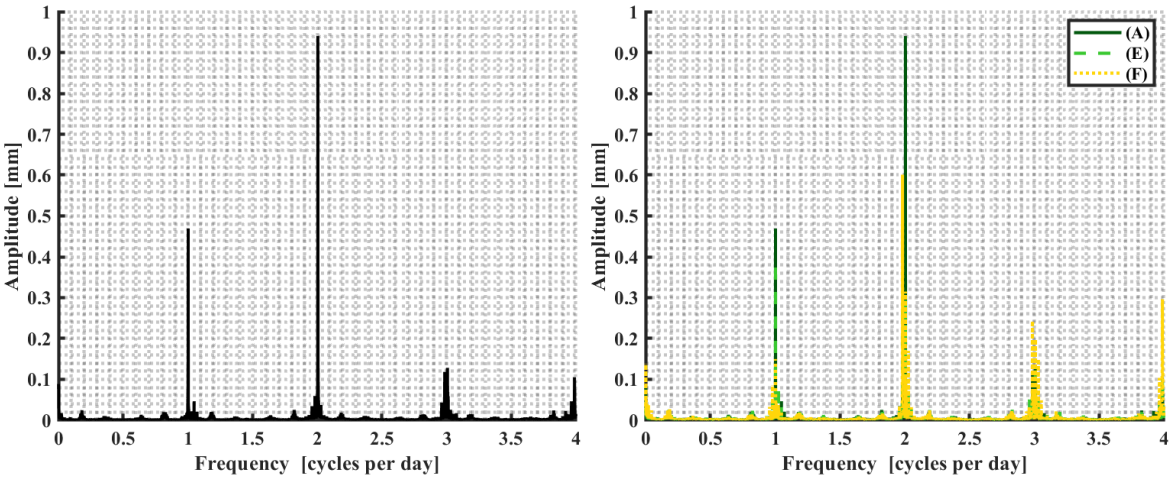


(a) Frequencies for scenario (A)

(b) Frequencies for scenario (A), (E) and (F)

**Figure 7.9:** Frequencies identified from the 3-year impact of ΔPCC on the Up-component using Fourier transformations.

Figure 7.9(b) additionally presents the obtained frequencies for cases (E) and (F). Generally, the three previously mentioned cycles are observable, though their magnitudes differ. Furthermore, the orbital periods, such as the example of one cycle per day (11 h 58 min), vary by less than a minute. This variation is due to individual satellites having unique repetition times (Dilssner, 2007). To thoroughly analyze the occurring frequencies and to detect seasonal signals, a longer time period would need to be processed.

### 7.2.3 Location-dependency

Figure 7.10 exemplifies the impact of GPS L1/L2 IF-LC ΔPCC on the topocentric Up-component using a world map. The impact is calculated for April 1st, 2023, as a daily solution with a sampling rate of 5 min, while the other processing parameters are as specified in Section 7.2.2. The impact is calculated for geographic locations on Earth with a step size of 5° for both latitude and longitude. Also, the GPS ground tracks are shown by red dots.

Overall, the impact ranges from 2 mm to 16 mm, with the highest impact observed near the poles. Furthermore, a strong latitude dependency is evident, while only minor variations are observed across longitudes. This is related to the GPS orbital parameters, particularly the inclination of approximately 55°. This inclination is why the red-colored ground tracks of the GPS satellites are confined to a range of approximately ± 55° latitude. Additionally, some higher differences near the equator are visible, indicated in turquoise, which can also be linked to the satellite ground tracks.

Figure 7.11 illustrates the impact of ΔPCC on additional geodetic parameters. As observed in Figure 7.7 and Figure 7.8, the impact on the East-component and the tropospheric parameter is negligibly small (less than 1 mm). Nonetheless, an interesting, albeit minor, behavior is detectable around the equator.

The impact on the North-component exhibits higher values around latitudes of 0° and 30°, as well as approximately between -45° and -75°. This analysis reaffirms that the impact of ΔPCC on geodetic parameters is influenced by the structure of the difference patterns, as dictated by the local distribution of satellites.

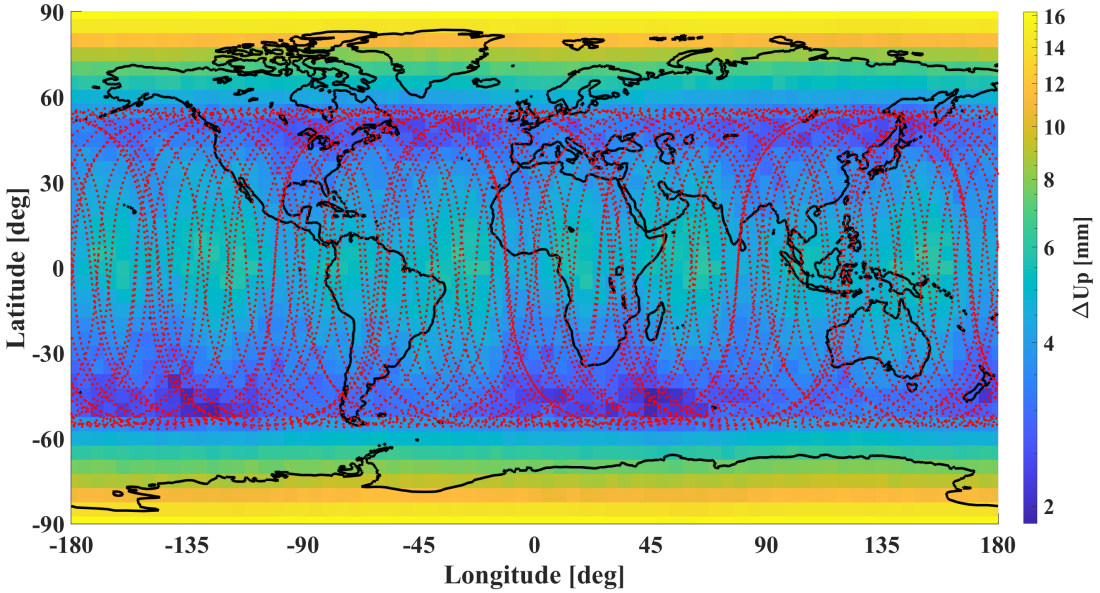


**Figure 7.10:** Impact of ΔPCC on the topocentric Up-component, calculated on a regular 5° latitude and longitude grid. The visualization highlights variations in the impact across different geographic locations.

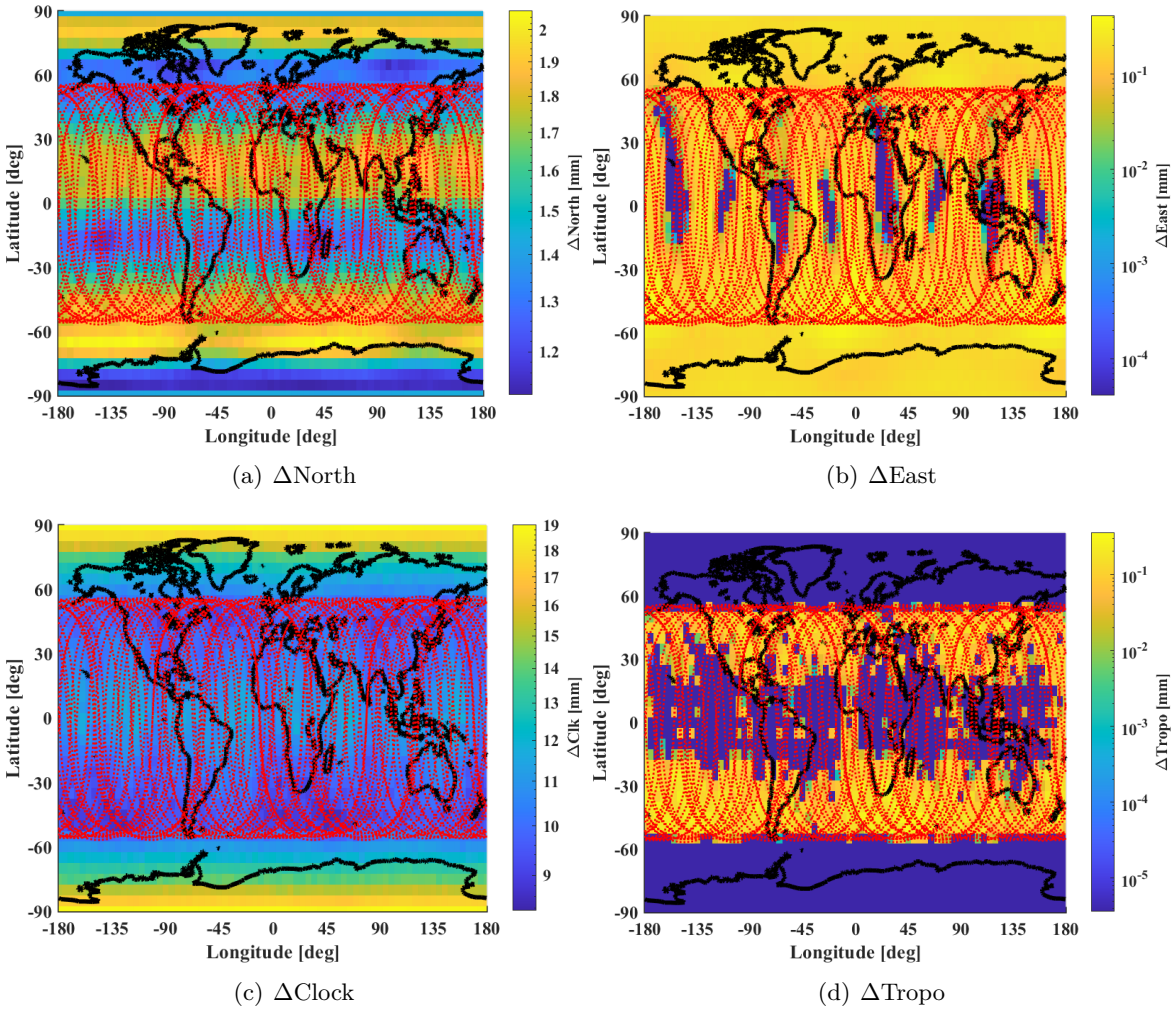


(a) ΔNorth (b) ΔEast

(c) ΔClock (d) ΔTropo

**Figure 7.11:** Impact of ΔPCC on geodetic parameters, calculated on a regular 5° latitude and longitude grid. Note the different scales.

### 7.2.4 GNSS-based Frequency Transfer

To evaluate the impact of different PCC sets on GNSS-based frequency transfer, a common-clock, short baseline setup is used. Two stations, `PTBB` and `MEI2`, form a 295 m baseline, each equipped with the same type of GNSS receiver. Both stations are located at the Physikalisch-Technische Bundesanstalt (PTB) in Brunswick, Germany, as shown in Figure 7.12(a). Further details on the measurement setup can be found in Krawinkel et al. (2022).

In this analysis, PCC values for a *LEIAR25.R4 LEIT* antenna, obtained from an individual chamber calibration, are used at `PTBB` and remain unchanged throughout the analysis. At `MEI2`, a *LEIAR20 LEIM* antenna is used, and five different PCC sets are applied successively to the observations:

(A) Type-mean calibration (method `ROBOT`), 5° resolution

(B) Individual calibration (IfE), 5° resolution

(C) Individual calibration (IfE), 1° resolution

(D) Individual calibration (IfE), method `COEFF`

(E) Type-mean calibration (method `CHAMBER`), 5° resolution.

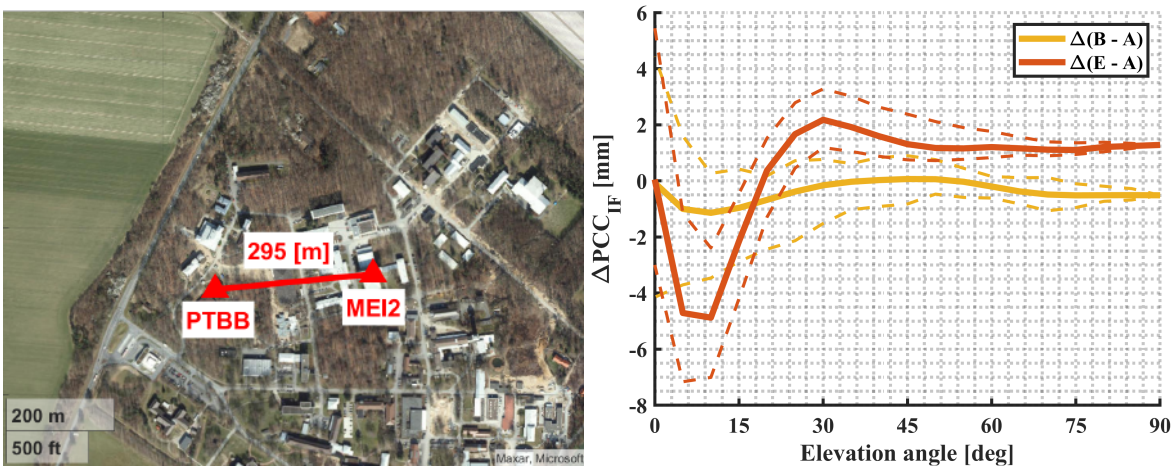


(a) Station locations at the PTB in Brunswick, Germany

(b) ΔPCC for GPS L1/L2 IF-LC

**Figure 7.12:** Measurement setup (a) and GPS ΔPCC as mean differences per elevation angel bin for analyzing the impact of ΔPCC on GNSS-based frequency transfer.

To analyze the impact on frequency transfer, differential receiver clock time series using PPP and SD approaches are utilized. Details on the processing schemes are available in Krawinkel et al. (2022); Elmaghraby et al. (2023). For both approaches, all processing parameters are kept constant, except for the receiver antenna PCC at station `MEI2`, which is modified accordingly.

As reported in Kröger et al. (2023), the maximum GPS L1 differences at the pattern level for gridded values with a resolution of 5° (cases (A), (B), and (E)), reach up to 1.8 mm for Δ(B - A) and 3.8 mm for Δ(E - A). In the PPP approach, IF-LC observations are utilized, which amplifies the ΔPCC, as discussed in Section 3.2.

Figure 7.12(b) presents ΔPCC from GPS L1/L2 IF-LC. It is evident in both scenarios that an offset is observed at 90° elevation angle. This offset could result from a difference in $\mathrm{PCO}_{\mathrm{Up}}$ and/or a differential constant part $r$. While the elevation-dependent differences (solid lines) for Δ(B - A) show only small variations across the elevation angle range, Δ(E - A) exhibits increasing differences at lower elevation angles. For both cases, the differences over azimuthal and elevation angles become more pronounced with decreasing elevation angles. Overall, the maximum difference for Δ(B - A) is 5.47 mm, and for Δ(E - A), it is -7.61 mm. A detailed analysis of how different grid resolutions affect position estimates, including both static and kinematic scenarios, is provided in Section 6.5.

Figure 7.13(a) shows the estimated differential receiver clock error, $\Delta\delta t_{Rx}$, between `PTBB` and `MEI2`, derived using the PPP approach with GPS L1/L2 IF-LC observations. Data from seven days in late April 2021 are analyzed. The overall time series varies between ±0.15 ns, corresponding to approximately ±4.5 m. It is evident that the different PCC sets create an offset in the estimated differential receiver clock errors. Constant parts $r$ within PCC sets are mapped into the receiver clock error, while, for instance, $\Delta\mathrm{PCO}_{\mathrm{Up}}$ components are mapped into the topocentric Up-component. This suggests that each PCC set contains a different constant part within its pattern. The largest offset is caused by PCC set (E), as indicated by the mean values represented by dashed lines. These values are summarized in Table 7.4.

Figure 7.13(b) depicts the results from the SD approach. It is clear that the overall variations are smaller compared to the time series obtained via PPP. In this case, the differential receiver clock error time series ranges from -0.04 ns to +0.06 ns. Again, different PCC sets introduce

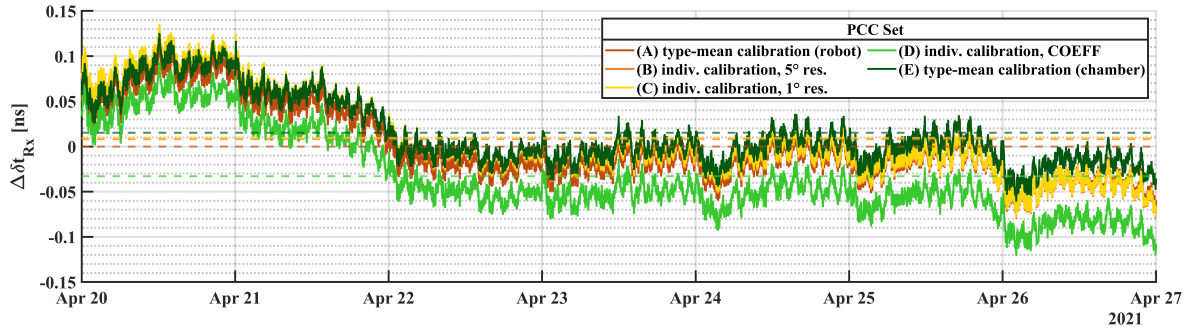


(a) Differential receiver clock error obtained by PPP GPS L1/L2 IF-LC observations.

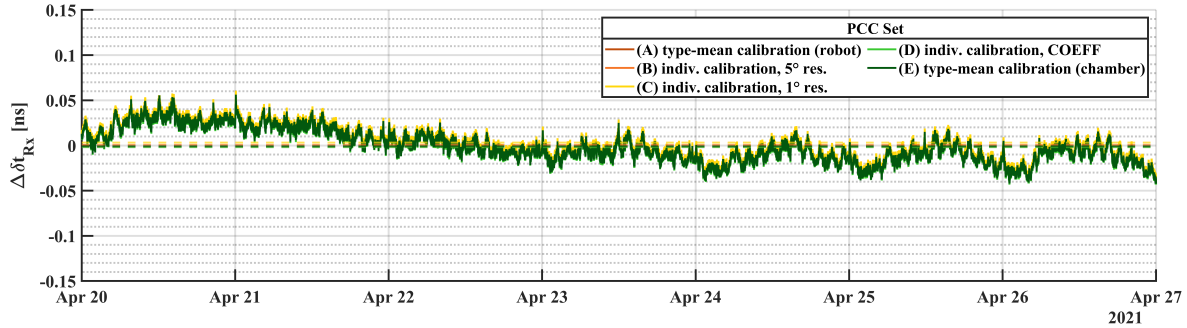


(b) Differential receiver clock error obtained by SD GPS L1 observations

**Figure 7.13:** Resulting differential receiver clock error time series, obtained by applying different PCC sets, to assess the impact on frequency transfer.

offsets into the time series, but the magnitude is smaller compared to the mean values of PPP. This comparison can be directly made by referencing Table 7.4. The reason is that for PPP, the IF-LC is computed, which results in higher $\Delta$PCC values than those obtained from purely L1 data processing, as carried out by the SD method. Consequently, the introduced offsets are also smaller for method SD.

By comparing the mean values of the time series obtained using PPP and SD, it cannot be directly concluded that any particular PCC set is most appropriate. Ideally, the time series should have a zero mean. In the case of PPP, this condition is most closely met by set (A). For SD, the smallest absolute mean value is achieved by set (E), closely followed by set (B).

Since frequency stability is of most importance for GNSS-based frequency transfer, Figure 7.14 illustrates the Modified Allan Deviation (MDEV) for both PPP and SD. In general, the frequency stability ranges from $10^{-13}$ up to $2.4 \cdot 10^{-16}$ for PPP with an averaging time of $\approx 17\,\text{h}$ (61440 s), and up to $6.8 \cdot 10^{-17}$ for SD with an averaging time of $\approx 1.5\,\text{days}$ (122880 s). For both methods, no significant impact of the selected PCC set on frequency stability is

**Table 7.4:** Mean differential receiver clock error values for PPP and SD methods, while applying different PCC sets.

| **PCC Set** | **PPP** [ns] | **SD** [ns] |
|---|---|---|
| (A) | -5.16 $\cdot 10^{-5}$ | -0.0010 |
| (B) | 0.0080 | 7.02 $\cdot 10^{-4}$ |
| (C) | 0.0096 | 0.0031 |
| (D) | -0.0328 | -0.0019 |
| (E) | 0.0153 | -8.70 $\cdot 10^{-4}$ |

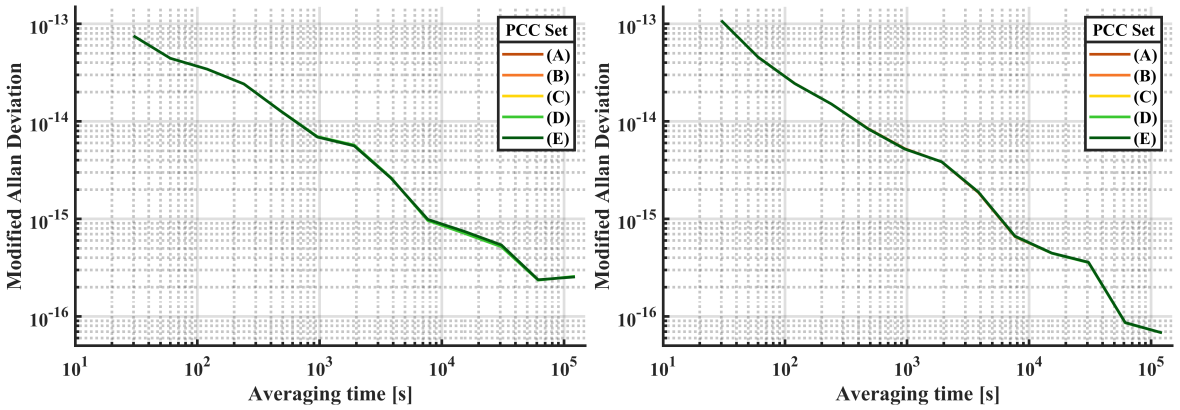


(a) PPP GPS L1/L2 IF-LC (b) SD GPS L1

**Figure 7.14:** MDEV of estimated differential receiver clock errors for PPP and SD methods, while applying different PCC sets.

observed. For a more in-depth analysis of the general aspects of frequency stabilities obtained through PPP or SD, readers are referred to the detailed discussions in Krawinkel et al. (2022) and Elmaghraby et al. (2023).

Overall, the analyses indicate that the different PCC sets are mapped as offsets into the differential receiver clock time series for GNSS-based frequency transfer. Given that the variations in the analyzed $\Delta$PCC at the pattern level are of a small magnitude ($\Delta\text{PCC} < 7.2\,\text{mm}$), no significant impact on frequency stability is observed.

# 8 Conclusions

## Summary

This thesis demonstrates foremost, the successful estimation of multi-GNSS, multi-frequency PCC using a robot and real GNSS signals. It offers a comprehensive evaluation of the processes involved in estimating, comparing, and analyzing PCC sets, revealing crucial insights into their impact on geodetic parameters. By investigating a myriad of strategies for comparing PCC sets ($\Delta$PCC), a standardized simulation approach capable of assessing the $\Delta$PCC impact on various geodetic parameters in multi-GNSS, multi-frequency settings has been developed. Along with the introduction of various characteristic values, describing $\Delta$PCC, the developed approach represents a substantial step towards standardizing the comparison of different PCC sets.

The PCC estimation algorithm, based on Kersten (2014) and further developed, is presented, which successfully estimates multi-GNSS, multi-frequency PCC for newer signals and systems. A major innovation in this work is the parameterization of PCC using an adapted version of HSH functions. This innovation significantly reduces the condition number of the NES, allowing for the calculation of reasonable formal errors for estimated PCC. Consequently, it can be concluded that the challenge of the observation distribution on the antenna hemisphere for estimating PCC has been effectively addressed.

The successful estimation of PCC for three different antenna types (geodetic pinwheel antenna, geodetic 3D choke ring antenna, and mass-market antenna) is presented, along with the quality assessment of the estimated PCC. It is shown that the magnitude of the resulting PCC is correlated with the actual dimensions of the antennas. The quality assessment shows that the residuals generally exhibit expected behavior across the different antenna types and various frequencies, except for GL2W, likely due to receiver settings. However, GL2L PCC, which also corresponds to the GPS L2 frequency, can be applied instead. The formal errors of the estimated PCC indicate this and show that the PCC are estimated precisely (ranging from 0.05 mm to 0.45 mm), whereas the standard deviations for the mass-market antenna are higher (0.2 mm to 0.8 mm) due to noisier observations. These findings are also reflected in the a posteriori variance factors.

In contrast to other GNSS systems, GLONASS uses FDMA for certain frequencies instead of CDMA to uniquely assign individual satellites. Since PCC are frequency-dependent, the GLONASS PCC for FDMA signals result from the frequencies of satellites contributing observations to the LSA. It is demonstrated that the estimated PCC accurately represent the frequency-dependent PCC for the respective GLONASS center frequencies.

An in-depth analysis of the repeatability of individual calibrations shows that maximum differences of up to 3 mm are present for the selected AUT and investigated frequencies. A

comprehensive study reveals that the similarity between two PCC sets, as estimated from individual sets, is influenced not primarily by the distribution of observations on the antenna hemisphere, but significantly by the quality of those observations.

Analyses were conducted to examine the impact of different receivers on estimated PCC. For the investigated antenna-receiver combinations (using one single antenna connected to three different receiver types) and across the analyzed frequencies, the ΔPCC values are generally less than 2.5 mm, with larger differences occurring at low elevation angles. Since a zero baseline was used to ensure equal observation distribution, the differences arise due to the varying quality of the observations.

For identical frequencies, even those from different GNSS, identical PCC values are typically provided in the ANTEX file. However, receivers may process signals from different GNSS differently to some extent. Therefore, investigations were conducted to assess differences between identical frequencies from different GNSS as well as identical frequencies with different tracking modes. Generally, ΔPCC are smaller than 2.2 mm, except for GL2W/GL2L. As stated previously, this is due to unexpectedly high GL2W observation errors. The assessment of the impact of ΔPCC on geodetic parameters reveals a range from -4 mm to 2 mm. The topocentric Up-component and the receiver clock error are the parameters most affected parameters. Overall, the impact of ΔPCC on the position domain is relatively small. For instance, in the case of PPP, it remains below the expected position accuracy. Therefore, in this specific scenario, using a single frequency-dependent PCC set for various GNSS is sufficient. However, for other antennas, and especially when calculating an IF-LC, where ΔPCC are generally amplified, different outcomes may result.

Different calibration institutions use varying settings and methods to calibrate PCC, making it essential to validate these approaches and understand the reasons behind any differences. To this end, PCC were estimated using different degrees and orders for the HSH expansions. A comprehensive literature review revealed that expansions with degrees and orders of 8 and 5, 8 and 8, or 12 and 12 are commonly used. The analyses indicate that the impact on the pattern level from these differences is less than 1 mm, and the impact on the position domain is less than 0.7 mm. However, choosing a lower degree and order results in larger differences. In light of this, SVD of ΔPCC is conducted, clearly showing that fine structures can be revealed using this method.

Special attention was given to testing different methods for stabilizing the NES in PCC estimation to fully demonstrate the capabilities of the newly implemented HSH functions used for estimating PCC. It is shown that using an adapted version of HSH functions instead of SH functions leads to a stable NES without introducing additional restrictions, allowing for adequate estimation of formal errors. Closed-loop simulations further demonstrate that adding white noise with a standard deviation of 2.2 mm has a maximum impact of 1.6 mm on the estimated PCC. In contrast, without any modifications to the NES, large constant offsets are introduced to the PCC. The maximum impact of a large outlier added to the observation vector for the HSH approach is 0.2 mm, while reducing the observations impacts the results by ±0.2 mm. These findings highlight the effectiveness of using HSH functions.

Two additional weighting schemes have been evaluated, demonstrating an impact of up to 4 mm on the pattern level. These schemes help ensure that the residuals better follow a standard normal distribution. However, these weighting schemes depend on the specific antenna-receiver combination used, require pre-estimated PCC (such as a *type-mean* calibration), and the results are influenced by the determined noise factors.

To summarize, several comprehensive and detailed analyses of specific steps and processing parameters have generally shown the following outcomes:

- The largest influence on the repeatability of PCC estimation is the variation in observation quality, rather than differences in observation distribution on the antenna hemisphere. This factor also has the highest order of magnitude across all analyzed research questions.
- The impact of the receiver used for antenna calibration is less than 2 mm.
- Changes in the degree and order for HSH expansions result in differences below 1 mm for typically used values, both at the pattern level and in the position domain.
- Two additional weighting schemes have successfully demonstrated their ability to reflect the noise behavior of observations, resulting in outcomes that more closely follow a standard normal distribution.
- The commonly used resolution of 5° for elevation and azimuth angles in gridded PCC has been shown to effectively capture the full PCC information, as the differences compared to a *direct* method (using azimuth and elevation angles from visible satellites directly) are below 0.5 mm, even in kinematic scenarios.

In conclusion, all the variations introduced by altering specific settings are below the typically expected position accuracy and precision. Nonetheless, these variations are significant since PCC are provided to a hundredth of a millimeter. It is also important to consider that the influence may vary if other data sets or frequencies are analyzed, and that the individual parameters are mutually dependent.

The thesis underscores the challenges of independently validating PCC within the observation domain due to predominant error sources, such as MP effects. It is demonstrated that different PCC sets can be validated by applying them to SD in a short baseline, common clock setup. However, some key factors should be considered, such as applying an a priori $PCO_{Up}$ to the *uncorrected* SD time series to prevent large drifts, and using two different types of antennas to ensure PCC do not cancel out through differencing. It is shown that applying PCC estimated with the developed algorithm to *uncorrected* SD time series can achieve mean improvements in standard deviations ranging from 0.52% to 1.33%. The overall magnitude of these improvements is relatively low due to the accurate a priori PCO, as only $\Delta$PCC between both stations remain, and other error sources complicate the validation process. Furthermore, this validation strategy depends not only on the measurement setup itself but also on factors such as the PCC set applied at the reference station and general processing parameters like elevation cut-off angles. Consequently, a new approach for validating PCC, based on dSD during the calibration process, has been proposed. Initial results are promising, showing mean improvements in standard deviation of the dSD time series of up to 8%, but further investigation is needed.

### Outlook

A clear validation strategy to assess the correctness of estimated PCC is still lacking. Data sets recorded within the IGS *RingCalVal* project offer a valuable resource: Identical antennas are individually calibrated at different calibration facilities, and static measurements with these antennas were performed. These datasets can serve as an excellent source for gaining deeper insights into the validation of PCC. For instance, the recently tested validation strategy, which has shown promising initial results by using dSD and the antenna calibration process, can be further evaluated using these datasets.

Future work could focus on calibrating additional antenna types, with a particular emphasis on everyday objects equipped with GNSS antennas. Devices such as smartphones are increas-

ingly used for precise and accurate positioning. Smartphones, in particular, are already widely utilized, and initial calibration results for these devices have been published. It is important to study the interaction of GNSS signals with other radio waves, such as Bluetooth, mobile networks, and Wi-Fi. Initial investigations in the *ACCURAUTO* project (Kröger et al., 2024) have shown that CPC can change depending on which additional radio waves are activated. This suggests that the electronic reception point may shift, thus influencing the CPC and possibly the PCC as well. In addition to smartphones, smartwatches are also used for positioning and their performance has been investigated and reported in scientific publications. It would be valuable to determine the PCC for these devices as well. For both smartwatches and smartphones, it would be of interest to analyze whether *type-mean* calibrations accurately represent the PCC of individual devices. Given the constraints of limited production costs and performance requirements, there may be larger deviations in the PCC among individual devices due to higher production tolerances.

Furthermore, multi-element antennas could be calibrated in the near future. As spoofing and jamming of GNSS signals increase, these multi-band antennas are expected to become increasingly important. Multi-element GNSS antennas enhance protection against spoofing and jamming through beam forming and spatial filtering, allowing them to focus on authentic signals while nullifying interference. They also improve signal resilience and detection capabilities by analyzing signal characteristics across multiple elements, thereby enhancing positioning accuracy and reliability. However, precise positioning and navigation require exact knowledge of the phase centers, making accurate calibration of these antennas essential.

# A

# Estimated PCC

In this section, the estimated PCC or PCC* for three different antennas are presented.

## A.1 Geodetic Pinwheel Antenna: NOV703.GGG R2

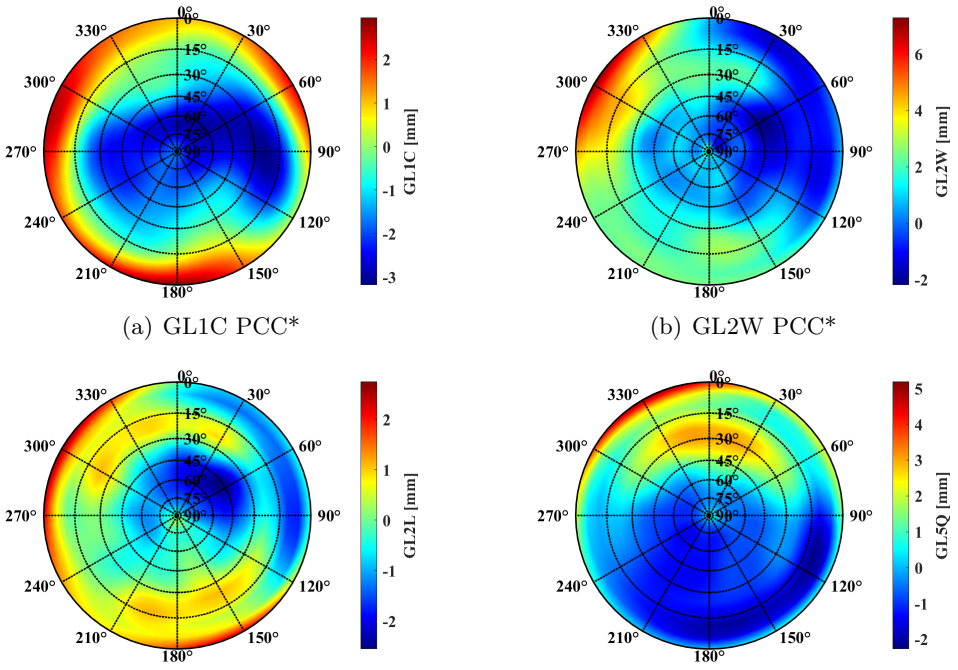


(a) GL1C PCC*

(b) GL2W PCC*

(c) GL2L PCC*

(d) GL5Q PCC*

**Figure A.1:** Estimated NOV PCC* for GPS frequencies. Note the different scales for the color-coded PCC*.

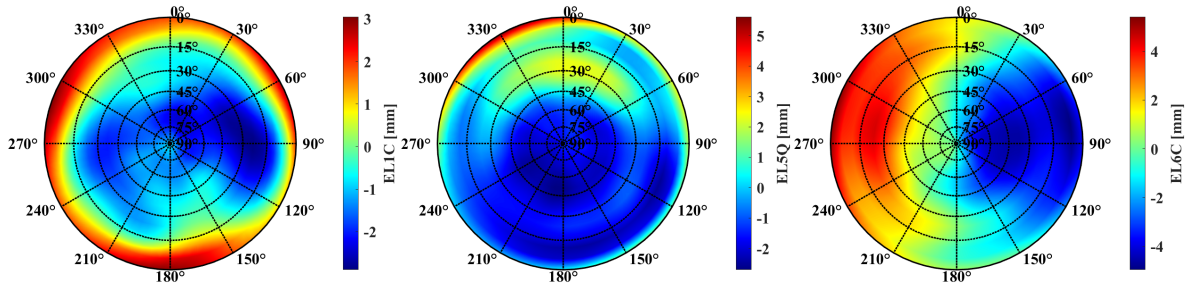


(a) EL1C PCC* (b) EL5Q PCC* (c) EL6C PCC*

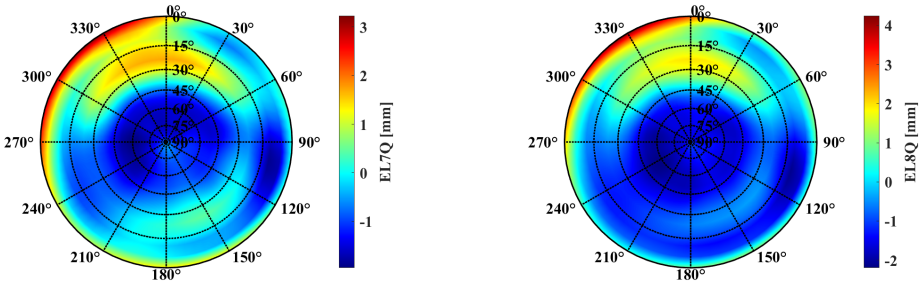


(d) EL7Q PCC* (e) EL8Q PCC*

**Figure A.2:** Estimated NOV PCC* for Galileo frequencies. Note the different scales for the color-coded PCC*.

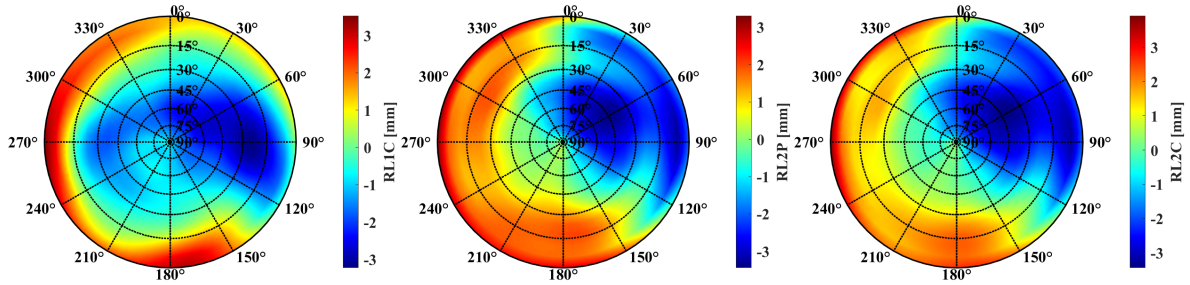


(a) RL1C PCC* (b) RL2P PCC* (c) RL2C PCC*

**Figure A.3:** Estimated NOV PCC* for GLONASS frequencies. Note the different scales for the color-coded PCC*.

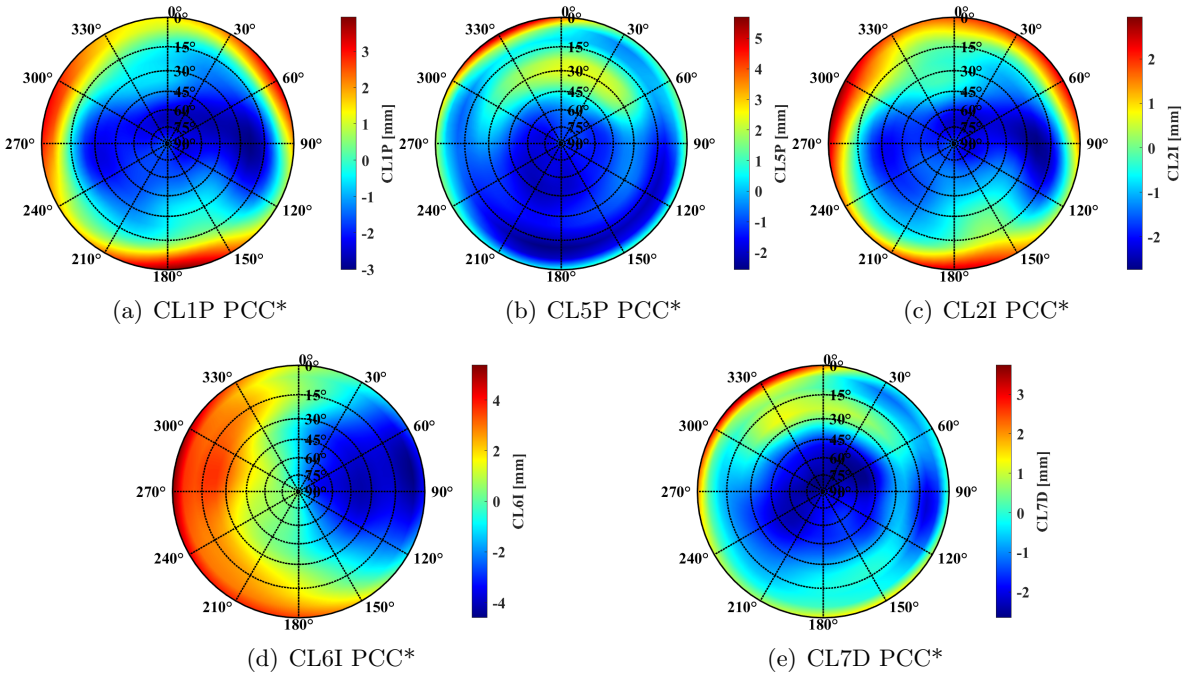


(a) CL1P PCC* (b) CL5P PCC* (c) CL2I PCC*

(d) CL6I PCC* (e) CL7D PCC*

**Figure A.4:** Estimated NOV PCC* for BeiDou frequencies. Note the different scales for the color-coded PCC*.

## A.2 Geodetic 3D Choke Ring Antenna: LEIAR2.R3 NONE

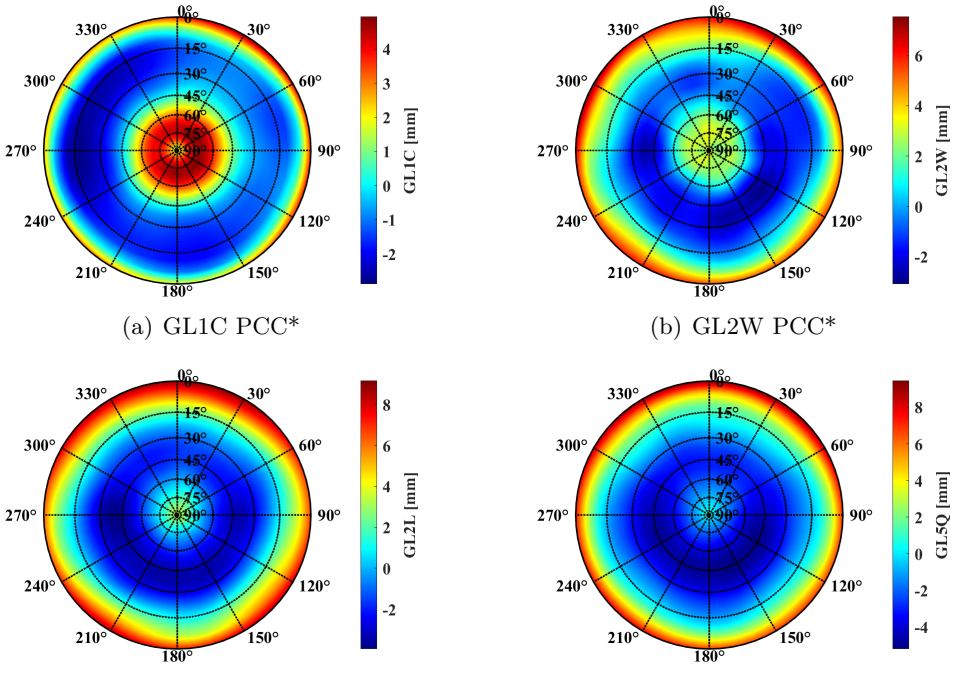


(a) GL1C PCC* (b) GL2W PCC*

(c) GL2L PCC* (d) GL5Q PCC*

**Figure A.5:** Estimated LEI PCC* for GPS frequencies. Note the different scales for the color-coded PCC*.

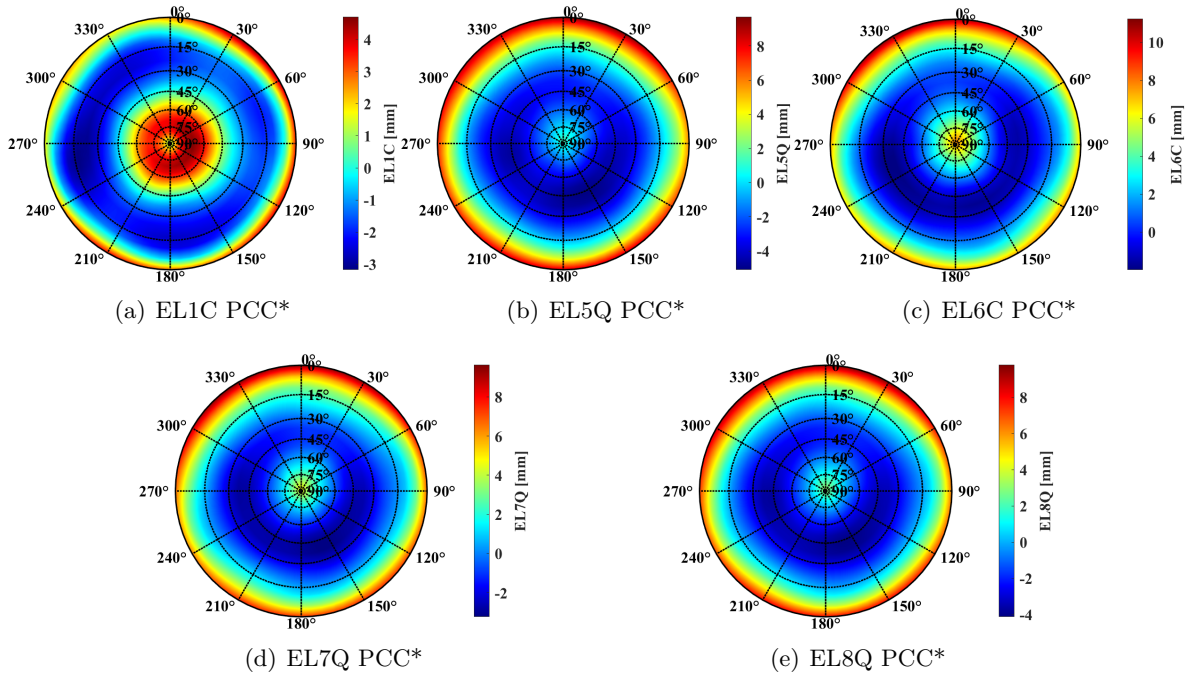


(a) EL1C PCC* (b) EL5Q PCC* (c) EL6C PCC*

(d) EL7Q PCC* (e) EL8Q PCC*

**Figure A.6:** Estimated `LEI` PCC* for Galileo frequencies. Note the different scales for the color-coded PCC*.

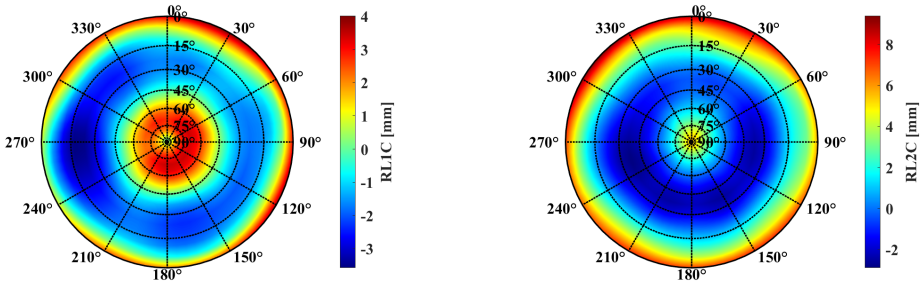


(a) RL1C PCC* (b) RL2C PCC*

**Figure A.7:** Estimated `LEI` PCC* for GLONASS frequencies. Note the different scales for the color-coded PCC*.

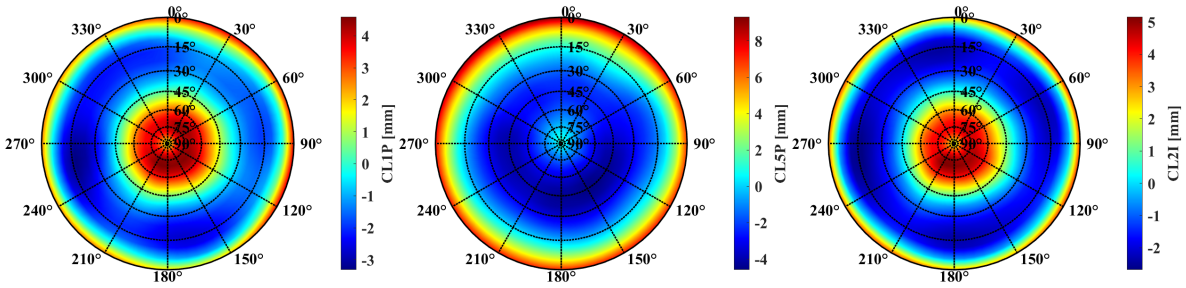


(a) CL1P PCC* (b) CL5P PCC* (c) CL2I PCC*

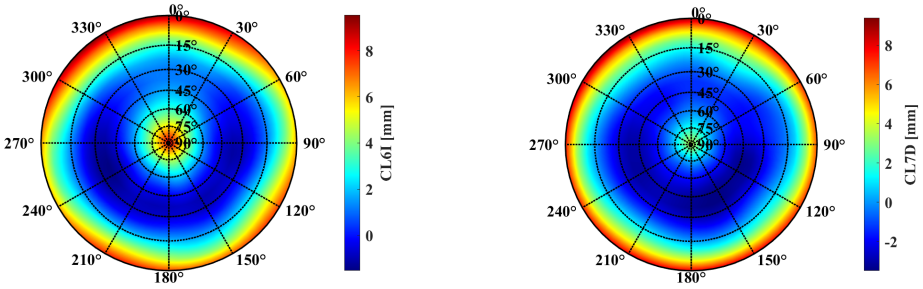


(d) CL6I PCC* (e) CL7D PCC*

**Figure A.8:** Estimated `LEI` PCC* for BeiDou frequencies. Note the different scales for the color-coded PCC*.

## A.3 Mass Market Antenna: ANN-MB1 NONE

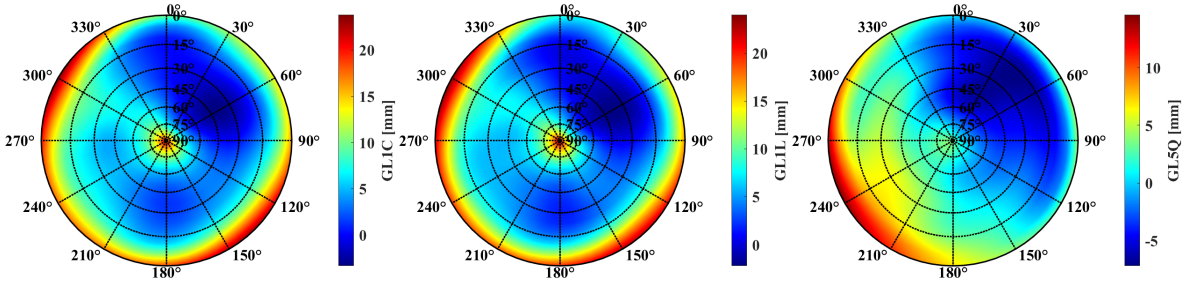


(a) GL1C PCC (b) GL1L PCC (c) GL5Q PCC

**Figure A.9:** Estimated `UBX` PCC for GPS frequencies. Note the different scales for the color-coded PCC.

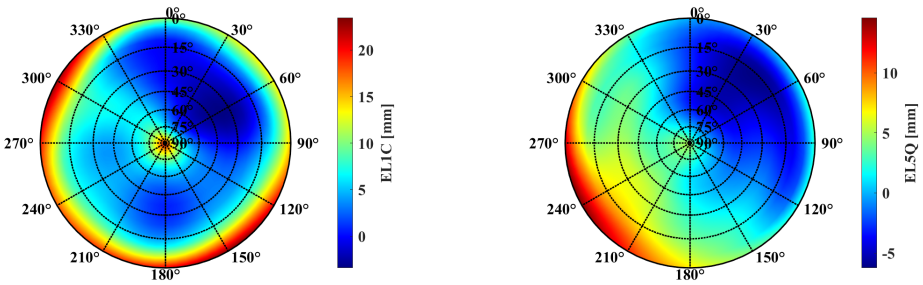


(a) EL1C PCC (b) EL5Q PCC

**Figure A.10:** Estimated `UBX` PCC for Galileo frequencies. Note the different scales for the color-coded PCC.

# B

# Quality Assessment of Estimated PCC

## B.1 LEIAR25.R3 NONE

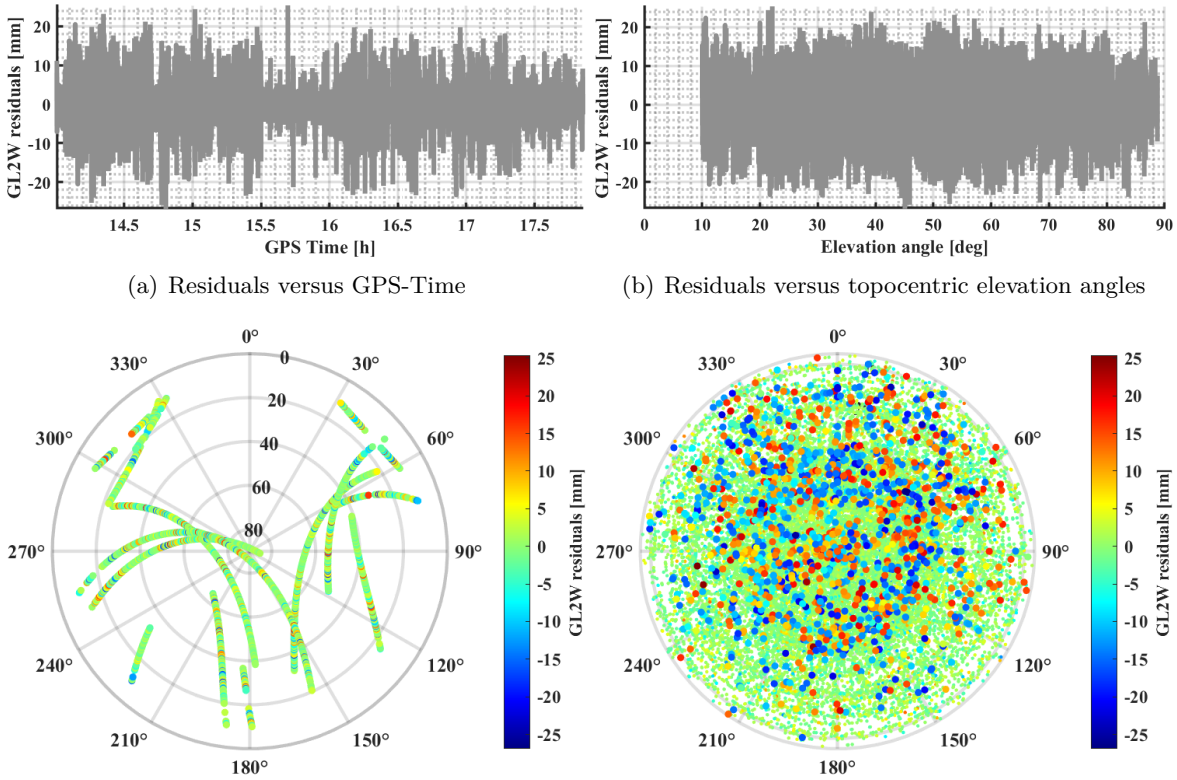


(a) Residuals versus GPS-Time

(b) Residuals versus topocentric elevation angles

(c) Stereographic projection in topocentric frame

(d) Stereographic projection in antenna frame

**Figure B.1:** Residuals of estimated LEI GL2W PCC.

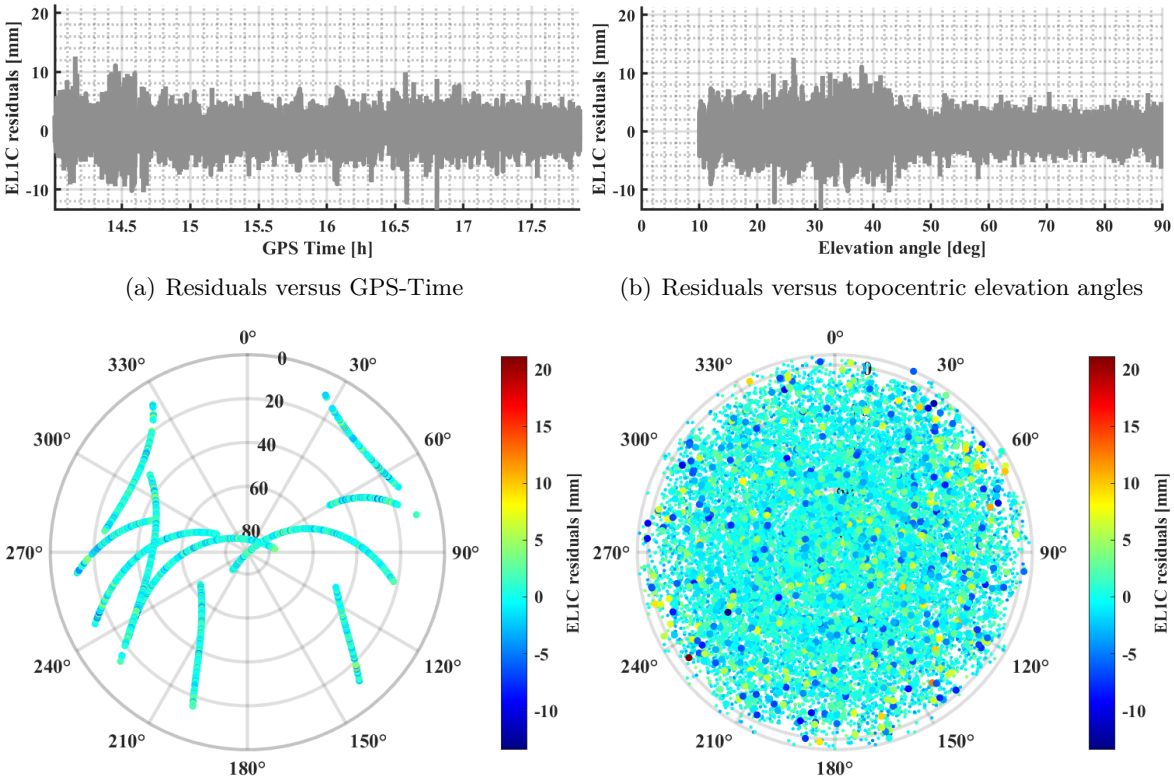


(a) Residuals versus GPS-Time

(b) Residuals versus topocentric elevation angles

(c) Stereographic projection in topocentric frame

(d) Stereographic projection in antenna frame

**Figure B.2:** Residuals of estimated `LEI` EL1C PCC.

## B.2 ANN-MB1 NONE

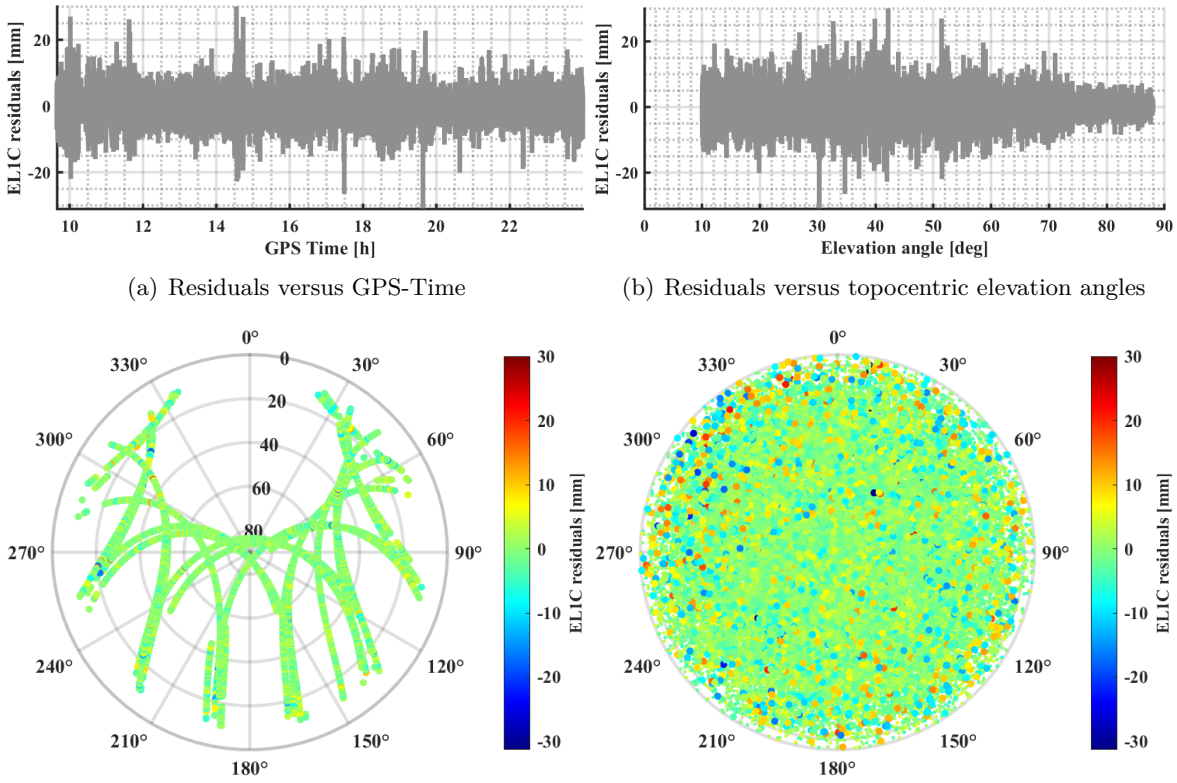


(a) Residuals versus GPS-Time

(b) Residuals versus topocentric elevation angles

(c) Stereographic projection in topocentric frame

(d) Stereographic projection in antenna frame

**Figure B.3:** Residuals of estimated UBX EL1C PCC.

# Bibliography


Araszkiewicz, A. and Völksen, C. (2016). The impact of the antenna phase center models on the coordinates in the EUREF Permanent Network. *GPS Solutions*, 21(2):747–757.

Baire, Q., Bruyninx, C., Legrand, J., Pottiaux, E., Aerts, W., Defraigne, P., Bergeot, N., and Chevalier, J. (2014). Influence of different GPS receiver antenna calibration models on geodetic positioning. *GPS solutions*, 18(4):529–539.

Balmino, G. (2009). Efficient propagation of error covariance matrices of gravitational models: application to GRACE and GOCE. *Journal of Geodesy*, 83(10):989–995.

Bay, H., Ess, A., Tuytelaars, T., and Van Gool, L. (2008). Speeded-Up Robust Features (SURF). *Computer Vision and Image Understanding*, 110(3):346–359.

Bergstrand, S., Jarlemark, P., and Herbertsson, M. (2020). Quantifying errors in GNSS antenna calibrations. *Journal of Geodesy*, 94(10):1–15.

Beyerle, G. (2009). Carrier phase wind-up in GPS reflectometry. *GPS Solutions*, 13:191–198.

Bilich, A. (2021). GNSS Antenna Calibrations at NGS. NGS Webinar Series. https://geodesy.noaa.gov/web/science_edu/webinar_series/gnss-antenna-calibration.shtml. Accessed 06/10/2024.

Bilich, A., Mader, G., and Geoghegan, C. (2018). 6-axis robot for absolute antenna calibration at the US National Geodetic Survey. In: *IGS Workshop 2018, October 2018, Wuhan, China.* Poster.

Bisnath, S. (2021). Relative Positioning and Real-Time Kinematic. In: Morton, Y. J., van Diggelen, F., Spilker Jr, J. J., Parkinson, B. W., Lo, S., and Gao, G. (Ed.), *Position, navigation, and timing technologies in the 21st century: Integrated satellite navigation, sensor systems, and civil applications, volume 1*, pp. 481–502. John Wiley & Sons, Inc., Hoboken, New Jersey.

Böder, V., Menge, F., Seeber, G., Wübbena, G., and Schmitz, M. (2001). How to Deal With Station Dependent Errors, New Developments of the Absolute Field Calibration of PCV and Phase-Multipath With a Precise Robot. In: *ION GPS, September 2001, Salt Lake City, USA*, pp. 2166–2176.

Braasch, M. S. (2017). Multipath. In: Teunissen, P. J. and Montenbruck, O. (Ed.), *Springer Handbook of Global Navigation Satellite Systems*, pp. 444–468. Springer International Publishing AG.

Brekenkamp, M., Kröger, J., and Schön, S. (2022). Einfluss von Phasenzentrumskorrekturen auf die Positionsebene: ein simulativer Ansatz. In: *Frontiers of Geodetic Science, October 2022, Essen, Germany.* Presentation.

Breva, Y. (2025). *On the Observation Quality of Robot-based GNSS Antenna Calibration for Determining Codephase Corrections.* Diss., Deutsche Geodätische Kommission (DGK) bei der Bayerischen Akademie der Wissenschaften (BADW), No. 407.

Breva, Y., Addo, E., Caizzone, S., Kröger, J., Kersten, T., and Schön, S. (2024a). MAESTRO: Understanding Multipath – Antenna – Receiver Interactions for Calibrating Code Phase Variations of GNSS Receiving Antennas. In: *IGS Symposium and Workshop 2024: 30 years of IGS, July 2024, Bern, Switzerland.* Poster.

Breva, Y., Kröger, J., Kersten, T., and Schön, S. (2019). Estimation and validation of receiver antenna codephase variations for multi GNSS signals. In: *7th International Colloquium on Scientific and Fundamental Aspects of GNSS, September 2019, Zurich, Switzerland.*

Breva, Y., Kröger, J., Kersten, T., and Schön, S. (2024b). How Observation Noise impacts the Estimation of Codephase- and Phase-Center Correction with a Robot in the Field. In: *EGU General Assembly 2024, April 2024, Vienna, Austria.* Presentation.

Breva, Y., Kröger, J., Kersten, T., and Schön, S. (2024c). On the Impact of GNSS Receiver Settings on the Estimation of Codephase Center Corrections. In: Freymueller, J. T. and Sánchez, L. (Ed.), *Gravity, Positioning and Reference Frames*, pp. 101–108, Cham. Springer Nature Switzerland.

Brunner, F., Hartinger, H., and Troyer, L. (1999). GPS signal diffraction modelling: the stochastic SIGMA-$\Delta$ model. *Journal of Geodesy*, 73:259–267.

Caizzone, S., Circiu, M.-S., Elmarissi, W., Enneking, C., Felux, M., and Yinusa, K. (2018). Multipath rejection capability analysis of GNSS antennas. In: *Proceedings of the 31st International Technical Meeting of the Satellite Division of the Institute of Navigation (ION GNSS+ 2018)*, pp. 3478–3489.

Caizzone, S., Circiu, M.-S., Elmarissi, W., Enneking, C., Felux, M., and Yinusa, K. (2019). Antenna influence on Global Navigation Satellite System pseudorange performance for future aeronautics multifrequency standardization. *Navigation*, 66(1):99–116.

Caizzone, S., Schönfeldt, M., Elmarissi, W., and Circiu, M.-S. (2021). Antennas as Precise Sensors for GNSS Reference Stations and High-Performance PNT Applications on Earth and in Space. *Sensors*, 21(12):4192.

Copernicus Climate Change Service (2023). ERA5 hourly data on single levels from 1940 to present. https://doi.org/10.24381/cds.adbb2d47. Accessed 28/12/2024.

Dawidowicz, K. (2013). Impact of different GNSS antenna calibration models on height determination in the ASG-EUPOS network: a case study. *Survey Review*, 45(332):386–394.

Dawidowicz, K. (2018). Differences in GPS coordinate time series resulting from the use of individual instead of type-mean antenna phase center calibration model. *Studia Geophysica et Geodaetica*, 62:38–56.

Dawidowicz, K. and Bakuła, M. (2024). Impact of using type mean vs. individual receiver antenna PCC in multi-GNSS PPP. *Survey Review*, 56(398):413–425.

Dawidowicz, K. and Krzan, G. (2016). Analysis of PCC model dependent periodic signals in GLONASS position time series using Lomb-Scargle periodogram. *Acta Geodynamica et Geomaterialia*, 13(3 (183)):299–314.

Dawidowicz, K., Rapiński, J., Śmieja, M., Wielgosz, P., Kwaśniak, D., Jarmołowski, W., Grzegory, T., Tomaszewski, D., Janicka, J., Gołaszewski, P., et al. (2021). Preliminary Results of an Astri/UWM EGNSS Receiver Antenna Calibration Facility. *Sensors*, 21(14):4639.

Dilssner, F. (2007). *Zum Einfluss des Antennenumfeldes auf die hochpräzise GNSS-Positionsbestimmung*. Diss., Leibniz Universität Hannover.

Dilssner, F., Seeber, G., Wübbena, G., and Schmitz, M. (2008). Impact of near-field effects on the GNSS position solution. In: *Proceedings of the 21st International Technical Meeting of the Satellite Division of the Institute of Navigation (ION GNSS 2008)*, pp. 612–624.

Elmaghraby, A., Krawinkel, T., Schön, S., Piester, D., and Bauch, A. (2023). On Error Modeling in GNSS-based Frequency Transfer: Effects of Temperature Variations and Satellite Orbit Repeat Times. In: *Proceedings of the 54th Annual Precise Time and Time Interval Systems and Applications Meeting*, pp. 23–37, Long Beach, California.

EPN (2019). Antenna calibration values for EPN stations. ftp://epncb.eu/pub/station/general/indiv_calibrations. Accessed 01/05/2023.

Fuhrmann, T., Luo, X., Knöpfler, A., and Mayer, M. (2015). Generating statistically robust multipath stacking maps using congruent cells. *GPS Solutions*, 19:83–92.

Gautron, P., Krivanek, J., Pattanaik, S. N., and Bouatouch, K. (2004). A Novel Hemispherical Basis for Accurate and Efficient Rendering. *Rendering Techniques*, 2004:321–330.

Geiger, A. (1988). Modeling of phase center variation and its influence on GPS-positioning. In: Groten, E. and Strauss, R. (Ed.), *GPS-Techniques Applied to Geodesy and Surveying*, Volume 19 of *Proceedings of the International GPS-Workshop Darmstadt, April 10 to 13, 1988*, pp. 210–222. Springer-Verlag.

GLONASS.IAC (2025). Official GLONASS Website. https://glonass-iac.ru/en/sostavOG/. Accessed 05/01/2025.

GPS.GOV (2024). Official U.S. goverment information about the Global Positioning System (GPS) and related topics. https://www.gps.gov/systems/gps/space/. Accessed 23/10/2024.

Hartinger, H. and Brunner, F. K. (1999). Variances of GPS phase observations: the SIGMA-$\epsilon$ model. *GPS Solutions*, 2:35–43.

Hauschild, A. (2017a). Basic Observation Equations. In: Teunissen, P. J. and Montenbruck, O. (Ed.), *Springer Handbook of Global Navigation Satellite Systems*, pp. 561–582. Springer International Publishing AG.

Hauschild, A. (2017b). Combination of Observations. In: Teunissen, P. J. and Montenbruck, O. (Ed.), *Springer Handbook of Global Navigation Satellite Systems*, pp. 583–604. Springer International Publishing AG.

Hill, A., Moore, M., and Dawson, J. (2013). GNSS Antenna Calibration at Geoscience Australia. In: *American Geophysical Union, Fall Meeting, December 09-13, San Francisco, CA, USA*.

Hofmann-Wellenhof, B. and Moritz, H. (2006). *Physical Geodesy*. Springer Vienna.

Hu, Z., Cai, H., Jiao, W., Zhou, R., Zhai, Q., Liu, X., Kan, H., and Zhao, Q. (2022). Preliminary Results of iGMAS BDS/GNSS Absolute Antenna Phase Center Field Calibration. In: Yang, C. and Xie, J. (Ed.), *China Satellite Navigation Conference (CSNC 2022) Proceedings*, pp. 147–160, Singapore. Springer Nature Singapore.

Hu, Z. and Zhao, Q. (2018). Field Absolute Calibration of the GPS/BDS Receiver Antenna at Wuhan University: Preliminary Results. In: *IGS Workshop, November 2018, Wuhan, China.*

Huber, P. J. (1981). *Robust Statistics*. John Wiley & Sons.

Hugentobler, U. and Montenbruck, O. (2017). Satellite Orbits and Attitude. In: Teunissen, P. J. G. and Montenbruck, O. (Ed.), *Springer Handbook of Global Navigation Satellite Systems*, pp. 59–90. Springer.

IGS (2023). RINEX - The Receiver Independent Exchange Format Version 4.01.

IGS (2024). International GNSS Service Data Access. https://files.igs.org/pub/station/general/. accessed 01/12/2024.

JCGM (2008). *JCGM 100: evaluation of measurement data - guide to the expression of uncertainty in measurement (GUM)*. Sèvres, Cedex: Joint Commitee for Guides in Metrology (JCGM/WG1).

Johnston, G., Riddell, A., and Hausler, G. (2017). The International GNSS Service. In: Teunissen, P. J. and Montenbruck, O. (Ed.), *Springer Handbook of Global Navigation Satellite Systems*, pp. 967–982. Springer International Publishing AG.

Kallio, U., Koivula, H., Lahtinen, S., Nikkonen, V., and Poutanen, M. (2018). Validating and comparing GNSS antenna calibrations. *Journal of Geodesy*, 93(1):1–18.

Karimidoona, A. and Schön, S. (2023). Predicting C/N0 as a Key Parameter for Network RTK Integrity Prediction in Urban Environments. *Remote Sensing*, 15(19).

Kersten, T. (2014). *Bestimmung von Codephasen-Variationen bei GNSS-Empfangsantennen und deren Einfluss auf die Positionierung, Navigation und Zeitübertragung*. Diss., Deutsche Geodätische Kommission (DGK) bei der Bayerischen Akademie der Wissenschaften (BADW), No. 740.

Kersten, T., Bilich, A., Sutyagin, I., and Schön, S. (2024a). A Global Collaboration to Enhance GNSS Receiver Antenna Calibration: The IGS Antenna Ring Campaign. In: *EGU General Assembly 2024, April 2024, Vienna, Austria.* Presentation.

Kersten, T., Kröger, J., and Schön, S. (2022). Comparison concept and quality metrics for GNSS antenna calibrations: Cause and effect on regional GNSS networks. *Journal of Geodesy*, 96(7):48.

Kersten, T. and Schön, S. (2012). Von der Komponentenkalibrierung zur Systemanalyse: Konsistente Korrekturverfahren von Instrumentenfehlern für Multi-GNSS - Schlussbericht zum BMBF/DLR Vorhaben 50NA0903. *Institut für Erdmessung*, pp. 105.

Kersten, T. and Schön, S. (2017). GPS code phase variations (CPV) for GNSS receiver antennas and their effect on geodetic parameters and ambiguity resolution. *Journal of Geodesy*, 91(6):579–596.

Kersten, T., Sutyagin, I., Bilich, A., and Schön, S. (2024b). Uniting Global Efforts to Calibrate GNSS Antennas: Models, analyses and pilot results. In: *IGS Symposium and Workshop 2024: 30 years of IGS, July 2024, Bern, Switzerland.* Presentation.

Kersten, T., Sutyagin, I., Bilich, A., and Schön, S. (2024c). Uniting Global Efforts to Calibrate GNSS Antennas: Models, analyses and pilot results. In: *IGS Symposium and Workshop 2024: 30 years of IGS, July 2024, Bern, Switzerland.* Poster.

Koppmann, V. (2018). Bestimmung neuer ITRF14 und ETRS89 Referenzkoordinaten für das GNSS-Labornetzwerk des Institut für Erdmessung. Bachelor thesis, Leibniz Universität Hannover.

Kouba, J., Lahaye, F., and Tétreault, P. (2017). Precise Point Positioning. In: Teunissen, P. J. and Montenbruck, O. (Ed.), *Springer Handbook of Global Navigation Satellite Systems*, pp. 723–752. Springer International Publishing AG.

Krawinkel, T., Elmaghraby, A., and Schön, S. (2022). Exploring the Technical Limits of GNSS-based Frequency

Transfer. In: *Proceedings of the 53rd Annual Precise Time and Time Interval Systems and Applications Meeting*, pp. 188–198, Long Beach, California.

Kröger, J., Breva, Y., Kersten, T., and Schön, S. (2019a). Bestimmung und Validierung von Phasenzentrumsvariationen für Multi-GNSS-Signale. In: *Frontiers of Geodetic Science, September 2019, Stuttgart, Germany.* Poster.

Kröger, J., Breva, Y., Kersten, T., and Schön, S. (2019b). Determination of phase center corrections for Galileo signals. In: *7th International Colloquium on Scientific and Fundamental Aspects of GNSS, September 2019, Zurich, Switzerland.*

Kröger, J., Breva, Y., Kersten, T., and Schön, S. (2019c). Phase Center Corrections for new GNSS-Signals. In: *EGU General Assembly 2024, April 2019, Vienna, Austria.*, Nummer 21 in Geophysical Research Abstracts. Presentation.

Kröger, J., Breva, Y., Kersten, T., and Schön, S. (2021). Are Phase Center Corrections Identical for Identical Frequencies from Different GNSS? In: *FIG e-Working Week 2021 : Smart Surveyors for Land and Water Management - Challenges in a New Reality, June 2021, Virtual.*

Kröger, J., Breva, Y., Kersten, T., and Schön, S. (2024). Recent Antenna Calibration Developments at IFE. In: *IGS Symposium and Workshop 2024: 30 years of IGS, July 2024, Bern, Switzerland.* Poster.

Kröger, J., Elmaghraby, A., Krawinkel, T., Kersten, T., Breva, Y., and Schön, S. (2023). Impact of different phase center correction values on GNSS-based positioning and frequency transfer. In: *28th General Assembly of the International Union of Geodesy and Geophysics (IUGG), July 2023, Berlin, Germany.* Presentation.

Kröger, J., Kersten, T., Breva, Y., Brekenkamp, M., and Schön, S. (2022a). Impact of Different Phase Center Correction Values on Geodetic Parameters: A Standardized Simulation Approach. In: *EGU General Assembly 2022, April 2022, Vienna, Austria.* Presentation.

Kröger, J., Kersten, T., Breva, Y., and Schön, S. (2022b). How Do Different Phase Center Correction Values Impact GNSS Reference Frame Stations? In: *IAG International Symposium on Reference Frames for Applications in Geosciences (REFAG), October 2022, Thessaloniki, Greece.* Presentation.

Kröger, J., Kersten, T., Breva, Y., and Schön, S. (2022c). On the Potential of Image Similarity Metrics for Comparing Phase Center Corrections. In: Freymueller, J. and Sánchez, L. (Ed.), *International Association of Geodesy Symposia*, International Association of Geodesy Symposia, pp. 345–357.

Kröger, J., Kersten, T., Breva, Y., and Schön, S. (2021). Multi-frequency multi-GNSS receiver antenna calibration at IfE: Concept - calibration results - validation. *Advances in Space Research*, pp. 4932–4947.

Kröger, J., Ren, L., Wübenna, J., Tripathi, V., Caizzone, S., and Schön, S. (2024). Impact of GNSS receivers on GNSS antenna performance prediction for automotive scenarios. In: *11th ESA Workshop on Satellite Navigation Technologies and European Workshop on GNSS Signals and Signal Processing (NAVITEC)*, Noordwijk, The Netherlands. Presentation.

Kulemann, D. and Schön, S. (2023). Towards Integrity Monitoring of GNSS Velocity Estimates in Urban Environment. In: *ION GNSS+, The International Technical Meeting of the Satellite Division of The Institute of Navigation*, GNSS 2023. Institute of Navigation.

Larson, K. M., Small, E. E., Gutmann, E., Bilich, A., Axelrad, P., and Braun, J. (2008). Using GPS multipath to measure soil moisture fluctuations: Initial results. *GPS Solutions*, 12:173–177.

Liao, M., Lyu, X., Meng, Z., and You, Z. (2024). GNSS Spoofing Detection for Single Antenna Receivers via CNR Variation Monitoring. *Journal of Systems Engineering and Electronics*, 35(5):1276–1286.

Mader, G. L. and MacKay, J. R. (1996). Calibration of GPS Antennas. In: *IGS Analysis Center Workshop, March 1996, Silver Spring, USA*. Presentation.

Maqsood, M., Gao, S., and Montenbruck, O. (2017). Antennas. In: Teunissen, P. J. and Montenbruck, O. (Ed.), *Springer Handbook of Global Navigation Satellite Systems*, pp. 505–534. Springer International Publishing AG.

McGraw, G. A., Groves, P. D., and Ashman, B. W. (2021). Robust Positioning in the Presence of Multipath and NLOS GNSS Signals. In: Y. T. Jade Morton; Frank van Diggelen; Spilker Jr., J. J. B. W. P. (Ed.), *Position, Navigation, and Timing Technologies in the 21st Century: Integrated Satellite Navigation, Sensor Systems, and Civil Applications*, pp. 551–590. John Wiley & Sons, Inc., Hoboken, New Jersey.

Meiser, V. (2009). Kalibrierung des GNSS Antennenkalibrierroboters des Institut für Erdmessung mittels

Lasertracking. Technical Report.

Menge, F., Seeber, G., Völksen, C., Wübbena, G., and Schmitz, M. (1998). Results of the absolute field calibration of GPS antenna PCV. In: *Proceedings of the 11th International Technical Meeting of the Satellite Division of The Institute of Navigation (ION GPS 1998), September 15 - 18, Nashville, TN, USA*, pp. 31–38. (unpublished).

Meurer, M. and Antreich, F. (2017). Signals and Modulation. In: Teunissen, P. J. and Montenbruck, O. (Ed.), *Springer Handbook of Global Navigation Satellite Systems*, pp. 91–119. Springer International Publishing AG.

Misra, P. and Enge, P. (2011). *Global Positioning System: Signals, Measurements*. Ganga-Jamuna, Lincoln, 2006, 2nd edition edition.

Montenbruck, O., Steigenberger, P., and Villiger, A. (2024). Email in IGS AWG mailing list: ANTEX 2.0 Format Examples and Test data (IGS-AWG-552).

Morton, Y. J., Yang, R., and Breitsch, B. (2020). GNSS Receiver Signal Tracking. In: Morton, Y. J., van Diggelen, F., Spilker Jr, J. J., Parkinson, B. W., Lo, S., and Gao, G. (Ed.), *Position, Navigation, and Timing Technologies in the 21st Century*, pp. 339–375. John Wiley & Sons, Ltd.

Niemeier, W. (2008). *Ausgleichungsrechnung*. De Gruyter, Berlin, New York.

Novatel (2011). Novatel 703GGG.R2. Product Sheet, Novatel.

Rao, B. R., Kunysz, W., Fante, R. L., and McDonals, K. (2013). *GPS/GNSS Antennas*. Artech House Publishers, Norwood, USA.

Rebischung, P., Griffiths, J., Ray, J., Schmid, R., Collilieux, X., and Garayt, B. (2012). IGS08: the IGS realization of ITRF2008. *GPS Solutions*, 16:483–494.

Revnivykh, S., Bolkunov, A., Serdyukov, A., and Montenbruck, O. (2017). GLONASS. In: Teunissen, P. J. and Montenbruck, O. (Ed.), *Springer Handbook of Global Navigation Satellite Systems*, pp. 219–245. Springer International Publishing AG.

Rost, C. and Wanninger, L. (2009). Carrier phase multipath mitigation based on GNSS signal quality measurements. *Journal of Applied Geodesy*, 3(2):81–87.

Rothacher, M., Schaer, S., Mervat, L., and Beutler, G. (1995). Determination of Antenna Phase Center Variations using GPS Data. In: *IGS Workshop - Special Topics and new Directions, 15 - 18 May, 1995, Potsdam, BB, Germany*, pp. 16.

Rothacher, M. and Schmid, R. (2010). ANTEX: The Antenna Exchange Format, Version 1.4.

Schmid, R. (2013). IGS Antenna Working Group. In: Dach, R. and Yean, Y. (Ed.), *IGS Technical Report 2012*, pp. 141–147. IGS Central Bureau.

Schmid, R., Rothacher, M., Thaller, D., and Steigenberger, P. (2005). Absolute phase center corrections of satellite and receiver antennas. *GPS Solutions*, 9(4):283–293.

Schupler, B. and Clark, T. A. (1991). How different antennas affect the GPS observables. *GPS World*, 2(10):32–36.

Schön, S. and Kersten, T. (2014). Comparing antenna phase center corrections: challenges, concepts and perspectives. In: *IGS Analysis Workshop, June 23-27, Pasadena, California, USA*.

Sims, M. L. (1985). Phase Center Variation in the Geodetic TI 4100 GPS Receiver System's Conical Spiral Antenna. In: Goad, C. C. (Ed.), *Proceedings of the First International Symposium on Precise Positioning with the Global Positioning System, April 15-19, Rockville, USA*, Volume 1, pp. 227–244. International Union of Geodesy and Geophysics, International Association of Geodesy, U.S. Department of Defense and U.S. Department of Commerce.

Smyrnaios, M., Schön, S., Liso, M., and Jin, S. (2013). Multipath propagation, characterization and modeling in GNSS. *Geodetic sciences-observations, modeling and applications*, pp. 99–125.

Stępniak, K., Krzan, G., and Paziewski, J. (2023). Impact of individual antenna phase center models and multi-GNSS observations on tropospheric estimates. In: *EGU General Assembly 2023, April 2023, Vienna, Austria.* Presentation.

Sutyagin, I. and Tatarnikov, D. (2020). Absolute robotic GNSS antenna calibrations in open field environment.

*GPS Solutions*, 24(4):1–18.

Teunissen, P. J. (2021). GNSS Precise Point Positioning. In: Y. T. Jade Morton; Frank van Diggelen; Spilker Jr., J. J. B. W. P. (Ed.), *Position, Navigation, and Timing Technologies in the 21st Century: Integrated Satellite Navigation, Sensor Systems, and Civil Applications*, pp. 503–528. John Wiley & Sons, Inc., Hoboken, New Jersey.

Tranquilla, J. B. and Colpitts, B. G. (1989). GPS Antenna Design Characteristics for High-Precision Applications. *Journal of Surveying Engineering (ASCE)*, 115(1):2–14.

Tupek, A., Zrinjski, M., Barković, Đ., and Špoljar, K. (2024). Absolute GNSS Receiver Antenna Calibration at the Faculty of Geodesy–University of Zagreb. In: *9th International Conference Contemporary Achievements in Civil Engineering 2024*, pp. 604–616.

Tupek, A., Zrinjski, M., Švaco, M., and Barkovič, D. (2023). GNSS Receiver Antenna Absolute Field Calibration System Development: Testing and Preliminary Results. *Remote Sensing*, 15(18).

Villiger, A., Prange, L., Dach, R., Zimmermann, F., Kuhlmann, H., and Jäggi, A. (2019). GNSS scale determination using chamber calibrated ground and space antenna pattern. In: *Geophysical Research Abstracts*, Nummer 21.

Wang, Z., Bovik, A., Sheikh, H., and Simoncelli, E. (2004). Image quality assessment: from error visibility to structural similarity. *IEEE Transactions on Image Processing*, 13(4):600–612.

Wanninger, L., Sumaya, H., and Beer, S. (2017). Group delay variations of GPS transmitting and receiving antennas. *Journal of Geodesy*, 91:1099–1116.

Ward, P. W. (2017). GNSS Reeceivers. In: Kaplan, E. D. and Hegarty, C. J. (Ed.), *Understanding GPS/GNSS Principles and Applications*, GNSS Technology and Application Series, pp. 339–543. Artech House, third edition.

Wieser, A. (2007). *GPS based velocity estimation and its application to an odometer*. Shaker-Verlag, Aachen.

Willi, D. and Guillaume, S. (2019). Calibration of a six-axis robot for GNSS antenna phase center estimation. *Journal of surveying engineering*, 145(4):04019016.

Willi, D., Koch, D., Meindl, M., and Rothacher, M. (2018). Absolute GNSS Antenna Phase Center Calibration with a Robot. In: *Proceedings of the 31st International Technical Meeting of The Satellite Division of the Institute of Navigation (ION GNSS+ 2018)*, pp. 3909–3926.

Willi, D., Lutz, S., Brockmann, E., and Rothacher, M. (2020). Absolute field calibration for multi-GNSS receiver antennas at ETH Zurich. *GPS Solutions*, 24(1).

Won, J.-H. and Pany, T. (2017). Signal Processing. In: Teunissen, P. J. and Montenbruck, O. (Ed.), *Springer Handbook of Global Navigation Satellite Systems*, pp. 401–442. Springer International Publishing AG.

Wu, J., Wu, S., Hajj, G., Bertiger, W., and Lichten, S. (1993). Effects of antenna orientation on GPS carrier phase. *Manuscripta geodaetica*, 18:91–98.

Wübbena, G., Menge, F., Schmitz, M., Seeber, G., and Völksen, C. (1996). A New Approach for Field Calibration of Absolute Antenna Phase Center Variations. In: *Proceedings of the 9th International Technical Meeting of the Satellite Division of The Institute of Navigation (ION GPS 1996), September 17-20, Kansas City, MO*, pp. 1205–1214.

Wübbena, G., Schmitz, M., Menge, F., Böder, V., and Seeber, G. (2000). Automated Absolute Field Calibration of GPS Antennas in Real-Time. In: *Proceedings of the 13th International Technical Meeting of the Satellite Division of The Institute of Navigation (ION GPS 2000), September 19-22, Salt Lake City, UT, USA*, pp. 2512–2522. Institute of Navigation (ION).

Wübbena, G., Schmitz, M., and Propp, M. (2008). Antenna Group Delay Calibration with the Geo++ Robot-extensions to code observable. In: *IGS analysis workshop, poster, June*, pp. 2–6.

Wübbena, G., Schmitz, M., and Warneke, A. (2019). Geo++ Absolute Multi Frequency GNSS Antenna Calibration. In: *Presentation at the EUREF Analysis Center (AC) Workshop, October 16 - 17, Warsaw, Poland*. URL: http://www.geopp.com/pdf/gpp_cal125_euref19_p.pdf [29.01.2020].

Wübbena, G., Schmitz, M., Menge, F., Seeber, G., and Völksen, C. (1997). A New Approach for Field Calibration of Absolute GPS Antenna Phase Center Variations. *Navigation*, 44(2):247–255.

Yang, Y., Tang, J., and Montenbruck, O. (2017). Chinese Navigation Satellite Systems. In: Teunissen, P.

J. G. and Montenbruck, O. (Ed.), *Springer Handbook of Global Navigation Satellite Systems*, pp. 273–304. Springer.

Zeimetz, P. (2010). *Zur Entwicklung und Bewertung der absoluten GNSS-Antennenkalibrierung im HF-Labor*. Diss., Institut für Geodäsie und Geoinformation, Universität Bonn.

Zhou, R., Hu, Z., Zhao, Q., Chen, G., and Tao, J. (2023). Absolute field calibration of receiver antenna phase center models for GPS/BDS-3 signals. *Journal of Geodesy*, 97(9):83.

# List of Figures


2.1 Flowchart illustrating the structure of the fundamentals. . . . 6
2.2 Overview of center frequencies and respective frequency band specificators for BeiDou, Galileo, GLONASS, and GPS signals. . . . 7
2.3 GPS L1 antenna gain of a *NOV703GGG.R2 NONE* antenna for RHCP and LHCP signals. . . . 9
2.4 MPSI values for a *NOV703GGG.R2 NONE* antenna. . . . 11
2.5 $C/N_0$ values versus elevation angle and their influence on the standard deviation of carrier-phase noise. . . . 15
2.6 Sketches of observation differencing strategies. . . . 20
2.7 Extract from the *antenna.gra* file for a *LEIAR25.R3/LEIAR25.R4* antenna. . . . 24
2.8 Geometric interpretation of PCC. . . . 24
2.9 Minimal example for representing PCC in the ANTEX format. . . . 25
2.10 General calibration setups for method CHAMBER and ROBOT. . . . 27
2.11 General measurement setup for method CHAMBER. . . . 29

3.1 Different representations of $\Delta\text{PCC}_{\text{sim}}$. . . . 39
3.2 Representation of $\Delta\text{PCC}_{\text{sim}}$ broken down into its individual components. . . . 39
3.3 Different representations of $\Delta\text{PCC}_{\text{real}}$ for GPS L1 and L2. . . . 40
3.4 Different graphical representations of $\Delta\text{PCC}_{\text{sim}}$ and $\Delta\text{PCC}_{\text{real}}$ for comparing different sets of PCC. 41
3.5 Uncorrected GL1C SD (PRN12) with color-coded ΔPCC between *NOV703GGG.R2 NONE* and *LEIAR25.R3 LEIT* antenna from different calibration facilities. . . . 46
3.6 Flowchart illustrating the main components and steps of the developed simulation approach. . 47
3.7 Selected IGS stations for visualizing weighting matrix $\mathbf{P_2}$. . . . 48
3.8 Local satellite distributions for three selected IGS stations. . . . 49
3.9 Impact of $\Delta\text{PCC}_{\text{sim}}$ and $\Delta\text{PCC}_{\text{real}}$ at different geographic locations for various frequencies and linear combinations. . . . 50
3.10 Impact of ΔPCC on geodetic parameters: comparison between simulation and PPP using real observation data. . . . 52

4.1 Calibration of the robot used for antenna calibrations at IfE. Calibration of the robot is carried out in the 3D-Labatory of the GIH. . . . 54
4.2 Sketch of the robot mounted on the geodetic pillar and the fixed point in space, around which the robot is tilting and rotating the AUT. . . . 55
4.3 Flowchart representing the overall process of data acquisition and preprocessing for determining PCC. . . . 56
4.4 Digital model of the calibration facility environment at IfE. . . . 57
4.5 Distribution and number of observations of GPS GL1C and Galileo EL1C during a *standard* calibration (duration ≈ 4.5 h). . . . 58
4.6 Robot poses for calibration of a *NOV703GGG.R2* antenna. . . . 59
4.7 Relation between topocentric and antenna frame. . . . 60
4.8 Distribution of time differences Δt between consecutive dSD epochs for one calibration set. . . . 60
4.9 Comparison of dSD time series without and with corrected PWU correction values. . . . 62
4.10 Proportion of theoretically possible observations in the antenna frame per GNSS and 5° elevation bin. . . . 63
4.11 Tunable parameters for separating PCC into PCO, PCV, and constant $r$ components. . . . 67
4.12 Illustration of averaged PCC* per elevation angle, where the individual components were separated using different methods, before computing PCC*. . . . 69
4.13 PCO and $r$ components extracted from PCC by different methods. . . . 69
4.14 Pure PCV, separated from PCC using different methods, depicted as averaged variations per elevation angle. . . . 70
4.15 Flowchart illustrating the overall process of the closed-loop simulation process, detailing each major step of the methodology. . . . 72
4.16 Averaged ΔPCC values per elevation angle from closed-loop simulations using different strategies. 73

5.1 AUTs mounted on robot . . . 75
5.2 Estimated GL1C PCC for antennas NOV, LEI and UBX. . . . 76
5.3 Estimated NOV PCC* for selected GPS and Galileo frequencies . . . 77

5.4 Estimated NOV PCC* for various frequencies and systems, represented as mean values per elevation angle. . . . 78
5.5 Analysis of estimated NOV PCC for GLONASS frequencies. . . . 79
5.6 Residuals of estimated NOV GL1C PCC. . . . 80
5.7 Residuals of estimated NOV GL2W PCC. . . . 80
5.8 Residuals of estimated NOV GL2L PCC. . . . 81
5.9 Residuals of estimated NOV EL1C PCC. . . . 81
5.10 Quality metrics of estimated NOV PCC. . . . 82
5.11 Averaged formal errors per 5° elevation angle for estimated NOV PCC. . . . 82
5.12 Estimated LEI PCC* for selected GPS and Galileo frequencies. . . . 83
5.13 Estimated LEI PCC* for various frequencies and systems, represented as mean values per elevation angle. . . . 84
5.14 Residuals of estimated LEI GL1C PCC. . . . 84
5.15 Quality metrics of estimated LEI PCC. . . . 85
5.16 Averaged formal errors per 5° elevation angle for LEI PCC. . . . 85
5.17 Estimated UBX PCC for selected GPS and Galileo frequencies. . . . 86
5.18 Estimated UBX PCC for GPS and Galileo frequencies represented as mean values per elevation angle. . . . 87
5.19 Residuals of estimated UBX GL1C PCC. . . . 87
5.20 Quality metrics of estimated UBX PCC. . . . 88
5.21 Averaged formal errors per 5° elevation angle for UBX PCC. . . . 88
5.22 Comparison between estimated GL1C PCC* and input observations for all three antennas. . . . 89
5.23 Comparison between estimated GL2W PCC* and input observations for NOV and LEI. . . . 89
5.24 Comparison between estimated EL1C PCC* and input observations for all investigated antennas 90
5.25 Comparison of a priori variance factors and variance of input dSD among NOV, LEI, and UBX PCC for selected frequencies. . . . 90
5.26 MP-LC and ΔMP-LC for the three investigated AUTs and the antenna mounted on the reference station *MSD8*. . . . 91
5.27 Calibration times of the seven individual sets on DOY047 and DOY048 in year 2023. . . . 93
5.28 Robot poses for seven individual calibration sets. . . . 93
5.29 Number of used observations per calibration set and frequency. . . . 94
5.30 Cumulative histogram of absolute values of ΔPCC for all possible set combinations. . . . 95
5.31 ΔPCC for the defined cases, shown as mean differences per elevation angle. . . . 95
5.32 ΔPCC presented as mean differences per elevation angle, along with differences in available observations per 5° elevation angle bin. . . . 96
5.33 Distribution of differences in the number of observations for the three defined cases, displayed as stereographic projections. . . . 96
5.34 Illustration of quality parameters after LSA to compare similarity of different PCC sets. . . . 97
5.35 Cumulative histogram of unnormalized dSD residuals for the above defined cases. . . . 97
5.36 Differences of *mixed* GLONASS frequencies to the respective *center* frequency. . . . 98
5.37 Measurement setup used to analyze the PCC estimation repeatability with different receivers. . 99
5.38 Impact of different receivers on estimated GL1C PCC, presented as averaged PCC* and averaged ΔPCC per elevation angle. . . . 99
5.39 Impact of different receivers on estimated GL5Q/GL5X PCC, presented as averaged PCC* and averaged ΔPCC per elevation angle. . . . 100
5.40 Impact of different receivers on estimated EL1C/EL1X PCC, presented as averaged PCC* and averaged ΔPCC per elevation angle. . . . 101
5.41 Input dSD and residuals after GL1C PCC estimation with different receivers. . . . 102
5.42 Input dSD and residuals after GL5Q/GL5X PCC estimation with different receivers. . . . 102
5.43 Input dSD and residuals after EL1C/EL1X PCC estimation with different receivers. . . . 103
5.44 NOV ΔPCC between identical frequencies from different GNSS. . . . 104
5.45 Impact of ΔPCC between identical frequencies (from different GNSS) on position solutions using the developed simulation approach. . . . 105
5.46 Impact of ΔPCC between identical frequencies (from different GNSS) on geodetic parameters. 106
5.47 Comparison of estimated NOV PCC with type-mean calibrations from the file *igs20_2343.atx*. . 107

6.1 Flowchart illustrating the calibration procedure, highlighting adjustable parameters. . . . 110
6.2 Input dSD versus GPS time for calibrations with identical robot poses. Sets 1 and 2 are conducted with the same GPS satellite constellation as far as possible, considering sidereal repetition time. 111
6.3 Input dSD for all visible satellites versus robot pose index for calibrations with identical robot poses. . . . 112
6.4 Differences in the number of observations for selected GPS and Galileo frequencies. . . . 113
6.5 Averaged PCC* and ΔPCC per elevation angle bin between calibration sets, used to analyze the impact of calibration time and length on resulting PCC. . . . 114

6.6 Properties of PCC estimations with varying degrees and orders for HSH expansions. . . . . 115
6.7 Estimated GL1C PCO and $r$ components using different degrees and orders for HSH expansions 117
6.8 Averaged PCC* per elevation angle, estimated with different degree and orders for HSH expansions. 117
6.9 Stereographic projections of $M_i$ matrices resulting from SVD of PCC, estimated using different HSH expansions: HSH(1,0), HSH(1,1), and HSH(2,1). . . . . 119
6.10 Illustration of ΔPCC between different PCC parametrizations using various HSH expansions. . 120
6.11 Impact of PCC estimated using different degrees and orders in the HSH expansion. Differences are calculated relative to HSH(12,12), and the impact is averaged over three days. In addition, minimum and maximum values are presented, too. . . . . 120
6.12 Flowchart illustrating the analysis strategy for investigating the impact of stabilization methods on the NES within the PCC estimation algorithm. . . . . 122
6.13 Comparison of PCC estimated using different stabilization methods with respect to method (A), represented as mean differences per elevation angle. . . . . 123
6.14 ΔGL1C PCC resulting from PCC estimations using different methods to stabilize the NES, depicted as stereographic projections. . . . . 124
6.15 Averaged standard deviations $\sigma$ per elevation angle bin of estimated GL1C PCC using different stabilization methods, with $\sigma_0^2 = 4.01\,\mathrm{mm}^2$ for all methods. . . . . 125
6.16 Residuals and residual differences with respect to method (A) from closed-loop simulations, validating different methods to stabilize the NES. . . . . 126
6.17 Ratio of $\hat{0}^2$ to $\sigma_0^2$ for different methods to stabilize the NES. . . . . 127
6.18 Simulated dSD, real dSD, and simulated dSD with added white noise characterized by $\sigma$=4 mm and $\mu$=0 mm (WN(0,4)) for PRN01. . . . . 127
6.19 Results of closed-loop simulations with added identical white noise sequences to simulated GL1C dSD in terms of maximum, absolute deviations, standard deviations and mean ΔPCC. . . . . 128
6.20 Results of closed-loop simulations with added identical white noise sequences to simulated CL2I dSD in terms of maximum, absolute deviations, standard deviations and mean ΔPCC. . . . . 129
6.21 Results of closed-loop simulations with added identical white noise sequences to simulated GL1C and CL2I dSD, depicted as absolute ΔPCC values in cumulative histograms. . . . . 130
6.22 Stereographic projections of Δ GL1C PCC resulting from one single closed-loop simulation with identical white noise sequences. . . . . 130
6.23 Overlapping representation of original dSD time series with highlighted *leverage observation* from PRN06 and the corresponding modified *leverage observation* with an added offset of 3 cm. . . . 131
6.24 GL1C ΔPCC represented as averaged differences per elevation angle bin, from a closed-loop simulation where a 30 mm outlier was added to the determined *leverage observation*. . . . . 132
6.25 GL1C ΔPCC represented as averaged differences per elevation angle, from a closed-loop simulation where approximately 16% of all observations (6274 observations from PRN12) were removed. 133
6.26 Flow chart for developing and applying different weighting models for PCC estimation. . . . . 134
6.27 Illustration of input dSD time series used to determine noise factors $a_\sigma^2$. . . . . 134
6.28 Normalized residuals for different values of $a_\sigma^2$. . . . . 135
6.29 Averaged PCC differences per elevation angle bin between PCC estimated with unit-weighting and developed weighting schemes for three AUTs and selected GPS and Galileo frequencies. . . 136
6.30 Cumulative histograms showing the absolute and normalized GL1C residuals for three different antenna types, using various weighting schemes. . . . . 138
6.31 Averaged formal errors per elevation angle bin of GL1C PCC estimated using different weighting schemes. . . . . 138
6.32 Averaged formal errors per elevation angle bin and cumulative histogram of absolute normalized residuals of GL5Q PCC for LEI, estimated using different weighting schemes. . . . . 138
6.33 Averaged PCC differences per elevation angle bin between PCC estimated with unit-weighting and developed weighting schemes for different antenna-receiver combinations and selected GPS and Galileo frequencies. The NOV antenna is used for all combinations. . . . . 139
6.34 Influence of PCC grid resolution on bi-linearly interpolated correction values (re-sampling), presented as mean ΔPCC per elevation angle bin. . . . . 141
6.35 Influence of different PCC grid resolutions on estimated PCO and constant $r$ parts . . . . . 142
6.36 Stereographic projections depicting the impact of different PCC resolutions on LOS correction values. . . . . 143
6.37 Impact of different PCC grid resolutions ($\Delta(1^\circ - 5^\circ)$) on geodetic parameters using the developed simulation approach. . . . . 144
6.38 Kinematic trajectories used to analyze the impact of PCC grid resolutions on position estimates. 144
6.39 Analyses of different PCC grid resolutions on 3D topocentric position estimates for the open-sky experiment, shown as absolute differences w.r.t. the *direct* method. . . . . 145
6.40 Analyses of different PCC grid resolutions on 3D topocentric position estimates for the urban experiment, shown as absolute differences w.r.t. the *direct* method. . . . . 145

7.1 Measurement setup for validating estimated NOV PCC in the observation domain using a short baseline, common-clock configuration. . . . 148
7.2 Resulting SD time series along with different PCC correction values for GL1C and EL1X frequencies. . . . 149
7.3 Improvements achieved by applying different GL1C correction values to dSD time series during a calibration procedure. The improvement is evaluated in terms of the mean standard deviation of the dSD. . . . 151
7.4 Distribution of 16 of 17 stations used for analyzing the impact of ΔPCC on reference station. In addition to these stations located in Germany, station ISTA located in Istanbul, Turkey, is additionally considered. . . . 152
7.5 Impact of varying individual PCC calibrations, either obtained from method ROBOT or method CHAMBER, on geodetic parameters. . . . 153
7.6 Differences between the results of the simulation approach and the PPP-processed real data concerning the impact of varying PCC sets on geodetic parameters. . . . 153
7.7 Impact of ΔPCC on geodetic parameters with varying processing parameter. The impact is presented over a three-year time span. . . . 155
7.8 Impact of ΔPCC on geodetic parameters with varying processing parameters. . . . 156
7.9 Frequencies identified from the 3-year impact of ΔPCC on the Up-component using Fourier transformations. . . . 156
7.10 Impact of ΔPCC on the topocentric Up-component, calculated on a regular 5° latitude and longitude grid. The visualization highlights variations in the impact across different geographic locations. . . . 157
7.11 Impact of ΔPCC on geodetic parameters, calculated on a regular 5° latitude and longitude grid. 158
7.12 Measurement setup and GPS ΔPCC as mean differences per elevation angel bin for analyzing the impact of ΔPCC on GNSS-based frequency transfer. . . . 159
7.13 Resulting differential receiver clock error time series, obtained by applying different PCC sets, to assess the impact on frequency transfer. . . . 160
7.14 MDEV of estimated differential receiver clock errors for PPP and SD methods, while applying different PCC sets. . . . 161

A.1 Estimated NOV PCC* for GPS frequencies. . . . 167
A.2 Estimated NOV PCC* for Galileo frequencies. . . . 168
A.3 Estimated NOV PCC* for GLONASS frequencies. . . . 168
A.4 Estimated NOV PCC* for BeiDou frequencies. . . . 169
A.5 Estimated LEI PCC* for GPS frequencies. . . . 169
A.6 Estimated LEI PCC* for Galileo frequencies. . . . 170
A.7 Estimated LEI PCC* for GLONASS frequencies. . . . 170
A.8 Estimated LEI PCC* for BeiDou frequencies. . . . 171
A.9 Estimated UBX PCC for GPS frequencies. . . . 171
A.10 Estimated UBX PCC for Galileo frequencies. . . . 171

B.1 Residuals of estimated LEI GL2W PCC. . . . 173
B.2 Residuals of estimated LEI EL1C PCC. . . . 174
B.3 Residuals of estimated UBX EL1C PCC. . . . 175

# List of Tables


1.1 Main contributions of this thesis. . . . 3

2.1 Typical MPSI values and their interpretation. . . . 12
2.2 Frequency specifications for GNSS frequencies in ANTEX and RINEX files. . . . 16
2.3 Conspectus of different GPS and Galileo coefficients $\beta_1$ and $\beta_2$ for calculating the IF-LC and their resulting noise amplification factors $f_\sigma$. . . . 18
2.4 Major GNSS error sources. . . . 20
2.5 PPP a priori corrections and their magnitudes. . . . 23
2.6 Summary of different calibration facilities using method ROBOT. . . . 36

3.1 Characteristic values for comparing different sets of PCC and their dependency on the constant part $r$. Values are given for $\Delta\mathrm{PCC}_{\mathrm{real}}$. . . . 42
3.2 Characteristic values of $\Delta\overline{PCV}_{\mathrm{real}}$ ($(z = 0) \neq 0$) for GPS L1, L2 frequencies and linear combinations . . . . 43

4.1 Methods for separating PCC into PCO, PCV and $r$ components. . . . 68
4.2 PCC values at 90° elevation angle for selected cases, demonstrating different strategies for separating PCC into its individual components. . . . 70
4.3 Strategies for conducting closed-loop simulations to validate the PCC estimation algorithm. . . . 73

5.1 Assigned GLONASS frequency channels to individual satellites. . . . 78
5.2 Overview of GPS and Galileo frequencies tracked by different receivers. . . . 100
5.3 Overview of GLONASS and BeiDou frequencies tracked by different receivers. . . . 100
5.4 Variances of input dSD for different receivers and selected GPS and Galileo frequencies. . . . 103
5.5 A posteriori variance factors of estimated PCC by different receivers for selected GPS and Galileo frequencies. . . . 103
5.6 NOV ΔPCC between identical frequencies (from different GNSS). . . . 104

6.1 Standard deviations $\sigma$ of input dSD. . . . 112
6.2 Maximum number of observation differences within each 5° azimuth and elevation bin. . . . 112
6.3 Interpretation of estimated HSH coefficients. . . . 116
6.4 Condition numbers of NES for various frequencies and stabilization methods. . . . 123
6.5 Constant $r$ values subtracted from PCC, estimated with various stabilization methods, to facilitate improved comparison between different PCC sets. . . . 124
6.6 Determined noise factors $a_\sigma^2$ for elevation-dependent and $C/N_0$-dependent weighting schemes for GPS and Galileo frequencies (AUT: NOV, receiver: *Septentrio PolaRx5TR*). . . . 135
6.7 Determined noise factors $a_\sigma^2$ for elevation-dependent and $C/N_0$-dependent weighting schemes for GLONASS and BeiDOu frequencies (AUT: NOV, receiver: *Septentrio PolaRx5TR*). . . . 135
6.8 Comparison of GL1C condition numbers for different AUTs and weighting schemes. . . . 137
6.9 Comparison of GL1C a posteriori variance factors for different AUTs and weighting schemes. . . . 137
6.10 Determined noise factors for different antenna-receiver combinations using the identical AUT – a *NOV703GG.R2 NONE*. . . . 140
6.11 Summary of impacts on PCC: Maximum differences at the pattern level and influences on the position domain based on various investigation scenarios. . . . 146

7.1 Improvements achieved by applying different GL1C correction values to SD time series, evaluated in terms of the overall mean and maximum standard deviation for a single satellite arc. . . . 150
7.2 Impact of different elevation cut-off angles on the mean improvement of SD time series, with the application of an individual PCC set for the antenna at the reference station. . . . 150
7.3 Varying processing parameters used to assess the impact of ΔPCC on geodetic parameters. . . . 154
7.4 Mean differential receiver clock error values for PPP and SD methods. . . . 160

# Acronyms

| | |
|---|---|
| **AltBOC** | Alternative BOC |
| **ANTEX** | Antenna Exchange Format |
| **AR** | Axial Ratio |
| **ARP** | Antenna Reference Point |
| **AUT** | Antenna Under Test |
| **AWG** | Antenna Working Group |
| **BDS** | BeiDou Navigation Satellite System |
| **BOC** | Binary Offset Carrier |
| **BPA** | Bottom of Preamplifier |
| **BPSK** | Binary Phase Shift Keying |
| **$C/N_0$** | Carrier-to-Noise-Power-Density Ratio |
| **CC** | Codephase Center |
| **CDMA** | Code Division Multiple Access |
| **CPC** | Codephase Center Corrections |
| **DD** | Double Differences |
| **dDD** | time-differenced Double Differences |
| **DLL** | Delay Lock Loop |
| **DLR** | Deutsches Zentrum für Luft- und Raumfahrt |
| **DOP** | Dilution Of Precision |
| **DOY** | Day Of Year |
| **dSD** | time-differenced Single Differences |
| **ECEF** | Earth-Centered, Earth-Fixed |
| **EPN** | European Permanent Network |
| **ETH** | Eidgenössische Technische Hochschule |
| **FBR** | Front-to-Back Ratio |
| **FDMA** | Frequency Division Multiple Access |
| **FNBW** | First-Null Beam Width |
| **GBAS** | Ground Based Augmentation System |
| **GD** | Group Delay |
| **GDV** | Group Delay Variations |
| **GF-LC** | Geometry-Free Linear Combination |
| **GFZ** | GeoForschungsZentrum |
| **GIH** | Geodetic Institute Hannover |
| **GLONASS** | Globalnaja Nawigazionnaja Sputnikowaja Sistema |
| **GNSS** | Global Navigation Satellite System |
| **GPS** | Global Positioning Service |
| **GSA** | Geoscience Australia |
| **GUM** | Guide to the Expression of Uncertainty in Measurement |
| **HPBW** | Half Power Beam Width |
| **HSH** | Hemispherical Harmonics |
| **IF-LC** | Ionosphere-Free Linear Combination |
| **IfE** | Institut für Erdmessung |
| **IGS** | International GNSS Service |
| **IKN** | Institut für Kommunikation und Navigation |
| **IRNSS** | Indian Regional Navigation Satellite System |
| **ISB** | Inter System Biases |
| **ITRF** | International Terrestrial Reference Frame |
| **ITU** | International Telecommunications Union |
| **LC** | Linear Combination |
| **LHCP** | Left-Hand Circular Polarization |
| **LOS** | Line-of-Sight |
| **LSA** | Least-Squares Adjustment |
| **MDEV** | Modified Allan Deviation |
| **MP** | Multipath |
| **MP-LC** | Multipath Linear Combination |
| **MPR** | Multipath Ratio |
| **MPSI** | Multipath Suppression Indicators |

| | |
|---|---|
| $\mathbf{N}_G$ | Geographic North |
| $\mathbf{N}_M$ | Magnetic North |
| **NCO** | Numerically Controlled Oscillator |
| **NES** | Normal Equation System |
| **NGS** | National Geodetic Survey |
| **NO** | North Offset |
| **NOM** | North Orientation Mark |
| **NRP** | North Reference Point |
| **NTP** | Network Time Protocol |
| **NWA** | Network Analyzer |
| **OMC** | Observed-Minus-Computed |
| **PC** | Phase Center |
| **PCC** | Phase Center Corrections |
| **PCO** | Phase Center Offset |
| **PCV** | Phase Center Variations |
| **PDOP** | Position Dilution Of Precision |
| **PLL** | Phase Lock Loop |
| **PPP** | Precise Point Positioning |
| **PPS** | Pulse-Per-Second |
| **PRN** | Pseudo Random Noise |
| **PTB** | Physikalisch-Technische Bundesanstalt |
| **PWU** | Phase Wind-Up |
| **RDSS** | Radio Determination Satellite Service |
| **RF** | Radio Frequency |
| **RHCP** | Right-Hand Circular Polarization |
| **RINEX** | Receiver Independent Exchange Format |
| **RMS** | Root Mean Square |
| **RNSS** | Radio Navigation Satellite Service |
| **RP** | Radiation Pattern |
| **RTK** | Real-Time Kinematic |
| **SD** | Single Differences |
| **SenB** | Senatsverwaltung für Stadtentwicklung Berlin |
| **SH** | Spherical Harmonics |
| **SPP** | Single Point Positioning |
| **SSIM** | Structural SIMilarity |
| **SURF** | Speeded-Up Robust Features |
| **SVD** | Singular Value Decomposition |
| **TD** | Tripple Differences |
| **VCM** | Variance Covariance Matrix |
| **VLBI** | Very Long Baseline Interferometry |
| **VSWR** | Voltage Standing Wave Ratio |
| **ZTD** | Zenith Total Delay |
| **ZWD** | Zenith Wet Delay |

# Acknowledgement

I am immensely grateful to Prof. Dr.-Ing. Steffen Schön for giving me the opportunity to work on my PhD at the Institut für Erdmessung (IfE). His constant support and the many fruitful discussions we've had were invaluable to my doctoral journey. Without his guidance and input, this work would not have reached its current form. My time at the institute was greatly enriched by the insights I gained from him.

I would also like to express my gratitude to the reviewers, Prof. Dr.-Ing. habil. Christian Heipke and Prof. Dr. Rolf Dach, for reading the thesis and providing valuable comments.

Special thanks go to Dr.-Ing. Tobias Kersten for his profound advice throughout the entire process. With great patience, he introduced me to the topic of GNSS receiver antenna calibration and consistently supported me with his insights and assistance.

I am thankful to my good friends Dr.-Ing. Annike Knabe, Dr.-Ing. Yannick Breva, and Thomas Maschke, who not only enriched my everyday work at the IfE but also ensured many discussions and enjoyable hours after work. Special thanks to Thomas Maschke, who was always extremely helpful, especially with practical experiments. A heartfelt thanks to Dr.-Ing. Yannick Breva, with whom I shared an office for most of my time at IfE and who continuously provided expert discussions.

Further thanks go to all my colleagues at IfE for their support during my time at the institute. Many have become dear friends. In particular, I would like to thank Anat Schaper for her thoroughly proofreading of my work and for providing many helpful comments and tips.

Last but not least, I wish to express my deepest gratitude to my family and friends, who have shown unwavering understanding, support, and love throughout this entire journey.